Physical and numerical modelling of particle settlement in a turbulent flow: implication for the settlement of algal propagules

---

A thesis submitted in partial fulfilment of the requirements for the

Degree

of Doctor of Philosophy in Ecology

in the University of Canterbury

by S. DELAUX

Department of Biological Sciences, University of Canterbury

National Institute of Water and Atmospheric Research Ltd

2009

Table of contents

Acknowledgements

I would like to express my most sincere gratitude to Dr. Stevens, Dr. Popinet and Pr. Schiel for supervising my Ph.D. I would especially like to thank them for all the inspirational discussions, their constant enthusiasm, support and availability and for believing in me.

Many thanks to the reviewers for taking the time to review this thesis.

Thanks to Dr. Taylor and Dr. Nokes for helpful collaboration and discussions.

I am very grateful to the Marsden fund of the Royal Society of New Zealand; the University of Canterbury and the National Institute of Water and Atmospheric Research Ltd, for funding this thesis.

Many thanks to the New Zealand Marine Sciences Society, and the New Zealand Mathematical Society, for their financial support which allowed me to present part of my work at the International Congress on Industrial and Applied Mathematics in Zurich (Switzerland) in 2007.

Thanks to Dr. Haarvard Holm for helping me to get access to the NOTUR Linux cluster Stallo.

Many thanks to Craig, Stéphane and my parents for their support and taking time to talk during the hardest phases of this Ph.D.

Thanks to Vanessa and Stéphane for helping me get installed in Wellington.

Thanks to Cédric for sharing most of these four years.

Thanks to Melissa for her support and standing by me during this very busy last year and a half.

Thanks to my grandmother for her support despite the long distance between France and New Zealand, and the very few occasions we had to catch up.

Thanks to Cathy, Melanie, Michelle (my biology mentor), Rym, Luc, Bastien, Natalie, Raph, Suzy, Pierre and the other students who passed by NIWA who made these four years very enjoyable.

Thanks to the different people who visited me in Wellington, the people who kept encouraging me (including my NIWA colleagues), and the guys from soccer who really helped me release negative energy when needed.

Abstract

A fundamental stage in rocky-shore seaweed life history is the recruitment process involving external fertilisation and then settlement of the propagules on a suitable substrate. The ultimate step in this settlement stage is the crossing of the viscous sub-layer and attachment to the substrate. Given the extreme conditions met in the intertidal zone, propagules can be dislodged at any time before they secure a strong enough anchoring.

Flow conditions and propagule properties are key to this process. The settlement process under turbulent conditions was recreated within a stirred benthic chamber for five different species. Whereas propagule properties (size, density) vary with species, and propagules are adapted to the different conditions in the intertidal, they exhibit the same settlement behaviour. They nevertheless exhibit different settling velocities and settlement thresholds. Several methods of characterisation of the tank flow from particle tracking velocimetry and acoustic Doppler velocimetry data are reviewed, as well as an analytical model. Turbulent settling was found to be independent of the well-mixed tank bulk flow and to depend only on the boundary-layer mechanics. A model of settlement threshold is presented from which propagule mucilage adhesiveness estimates are derived, leading to good correlations between adult plant exposure and the stickiness of its propagules and to the conclusion that settlement can only occur in calm conditions.

To extend the work, computational fluid dynamic techniques are developed by extending the Gerris Flow Solver. A 2-D approach to tank modelling and a pilot study of expansion to 3-D is described. This extends the perspective given by the experiments, notably through output of the hydrodynamical forces experienced by the propagules. Finally, in the view of realizing direct numerical simulations of propagule behaviour in the viscous sub-layer, a new and unique 2-D/3-D fully conservative solid/fluid interaction model is developed and tested with success.

Glossary

a_k Fourier coefficient associated with the frequency k

d_p propagule diameter (m)

d_i propagule stopping distance (m)

d_r substrate roughness characteristic size (m)

g gravity field acceleration ($m.s^{-2}$)

h water-column or tank height (m)

l integral scale (m)

p pressure (kg.m^{-1}.s^{-2})

$\bar{p}$ mean component of the pressure field (kg.m^{-1}.s^{-2})

p' fluctuation component of the pressure field (kg.m^{-1}.s^{-2})

r propagule radius (m)

rpm rotations per minute

t time (s)

x x-component of the position vector (m)

y y-component of the position vector (m)

z z-component of the position vector (m)

u x-component of the velocity field ($m.s^{-1}$)

$\bar{u}$ x-component of the mean velocity field ($m.s^{-1}$)

u' x-component of the fluctuation part of the velocity field ($m.s^{-1}$)

u'_i i th component of the fluctuation part of the velocity field ($m.s^{-1}$)

u_* friction velocity ($m.s^{-1}$)

u_p propeller characteristic velocity ($m.s^{-1}$)

u_η Kolmogorov velocity scale ($m.s^{-1}$)

u_∞ outer flow mean speed ($m.s^{-1}$)

v y-component of the velocity field ($m.s^{-1}$)

$\bar{v}$ y-component of the mean velocity field ($m.s^{-1}$)

v' y-component of the fluctuation part of the velocity field ($m.s^{-1}$)

w z-component of the velocity field ($m.s^{-1}$)

$\bar{w}$ z-component of the mean velocity field ($m.s^{-1}$)

w' z-component of the fluctuation part of the velocity field ($m.s^{-1}$)

$\boldsymbol{u}$ fluid velocity vector ($m.s^{-1}$)

$\boldsymbol{x}$ position vector (m)

A_p propagule adhesiveness (kg.$m.s^{-2}$)

ADV accoustic Doppler velocimetry

C_d drag coefficient

C_f skin friction drag coefficient

C_l lift coefficient

C_s Smagorinsky constant

D mass eddy-diffusion or turbulent diffusion ($m^2.s^{-1}$)

$\bar{D}$ average mass eddy-diffusion or turbulent diffusion ($m^2.s^{-1}$)

D_p propagule eddy-diffusion or turbulent diffusion ($m^2.s^{-1}$)

D_{TP} propagule turbulent diffusion ($m^2.s^{-1}$)

DNS direct numerical simulation

$E(k)$ energy associated with the frequency k ($m^2.s^{-2}$)

F_a adhesion forces (kg.$m.s^{-2}$)

F_d viscous drag forces (kg.$m.s^{-2}$)

F_l lift forces (kg.$m.s^{-2}$)

$\bar{G}$ filter function

H_w wave height (m)

KE kinetic energy ($m^2.s^{-2}$)

K_m scalar molecular diffusivity ($m^2.s^{-1}$)

L flow characteristic length scale (m)

L_w wave wavelength (m)

LES large-eddy simulation

N propeller speed (rotation per s)

N^* number of settled zygotes per unit area (m^{-2})

M moment of surface stress (kg.$m^2.s^{-2}$)

Pe Péclet number

Po Power number

Pr Prandtl number

Pr_t turbulent Prandtl number

PTV particle tracking velocimetry

Q propeller discharge flow ($m^3.s^{-1}$)

Re Reynolds number

Re_p buoyant particle Reynolds number

Re_{*p} friction particle Reynolds number

Re_{*} wall Reynolds number

Ro Rouse number

R_V ration of Stokes velocity to turbulent fluctuations

R_ρ propagule reduced density ratio

R_σ ratio of the propagule weight to the shear force at the bottom of the water column

Sc Schmidt number

S_{ij} rate of strain tensor (s^{-1})

$\overline{S_{\mathrm{ij}}}$ mean rate of strain tensor (s^{-1})

T_w wave period (s)

TKE turbulent kinetic energy ($m^2.s^{-2}$)

U streamwise characteristic velocity scale ($m.s^{-1}$)

V transverse characteristic velocity scale ($m.s^{-1}$)

V_p propagule settling velocity ($m.s^{-1}$)

W spanwise characteristic velocity scale ($m.s^{-1}$)

W_p propagule weight (kg)

V_s propagule Stokes velocity ($m.s^{-1}$)

V_t characteristic length scale of the turbulent fluctuations ($m.s^{-1}$)

δ_{ij} Kronecker's delta function

δ_ν viscous sub-layer thickness (m)

δ_t turbulent boundary-layer thickness (m)

ϵ energy dissipation rate ($m^2.s^{-3}$)

$\bar{\epsilon}$ mean energy dissipation rate ($m^2.s^{-3}$)

η Kolmogorov length scale (m)

κ von Karmann's constant

ν_f seawater kinematic viscosity ($m^2.s^{-2}$)

ν_t eddy or turbulent viscosity ($m^2.s^{-2}$)

μ_f seawater dynamic viscosity ($m^2.s^{-2}$)

μ_R particle diffusivity coefficient

ρ_f seawater density ($\mathrm{kg}.m^{-3}$)

ρ_p propagule density ($\mathrm{kg}.m^{-3}$)

τ_{ij} subgrid-scale stress tensor ($m^2.s^{-2}$)

τ_w wall shear stress ($\mathrm{kg}.m^{-1}.s^{-2}$)

τ_η Kolmogorov time scale (s)

θ propagule residence time (s)

θ_m mixing time (s)

$\Phi(k)$ the power spectral density associated with the frequency k

Θ propagule mean residence time (s)

∇ nabla operator

^{t} transposition operator

$^-$ ensemble average

Chapter 1
Introduction

1.1 The ecological problem

1.1.1 Seaweed propagule settlement

Despite hosting often hostile hydro-dynamical conditions, New Zealand's intertidal rocky shores sustain ecosystems composed of a large variety of species. A rich flora of seaweeds dominates and defines these communities [Schiel(1990)], forming habitat for many species. Key to the perpetuation of these ecosystems is the survival of the seaweed flora. Its extreme wave climate makes the rocky intertidal zone a physically challenging region for the survival and propagation of marine organisms [Stevens et al.(2002)] [Denny(1988)] [Koehl and Wainwright(1977)]. As for many other living organisms, the critical life-stage of fucoid algae has been identified to be the settlement period of their propagules [Vadas et al.(1992)] [Hadfield(1986)] [Walters et al.(1999)]. Several millions of propagules can be released at a time [Schiel and Foster(2006)] by a single macrophyte and success requires fertilisation, arrival on a suitable substrate, initial and permanent attachment on this same substrate [Clayton(1992)] [Norton(1992)].

Fucoid algae produce non-motile eggs that can be considered as passive drifters [Chapman(1995)], and have to reach the substratum by a combination of passive sinking and turbulent advection [Hendriks et al.(2006)]. Attachment takes places within the benthic boundary layer, a region of the flow dominated by the viscosity of the seawater. In order to reach the substrate, algal propagules need to cross this benthic boundary layer [Hendriks et al.(2006)] [Hurd(2000)].

Initial attachment of algal zygotes is realized through the use of specific adhesive mechanisms [Taylor and Schiel(2003)] which generally are the secretion of mucilage around the zygotes that hardens with time [Fletcher and Callow(1992)]. Little is known about the properties of these mucilages but they might be similar to the the secretion of glycoprotein adhesive observed by Callow and Callow [Callow and Callow(2002)] on the spores of the green alga *Enteromorpha*. When initial attachment is a success, the settlement process is not over and the propagules

still have to consolidate their attachment. It takes several hours of progressive increase of their attachment strength for the propagule to be considered as definitely attached [Finlay et al.(2002)] [Taylor and Schiel(2003)]. During this time, the propagules remain vulnerable and can still get resuspended by near-bottom turbulence [Crimaldi et al.(2002)].

Because of its numerous facets, a global understanding of the process of seaweed zygotes settling requires a multi-disciplinary approach involving botany, ecology, physics, chemistry and eventually numerical modelling.

1.1.2 Species

Five different kinds of seaweed propagules have been considered in this work. Three of them, *Hormosira banksii*, *Cystophora torulosa* and *Durvillaea antarctica* are New Zealand species, while the two others, *Fucus gardneri* and *Pelvetiopsis limitata*, originate from Oregon, USA. In a wide sense, a propagule is any plant material used for the purpose of plant propagation. Here for all of the studied species propagule is synonym with fertilized egg.

Characteristic of the most energetic locations on New Zealand and Chile's intertidal rocky shore [Hay(1994)], *Durvillaea antarctica* (Fucales, Durvillaeales) is a large brown seaweed anchored to the shore by a large holdfast terminated by several long blades (Figure 1.1). Besides its settlement ability, *Durvillaea antarctica* manages to survive in such extreme environments through its floating blades that help the kelp from sustaining mechanical damage when being exposed to oscillatory wave motion [Stevens et al.(2002)].

Figure 1.1. In situ photography of *Durvillaea antarctica* (left) and scanning electron microscopy picture of a propagule of *Durvillaea antarctica* taken by Dr. David I. Taylor.

Hormosira banksii (Fucales, Hormosiraceae) [Adams(1994)], also called Neptune's necklace, is a common seaweed found in rock pools at mid-tide levels and is characterised by strings of olive-brown hollow beads [Huisman(2000)]. Their buoyancy allows them to stand up in water to obtain more sunlight and to move with the flow of the current.

Cystophora torulosa (Fucales, Cystoseiraceae) is an intertidal seaweed of golden-brown color usually about one metre long made of one main stem with many lateral branches. It can generally be found on the rocks or in less exposed area such as tidal pools [Adams(1994)].

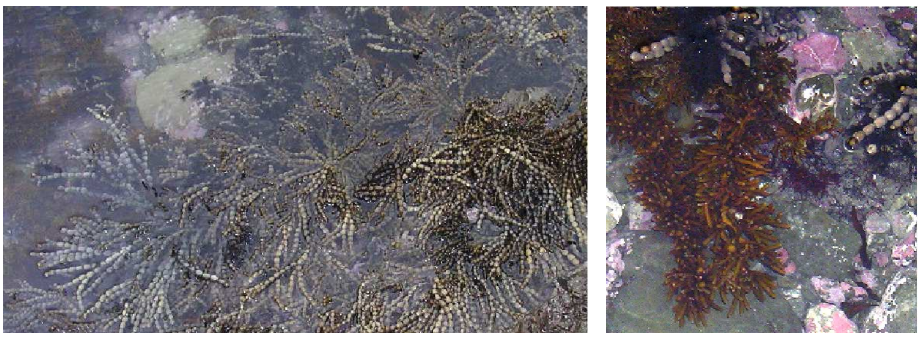

Figure 1.2. In situ photography of *Hormosira banksii* (left) and *Cystophora torulosa* (right).

The two other species are North-American species. *Fucus gardneri* (Fucales, Fucaceae) [Abbott and Hollenberg(1976)], also called rock weed, is one of the most abundant brown seaweeds. It inhabits the high to mid intertidal in both exposed and sheltered areas (Figure 1.3).

Pelvetiopsis limitata (Fucales, Fucaceae) [Abbott and Hollenberg(1976)] is a densely branched fucoid algae of tan to olive color mainly found on wave-exposed shores (Figure 1.3).

Figure 1.3. In situ photographs of *Pelvetiopsis limitata* (left) and *Fucus gardneri* by Daniel Mosquin (http://www.ubcbotanicalgarden.org).

All of these species of brown algae commonly inhabit the intertidal and are often exposed to extreme flow conditions. They all are fucoid algae which is the order of algae that dominates most of the intertidal and shallow subtidal rocky reef communities in the world [Stephenson and Stephenson(1949)]. Their presence affects their local environment by affecting nutrient storage [Hurd(2000)] [Stevens et al.(2003)] and sedimentation [Leonard and Luther(1995)] [Lopez and Garcia(1998)] [Palmer et al.(2004)]. Most importantly, they provide habitat and more sheltered conditions that many species of algae and inverteb-

rates require to persist in the middle and upper intertidal zones [Lewis(1964)]. This makes them key species affecting the biodiversity on temperate shores of the world [Chapman(1995)] [Schiel(2004)] [Schiel and Foster(2006)].

1.1.3 Propagule characteristics

Central to the study of propagule attachment is a need of knowing the basic characteristics of the different propagules. In particular, the size and the density of a propagule are two of the main quantities required to describe its interaction with the surrounding environment.

The diameter of the propagules was determined by Dr. David Taylor [Stevens et al.(2008)] by averaging the diameter of a 100 newly liberated eggs of each species (Table 1.1). These diameters were measured in a Petri dish using a micro-meter beneath a 100x binocular light microscope.

The densities were derived from experimentally measuring the sinking rates of newly liberated propagules and Stokes' law for sinking particles (Equation 1.1). The settlement speeds were measured in a settling column using particle tracking velocimetry (PTV). The PTV method is described in the next chapter. The measured sinking speeds being small, inertial effects should be negligible, and assuming that propagules can be assimilated to spherical particles, the Stokes sinking velocity should be a reasonable approximation of their sinking speed.

Stokes' law [Batchelor(1967)] is obtained using Newton's second law of mechanics [Newtown(1687)]. The propagules are sinking at a constant speed, with the viscous drag and Archimedes force acting against the propagule sinking and the sinking being due to gravity.

Gravity and Archimedes force can be expressed as a volume force exerted on the spherical propagule:

$$\frac{1}{6}\,\pi\, d_p^3\,(\rho_P - \rho_f)\, g.$$

The viscous drag is proportional to the velocity and to the radius of the propagule.

$$-\,3\,\pi\,\rho_f\, d_p\,\nu\, V_s.$$

Equating the two forces leads to the previously quoted expression of Stokes's sinking velocity

$$V_s = \frac{1}{18}\,\frac{1}{\nu_f}\left(\frac{\rho_p - \rho_f}{\rho_f}\right) g\, d_p^2 \tag{1.1}$$

with d_p the radius of the particle, g the gravity field acceleration, ρ_p the density of the particle, ρ_f the density of the fluid and ν_f the kinematic viscosity of the fluid [Lamb(1994)].

Using equation 1.1, the densities of the propagules are given by

$$\rho_p = \rho_f + 18\frac{V_s\ \rho_f \nu_f}{(d_p/2)^2 g} \tag{1.2}$$

with $\rho_f = 1024.3133$ kg.m^{-3} the measured density of the sea-water (a densimeter was used to measure the sea-water density) and $\nu_f = 1.003931.10^{-6}\, m^2.s^{-1}$ the dynamic viscosity of sea-water.

The physical properties of the zygotes are summarised in Table 1.1. The largest propagules are the ones of New Zealand species *Cystophora torulosa* and the Oregon species *Pelvetiopsis limitata* with diameters respectively of $101.0\,\mu m$ and $103.0\,\mu m$. With densities of $1.14\,g.\mathrm{cm}^{-3}$ these two types of propagules have very similar physical characteristics. The smallest propagules are the zygotes of *Durvillaea antarctica* with a diameter about three times smaller than the one of the previous species ($29.3\,\mu m$). As well as being the smallest propagules, *Durvillaea antarctica*'s zygotes are the densest with a density of $1.66\,g.\mathrm{cm}^{-3}$, by far the densest propagules in this group. In between, *Hormosira banksii* was found to have a diameter of $101.0\,\mu m\,(1.22)$ for a density of $1.25\,g.\mathrm{cm}^{-3}$ which is much less dense than *Durvillaea antarctica* but still significantly heavier than all the other species. The second Oregon species, *Fucus gardneri,* has a diameter of $74.0\,\mu m\,(1.86)$ for a density of $1.15\,g.\mathrm{cm}^{-3}$ which is close to the densities of *Cystophora torulosa* and *Pelvetiopsis limitata*'s.

Table 1.1. Physical properties of the seaweed zygotes of interest. The density was derived from the sinking rate using Stokes equation(1.2).

Species	Diameter $\mu m \pm s.e.$	Sinking rate mm.$s^{-1} \pm s.e.$	Density $g.\mathrm{cm}^{-3} \pm s.e.$
Durvillaea antarctica	29.3 (0.41)	0.29 (0.028)	1.66 (0.25)
Hormosira banksii	60.8 (0.158)	0.44 (0.075)	1.25 (0.15)
Cystophora torulosa	101.0 (1.22)	0.62 (0.078)	1.14 (0.06)
Fucus gardneri	74.0 (1.86)	0.37 (0.012)	1.15 (0.02)
Pelvetiopsis limitata	103.0 (1.64)	0.63 (0.032)	1.14 (0.02)

1.2 Physics and characteristic quantities

The process of settlement (Figure 1.4) that sees a propagule being released from an adult algae securing itself a spot on a suitable substrate can be decomposed in three phases or sub-problems:

- the sinking of the zygotes through the water column.

- the crossing of the boundary layer and initial attachment on the substratum.

- the eventual detachment of the propagules from the substratum.

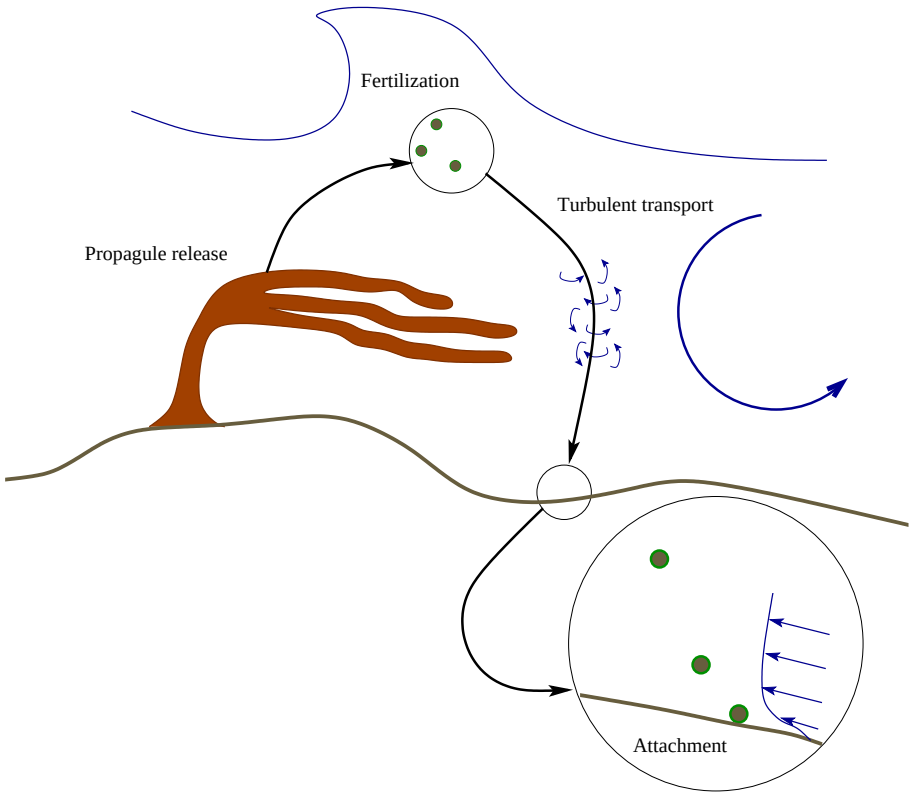

Figure 1.4. Propagule settlement process from release by the adult plant to attachment in the viscous sub-layer.

One common point between these sub-problems is the omnipresence of turbulence within the water column and in the vicinity of the sea-bed [Hendriks et al.(2006)]; nevertheless, a clear distinction has to be made between near-substratum velocity fluctuations and water column turbulence, with near-substratum velocity fluctuations being strongly influenced by boundary layer effects.

Because the final stages of propagule settlement are taking place in this environment and strongly rely on its physics, it is worth making a comprehensive introduction of the concept of boundary-layer and its characteristic turbulent velocity scale, the friction velocity. After an introduction to waves on the shore, these concepts will be presented.

1.2.1 Ocean waves

A consequence of the many interactions of oceans with external forces is the creation of waves of various types (sound, capillary, gravity, internal and planetary) [Massel(1996)]. Whereas tidal waves contain the most energy, wind-induced gravity ocean waves have a major impact on the seashore [Stevens et al.(2008)].

A first approach to ocean waves is the linear or Airy wave theory [Airy(1841)]. Despite the strong assumptions associated with this theory, its range of application is extensive [Young(1999)] and it continues to be used as a basis for engineering and scientific approaches to ocean waves (e.g. [Massel(1996)] [Young(1999)] [Denny(1988)] [USACE(1977)]).

Gravity forces, acting on water particles displaced from equilibrium at the ocean surface induce gravity waves [Massel(1996)] which can be described by a sine wave characterised by a wave height H_w, a period T_w and a wavelength L_w (Figure 1.5). The distance to the ocean bed or more exactly the ratio of the distance to the ocean bed over the wave-length $\frac{h}{L_w}$ is a key parameter to wave description. For $\frac{h}{L_w}>\frac{1}{2}$, the influence of the ocean bed is negligible and the waves are classified as deep water waves. For $\frac{h}{L_w}<\frac{1}{4}$, water depth is of great importance and the waves are classified as shallow water waves.

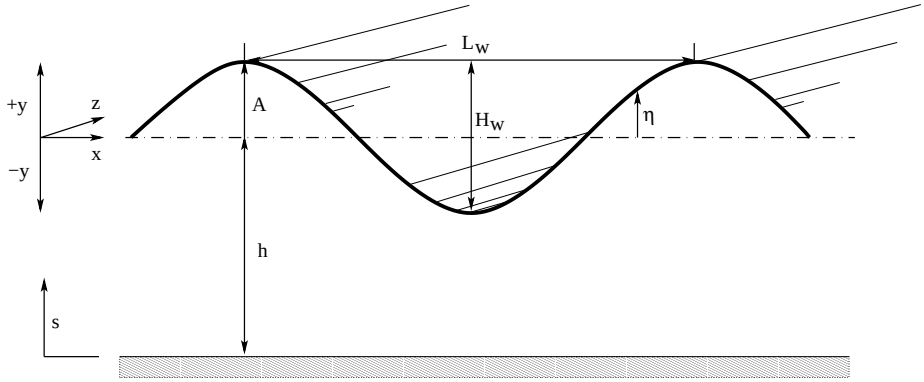

Figure 1.5. Definition of terms used to describe surface wave.

In both cases, water waves can be described by Airy's linear wave theory [Airy(1841)] and their horizontal and vertical local fluid velocities are given by

$$\begin{cases} u = \left(\frac{\pi H_w}{T_w}\right)\cos\left(\frac{2\pi x}{L} - \frac{2\pi t}{T_w}\right)\left[\frac{\cosh(\frac{2\pi}{L}(y+h))}{\sinh(\frac{2\pi}{L}\ h)}\right] \\ v = \left(\frac{\pi H_w}{T_w}\right)\sin\left(\frac{2\pi x}{L} - \frac{2\pi t}{T_w}\right)\left[\frac{\sinh(\frac{2\pi}{L}\ (y+h))}{\sinh(\frac{2\pi}{L}\ h)}\right] \end{cases} . \tag{1.3}$$

For deep water waves, Airy's wave theory [Airy(1841)] predicts a circulation motion of fluid particles with no neat mean fluid displacement. The amplitude of this circular motion decreases exponentially with the distance from the water's surface. In shallow waters, the influence of the seabed changes the motion of fluid particles into elliptical orbits with a non-zero contribution to bottom stress. As well, wave celerity and wave-length become depth-dependent.

Equations 1.3 gives a representation of water motion for waves of a given amplitude and period when they are traveling at a constant depth h. When a wave moves inshore, it moves from deep to shallow water in a process known as shoaling. One notably sees the height of the wave increase when

depth decreases. By equating the energy transported by a deep water wave and a shallow water wave (still according to the linear theory), the height of the waves can be related as [Denny(1988)]

$$\frac{H_w}{H_0} = \sqrt{\frac{\sinh(\frac{4\,\pi}{L}\,h)}{\sinh(\frac{4\,\pi}{L}\,h) + \frac{4\,\pi}{L}\,h} \frac{1}{\tanh(\frac{4\,\pi}{L}\,h)}}, \tag{1.4}$$

where H_0 is the wave height in the deep sea. When h is large, $H_w \sim H_0$ whereas when h decreases, H_w becomes larger than H_0. H_w keeps increasing when the depth diminishes until the waves eventually breaks (Figure 1.6).

Breaking does not completely absorb the wave's energy and the wave in the form of a turbulent bore of similar celerity continues [Denny(1988)] (see Figure 1.6). In many cases, it is this post-breaking flow that has the greatest contact with organisms on the shore [Denny(1988)]. Because exceptionally high waves typically break far from the shore, they are likely to have lost much of their energy to turbulent dissipation by the time they can interact with plants and animals in the intertidal zone [Thornton and Guza(1983)]. In this fashion, wave breaking can set a limit to the exposure of intertidal sites [Helmuth and Denny(2003)]. Nevertheless, smaller waves do reach and break on the shore.

On the steep slopes found on the rocky shores, waves generally break when their height is approximately equal to the local water depth [Galvin(1972)]. Flow speed, created by a breaking wave straight after breaking, is comparable to the phase speed of the wave, and may vary between the orbital flow speed and the shallow water phase speed of the wave [Stevens et al.(2008)]. Water velocity on rocky shores therefore remains mainly dependent on the waves' amplitude and time period as well as the topography of the rocky shores.

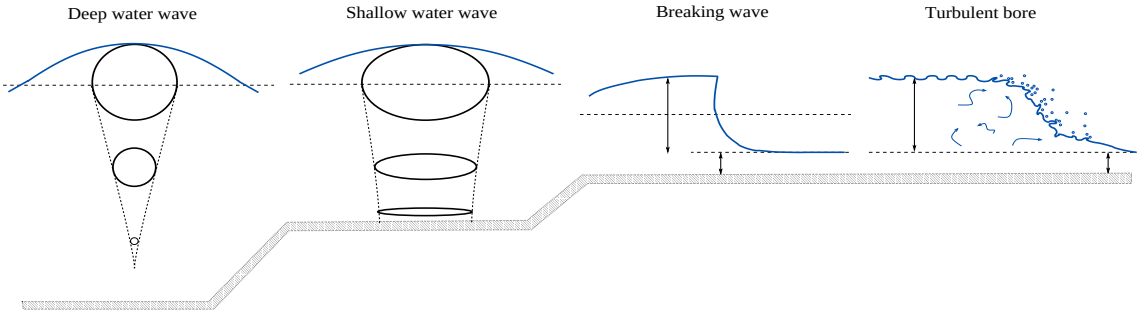

Figure 1.6. Potential evolution of a single wave from deep water to shore.

Typical wave records for the New Zealand shores can be found in [Stevens et al.(2008)]. Waves are predominantly around 10 seconds in period. Wave height ranges between 0 and 5 meters, with only 1% of the waves of 3 meters or greater in significant wave height. This is the context in which propagule settlement for *Durvillaea antarctica, Hormosira banksii* and *Cystophora torulosa* takes place.

1.2.2 Boundary-layers and the concept of friction velocity

The concept of the fluid boundary-layer was first introduced by Ludwig Prandtl in 1904 [Prandtl(1904)]. The boundary-layer is defined as the layer of fluid immediately adjacent to a solid surface where the frictional effects due to the solid boundary through the fluid viscosity are relevant. It may also be described as the region where viscous effects are of importance, or where inertial and viscous effects are of the same order of magnitude. Quantitatively this can be defined as the region where the mean flow velocity is smaller than 99% of the mean outer flow.

The later definition makes it obvious that despite having their own dynamics, boundary-layers are in constant interaction with the outer flow. In all cases, boundary-layers are regions of strong gradients playing a key role in flows particularly though the generation of vorticity and eddies [Tritton(1988)], as well as being the fluid environment adjacent to any settlement surface.

As with fluid flows in general, two types of boundary-layers can be discerned: laminar or turbulent boundary layers. Algal propagule settlement typically takes place in a turbulent environment and is therefore related to turbulent boundary-layer. In fully turbulent flows, the turbulent boundary-layer can be divided into two sub-layers, the turbulent sub-layer were inertial and viscous effects are of same order of magnitude and the laminar sub-layer, adjacent to the substrate, where viscosity is mainly relevant. Both sub-layer have to be crossed by the propagules during the last stage of their settlement process and are therefore of interest.

As any incompressible fluid flow, boundary-layer dynamics is believed to be described by the incompressible Navier-Stokes equations of fluid flow [Schlichting and Gersten(2004)]

$$\begin{cases} \rho_f \left(\dfrac{\partial \boldsymbol{u}}{\partial t} + \boldsymbol{u}.\nabla \boldsymbol{u} \right) = -\nabla p + \nabla.\left(\mu_f \left(\nabla \boldsymbol{u} + \nabla^t \boldsymbol{u} \right) \right) \\ \nabla.\boldsymbol{u} = 0 \end{cases},$$

where $\boldsymbol{u}$ is the velocity, p the pressure, ρ_f the fluid density and μ_f the fluid dynamic viscosity.

Dimensional analysis can be used on the full Navier-Stokes equations to derive the boundary-layer equations for both laminar and turbulent boundary-layers.

Laminar boundary-layer equations

In laminar flows, the whole boundary-layer is governed by the outer flow, i.e. the ambient flow speed. Assuming a two-dimensional boundary layer governed by an outer flow parallel to the solid surface of characteristic velocity U, that L is the characteristic length scale of the flow, δ_ν the size of the viscous boundary-layer and V the characteristic velocity scale of the transverse flow, then in the boundary-layer $L \gg \delta_\nu$ and $U \gg V$.

From these two inequalities, the 2D steady incompressible Navier-Stokes equations can be simplified leading to the equations, [Schlichting and Gersten(2004)]

$$\begin{aligned} u\frac{\partial u}{\partial x}+v\frac{\partial u}{\partial y} &= -\frac{\partial p}{\partial x}+\nu\frac{\partial^2 u}{\partial y^2} \\ \frac{1}{\rho}\frac{\partial p}{\partial y} &= 0 \\ \frac{\partial u}{\partial x}+\frac{\partial v}{\partial y} &= 0 \end{aligned} \tag{1.5}$$

where x is the stream-wise direction, y is the span-wise direction and y the direction normal to the solid boundary.

Inertia $\left(u\frac{\partial u}{\partial x}+v\frac{\partial u}{\partial y}\right)$ and viscous terms $\left(\nu_f\frac{\partial^2 u}{\partial y^2}\right)$ are of the same order of magnitude in the viscous boundary-layer. By dimensional analysis, $u\frac{\partial u}{\partial x}$ which scales with $\frac{U^2}{L}$ and $\nu\frac{\partial^2 u}{\partial y^2}$ which scales like $\nu\frac{U}{\delta_\nu^2}$ are of the same order of magnitude. Therefore,

$$\frac{U^2}{L}\sim\nu\frac{U}{\delta_\nu^2}$$

which leads to a scaling for the size of the viscous boundary-layer,

$$\frac{\delta_\nu}{L}\sim\left(\frac{\nu}{UL}\right)^{1/2}=\mathrm{Re}^{-1/2}.$$

Re, the ratio of inertial to viscous effects is the Reynolds number of the outer flow. For problems involving solid boundaries, the characteristic length scale L is a constant, therefore the viscous boundary-layer thickness δ_ν scales with $\mathrm{Re}^{-1/2}$. This shows that, despite being an isolated thin zone where the dynamics of the flow is dictated by the presence of a wall, the viscous boundary-layer's properties can still be estimated from the characteristics of the mean flow (outer flow Reynolds number).

When Re increases, the boundary-layer becomes thinner and hosts stronger gradients until flow instabilities eventually grow and the boundary-layer becomes turbulent.

Turbulent boundary-layer equations

For turbulent flows, the boundary-layer is unstable. Inertial and viscous effects are still governing the dynamic of the boundary-layer, but it is no longer possible to characterise the boundary-layer dynamics and thickness using the outer flow Reynolds number.

Turbulent boundary-layers can be subdivided into two regions (Figure 1.7), closest to the surface is the viscous sub-layer where the flow is dominated by molecular viscosity and the turbulent sub-layer where inertial forces as well as viscosity are relevant

The viscous sub-layer or inner layer, situated in the direct vicinity of the wall, is laminar and described by the laminar boundary-layer equations (Equation 1.5). It is not constantly laminar as turbulence bursts can modify its size and dynamics from time to time but, on average, laminar is a good description.

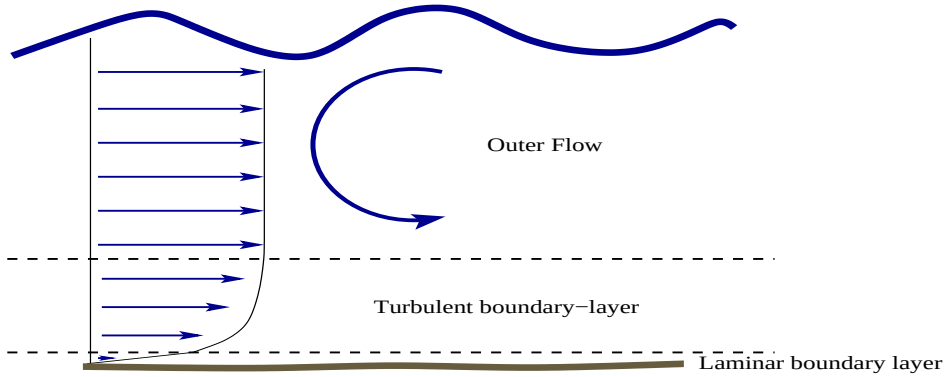

Figure 1.7. Benthic boundary layer driven by orbital wave-motion with mean-velocity profile on the left.

The turbulent boundary layer is adjacent to the viscous laminar boundary layer and extends to the area where its velocity is comparable to the one of the outer flow. The existence of the turbulence within the boundary layer changes its dynamics quite dramatically. In particular, the turbulent velocity fluctuations create extra stress that plays an important role in the boundary-layer dynamics and transfer processes (e.g. [Stevens et al.(2003)] [Oldham et al.(2004)]).

The boundary-layer equations for a turbulent boundary-layer can be obtained by applying the Reynolds decomposition (decomposition of the velocity u in mean $\bar{u}$ and fluctuations u') on the laminar boundary-layer equations (equations 1.5):

$$\begin{aligned}
&\bar{u}\,\frac{\partial \bar{u}}{\partial x} + \bar{v}\,\frac{\partial \bar{u}}{\partial y} = -\frac{1}{\rho}\,\frac{\partial \bar{p}}{\partial x} + \nu\frac{\partial^2 \bar{u}}{\partial y^2} - \frac{\partial}{\partial y}(\overline{u'v'}) \\
&\frac{\partial \bar{p}}{\partial y} = 0 \\
&\frac{\partial \bar{u}}{\partial x} + \frac{\partial \bar{v}}{\partial y} = 0.
\end{aligned}$$

The only difference with the viscous boundary-layer equation is the addition of the turbulent stress or Reynolds stress through the term $\frac{\partial}{\partial y}(\overline{u'v'})$.

The existence of this Reynolds stress term makes it impossible to link the boundary flow to the Reynolds number of the outer flow. Like the viscous boundary-layer in a laminar flow, the size of the turbulent sub-layer is partially governed by the outer-flow as the boundary-layer thickness is still defined from the outer-flow velocity. Nevertheless, the velocity profile within the turbulent boundary-layer is also affected by the turbulent-stress, which cannot be related to the mean flow without further assumptions.

Friction velocity u_*

The key problem when it comes to characterising the flow within the turbulent boundary-layer is the absence of a simple characteristic velocity scale. Such a quantity can be derived from an idealised description of the boundary layer.

In the case of a pure shear flow, $\bar{u} = \bar{u}(y)$, continuity equation implies that $\bar{v} = v_0$ and $\nabla \bar{p} = 0$. The boundary-layer equations turn into

$$v_0 \frac{\partial \bar{u}}{\partial y} = \nu \frac{\partial^2 \bar{u}}{\partial y^2} - \frac{\partial}{\partial y}(\overline{u'v'}) = \frac{\partial}{\partial y}\left(\nu \frac{\partial}{\partial y} \bar{u} - \overline{u'v'} \right).$$

If we integrate the previous equation in between $y = 0$ and $y = y_0$, we get

$$v_0(\bar{u}(y_0) - \bar{u}(0)) = \left[\left(\nu \frac{\partial}{\partial y} \bar{u} - \overline{u'v'} \right)_{y=y_0} - \left(\nu \frac{\partial}{\partial y} \bar{u} - \overline{u'v'} \right)_{y=0} \right].$$

The velocity being equal to zero on the wall, and if y_0 is taken far enough from the substrate so that the Reynolds stress is much bigger than the viscous stress,

$$v_0 \bar{u}(y_0) = - \overline{u'v'}(y_0) - \left(\nu \frac{\partial}{\partial y} \bar{u} - \overline{u'v'} \right)_{y=0}$$

defining the friction velocity u_* so that the total stress at the wall ($y = 0$) is equal to ρu_*^2, we get

$$v_0 \bar{u}(y_0) = - \overline{u'v'}(y_0) - u_*^2.$$

In most turbulent boundary-layer, $v_0 = 0$ [Tennekes and Lumley(1972)], therefore, for any y_0 for which the viscous stress is negligible,

$$\overline{u'v'}(y_0) = - u_*^2 \tag{1.6}$$

This shows that as well as being representative of the shear stress exerted on the solid boundary, the friction velocity u_* is directly linked to the intensity of the turbulence within the boundary-layer, and is a good characteristic velocity for the velocity fluctuations within the boundary-layer.

So far, u_* has been linked to local properties of the boundary-layer flow on the boundary and within the boundary layer. As mentioned earlier, the viscous sub-layer adjacent to the wall behaves as a laminar layer. The wall shear stress, τ_w, can then be derived from the mean velocity field as

$$\tau_w = \mu \left(\frac{\partial u}{\partial y} \right)_{y=0} = \rho u_*^2.$$

This way the friction velocity is related to the mean velocity field and as in the viscous sub-layer the velocity increases linearly with the distance to the bottom, u_* is linked to the whole mean flow within the laminar sub-layer as [Tritton(1988)]

$$u = \frac{u_*^2}{\nu} y.$$

Dimensional analysis tells us that within the turbulent boundary layer, the gradient of mean velocity is a function of the characteristic quantities available, ρ, u_* and y the distance to the bottom. The only combination of these parameter that has the required dimension is u_*/y [Landau and Lifchitz(1976)], which leads to

$$\frac{du}{dy} = \frac{u_*}{\kappa y}, \tag{1.7}$$

with κ the non-dimensional von Karmann constant.

Integrating equation 1.7 leads to the expression of the mean velocity profile in the turbulent sub-layer as

$$u = \frac{u_*}{\kappa}(\ln y + c),$$

where c is an integration constant. This is the logarithmic velocity profile of the turbulent boundary-layer. Despite being quite an idealised model and being particularly adapted to turbulent channel flows, the logarithmic velocity profile has been and is still extensively used in near wall turbulent studies [Piomelli and Balaras(2002)].

In summary, four key notions have been described in these paragraphs: the laminar viscous sub-layer, the turbulent logarithmic boundary layer, the Reynolds stress and the friction velocity. The two first notions are properties of the mean flow, the third one is a property of the fluctuation (local property). Because it is at the same time relevant to turbulent fluctuations and to the mean velocity profile in both turbulent and viscous sub-layer, the friction velocity is central to boundary-layer characterisation and all boundary-layer processes are at some extent related to u_*.

1.2.3 Turbulent transport and eddy-diffusivity

An important concept is that of eddy-diffusivity or turbulent-diffusion which defines the rate of spreading and unlike u_* is not a boundary-layer related velocity scale, but is relevant to turbulent mixing and transport in any turbulent flow.

The literature on turbulent mixing and processes is abundant and complex. It is used in a diverse range of applications including oceanography [Gargett(1984)] [Ivey et al.(2008)], atmospheric sciences [Taylor(1915)] [Fleagle and Businger(1980)] [Sutton(1932)], or numerical modelling which although studying the same processes, do not always use the same terminology.

Strictly speaking, turbulent diffusivity in general is a process that applies to scalar quantities (heat, salt...). Being a transport process governed by a velocity field and its fluctuations, the term turbulent-diffusivity should not be applied to momentum (turbulent or eddy diffusivity of momentum) which as the transport of a quantity by itself is bound to be something strongly non-linear and is called eddy-viscosity or turbulent-viscosity.

In both cases, we will see that the use of the term diffusivity or diffusion is of no phenomenological sense as it is only an analogy with the molecular diffusivity and does not have a true physical meaning. It is a property of the flow, not of the fluid [Tennekes and Lumley(1972)].

Let us consider the advection-diffusion of a scalar quantity c by an incompressible velocity field $\boldsymbol{u}$,

$$\partial_t c + \boldsymbol{u}.\nabla c = K_m \nabla^2 c,$$

where K_m is the molecular diffusivity of c.

Using the « Reynolds' decomposition » idea, the velocity field and the quantity c can be decomposed as

$$\begin{aligned} c &= \bar{c} + c' \\ \boldsymbol{u} &= \bar{\boldsymbol{u}} + \boldsymbol{u}' \end{aligned}$$

where $\bar{}$ represents the ensemble averaging and $'$ represents the fluctuations. This leads to

$$\partial_t \left(\bar{c} + c'\right) + (\bar{\boldsymbol{u}} + \boldsymbol{u}').\nabla\left(\bar{c} + c'\right) = K_m \nabla^2\left(\bar{c} + c'\right).$$

The whole equation can now be averaged in a statistical sense (ensemble-averaged). As derivatives can permute with the averaging and the ensemble averaged quantities are still time-dependent, we get

$$\partial_t \bar{c} + \bar{\boldsymbol{u}}.\nabla\bar{c} + \overline{\boldsymbol{u}'.\nabla c'} = K_m \nabla^2 \bar{c}\,. \tag{1.8}$$

As $\boldsymbol{u}$ is incompressible we have $\nabla.\boldsymbol{u} = 0$, which after ensemble average leads to $\nabla.\bar{\boldsymbol{u}} = 0$ and therefore non-divergence on the velocity fluctuations $\nabla.\boldsymbol{u}' = 0$, which can be used to rewrite equation 1.8:

$$\partial_t \bar{c} + \bar{\boldsymbol{u}}.\nabla\bar{c} + \nabla\overline{\boldsymbol{u}'c'} = K_m \nabla^2 \bar{c}\,. \tag{1.9}$$

The temporal variation of the averaged field $\bar{c}$ depends on three terms:

- $\bar{\boldsymbol{u}}.\nabla\bar{c}$ is the advection of the mean $\bar{c}$ by the mean velocity field.
- $K_m \nabla^2\bar{c}$ is the molecular diffusion of the mean $\bar{c}$ field.
- $\nabla\overline{\boldsymbol{u}'c'}$ is the eddy flux of c.

This is as far as we can describe the influence of « turbulent diffusion » on the mean flow without making any more assumption than considering fluids as a continuum. $\boldsymbol{u}'$ and c' being quantities very hard to measure and predict, there is a need for modelling the eddy flux term as something more accessible and easier to deal with.

Equation 1.9 is linear in c, and therefore, if c' is equal to 0 at $t = 0$, c' and $\nabla\bar{c}$ will be linearly related. This implies that the eddy flux $\nabla\overline{\boldsymbol{u}'c'}$ will be linearly dependent on the mean gradient $\nabla\bar{c}$ as well.

If we assume that the mean and the fluctuations of c are independent, then the eddy flux can be developed in a series of the form [Young(2000)]

$$(\overline{\boldsymbol{u}'c'})_i = -\mathcal{D}^{(1)}_{\mathrm{ij}} * \partial_{x_j}\bar{c} - \mathcal{D}^{(2)}_{\mathrm{ijk}} * \partial_{x_j}\partial_{x_k}\bar{c} + \ldots.,$$

where $*$ is the convolution operator and $\mathcal{D}_{\mathrm{ij}}$ are tensors. If the mean field varies slowly compare to the fluctuations, then the terms of second order and more can be neglected, leading to

$$(\overline{\boldsymbol{u}'c'})_i = -\mathcal{D}^{(1)}_{\mathrm{ij}} * \partial_{x_j}\bar{c}\,.\mathrm{dx} \tag{1.10}$$

If we assume as well that the velocity ensemble is isotropic, homogeneous and reflexionally invariant, then we can write [Young(2000)]

$$(\overline{\boldsymbol{u}'c'})_i = -D\,\partial_{x_i}\bar{c} \;\text{ or }\; (\overline{\boldsymbol{u}'c'}) = -D\,\nabla\,\bar{c}\,. \tag{1.11}$$

D is the eddy-diffusivity or eddy-diffusion coefficient or turbulent-diffusion.

Despite eddy-diffusion being a property of the flow, turbulent transport remains strongly dependent on molecular processes as turbulence carries energy from the large to the small scales were molecular diffusion operates.

While there are few situations where the assumptions of isotropy, homogeneity and reflexionality are satisfied, the use of eddy-diffusivity is more than common and has proved to be successful in many domains (see [Ivey et al.(2008)] [Yadav et al.(2003)]).

The formulation of turbulent transport in term of eddy-diffusion makes things much easier from a mathematical point of view for two reasons. First, diffusion operators (Laplacians) are linear operators which are far easier to deal with than non-linear operators determined by the fluctuations of the scalar and the velocity field. Second, it allows us to remove the fluctuations term in the ensemble average equations, which makes the number of variables drop and closes the problem. If the mean velocity field is known, the equation for the ensemble-averaged scalar field can be solved.

A similar approach has been used in the non-linear case of momentum transport, in the context of the turbulence closure problem, with the eddy-viscosity assumption introduced by Boussinesq in 1877 [Boussinesq(1877)]. Many turbulence models have used the eddy-viscosity in the turbulent Navier-Stokes equations, to model the influence of the Reynolds stress in the large-eddy simulation or in Reynolds Averaged Navier-Stokes based models. Also, eddy-diffusivity type models have been developed as well to model the dispersion of particles in a turbulent fluid with particle eddy-diffusion coefficients defined from particle/turbulence interactions.

1.2.4 Non-dimensional parameters

Two of the key physical notions regarding turbulence have been introduced, the parameterisation of the settlement problem can now be introduced.

Because of the non-motile nature of the propagules of interest, seaweed propagule settlement can be described and parameterised using a limited number of physical quantities :

- Propagule properties:

  - d_p the propagule diameter in m.

  - ρ_p the propagule density in $\mathrm{kg}\,m^{-3}$.

  - A_p the propagule adhesiveness, force per unit of area characteristic of the propagule's stickiness in Nm^{-2}

- Seawater properties:

  - ρ_f the seawater density in $\mathrm{kg}\,m^{-3}$.

  - ν_f the kinematic viscosity of seawater in $m^2\,s^{-1}$.

- Domain properties

  - h the water column size in the case of turbulent sinking in m.

  - d_r the characteristic size of the roughness element on the substratum in m.

- Properties of the flow

  - u_*, the friction velocity, characteristic of the near-bottom turbulent fluctuations in $m\,s^{-1}$.

  - V_t, a characteristic length scale representative of the turbulent fluctuations in the water column in $m\,s^{-1}$.

  - D the eddy diffusion coefficient characteristic of the turbulent transport in the water column in $m^2\,s^{-1}$.

  - δ_ν the laminar boundary layer thickness in m.

  - T_w the wave period in s.

  - H_w the wave height in m.

- And other parameters like

  - g the gravitational acceleration in $m\,s^{-2}$.

  - D_p the particle diffusivity due to Brownian motion in $m^2\,s^{-1}$.

Depending on the angle of approach some of these quantities are not always relevant or redundant. Nevertheless, the number of parameters listed here gives an idea of the complexity of the whole problem.

Propagule sinking

Dimensional analysis theory (Vaschy-Buckingham's Pi theorem [Vaschy(1892)] [Buckingham(1914)]) tells us that "Any dimensionless result of a problem, defined by n dimensional independent parameters in which m fundamental units appears, is a function of $(n - m)$ independent dimensionless parameters".

For example in the case of the propagule sinking in absence of turbulence, we desire to know the mean sinking velocity of the propagule V_p. In term of dimensional parameter, $V_p = V_p(d_p, \rho_p, \rho_f, \nu, g)$. There are five dimensional parameters for three dimensional units (kg, m and s), therefore these five parameters can be grouped together in two non-dimensionless parameters which are sufficient to parameterise the mean sinking speed of the propagule.

A first non-dimensional parameter can be the reduced density ratio between the propagules and seawater:

$$R_\rho = \frac{\rho_p - \rho_f}{\rho_f}.$$

The denser the propagules, the higher R_ρ is. For buoyant propagules R_ρ is negative, for non-buoyant propagules R_ρ is positive.

A velocity scale associated with a the gravitational sinking of a particle when inertial effects are negligible, the Stokes sinking velocity, can be defined using the dimensional parameters as

$$V_s = \frac{1}{18}\frac{1}{\nu_f}\left(\frac{\rho_p - \rho_f}{\rho_f}\right) g\, d_p^2.$$

Using the Stokes velocity, a second non-dimensional parameter for the sinking propagule in the absence of turbulence is the buoyant particle Reynolds number

$$\mathrm{Re}_p = \frac{d_p V_s}{\nu_f},$$

representative of the ratio of the inertial effects to the viscous effects experienced by the particle. For Reynolds number higher than one, a wake forms behind the particle which needs to be taken into account in the particles' dynamics.

R_ρ and Re_p are sufficient to parameterise the mean velocity of the propagule.

If particle sinking takes place in a turbulent environment, then one more parameter, a characteristic velocity scale representative of the turbulent fluctuations, is involved for no more dimensional units. One more non-dimensional parameter is needed and can be taken as the ratio of Stokes sinking speed to the turbulent fluctuations

$$R_V = \frac{V_s}{V_t}.$$

The settlement speed of the propagule in a turbulent flow should therefore be possible to parameterise using the three non-dimensional numbers R_ρ, Re_p and R_V.

Alternatively, turbulent transport of a propagule can be represented as a particle turbulent diffusivity, D_p, which is dependent on propagules properties and flow properties. The importance of advection by the Stokes velocity compared to turbulent transport for a propagule in the water column can be quantified using another non-dimensional number, the Péclet number (e.g. [Deleersnijder et al.(2006)]),

$$\mathrm{Pe} = \frac{V_s\, h}{D_p},$$

were h is the depth of the water column.

Boundary-layer crossing

Stevens et al. [Stevens et al.(2008)] developed a non-dimensional scaling approach of the boundary-layer crossing problem. Propagules sizes, buoyancy effects, propagule inertia, and Brownian motion were quantified in terms of length-scale relatively to the viscous boundary-layer size. The friction particle Reynolds number, Re_{*p}, was found to control or have a strong influence on all relevant processes. Expression of Re_{*p} for the range of wave-climate typically experienced by the propagules (u_* ranges from 1e-3 to 0.1 $m.s^{-1}$) lead to the conclusion that buoyancy dominates the sinking. Buoyancy being strongly dependent on propagules' properties, the problem is highly species dependent. As well, mucous properties could have a major impact on buoyancy.

Propagule detachment

After settlement there is still a period of several hours when the propagules can be washed of the substrate by turbulence burst/inrush [Soltani and Ahmadi(2001)] generated by the waves. In the near-substrate area, turbulence is usually characterised by a different velocity scale, the friction velocity u_*.

Similarly, the propagule detachment problem is parameterised by a finite number of dimensional parameter $d_p, \rho_p, A_p, \rho_f, \nu, u_*, g$ and d_r. Assuming the problem is to characterise the adhesiveness of the propagules, A_ρ, therefore, $\mathrm{A}_\rho = A_\rho(d_p, \rho_p, \rho_f, \nu, u_*, g\,, d_r)$. Five non-dimensional number are therefore relevant to the problem.

A friction particle Reynolds number can be defined as (e.g. [Stevens et al.(2008)])

$$\mathrm{Re}_{*p} = \frac{d_p\, u_*}{\nu},$$

a density ratio as

$$R_\rho = \frac{\rho_p}{\rho_f},$$

a roughness ratio as the characteristic size of a roughness element to the size of a propagule

$$R_r = \frac{d_r}{d_p},$$

and a ratio of the propagule weight to the shear force at the bottom of the water column

$$R_\sigma = \frac{\pi}{6} d_p \frac{\rho_p - \rho_f}{\rho_f} \frac{g}{u_*^2}.$$

Detachment can then be parameterised by four non-dimensional parameters $\mathrm{Re}_{*p}, R_\rho, R_r$ and R_σ.

1.3 Computational fluid dynamics

With the constant progress made in computer technology especially in the last 20 years, numerical modelling is becoming an evermore powerful tool for the study of physical problems. Numerical models give a simplified representation of reality but in exchange allow to control all the parameters of the problem which is always hard to achieve in the case of a real system. They remain nevertheless able to handle complex problems and have been applied successfully in many domains.

Many examples can be found in the literature of computational fluid dynamics (CFD) approaches to the modelling of interaction between flows and living organisms including studies of blood platelet aggregation [Fogelson(1992)] [Wang and Fogelson(1999)], bacterial swimming [Dillon et al.(1995)], tissue or blood cell deformation under shear flow or blood flow in the heart [Peskin(1977)] [Peskin(1972)].

CFD modelling of seaweed propagules behaviour has been one of the aim of this Ph.D.. Beside the model by itself (equations), a critical point is the choice of a CFD framework. In the following paragraphs, the software (Gerris Flow Solver), numerical approach and motivation are briefly introduced.

1.3.1 The Gerris Flow Solver

The Gerris Flow Solver [Popinet(2003)] (Gerris) is an open-source fluid dynamics equations solver developed by Dr. Stéphane Popinet at the National Institute of Water and Atmospheric Research (NIWA) in Wellington, New Zealand. It is published under the GNU General Public License and is free to download from http://gfs.sf.net.

A few of the problems it has been applied to are:

- air flow around a research vessel [Popinet(2003)]

- hydrodynamic tidal modelling of Cook Strait [Msadek(2005)] [Popinet and Rickard(2007)]

- direct numerical simulation of self-propelled swimming of 3D bionic fish school [Wu and Wang(2007)]

- air-water flow around a Series 60 cargo ship [Popinet(2001a)]

- atomisation
- wave breaking
- droplet dynamics

Gerris can solve the incompressible 2D/3D Navier-Stokes equations,

$$\begin{cases} \rho\left(\dfrac{\partial \boldsymbol{u}}{\partial t} + \boldsymbol{u}\cdot\nabla\boldsymbol{u}\right) = -\nabla p + \nabla\cdot\left(\mu\left(\nabla\boldsymbol{u} + \nabla^T\boldsymbol{u}\right)\right) + \boldsymbol{s} \\ \nabla\cdot\boldsymbol{u} = 0 \end{cases},$$

where $\boldsymbol{u}$ is the velocity field, p the pressure field, $\boldsymbol{s}$ a source term, ρ the density of the fluid and μ the viscosity of the fluid.

Beside the open-source philosophy of the code, the main characteristics of the code are its the finite-volume (conservative) formulation and its adaptive-quadtree/octree structure. Both features are choices and have their advantages and drawbacks and will be explained later.

Many different types of numerical approaches to the Navier-Stokes equations exist, all based on different types of formulations. Among the most famous are finite-differences, finite-element, spectral and finite-volume methods.

Finite-difference and finite-element methods are based on approximations of the local equations by development in series of polynomials. Finite-difference are usually well-suited to Cartesian grids and reasonably easy to design and implement. Different schemes can have various properties and there is usually no rule regarding the physical properties of the different schemes.

Spectral methods rely on a transposition of the equations to the frequency domain where differential operators usually have a much simpler formulation. Spectral methods are elegant from a mathematical point of view. The main drawback of these methods is the difficulty in implementation the boundary conditions as soon as the domain is not periodical. Spectral methods' resolution is directly related to a truncation of the energy spectrum of the problem's solution and therefore usually do not ensure conservation of the energy in the system.

Finite-volume methods are based on the conservative formulation of the Navier-Stokes equations, leading to a formulation of the numerical scheme in terms of mass fluxes. This ensures local and global exact conservation of mass. Mass and momentum conservation is the main argument in favour of finite-volume methods as it means that beside being based on mathematical arguments, finite-volume models are satisfying exactly two of the most fundamental laws of physics. This property comes usually at the cost of additional geometrical operations when complex geometries are involved. The Gerris Flow Solver belongs to these finite-volume methods and ensures exact mass and momentum conservation.

The second main feature of the Gerris Flow Solver is its quadtree/octree mesh structure (Figure 1.8) which will be described in details in chapter 5. “Quad” and “oct” stand for the use of squares (2D) or cubic (3D) cells for the discretisation of the domain. “Tree” corresponds to the data structure used to store the whole computational mesh. This kind of storage, besides its technical properties, allows relatively simple manageability of the mesh and makes it particularly easy to add or remove cells at any location in the computational domain. In other words, quadtrees/octrees are very convenient to handle complex meshes involving non-uniform resolution.

The algal propagule settling problem, just like many other problems, involves a variety of scales from that of the size of propagules (a few microns) to wave height (meters) or tank size (14 cm). The quadtree/octree mesh structure of the Gerris Flow Solver allows to adapt the simulation mesh to conform to the repartition of the small and large scales structures of the problem of interest. That way, resolution is optimised so that only the regions where small scale resolution is needed are refine very finely. As well, the high flexibility of the quadtree/octree structure allows to manage a grid that conforms to the the evolution in time of the location of both the small and the large structures of interest by refining or coarsening the mesh during the simulation.

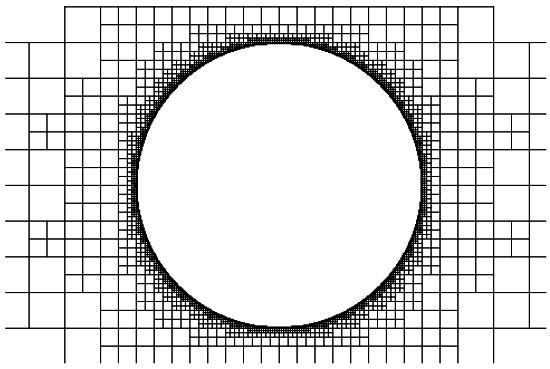

Figure 1.8. Quadtree adaptive mesh around a circular solid

Besides the major themes of mesh adaptivity and finite-volume, there are several other properties of importance :

- various boundary conditions (Dirichlet, Neumann, Fourier...(see chapter 5)) can be applied on the domain’s boundary, for all primitive variables.

- the fluids’ physical properties (density, viscosity) can be defined as functions allowing spatial variability of these properties or the use of complex rheology laws.

- multiphase flow simulations can be realized notably using a volume-of-fluid interface tracking method.

- source terms for any quantity can be used.

- Gerris can deal with static solid boundaries of complex shapes represented as triangulated surfaces or user-defined functions.

1.3.2 Numerical work

In the scope of this Ph.D., it was first imagined that part of seaweed propagule detachment could be studied numerically at the scale of the propagule by realizing direct numerical simulations of a propagule in a turbulent flow. In that context propagules could be modelled as solid spheres fully interacting with the surrounding flow (as opposed to Lagrangian particles) eventually surrounded by a layer of a very viscous fluid (mucilage). It was hoped the use of an adaptive mesh would help to overcome the very high needs in computer resources required by direct numerical simulation.

To realize such simulation one of the main feature missing in the Gerris Flow Solver is solid moving objects or a solid/fluid interaction model. The code was not *a priori* designed for moving objects, but the implementation of such a model was decided because of its usefulness for propagule modelling as well as the number of other applications it could be used to in different contexts.

The implementation of the solid/fluid interaction model is detailed in chapter 5. It was tested notably in the context of a 2D flow around a cylinder or sphere and gave excellent results. The model is of great interest as a numerical method as being the only quadtree 2D/3D finite-volume solid/fluid interaction model for incompressible fluid I am aware of.

1.3.3 Open-source

The introduction to the Gerris Flow Solver would not be complete without a paragraph on Open-Source development. The Gerris Flow Solver is published and distributed under the GNU General Public License which ensures that anybody can freely access, use and modify the Gerris Flow Solver and its sources.

It is believed that such an approach is beneficial to everybody and particularly suits an ideal conception of research and science in general to which some people adhere and towards which I have some inclination. Usually any progress or discovery in research is sanctioned by the writing and publication of a journal article or a conference talk or poster. Besides satisfying the hierarchy, publications aim at making work available to other researchers so that they can build from the progresses or the mistakes of others. As well, especially in the case of conference presentations, discussions can arouse with other scientists which can prove useful in terms of feedback and be a great contribution to the presented work and sometimes lead the way to future collaborations.

The idea of open-source development is not far from this conception of publications. Any development made on the code is almost immediately accessible to other people who can have different levels of interest in the code. Some people will only be interested in using the code for their own purposes, which could be eventually be industry-related work and not even end in a publication with acknowledgement of the code. They will eventually nevertheless, by their use of the code, contribute to the creation of a documentation on the code by asking question on the mailing list and to the improvement of the code by reporting the bugs met during their use of the code. Some people are going to use the code and provide useful information about the code behaving well in certain configurations. Some people are going to use the code, fix the problems they have encountered and publish patches that fix the code. Some people will use the code as a base of work and add their own improvements or new algorithm and eventually share them.

In this system each user has its own usefulness and contributes in it own way to the progress of the code. The code then benefits from the work of a whole community of people instead of only the main(s) developer(s).

I have been involved in the Gerris Flow Solver community since what could be called the early hours. The use and development of the Gerris Flow Solver as part of this Ph.D. was certainly not the most straightforward approach to find answers to the seaweed egg settlement problem, but was a fantastic opportunity to extend the use of the code to new horizons notably through the implementation of a solid/fluid interaction model. The developments realized in the context of this Ph.D. are to be added to the main branch of the Gerris Flow Solver and will hopefully prove a useful addition to Dr. Stéphane Popinet's work and be applied to many other problems.

This paragraph reflects only my personal opinion and certainly does not constitute a complete discussion of all aspect of open-source software development. More on this topic can be found on the web-page of Dr. Zaleski (http://www.lmm.jussieu.fr/~zaleski/zaleski.html).

1.4 Aims and outline

Originally, very little was known about the propagules and their settling behaviour. Therefore a number of relatively simple questions needed to be addressed :

- What are the key parameters to propagule settlement?
- Can we design a model of propagule removal?
- Can we quantify some of the properties of the propagules?
- How to investigate propagule behaviour in the boundary-layer?

Ultimately, answering the previous questions allows to draw a more global picture of the propagule settlement and understand their settling strategies.

The framework of this thesis is a broad multi-disciplinary project focusing on the settlement process (attachment/detachment) of seaweed zygotes of a rocky substrate in turbulent conditions. The main aim of the project is to understand the physical processes and determine the physical properties of the propagules. One of the key points was to tackle the problem from several angles by involving ecologists, physicists, chemists and numerical modellers. For that reason, this thesis covers at the same time some of the ecology, physics and numerical modelling aspects of this problem whilst also seeking to be at the cutting edge of each particular discipline.

The initial idea (historically) behind this Ph.D. is mainly developed in the fifth chapter with the implementation of a new fluid/solid interaction model in the Gerris Flow Solver. This new model potentially allows to realize accurate 3-D numerical simulation of the behaviour of a single propagule in the viscous boundary layer. This section stands out in the thesis as the model was implemented and tested but did not get as far as being applied to the initial problem.

The Chapters 2, 3 and 4 are much more inter-dependent and should be considered as a whole. In order to synchronise this work with the rest of the project, it was decided at the same time to take advantage of the propagule data obtained by Dr. David Taylor with his stirred tank. With that aim in view, understanding of the tank flow and interpretation of the propagule settlement data are successively explored in Chapters 2 and 3. Chapter 4 offers a different perspective with a numerical approach to those experiments, this with the objective of adding extra-information to the flow characterisation developed in Chapter 2.

More concisely:

Chapter 2 explores different methods of characterisation of the main properties of the tank flow in terms of meaningful physical quantities that can be related to the real environment. Successively, core flow and boundary flow are investigated.

Chapter 3 presents an investigation of the experimental results in the light of the physical quantities measured in Chapter 2. Just like core flow and boundary layer dynamics are considered in Chapter 2, propagule sinking and then propagule detachment are addressed, and several hypothesis tested in each case. Ultimately, propagule adhesiveness is estimated.

In Chapter 4 the setup of a 2-D and 3-D numerical model of the experimental stirred tank is reported. Inevitably, the problem of turbulence modelling is addressed in that section.

Chapter 5 deals with the development of a new numerical solid/fluid interaction model in the Gerris Flow Solver, followed by testing of the method on several benchmark test cases.

Chapter 2
Tank physics

2.1 Introduction

Stirred tanks have been used extensively for industrial purposes [Sheng et al.(1998)] [Micale et al.(2000)] as well as for research purposes [Oldham et al.(2004)], notably in the context of benthic hydrodynamics. They allow the generation of turbulence within a small volume using different types of stirring mechanisms like impellers, propellers or jets.

Stirred tanks are used for both their abilities to generate a strong turbulent core flow with a reduced mean flow [Variano and Cowen(2008)] and turbulent boundary-layers [Oldham et al.(2004)]. The properties of their core flow make them of particular interest for chemical processing where their mixing efficiency is particularly useful [Sheng et al.(1998)] [Micale et al.(2000)] [Nienow(1997)]. Their usually low mean flow, which limits the role of advection when turbulent transport is studied [Variano and Cowen(2008)], makes them very popular in the frame of particle/turbulence interaction [Brucato et al.(1998)] [Schwartzberg and Treybal(1968)]. It is as well a key advantage to study turbulence in isolation [Variano and Cowen(2008)]. In the context of boundary-layer hydrodynamics, stirred tanks allow the control of boundary-layer properties directly from the stirring mechanisms (e.g. [Buchholtz-TenBrink et al.(1989)]). One of their main uses remains the study of mass-transport in the boundary layer [Buchholtz-TenBrink et al.(1989)] and solute transport across the sediment-water interface [Oldham et al.(2004)].

Beyond the apparent simplicity of stirred-vessel devices, their flows are extremely complex, and much calibration work can be necessary to obtain an homogeneous enough system (e.g. [Buchholtz-TenBrink et al.(1989)]). The large-scale instabilities [Sheng et al.(1998)] that make stirred tanks' mixing abilities makes their dynamics very challenging to apprehend. The flow characteristics of stirred vessels have been approached from many different angles including single-point

LDV methods [Kresta and Wood(1993)], two-dimensional Particle Imaging Velocimetry (PIV) [Bakker et al.(1996)], theoretical models [Nienow(1990)] [Nienow(1997)] [Oldham et al.(2004)] or, more recently, computational fluid dynamics (CFD) [Sheng et al.(1998)] [Micale et al.(2000)].

Seaweed propagule settlement, because it involves both propagule turbulent sinking and boundary layer mechanics, can be investigated in its whole using a stirred tank. Following a short presentation of the experimental device in related work (D. Taylor, Canterbury University) for settlement experiments, flow characterisation in the boundary-layer and in the core of the tank is addressed from Particle Tracking Velocimetry (PTV) and Acoustic Doppler Velocimetry (ADV) measurements as well as theory.

2.2 Tank description

The tank used for the experiments was designed with the objective of generating strong turbulence in a small volume [Stevens and Taylor (Pers. Com.)].

The tank (Figure 2.1) consists of a cubic Perspex box of dimension $140 \times 140 \times 200$ mm; the actual volume of fluid contained in the tank during the experiments was $140 \times 140 \times 140$ mm. As well, the tank has been designed to host a settlement surface at the bottom. Hardi-flex was used for the following experiments, but it is possible (and was designed) to use a wide range of different surfaces to study the influence of the substrate on the settlement process [Stevens and Taylor(2005)]. Two propellers of 30 mm of diameter, facing each other on two of the vertical walls of the tank, are used to stir the tank. These are driven by 7.2 volt electric motors powered by a 5 Amp variable power supply, that allowed their speed to vary between 250 and 1500 rpm. A digital tachometer (Checkline CDT-100HD) was used to measure the rotating speed of the propellers. The two propellers were initially inserted at a 45° angle 45mm into the box at 65mm above the tank bottom.

Maintenance due to corrosion resulted in the locations of the propellers used for all the hydrodynamical part (laboratory work and numerical work) to be slightly different (Figure 2.1). Both propellers make a 45° angle with the wall they are attached to, but the stem of the left one is 0.35 m long and the one of the right one is 0.40 m long. In this case the experimental device is not symmetrical, which is very likely to change the large-scale structure of the flow. Nevertheless, there should be very little impact in term of the nature of the turbulence, stress on the bottom, and relation between propagule settlement and propeller speed in the tank, as bottom stress is proportional to the intensity of the mean circulation within the tank [Oldham et al.(2004)].

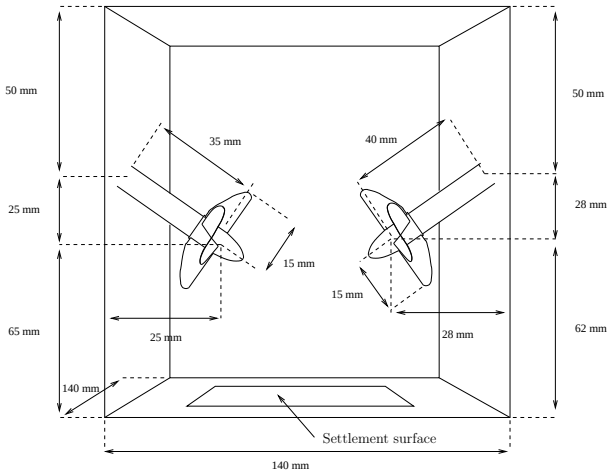

Figure 2.1. Dimensions of the stirred tank used for the experiments.

2.3 Flow measurements

Two types of measurements were realized in the stirred tank :

- 2 D measurements in the form of ensemble-averaged velocity field and turbulent kinetic energy were recorded in a cross-section of the tank using Particle Tracking Velocimetry (PTV) techniques.
- high-frequency 3 D velocity time series at a point were recorded using an Acoustic Doppler Velocimeter (ADV).

Whereas ADV measurements give access to the instantaneous velocity fluctuations in all directions during the whole time series, only one quantity, the Turbulent Kinetic Energy field (TKE), is representative of the velocity fluctuations in the PTV data. The TKE, defined as

$$\mathrm{TKE} = \frac{1}{2}\left(\overline{u'^2} + \overline{v'^2} + \overline{w'^2}\right),$$

is a measure of the energy of the velocity fluctuations.

Multiplying the velocity fluctuation equations (difference of the full Navier-Stokes and the Reynolds-averaged Navier-Stokes equations) by the velocity fluctuations leads to the TKE budget equation [Tennekes and Lumley(1972)]

$$\left[\frac{\partial}{\partial t} + u_j\frac{\partial}{\partial x_j}\right]\mathrm{TKE} = \frac{\partial}{\partial x_j}\left[-\frac{1}{\rho}p'\overline{u_i'\delta_{\mathrm{ij}}} - \frac{1}{2}\overline{u_i'u_i'u_j'} + \nu\frac{\partial}{\partial x_j}\mathrm{TKE}\right] - u_i'u_j'\frac{\partial u_i}{\partial x_j} - \nu\overline{\frac{\partial u_i'}{\partial x_j}\frac{\partial u_i'}{\partial x_j}}. \quad (2.1)$$

From this equation, one can see that TKE is generated from the mean shear stress, dissipated through the work done by the viscous stress and then transported by mean flow, velocity fluctuations, pressure variation and viscous stress. This makes the TKE a key quantity when it comes to local characterisation of a turbulent flow.

2.3.1 Particle Tracking Velocimetry

Particle Tracking Velocimetry is a velocity measurement technique based on high speed imagery of particles in a flow [Ohmi and Li(2000)]. It involves seeding the flow, suitable illumination and the acquisition of sequences of images.

The tank was seeded using Pliolite particles (15 mls, 90-120 μm diameter). These particles were illuminated with a 5 mm thick light sheet (Figure 2.2). A camera (PULNIX TM-1010) was used to take pictures of the illuminated particles at a frequency of 15 Hz. The images were then processed using the 'Fluid Stream' software [Nokes(2005)].

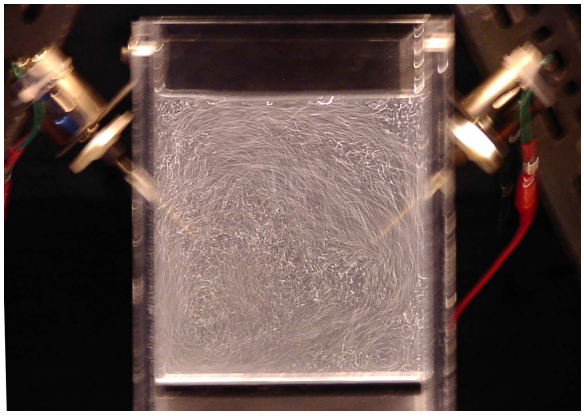

Figure 2.2. Stirred tank in action during PTV measurements (photo by Dr. David I. Taylor). The Pliolite particles of a 5 mm thick light sheet are illuminated. The motors can be seen on both sides of the tank.

The measurements were made in a slice parallel to the propeller axes located at 20 mm from the plane of symmetry of the tank, which corresponds to the distance where the settlement data were collected. Data were acquired for propeller speeds of 400, 500, 600 and 750 rpm. Some image sequences of the flow at 1000 rpm were also acquired but the camera frequency was too low to allow a proper tracking of the particles. For 1000 rpm, flow measurements were made using Acoustic Doppler Velocimetry (see later).

Velocity field

Superimposition of the velocity fields on the kinetic energy fields for 400, 600 and 750 rpm on Figure 2.3 show the bottom 55 mm of the tank where the propellers are not physically present.

The three plots are qualitatively similar and can all be decomposed into three zones:

– a downward very energetic flow in the middle of the slice where the fluid is propelled by the propellers. The velocities and consequently the kinetic energy are the highest in this region.

- a counter-clockwise recirculation in the bottom right corner. This recirculation is situated in the zone of low energy of the tank. The location of the recirculation is clearly related to propeller asymmetrical positioning with most of the bottom dynamics being dictated by the propeller the closest to the bottom (right hand one). The resolution does not allow confirmation, but visual inspection showed that there is a smaller recirculation (about 2mm in diameter) in the corner. This would be similar to the structures observed in the bottom corner of a cavity flow (see [Shankar and Deshpande(2000)]).
- the bottom part of a recirculation can be seen in the top left corner that is compressed between the flow from the right propeller and the wall.

On average there is a stagnation point not far from the middle of the slice. This is of great importance for a laminar flow as some of the settlement areas could have been located near or on this average stagnation point. However, due to the turbulent nature of the flow there should be no such real stagnation point.

As expected, the near-wall region typically sustains lower levels of kinetic energy, with viscosity inducing a velocity gradient in order to satisfy the no-slip boundary condition on the wall.

Despite the similar behaviours, several differences in the flow situation are noticeable:

- the distribution of the kinetic energy in the tank is far more uniform for low propellers speeds. For 400 RPM it is difficult to separate the water mass propelled by each of the propellers. The asymmetry in propeller location is only noticeable from the location of the recirculation. For higher speeds, the energy coming from each propeller is distinguishable. Strong interaction between both propeller flow (large velocity gradients) is associated with the production of turbulent kinetic energy in the slice. In that case bottom stress is driven by the propeller themselves and not by secondary eddies.
- a zone of relatively low energy is created along the left wall when the stirring is increased. This is due to a much faster velocity of the flow coming out of the right propeller.
- the total amount of kinetic energy in the tank increases with the stirring.

Turbulent kinetic energy

As TKE is generated from the mean shear stress, production of TKE in the tank is expected to be the strongest around the propellers where strong gradients of velocity are created and in the turbulent boundary-layer where the viscosity is responsible for the presence of strong mean velocity gradients.

In the three TKE plots (Figure 2.4) the regions of maximum TKE are located in the region

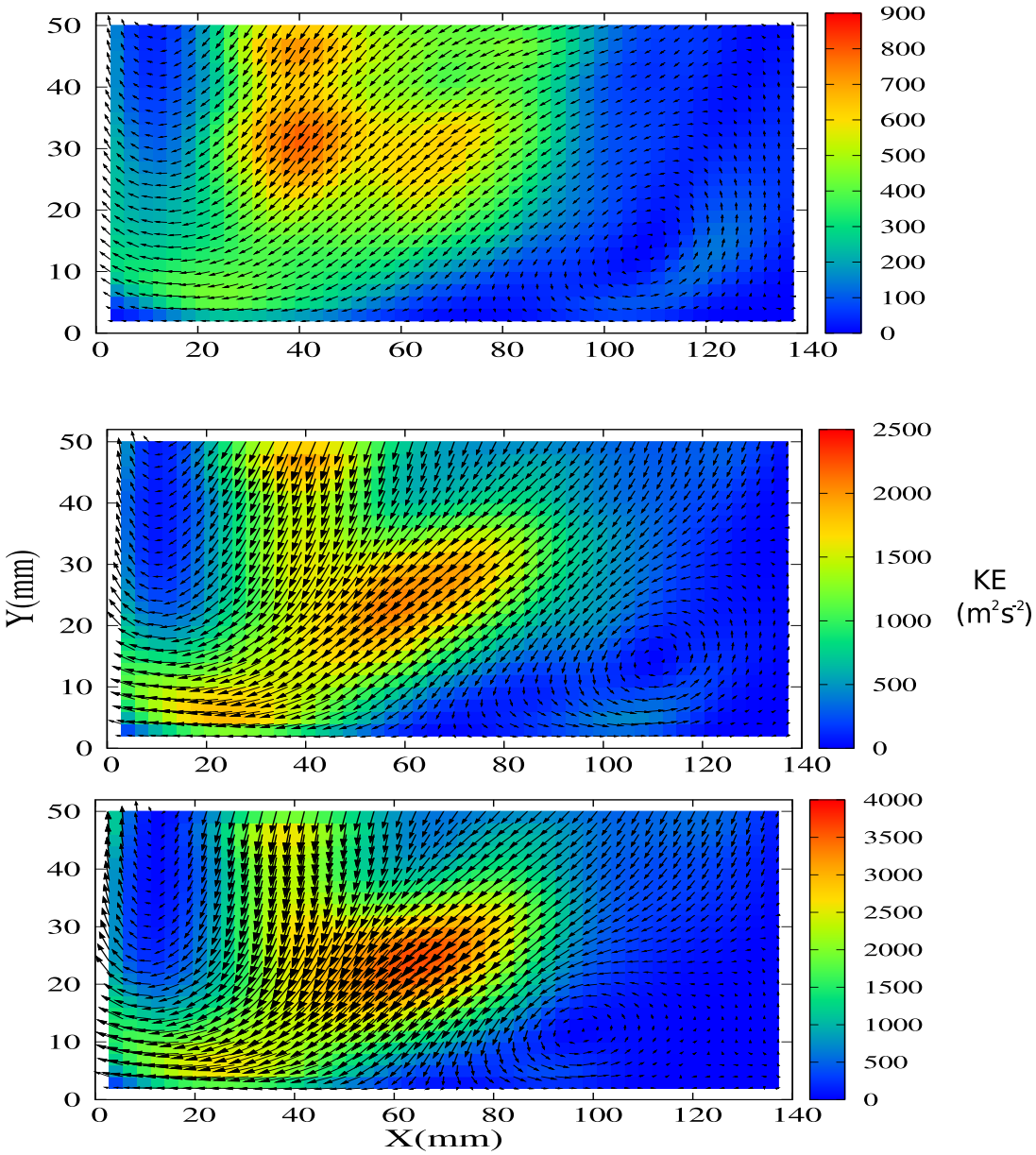

Figure 2.3. Kinetic Energy ($mm^2.s^{-2}$). PTV measurements in the bottom 55mm of tank. The slice is 20 mm from the centre line of the propellers which corresponds to the location of the settlement panel. Arrows denote the velocity field, colours denote the kinetic energy in $mm^2.s^{-2}$. From top to bottom stirring is 400 RPM, 600 RPM, 750 RPM. The same scale has been used for the velocity vector for all plots, unlike the colour scale that is different for each of the plots. The resolution of the measurements is about 2x2 mm. Each slice represents a time-average of the recorded quantities over 33 seconds.

where the flows from the two propellers are merging. The stronger the stirring, the higher the TKE and the local TKE maximum. It should also be noticed that the stronger the stirring, the less homogeneous the TKE distribution is in the slice, with the TKE maxima being located in the top of the slice for 400 RPM, and then being located at the place where the flow from both propellers is merging due to large velocity gradient (shear).

TKE seems to mainly be created from mean velocity gradient between the tank flow and the propelled flow and from the meeting of the fluid coming from both propellers.

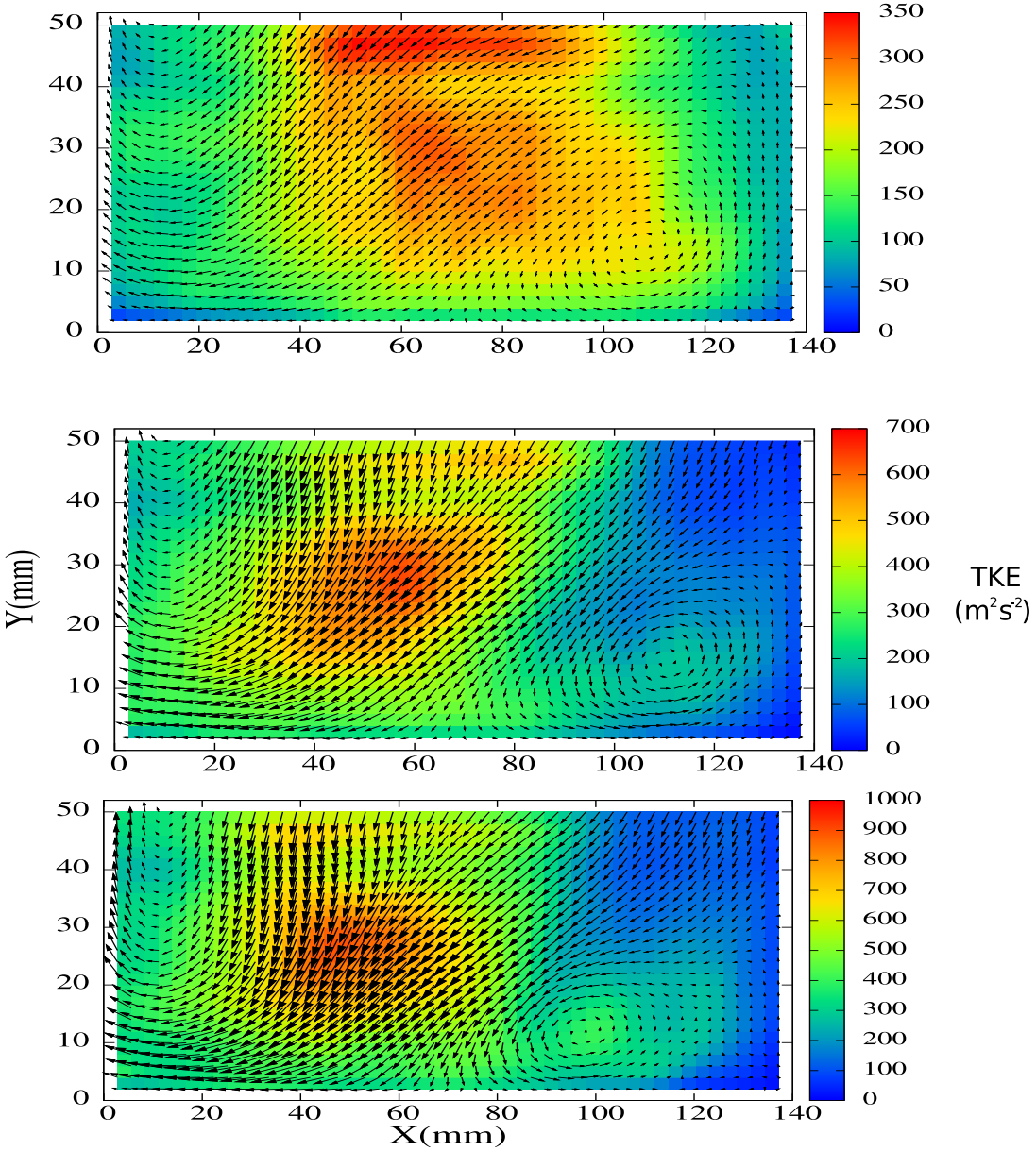

Figure 2.4. Turbulent Kinetic Energy ($mm^2.s^{-2}$). PTV measurements in the bottom 55mm of tank. The slice is 20 mm from the centre line of the propellers which corresponds to the location of the settlement panel. Arrows are for the velocity field, colours denote the TKE in $mm^2.s^{-2}$. From top to bottom stirring is 400 RPM, 600 RPM, 750 RPM. The same scale has been used for the velocity vector for all plots, unlike the colour scale that is different for each of the plots. The resolution of the measurements is about 2x2 mm. Each slice represents a time-average of the recorded quantities over 33 seconds.

Space-averaged quantities

Qualitatively, the maximum velocities and averaged TKE in the slice recorded in the tank are proportional to propeller speed (Table 2.1), whereas the total amount of TKE seems to increase faster at higher propeller speed. On average, the ratio of TKE over KE in the whole tank is always smaller than, but close to, 1. This changes near the bed where this ratio becomes > 1, and most of the time around 1.5 due to the presence of a turbulent boundary layer, but presumably < 1 in the viscous sub-layer.

Table 2.1. Data obtained from PTV measurements in the bottom 55mm of the tank. The slice is 20 mm from the centre of the propellers which corresponds to the place where the settlement quantification area were. The bottom layer is defined as being 2mm thick.

RPM	Maximum velocity ($mm.s^{-1}$)	Average KE in slice ($mm^2.s^{-2}$)	Average TKE in slice ($mm^2.s^{-2}$)	Average KE in bottom layer ($mm^2.s^{-2}$)	Average TKE in bottom layer ($mm^2.s^{-2}$)
400	28.03	200.40	174.62	36.73	63.04
500	39.42	265.65	223.87	51.93	85.50
600	50.81	409.27	283.20	144.84	149.68
750	67.89	589.27	445.46	176.64	243.83

2.3.2 Acoustic Doppler Velocimetry

The second type of velocity measurements that were made in the turbulent tank were made using Acoustic Doppler Velocimetry (ADV). ADV uses acoustic waves and Doppler effects to realize single-point velocity time-series measurements. These instruments have been used successfully in lab [Voulgaris and Trowbridge(1998)][Giri et al.(2004)] and field experiments [Kim et al.(2000)].

Compared to PTV measurements, the velocity field is only measured at one location at a time, but the ADV allows high frequency measurements (25 Hz here) and measures the three components of the velocity. This allows generation of energy spectra leading to characterisation of the nature of turbulence.

Originally, these ADV measurements were made to validate the tank numerical model (see Chapter 4). It is nevertheless of interest to investigate their content in the context of the characterisation of the tank flow.

A Sontek micro-ADV probe was used to record 1500 to 6000 points in a time-series at a frequency of 25 Hz (1 to 4 minutes long). Measurements were made at several locations in the tank for different rotational speeds of the propellers.

Poor data can result because of noise [Nikora and Goring(1998)] or aliasing of the Doppler signal [Goring and Nikora(2002)], which can produce a decorrelation of the signal [Garcia et al.(2005)] or create spikes in the signal. For these reasons, only data with a correl-

ation higher than 70% (Sontek ADV specifications) are used. To generate spectra, poor quality data cannot just be left aside, but have to be replaced. One possibility is to replace them by the overall mean of the signal [Goring and Nikora(2002)].

All velocity time series were despiked (Figure 2.5) using the Tukey 53H method [Otnes and Enochson(1978)] as described by Goring and Nikora [Goring and Nikora(2002)]. An estimation of the local mean was obtained through applying three operations to the discrete time series (u_i, v_i, w_i) :

- $u_i^{(1)}$ is the median of the five data points from u_{i-2} to u_{i+2}.
- $u_i^{(2)}$ is the median of the three data points from $u_{i-1}^{(1)}$ to $u_{i+1}^{(1)}$.
- $u_i^{(3)}$ is built from applying the Hann filter $u_i^{(3)} = \frac{1}{4}\Big(u_{i-1}^{(2)} + 2\ u_i^{(2)} + u_{i+1}^{(2)} \Big)$.

Each data point for which the distance of the data point to its local mean $|u_i - u_i^{(3)}|$ is larger than $k\,\sigma$, where σ is the standard deviation of u_i and k a threshold constant, is replaced by the mean of the time series. k was taken equal to 1.5 [Goring and Nikora(2002)].

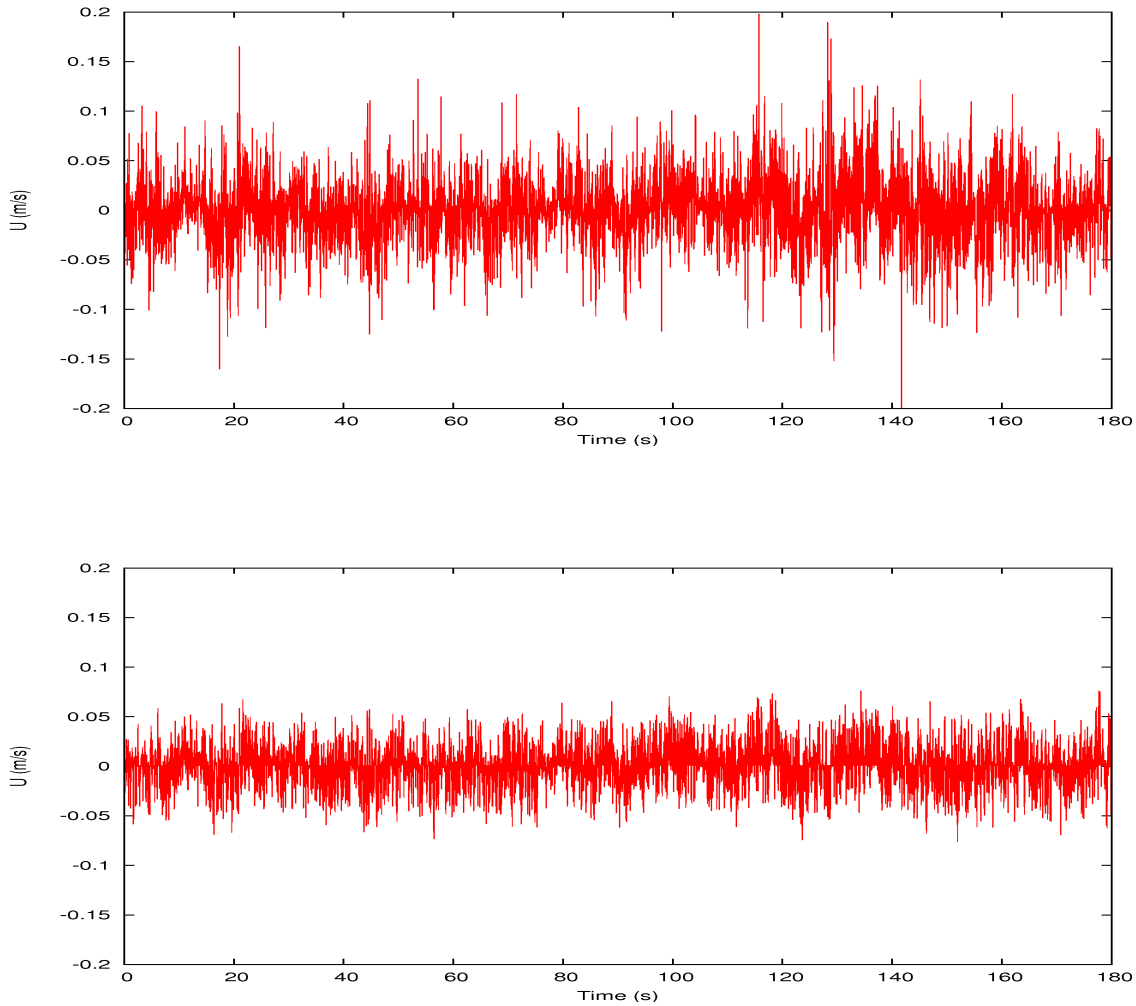

Figure 2.5. ADV time series before (top) and after (bottom) despiking.

Time series

ADV time series were analysed in two ways. Statistics on the mean velocity fluctuations were generated from basic treatment of the time series, and energy spectra were generated to study the local structure of the flow.

For each time series, mean velocities, standard deviation and maximum velocities were calculated. Distribution of fluctuations were calculated as well.

A clear drop in mean velocity and fluctuations can be observed in the upper region of the box (above the propellers) for low Reynolds numbers. No major difference exists between core flow and flow at 1.5 cm from the bottom for propeller speeds of 150 rpm. This suggests that the wall-effect is limited at this distance (Table 2.2).

Table 2.2. Statistics on ADV measurement at the centre of the tank at a distance y from the bottom. The propeller speed is 150, Umean is the mean horizontal flow, Umax the maximum velocity in the time series and Stdev the standard deviation.

rpm	150	150	150	150	150	150	150	150	150	150
y (mm)	16.9	28.	38.2	48.7	59.3	69.3	79.2	89.1	98.9	109.
Umean ($m.s^{-1}$)	0.028	0.042	0.024	0.035	0.024	0.021	0.020	0.018	0.003	0.003
Umax ($m.s^{-1}$)	0.258	0.22	0.229	0.215	0.197	0.198	0.202	0.149	0.135	0.136
Stdev ($m.s^{-1}$)	0.0806	0.056	0.083	0.0487	0.080	0.075	0.079	0.065	0.053	0.053

Lower mean velocities and fluctuations are found outside the propeller region (top and bottom) for higher rotation speeds (500 and 750 rpm). At a distance of around 2 cm from the bottom, amplitudes comparable to the ones of the core flow are found (Table 2.3).

For higher propeller speeds, there is clearly a very uneven distribution of stress on the bottom of the tank, with mean velocities of the order of 0.083 $m.s^{-1}$ recorded at a distance of around 0.6 cm from the wall in the middle of the tank, and mean velocities more than ten times smaller near the corners. Nevertheless, the maximum velocities recorded are still of the same order of magnitude suggesting that the regions of low mean velocity are not necessarily regions of low Reynolds stress (Table 2.4).

All these observations on mean velocity and mean fluctuations seem to match with what has already been observed in a single slice from the PTV measurements.

Differences can be observed in turbulence statistics and therefore structure between core flow and flow closer from the boundary. For the core flow, near normal distributions can be observed

for u', v' and w' which implies isotropic turbulence (Figure 2.6). This is not the case near the solid boundary where fluctuation distributions are non-symmetrical and therefore non-random (Figure 2.7).

Table 2.3. Statistics on ADV measurement at the centre of the tank at a distance y from the bottom. The propeller speed is 500 and 750. U is the velocity in the direction of the mean horizontal flow

rpm	500	750	500	750	500	750	500	750	500	750
y (mm)	99.	99.	69.7	69.9	48.9	48.9	28.5	28.5	17.3	17.3
Umean ($m.s^{-1}$)	0.017	0.011	0.031	0.042	0.041	0.046	0.016	0.016	0.008	0.018
Umax ($m.s^{-1}$)	0.139	0.169	0.157	0.218	0.148	0.199	0.115	0.0158	0.092	0.120
Stdev ($m.s^{-1}$)	0.044	0.053	0.067	0.0797	0.062	0.076	0.036	0.067	0.0233	0.047

Table 2.4. Statistics on ADV measurement at the Center, right and left of the box.

Position	Center	Left	Right
rpm	1000	1000	1000
y (mm)	6.9	7.2	5.4
Umean ($m.s^{-1}$)	0.083	0.007	0.005
Umax ($m.s^{-1}$)	0.973	1.611	0.665
Stdev ($m.s^{-1}$)	0.215	0.135	0.184

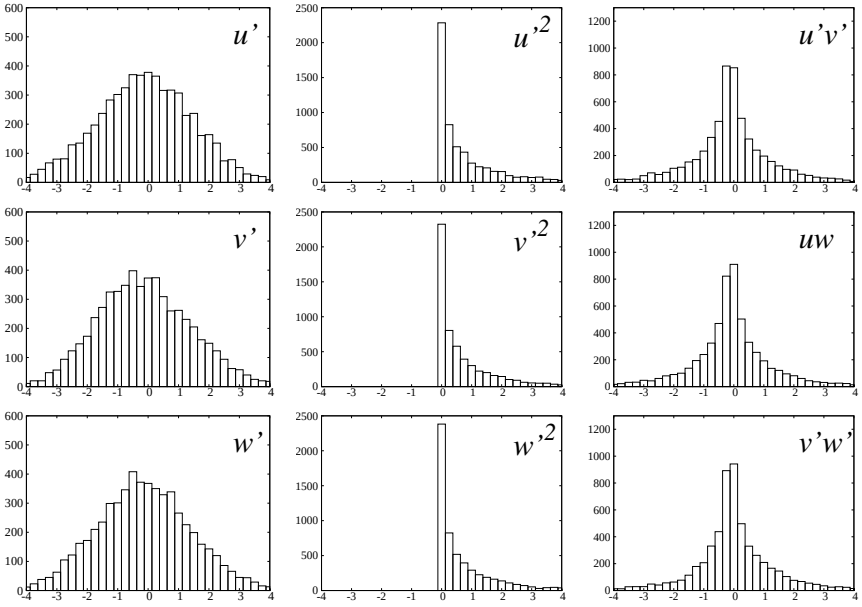

Figure 2.6. Typical normalised distribution of fluctuations in velocity components and moments as observed in the middle of the tank with propellers rotating at 1000 rpm. Vertical axis is the number of samples. Horizontal axis is $(X - \bar{X})/\sigma_X$ where X is the quantity, $\bar{X}$ its mean and σ_X its standard deviation.

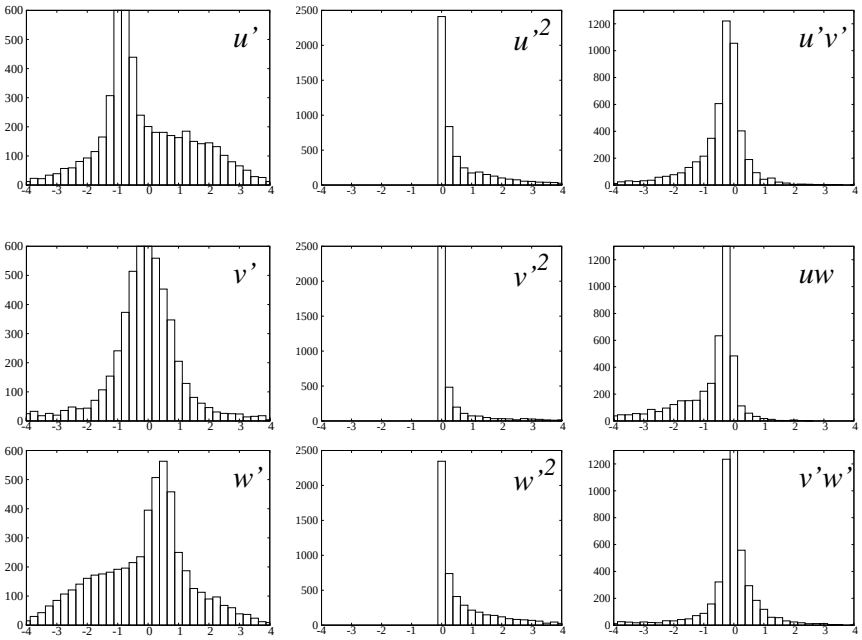

Figure 2.7. Typical normalised distribution of fluctuations in velocity components and moments as observed half a centimetre from the bottom with propellers rotating at 1000 rpm. Vertical axis is the number of samples. Horizontal axis is $(X - \bar{X})/\sigma_X$ where X is the quantity, $\bar{X}$ its mean and σ_X its standard deviation.

Spectra

Spectra were generated using a C routine based on the Fast Fourier Transform (FFT) implementation provided by the Gnu Scientific Library [Galassi et al.(1983)]. Mean velocities have been calculated from the despiked time-series. The coordinate system has then been changed so that the x-axis corresponds to the direction of the mean horizontal (parallel to the wall) velocity vector.

Spectra have been generated in this new coordinate system following a method used in an IDL routine from the Johns Hopkins University/Applied Physics Laboratory [Gotwols et al.(1990)].

The idea of this routine is that several spectra can be generated from splitting a time-series into several smaller time-series. These spectra can then be averaged to obtain final spectra containing a reduced level of noise. The price to pay for the noise reduction corresponds to less resolution in the low frequency range. For optimisation of the FFT efficiency, the smaller time-series are usually made of 2^n data points (1024 or 2048 in our case). The mean of the whole signal was subtracted from the time series prior to the Fourier transform.

To reduce the parasitic effects due to the finite nature of the time series (edge effects) a Hann window function (Figure 2.8) was applied to each time series. Besides reducing parasitic effects, the use of such a filtering window implies a loss of information near the edges of each data segment. For that reason, the initial time series was decomposed into a set of overlapping data sets.

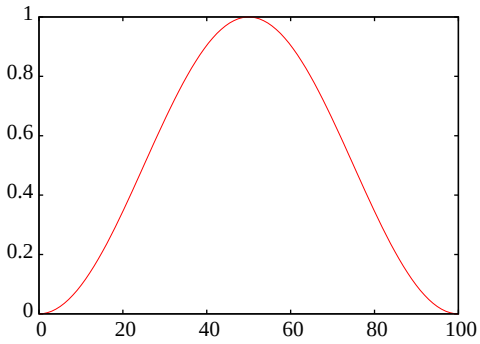

Figure 2.8. Hann function in the temporal domain for a 100 points data set.

The discrete Fourier coefficients were computed using the GSL FFT function [Galassi et al.(1983)]. Each Fourier coefficient is a complex number computed as:

$$a_k = \sum_{j=0}^{N-1} u_j \exp\left(-2\,\pi\,\boldsymbol{i}\,k\,\frac{j}{N}\right).$$

The energy spectrum $E(k)$ is then defined from the norm of the Fourier coefficients as

$$E(k) = \left(\frac{a_k\ \bar{a_k}}{N\ w_H} + \frac{a_{N-k}\ \overline{a_{N-k}}}{N\ w_H} \right) \Delta t = 2 \left(\frac{a_k\ \bar{a_k}}{N\ w_H} \right) \Delta t = 2 \left(\frac{a_k\ \bar{a_k}}{N\ w_H} \right) \frac{1}{F},$$

where $\bar{a_k}$ is the complex conjugate of a_k, N accounts for the absence of factor for the forward FFT transform, F is the frequency of the signal and w_H is a correction factor for the Hann function.

The spectral power density $\phi(k)$ can then be defined as

$$\phi(k) = \frac{E(k)}{T}$$

where T is the total duration of the signal and is equal as well to $\frac{\mathrm{F}}{\mathrm{N}}$, where F is the frequency of the signal and N the number of points in the time series. This gives a final expression for the spectral power density (PSD) of

$$\Phi(k) = 2\,\frac{a_k\ \bar{a_k}}{N^2\,w_H}.$$

Two typical examples of spectra are presented in Figure 2.9 and Figure 2.10. Figure 2.9 is representative of the core flow and Figure 2.10 of near-wall flow.

In the core flow, spectra can be decomposed into two distinct parts, an horizontal one with high peaks representative of the large scale structure of the flow and a downward slope representative of the inertial range or Kolmogorov cascade (see Chapter 4).

Several large peaks of energy can be observed in the low frequencies corresponding to the large anisotropic eddies. With a mean velocity of around 5 cm s^{-1} at the recording point and a tank size of 0.14 m, the characteristic frequency of the tank is around 0.36 Hz which should correspond to

the peak observed around that frequency. With the propeller located at about 65 mm from the bottom, the following group of peaks at higher frequency is likely to be representative of secondary eddies like the corner one observed in the PTV measurements (Figure 2.3).

The inertial range starts around 1.1 Hz. A clear -5/3 slope can be observed corresponding to the Kolmogorov energy cascade. Turbulence is statistically quasi-isotropic. Energy goes down from large to smaller eddies by vortex stretching (see Chapter 4).

No clear transition from inertial to dissipation range can be observed here, suggesting that the frequency implied by the Kolmogorov timescale is of the order or smaller than the cut-off frequency of the spectrum (12 Hz).

The Kolmogorov time-scale $\tau_\eta = \left(\frac{\nu}{\epsilon}\right)^{1/2} < \frac{1}{10}$, therefore the Kolmogorov length-scale $\eta = \left(\frac{\nu^3}{\epsilon}\right)^{1/4} < \sqrt{\frac{\nu}{10}} \sim 0.0003\,m$. The smallest structures of the flow should therefore be smaller than 0.3 mm.

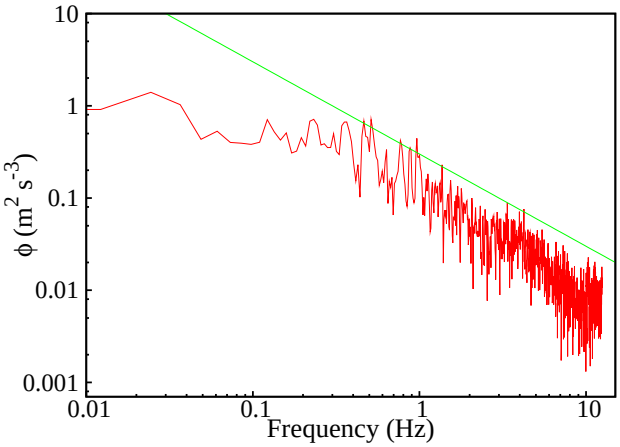

Figure 2.9. Energy spectrum for the vertical velocity component in the core flow at 1000 rpm. In green is the (-5/3) slope of Kolmogorov's spectrum.

In contrast to core flow spectra, near-wall spectra (Figure 2.10) do not have any apparent inertial range within the range of frequency covered here. This is due to the presence of much smaller anisotropic eddies in the turbulent boundary layer generated by the interaction with the wall. These eddies usually scale with the distance from the wall and can therefore be quite small.

Similarly, as for the core flow spectrum, a large peak can be observed around the characteristic frequency of the tank. The main circulation at the scale of the tank is still of importance even close to the wall as it drives the turbulent boundary-layer and sustains the anisotropic eddies of the boundary-layer. Despite the lower KE and TKE levels found in the vicinity of the wall, the size of the smallest eddies seems to be smaller than 0.3 mm.

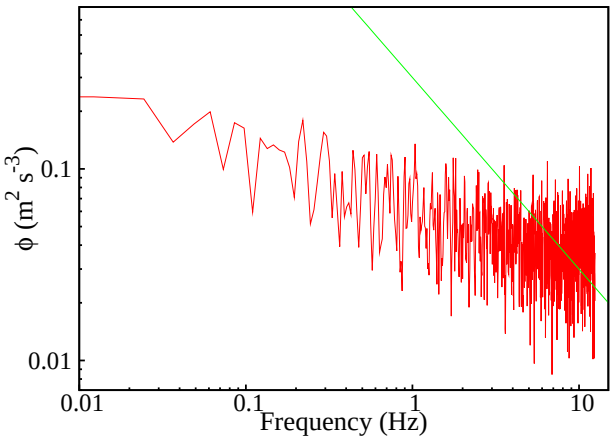

Figure 2.10. Energy spectrum for the vertical velocity component 6 mm from the Center of tank bottom at 1000 rpm. In green is the (-5/3) slope of Kolmogorov's spectrum.

In agreement with the need for two different characteristic quantities to characterise the turbulent processes involved in the turbulent sinking of the propagule through the core of the tank and the crossing of the turbulent boundary-layer, the near-wall area and core flow of the tank exhibit dramatically different turbulent spectra. Despite both of them being strongly influenced by the main circulation in the tank, the presence of the wall and the fluid viscosity constrain near-wall turbulence to remain anisotropic at a much smaller scale as turbulent energy is produced there at smaller scales.

2.4 Characterisation of the bottom stress

The special nature of the friction velocity u_* has been described in the Introduction. Its links to the mean velocity field, Reynolds stress and bottom stress, make it the ideal parameter to describe the bottom stress experienced by propagules on or near the substrate. Despite u_* being fundamentally linked to the notion of logarithmic boundary layer, it is still used in flows where the logarithmic profile does not apply. In these cases, it cannot be related to the mean velocity field, and it should just be seen as a quantity representative of the Reynolds stress or of bottom friction. For these reasons the friction velocity is a relevant quantity in the context of turbulent stirred tank and benthic chambers [Oldham et al.(2004)].

Numerous methods have been developed, notably in the context of oceanic boundary layers, to estimate the friction velocity from several types of experimental measurements [Kim et al.(2000)]. In the following, several of these methods are applied to the stirred tank PTV and ADV measure-

ments. As well, a theoretical model based on a 2D flow circulation assumption is applied.

2.4.1 Estimation of the friction velocity from a circulation model

Using the mass conservation equation and scaling arguments, Oldham et al. [Oldham et al.(2004)] expressed the friction velocity at the bottom of a stirred chamber as a function of propeller speed and tank and propeller dimensions. Following the work of Nienow [Nienow(1997)], the flow discharge, Q, for a propeller is proportional to propeller speed N and to propeller diameter D to the power of three

$$Q \backsim N D^3.$$

The velocity scale associated with the downward flow, W, is given by the flow discharge divided by the propeller area which scales as

$$W \sim N D.$$

Mass conservation,

$$\frac{\partial u}{\partial x} + \frac{\partial v}{\partial y} = 0,$$

leads to the relationship between vertical and horizontal characteristic lengths and velocities,

$$\frac{U}{B} \sim \frac{V}{h}$$

where B is the width of the stirred chamber and h the height from the substrate to the propellers. Assuming proportionality between the friction velocity and the mean velocity horizontal to the bottom, Oldham et al. [Oldham et al.(2004)] found

$$u_* = C\, N D \left(\frac{B}{h}\right),$$

where C is a constant.

For a axial flow impeller, their expression of the friction velocity is

$$u_* = 0.05\, N D \left(\frac{B}{h}\right),$$

where N is the propeller rate of rotation, D the propeller diameter.

In our case two propellers are used, which implies we get the double flow discharge compared to a single propeller system. Therefore,

$$u_* = 2 * 0.05 \frac{\text{rpm}}{60}\ 0.03 \left(\frac{0.15}{0.065}\right) = 0.000012\text{rpm}. \tag{2.2}$$

From equation 2.2, the friction velocity at the bottom of the stirred tank ranges from 0.012 ms^{-1} to 0.115 ms^{-1} for propeller speeds between 100 and 1000 (Table 2.5). This falls right into the range of friction velocity encountered in situ (0.001 to 0.1 $m.s^{-1}$ according to [Stevens et al.(2008)]).

Table 2.5. Estimation of the friction velocity at the bottom of the tank using Oldham et al.[Oldham et al.(2004)]'s method.

rpm	100	400	500	600	750	1000
$u_*(m\,s^{-1})$	0.012	0.046	0.058	0.069	0.086	0.115

2.4.2 Estimation of the averaged friction velocity from the PTV data

Logarithmic profile approach

The logarithmic profile approach is based on the relationship existing between the friction velocity and the mean velocity field. It is likely not well suited for stirred tank flows, especially as they usually exhibit large-scale instabilities. It remains nevertheless, one if not the only accessible theoretical model for near-wall flows.

Launder and Rodi [Launder and Rodi(1983)] reported the wide use of the logarithmic boundary layer profile to represent the near-wall flow turbulent jet modelling. The flow in the tank has some similarities with the radial wall jet described by Launder and Rodi [Launder and Rodi(1983)], with the propellers creating a downward flow that impacts the bottom of the tank. Consequently, fitting a logarithmic mean-velocity profile is one method to evaluate friction at the bottom of the tank.

The friction velocity, u_*, was determined from the mean PTV data collected in the tank, assuming a logarithmic profile for the boundary layer on average. The resolution of the PTV measurements is 2 mm, so it is not possible to observe the exact shape of the boundary-layer, especially as the two propellers input quite a lot of energy in regions relatively close to the bottom of the tank, which reduces the size of the boundary-layer.

Knowing the velocity or the kinetic energy at a resolution of 2 mm in a plan of the tank where the settlement experiments are realized, provides coarse averages of the local velocities that can be compared to integrations of the logarithmic layer profile in order to get u_*.

The size of the logarithmic layer is not known *a priori*, and therefore situations where the logarithmic layer is smaller or larger than 2mm have to be considered.

Let us call u_0 the average velocity within the bottom layer and u_∞ the mean velocity in the upper region of the flow. If the whole boundary layer is included within the bottom layer, the integration of the velocity profile is the following one:

For the viscous boundary layer of thickness $\delta_\nu = 5\,\nu/u_*$,

$$\int_0^{5\nu/u_*} \frac{u_*^2}{\nu}\, y\, \mathrm{d}y = \frac{25}{2}\nu \tag{2.3}$$

The logarithmic boundary layer ends around $\bar{u} = u_\infty$,

$$\frac{u_*}{\kappa}\ln\!\left(\frac{\delta_t\, u_*}{5\,\nu}\right) + 5\,u_* = u_\infty$$

then,

$$\delta_t = \frac{5\,\nu}{u_*}\exp\!\left(\frac{\kappa}{u_*}\,(u_\infty - 5\,u_*)\right).$$

the integration of the velocity profile over the logarithmic layer is

$$\int_{5\nu/u_*}^{\delta_t} \frac{u_*}{\kappa}\ln\!\left(\frac{y\,u_*}{5\,\nu}\right) + 5\,u_*\ \mathrm{d}y = \frac{5\,\nu}{\kappa}\left[\exp\!\left(\frac{\kappa}{u_*}(u_\infty - 5\,u_*)\right)\left(\kappa\frac{u_\infty}{u_*} - 1\right) - 5\kappa + 1\right]. \tag{2.4}$$

The integration of the velocity profile over the rest of the bottom layer is

$$\int_{\delta_t}^{0.002} u_\infty\,\mathrm{d}y = 0.002\,u_\infty - \frac{5\,\nu}{\kappa}\exp\!\left(\frac{\kappa}{u_*}(u_\infty - u_*)\right)\frac{u_\infty}{u_*}\,\kappa \tag{2.5}$$

The integration over the whole bottom layer (2.3)+(2.4)+(2.5) is equal to the integration of the velocity measured by PTV in the bottom layer:

$$\frac{25}{2}\nu - \frac{5\,\nu}{\kappa}\exp\!\left(\frac{\kappa}{u_*}(u_\infty - 5\,u_*)\right) + \frac{5\nu}{\kappa} - 25\nu + 0.002\,u_\infty = 0.002\,u_0.$$

This gives the following expression for the friction velocity:

$$u_* = \frac{\kappa\,u_\infty}{5\,\kappa + \ln\!\left(\frac{0.002\,\kappa}{5\,\nu}(u_\infty - u_0)\right) + 1 - \frac{5\,\kappa}{2}}. \tag{2.6}$$

If the turbulent boundary layer is not completely included in the bottom layer, then the integral of the velocity profile over the viscous sub-layer is the same as (2.3). The integration over the remaining part of the bottom layer is

$$\int_{5\nu/u_*}^{0.002} \frac{u_*}{\kappa}\ln\!\left(\frac{y\,u_*}{5\,\nu}\right) + 5\,u_*\ \mathrm{d}y = \frac{u_*}{\kappa}\,0.002\left(\ln(0.002) - 1 + \ln\!\left(\frac{u_*}{5\,\nu}\right) + 5\,\kappa\right) + \frac{5\,\nu}{\kappa}(1 - 5\,\kappa).$$

In total, the integral over the bottom layer equalled to the PTV data gives

$$0.002\,\frac{u_*}{\kappa}\left(\ln(0.002) - 1 + \ln\!\left(\frac{u_*}{5\,\nu}\right) + 5\,\kappa\right) = 0.002\,\bar{u} + \frac{25}{2}\nu - \frac{5\,\nu}{\kappa}. \tag{2.7}$$

It is not as simple as in the previous case to give an expression for u_*, and I used the root- finding function (Brent method) from the Gnu Scientific Library [Galassi et al.(1983)] interfaced with a C routine to get u_*. The results are displayed in Table 2.6.

Table 2.6. Results from the logarithmic layer integration model.

Propeller speed (RPM)	u_0 (mm.s^{-1})	u_∞ (mm.s^{-1})	u_* (mm.s^{-1})	δ_ν (mm)	δ_t (mm)
400	7.0	18.3	2.6	1.9	4.2
400	10.2	22.7	3.2	1.5	3.5
500	12.1	24.2	3.6	1.4	2.9
500	8.3	22.9	2.9	1.7	5.7
600	17.0	29.1	4.4	1.1	2.2
750	17.8	34.4	4.5	1.1	3.2
750	19.8	35.6	4.8	1.0	2.8

The values of u_* range from 2.6 mm.s^{-1} to 4.8 mm.s^{-1} which is right in the middle of the field estimation of Stevens et al. [Stevens et al.(2008)] (0.001 to 0.1 $m.s^{-1}$) and close to ten times lower than the estimations obtained from Oldham et al.'s theoretical model [Oldham et al.(2004)] for similar propeller speeds. The friction velocity seems to be proportional to propeller speed, which is consistent with the results from the theoretical model.

For such values of u_*, the logarithmic velocity profile predicts viscous sub-layer thicknesses of 1 to 2 mm, which is in all cases more than ten times the size of the larger propagules. This confirms than the propagule attachment and eventually detachment observed in the tank are happening within the viscous sub-layer.

The turbulent boundary layer has a maximum size of 5.7 mm. In all cases involving propeller rotation, the whole logarithmic layer is therefore included within the bottom 2 mm layer that corresponds to the resolution of the PTV data.

TKE approach

In the ADV literature [Kim et al.(2000)] (see next section), methods were found to relate the friction velocity to the turbulent kinetic energy. These methods rely only on estimations of the turbulent kinetic energy within the logarithmic layer and are not restricted to ADV data.

Given the absence of spatially distributed ADV measurements, and the spatially-averaged nature of the logarithmic profile estimations obtained previously, it was of interest to apply this method to our PTV measurements. Furthermore, the logarithmic velocity profile, even on average, is a very strong assumption to make that is likely to be far from reality.

The turbulent kinetic energy is a measurement of the intensity of turbulent fluctuations and is strongly related to the local Reynolds shear stress which is connected to the bottom shear stress. The TKE method (see ADV section) was applied first on the averaged TKE field in the bottom layer (Table 2.7) in order to get an estimation of the averaged friction velocity at the bottom of

the tank. The TKE field obtained from PTV is averaged over 2×2mm cells. With the laminar sub-layer estimated to be up to 1.9 mm thick in the previous paragraph, the bottom 2 mm are likely not to be the most representative region of the turbulent part of the boundary layer. For that reason, the TKE field in the 2 mm layer above this was considered to be more suitable for estimation of the Reynolds stress. y

Table 2.7. Friction velocity estimates using the TKE method on the space-averaged PTV data. The results in column 1 were obtained using the TKE in the 2 mm layer adjacent to the wall. Those in column 2 were obtained using the TKE in the following 2 mm and column 3 is for the next 2mm .

	1		2		3	
rpm	TKE $\mathrm{mm}^2.s^{-2}$	u_* $\mathrm{mm}.s^{-1}$	TKE $\mathrm{mm}^2.s^{-2}$	u_* $\mathrm{mm}.s^{-1}$	TKE $\mathrm{mm}^2.s^{-2}$	u_* $\mathrm{mm}.s^{-1}$
400	63	3.64	118	4.98	138	5.38
500	85	4.22	149	5.59	178	6.11
600	149	5.59	216	6.73	244	7.16
750	243	7.14	309	8.06	340	8.45

Table 2.8. Friction velocity estimates using the TKE method on the PTV data at the settlement area. The results in column 1 were obtained using the TKE in the 2 mm layer adjacent to the wall. Those in column 2 were obtained using the TKE in the following 2 mm and the column is for the next 2mm.

	1		2		3	
rpm	TKE $\mathrm{mm}^2.s^{-2}$	u_* $\mathrm{mm}.s^{-1}$	TKE $\mathrm{mm}^2.s^{-2}$	u_* $\mathrm{mm}.s^{-1}$	TKE $\mathrm{mm}^2.s^{-2}$	u_* $\mathrm{mm}.s^{-1}$
400	93	4.44	162	5.84	183	6.19
500	128	5.19	219	6.79	249	7.23
600	183	6.21	281	7.68	321	8.21
750	304	7.99	400	9.17	428	9.48

The estimation of friction velocity from the TKE (Tables 2.7 and 2.8) are larger than those obtained from the mean velocity profile by a factor of two. Given the uncertainty of the validity of the logarithmic profile approximation, this can be considered as a relatively good agreement. It has to be kept in mind that the PTV measurements have been realized within a cross-section of the tank. For that reason, the mean velocity field was considered to be 2D instead of 3D, which might lead to an underestimation of the mean velocity and therefore of the friction velocity u_*. It can be noted that this method also shows proportionality between the propeller speed and u_*.

Differences were found between estimations of u_* from the TKE in the bottom 2 mm or in the following 2 mm. Far smaller differences were found for these from the 2-4 mm and the 4-6 mm layers. Like the results from the previous methods, these estimations of u_* fall within the range of friction velocity predicted on the sea-bed when propagule settlement occurs.

Given the flow configuration in the tank, and the fact that the settlement experiments have been made only in a very localised area of the tank, the estimation of the friction velocity from the TKE are likely to be a good representation of the shear-stress experienced by the propagules. For that reason, they are considered as our best estimation of the friction velocity and are the ones used in the rest of the thesis.

2.4.3 Estimation of the friction velocity from ADV time series

Acoustic Doppler Velocimetry has been used extensively to estimate shear stress in the context of seabed stress [Green(1992)] [Huntley(1988)] [Soulsby and Dyer(1981)] [Stapleton and Huntley(1995)] [Kim et al.(2000)] or land/atmosphere interactions [Champagne et al.(1977)]. Four methods of estimation of the friction velocity, u_*, based on ADV measurements are reviewed in Kim et al. [Kim et al.(2000)]. Just like the methods used previously to estimate u_* from the PTV measurements, all four methods are to some extent related to the assumption of logarithmic layer and constant shear layer.

All estimates are extracted from velocity time series measured by ADV. Despite this similarity, all four methods are based on different quantities. In Kim et al. [Kim et al.(2000)], the bottom stress in a tidal boundary layer is calculated from ADV data using mean velocity field, TKE, Reynolds stress or energy dissipation rate as a base.

Logarithmic profile method

The method the closest from the logarithmic profile approach used on the PTV data is the logarithmic profile method or LB method. Under the assumption that the shear stress in the vicinity of the substrate is constant, it can be derived that the stream-wise mean velocity parallel to the wall is given by the logarithmic law

$$\bar{u} = \frac{u_*}{\kappa} \ln\left(\frac{y}{y_0}\right)$$

with y_0 an integration constant depending on the roughness of the substrate or analytically on the law chosen to describe the laminar sub-layer. If a linear velocity profile is assumed in the viscous sub-layer, then the velocity profile in the logarithmic layer is given by

$$\bar{u}\,(y) = \frac{u_*}{\kappa} \ln\left(\frac{y\,u_*}{5\,\nu}\right) + 5\,u_*. \tag{2.8}$$

ADV time series allow to calculate $\bar{u}$ for a given distance to the bottom y. u_* can then be estimated from solving equation 2.8.

COV method

The COV method is based on estimations of the near-bed Reynolds stress. Far enough (around 10 wall units) above the bed, the contribution of the viscous stress to the total stress becomes negligible [Tennekes and Lumley(1972)]. Therefore, the total stress reduces to the Reynolds stress

$$\sigma = \rho(-\overline{u'v'}).$$

The friction velocity is then directly related to the Reynolds stress by

$$u_* = \sqrt{-\overline{u'v'}}.$$

This method relies on the constant shear layer approximation, but is independent of the distance to the bottom except for the fact that the measurements have to be taken far enough from the substrate to be allowed to neglect the viscous stress and close enough so that the logarithmic profile still stands.

TKE method

The TKE method is another method based on an averaging of the velocity perturbations. It assumes that in the constant shear layer the amplitude of shear stress is proportional to the intensity of the turbulent kinetic energy:

$$|\sigma| = C_1 \frac{1}{2} \rho \left(\overline{u'^2} + \overline{v'^2} + \overline{w'^2} \right)$$

where C_1 is an empirical constant usually equal to 0.19 [Stapleton and Huntley(1995)]. Kim et al. [Kim et al.(2000)] suggested that similarly the bottom stress can be directly related to the vertical component of the velocity fluctuation as

$$|\sigma| = C_2 \frac{1}{2} \rho \, \overline{v'^2}.$$

They estimated the proportionally constant C_2 to be around 0.9.

The main assumption used in this model is the assumption of a linear relationship between Reynolds stress and TKE. The two other hypothesis are the constant shear layer approximation allowing one to utilise measurements, taken anywhere in the logarithmic layer, and the universality of the constants C_1 and C_2.

Inertial dissipation method

The last method is based on the turbulence cascade and equilibrium between the production and dissipation of turbulence. Assuming that near the substrate, production of turbulence is realized through shear production, rates of energy dissipation and shear production of energy can be equated [Kim et al.(2000)]

$$\varepsilon = \overline{u'v'} \frac{\partial \bar{u}}{\partial y}$$

using the logarithmic layer assumption, $\frac{\partial \bar{u}}{\partial y} = \frac{u_*}{\kappa\, y}$ and $-\overline{u'\, v'} = u_*^2$, which leads to

$$u_* = (\varepsilon\, \kappa\, y)^{1/3}$$

where κ is Von Kármán's constant (0.41) and z the distance to bottom.

The energy dissipation ε can be determined from the velocity power spectra, for which, according to Kolmogorov's spectrum theory, the inertial dissipation range has the form [Tennekes and Lumley(1972)] (see Chapter 4)

$$\phi_{\mathrm{ii}}(k) = \alpha_i\, \varepsilon^{2/3}\, k^{-5/3}$$

where $\phi_{\mathrm{ii}}(k)$ is the spectral density of the ith component of the velocity, k the wave number and the α_i is the 1D Kolmogorov constant.

Hence, in the inertial dissipation range, u_* can be finally expressed as [Kim et al.(2000)]

$$u_* = (\kappa\, z)^{1/3} \left(\frac{\phi_{\mathrm{ii}}(k) k^{5/3}}{\alpha_i} \right)^{1/2}.$$

The main difficulty with this method lies in the capture of the inertial range in near-bed spectra [Green(1992)]. Indeed, the inertial range corresponds to the range of frequency extending from the largest scales of isotropic turbulence to the viscous dissipation scales. The smallest near-wall structures (anisotropic turbulence) scale with the distance to the wall [Tennekes and Lumley(1972)], which implies that near the substrate the inertial range starts at a fairly high frequency. The viscous dissipation scale scales with the local Reynolds number, the wall Reynolds number

$$\mathrm{Re}_* = \frac{u_*\, \kappa\, y}{\nu}.$$

Therefore, the method relies on making measurements far enough from the bed but still in the logarithmic layer or at high enough friction velocity to have an inertial range large enough to be identified.

In theory, any of the three components of the velocity can be used to calculate u_*, but Kim et al. [Kim et al.(2000)] suggest that the vertical component is the one which is the less likely to be contaminated by other processes and therefore is likely to be the most representative of turbulence.

u_* estimations

Probe location in the horizontal plane is here only referred to as a region of the tank, but nevertheless, the exact distance between the tank bottom and the ADV probe is given with precision.

The different methods described for the estimation of friction velocity from ADV time series were applied to the measurements available in the bottom 4 mm. All time series were despiked and bad data were removed as explained earlier.

Comparisons between all methods for each time series show much variability (Table 2.9). Globally, good agreement is obtained between the TKE and COV methods, whereas higher friction velocities are globally found using only the y coordinate of the velocity field. These are around 1.5 times higher for propeller speeds of 75 to 750 and about 3 times for a propeller speed of 1000 rpm.

The COV method is the only approach which by definition gives a real measure of the Reynolds shear stress and should therefore provide a quantity closest to the effective friction velocity. This suggests that the TKE method should give a good estimation of the Reynolds shear stress. This is particularly important to realize as this method was used on the PTV data earlier.

The y-component approach of the TKE method should be more reliable than other components, as v' should be less biased by the influence of larger eddies and mean flow. The constant used in the method was derived from experimental data by Kim et al. [Kim et al.(2000)] in the context of tidally driven boundary layers and according to them its universality still requires confirming. Much lower values were found in all cases from the LB layer method, as it was observed earlier from the PTV data. Values here are even lower and tend to invalidate the assumption of the logarithmic layer profile for the mean velocities.

The inertial dissipation range on most of the velocity spectra generated from the ADV time series is hard to identify because of the noise, and when it can be identified is not smooth enough to lead to reliable estimations of u_*. For these reasons, the inertial dissipation method could not be used here. The use of much longer time series not available here and of averaging techniques should lead to smoother spectra from which more accurate estimations can be performed.

The remaining methods (LB, COV, TKE) are compared in Tables 2.9 and 2.10. Only the measurements at 500 and 750 rpm (Table 2.9) were made at exactly the same location and are coherent with an increase of the friction with propeller speed.

Comparisons with data at other locations do not lead to any obvious pattern of relationship between u_* and propeller speed. This can be explained by a very heterogeneous distribution of stress within the tank.

Table 2.9. Estimation of the friction velocity, u_*, from different methods, All ADV measurements were made in the bottom 4mm of the tank. Only the 500 and 700 rpm points correspond to the same (x,z) coordinate.

RPM	75	75	150	150	150	500	500	750	750
y (mm)	28.1	38.5	16.9	28.	38.2	17.3	28.5	17.3	28.5
u_* LB (mm.s^{-1})	1.9	1.1	2.7	3.	2.	1.0	1.5	1.8	1.6
u_* COV (mm.s^{-1})	12.	8.6	0.7	9.	4.	6.9	7.6	9.6	18.2
u_* TKE (mm.s^{-1})	13.	10.4	23.	22.	22.	6.2	9.2	12.3	16.8
u_* TKE-v' (mm.s^{-1})	18.	15.6	33.	33.	33.	12.1	12.6	20.3	27.2

Table 2.10. Estimation of the friction velocity, u_*, from different methods, All ADV measurements were made in the bottom 4mm of the tank. Locations are bottom center, left and right of the tank, propeller speed is 1000.

Position	Center	Left	Right
RPM	1000	1000	1000
y (mm)	6.9	9.5	7.2
u_* LB (mm.s^{-1})	8.	4.	1.
u_* COV (mm.s^{-1})	62.	35.	48.
u_* TKE (mm.s^{-1})	64.	43.	59.
u_* TKE-v' (mm.s^{-1})	25.	17.	22.

Five methods were applied to the available ADV data taken within the bottom 4 mm. The number of data points fulfilling all the criteria to be used in this section was limited, but several useful observations were made. Two of the methods, the inertial dissipation and the logarithmic boundary (LB) ones, both proved to be unusable in this context.

Comparisons to the COV method, which provides direct estimations of the near-bottom Reynolds-stress, showed apparent good agreement with the TKE method, which was not the case for the TKE-v' that only involves the vertical velocity fluctuations.

The magnitude of the friction velocities obtained here are hard to discuss as results are strongly dependent on the location where the measurement were made.

2.4.4 Discussion

The friction velocity, u_*, in a stirred tank was evaluated with six different methods. All of them, to some degree, are based on the constant shear or logarithmic boundary layer approximation. Nevertheless, they can still be seen as fundamentally different because they are each based on different measured quantities.

Three of these methods, the circulation model and the logarithmic profile are based on the mean flow. The circulation model is based on a characteristic velocity scale of the mean flow evaluated from an estimation of propeller discharge, whereas the logarithmic profile comes from measurements of the local mean velocities. All of the other methods are based on different approaches to the turbulent fluctuations recorded in the tank, with TKE, Reynolds stress or spectral distribution of the velocity fluctuations being the relevant quantities.

No consensus was found between the different methods with a factor of ten existing between the lowest estimations given by the logarithmic profile approach and the highest ones obtained from the theoretical model. The only characteristic common to all models was found to be proportionality between friction velocity at the bottom and propeller speed in rotation per minutes.

The logarithmic profile approach is likely the least suitable in the context of stirred tank modelling. The flow within the tank is fundamentally three-dimensional with large-scale instabilities and the mean velocity measurements are bound to at least partially reflect this reality. This makes the near-bottom flow far from a steady-state uni-directional flow required for the use of a logarithmic profile [Buchholtz-TenBrink et al.(1989)].

The circulation analytical approach is similar to the logarithmic profile approach as it assumes a direct link between friction velocity and mean velocity parallel to the bottom. It is nevertheless more of a scaling approach and the only approximation it really relies on is proportionality between mean circulation in the tank and u_*. As the model also predicts proportionality between circulation and propeller speed, the analytical approach is equivalent to a statistical correlation between propeller speed and friction velocity based on the assumption of proportionality. This assumption seem to be verified independently of the method. The correlation given by Oldham et al. [Oldham et al.(2004)] is based on their experimental measurements of the friction velocity by hot film sensors and are not universally constant. As noted by Oldham et al., u_* is likely to be dependent on vortical circulation in the tank which is geometry-dependent. It is most likely dependent on the location, with higher frictions velocities expected to be in the middle of the tank where both propellers are located, whereas the friction velocity should be lower in the PTV measurement slice, which is significantly off-center. This would explain partly why the circulation model tends to give much higher values for the friction velocity.

The approaches based on the ADV data did not lead to any reliable friction velocity estimates, but, they tend to show a high level of heterogeneity in the distribution of stress at the bottom. More importantly, good agreement is obtained in this context between TKE and Reynolds stress estimation of u_* suggesting that the TKE approach can be used in this context.

The friction velocity derived from the TKE obtained by PTV measurements are the most relevant to our stirred tank in the context of the settlement experiments realized on limited substratum areas. The value obtained on the settlement area at the 2 to 4 mm are used in the rest of this thesis.

2.5 Characterisation of core flow turbulence

Despite the existing links between core flow and friction velocity observed in the previous section, u_* is too closely related to near-wall turbulence to be used to characterise turbulence in the bulk of the tank. In this section, core flow turbulent mixing or diffusion in the case of mass and particle transport are addressed by analytical and experimentally-based approaches.

2.5.1 Tank mixing time-scale

Continuing the circulation approach presented in the friction velocity section, simple modelling of propeller discharge flow can be used to estimate the mixing time within a stirred tank.

According to the *bulk flow model approach* by Nienow [Nienow(1990)], a simple estimation of the mixing time for a stirred vessel (time when the system is effectively homogenised) is given by

$$\theta_m = \frac{5\,V}{F_l\,N\,D^3} \tag{2.9}$$

where V is the volume of the stirred vessel, N the propeller speed in revolution per second, D the propeller diameter and F_l the flow number defined as

$$F_l = \frac{Q}{N\,D^3}$$

where Q is the discharge flow of the propeller.

Using a flow number for a pitched bladed turbine of 0.73 as reported by Jaworski et al. [Jaworski et al.(1996)], the mixing time in our stirred tank can be estimated to

$$\theta_m = \frac{5\,(0.15)^3}{2\,0.73\,(\mathrm{rpm}/60)\,(0.03)^3} = \frac{20883}{\mathrm{rpm}}$$

therefore in the range 100-1000 rpm, the mixing time θ_m ranges between 209 and 20.9 s.

In a later paper, improved approximations were reported by Nienow [Nienow(1997)] with Ruszkowski [Ruszkowski(1994)] and Grenville et al. [Grenville et al.(1995)]'s estimation of the mixing time as

$$\theta_m = 5.9\,T^{2/3}\,(\bar{\epsilon}_T)^{-1/3}\left(\frac{D}{T}\right)^{-1/3}$$

where $\bar{\epsilon}_T$ is the mean dissipation rate and T the characteristic length-scale of the tank, which proved to be in very good agreement with experimental measurements. The bulk flow model can nevertheless provide order of magnitude of turbulent diffusion in the tank.

The mixing times derived from the bulk flow model (209 to 20.9 seconds) are close to the time-scales associated with propagule gravitational sinking speeds which are around 500 s. It is therefore conceivable that both turbulent mixing and gravitational sinking play equal roles in the settlement experiments realized in the tank. For that reason, a better evaluation of the turbulent transport was undertaken by the estimation of the eddy-diffusion in the tank.

2.5.2 Eddy-diffusion

I seek to relate turbulent "diffusion" to the quantities that were experimentally measured in the tank. While it is approximate, a one-dimensional profile was derived from an estimation of the eddy-viscosity based on the well know k-epsilon approach to turbulence modelling [Speziale(1991)] [Wilcox(2006)].

Turbulent Prandtl number

As it is a non-linear process, one could expect the eddy-diffusion (heat/mass) process to be easier to model than the eddy-viscosity (momentum) one which is fully non linear. Nevertheless, many more models were found in the literature to estimate the eddy-viscosity in a flow from the measurement of physical data, than for mass eddy-diffusion. This might come from the relative abundance of Reynolds stress experimental data with respect to eddy-diffusion measurement as suggested by Chang and Cowen [Chang and Cowen(2002)].

Temperature/mass eddy-diffusion and eddy-viscosity are linked by the turbulent Prandtl number, defined as the ratio of the eddy-viscosity to the the eddy-diffusion,

$$\mathrm{Pr}_t = \frac{\nu_t}{D},$$

by analogy to the molecular Prandtl number which is the ratio of the momentum diffusion ν (molecular kinematic viscosity) to thermal diffusion α_t,

$$\mathrm{Pr} = \frac{\nu}{\alpha_t}.$$

For mass eddy-diffusion, the Schmidt number, $\frac{\nu}{\alpha_m}$, where α_m is the molecular diffusion of the tracer, is equivalent to the Prandtl number. The turbulent Prandlt number depends on the Prandlt number itself [Mitrovic and Pavassiliou(2003)] as diffusion at molecular scales plays a role in turbulent transport. Technically, the Prandtl turbulent number is the ratio of eddy-viscosity to heat eddy-diffusion and not to mass eddy-diffusion. Nevertheless, for $\mathrm{Pr} = 1$, the Prandtl turbulent number is the ratio of eddy-viscosity to mass eddy-diffusion.

Many investigations have sought to estimate the turbulent Prandtl number Pr_t [Chang and Cowen(2002)] [Crimaldi et al.(2006)] [Reynolds(1975)] [Kays(1994)]. The simplest model for the Prandtl turbulent number is based on the Reynolds analogy assumption, which supposes that in a turbulent system the heat/mass flux is analogous to the momentum flux [Geankoplis(2003)] i.e. $\mathrm{Pr}_t = 1$. While the approximation has been experimentally proved in a limited number of cases (laminar flat-plate boundary layer at unity Prandtl number [Karniadakis et al.(1988)], gases when only skin friction is involved), it still leads to reasonably good (even if overestimated) computational results for scalar transport [Chang and Cowen(2002)].

Improved results have been obtained using $\mathrm{Pr}_t = 0.7$, these results being supported by laboratory work (using intrusive probes) and direct numerical simulation [Chang and Cowen(2002)]. Crimaldi et al. [Crimaldi et al.(2006)] report that analytical studies, direct numerical simulations and experimental results have demonstrated a good agreement with the Reynolds analogy for flow within the logarithmic boundary layer in wall-bounded flows with Pr_t values in between 0.85 and

1. They report far larger values of the turbulent Prandtl number in the viscous boundary layer due to a great decrease of the eddy diffusion in this region. As well, they mention the relatively small influence of the wall roughness on the turbulent Prandtl number.

Mitrovic and Papavassiliou studied dependence of the turbulent Prandtl number over the molecular Prandtl number in a flume by direct numerical simulation [Mitrovic and Pavassiliou(2003)]. They subdivided the flow in three zones:

- the "mean flow" zone, where the transport is mainly due to convection, where Pr has very little importance. There, Pr_t is shown to be in between 0.85 and 1 for low Prandlt/Schmidt numbers ($0.1 < \mathrm{Pr/Sc} < 10$), which is the case for seawater.

- the transition zone, where both turbulent and molecular transport are of importance. Here they observed a drop of Pr_t when approaching from the wall. In the transition zone the Prandtl/Schmidt number is of great importance. The greater the Pr/Sc, the further from the wall Pr_t is starting to decrease. Pr_t can go down to values of around 0.1/0.2.

- the viscous zone, near the wall, where the viscous transport dominates. The turbulent Prandtl number increases dramatically to reach high values, virtually infinite as eddy-viscosity tends towards 0 near the wall.

From these observations of wall-bounded flow where the mean velocity profile can be considered as logarithmic in the boundary layer, we can elaborate an approximation of the turbulent velocity profile to use in my model. A rough representation of the eddy diffusion in the tank, therefore will assume that we should use a Pr_t number that can be separated in three zones corresponding to the ones in Mitrovic and Papavassiliou [Mitrovic and Pavassiliou(2003)]. I will consider at first the following profile:

- $\mathrm{Pr}_t = 0.9$ outside the turbulent boundary layer.
- Pr_t linearly decreases from 0.9 to 0.2 within the logarithmic boundary layer.
- Pr_t linearly increases from 0.2 to 2.5 in the viscous sub-layer (Arbitrarily I take 2.5 as for the maximum Pr_t as it is the upper bound of Mitrovic and Papavassiliou [Mitrovic and Pavassiliou(2003)] Pr_t graphs.).

By assuming a turbulent Prandtl profile, turbulent diffusion can be estimated from the turbulent viscosity. I now need to estimate the turbulent viscosity from the physical data I have been able to measure in the tank (velocity, turbulent kinetic energy, velocity spectra) and the friction velocity u_* determined through the logarithmic layer assumption.

It is clear that the most reliable measurements I have of the turbulence in the whole tank are the turbulent kinetic energy field measured by particle tracking velocimetry over cross sections of the tank. For this reason, the use of an eddy viscosity model based on TKE is desirable.

Eddy-viscosity from the turbulent kinetic energy

A common approach to turbulence modelling in the context of the Reynolds-Averaged Navier-Stokes equations (RANS) is the k-epsilon model. In addition to the RANS equations two equations for the kinetic energy k and the energy-dissipation rate ϵ (epsilon) are solved. They allow a local estimation of the eddy-viscosity to model the influence of velocity fluctuations on the main velocity field [Speziale(1991)].

Knowing the kinetic energy and the energy-dissipation rate, eddy-viscosity can be expressed as [Speziale(1991)]

$$\nu_t = \rho_f C_\mu \frac{k^2}{\epsilon},$$

where C_μ is a constant which can be taken equal to 0.09 in the context of a standard k-epsilon model [Speziale(1991)]. Similar derivation of the eddy diffusion using a $k-$epsilon approach were used by Gross and al. [Gross et al.(1992)] to developed a 1-D model of larval settlement in a tidal or wave bottom boundary layer.

A rough approach to the estimation of the eddy viscosity in the tank can be made using the TKE profiles from PTV to obtain k and the estimation of the mean energy-dissipation rate derived from the simple tank model (see Chapter 4),

$$\bar{\epsilon} = 1.393e^{-9}\,\mathrm{rpm}^3.$$

The turbulent boundary layer is expected to be a region of special importance for the turbulent viscosity profile. Nevertheless, the PTV measurement only allows a resolution down to 2mm, which is coarse with respect to the boundary layer.

Within the assumption of constant shear stress layer [Tennekes and Lumley(1972)] the eddy viscosity profile in the turbulent boundary layer can be reconstructed. In the boundary layer, the sum of the viscous stress and the Reynolds stress is constant, and equal to ρu_*^2,

$$-u'v' + \nu\frac{\partial \bar{u}}{\partial y} = u_*^2 = |u'v'| + \nu\left|\frac{\partial \bar{u}}{\partial y}\right|.$$

If we introduce the turbulent diffusion, we get

$$|u'v'| + \nu\left|\frac{\partial \bar{u}}{\partial y}\right| = \nu_t\left|\frac{\partial \bar{u}}{\partial y}\right| + \nu\left|\frac{\partial \bar{u}}{\partial y}\right| = u_*^2,$$

which leads to

$$\nu_t = \frac{1}{\frac{\partial \bar{u}}{\partial y}} u_*^2 - \nu.$$

Using the logarithmic profile for the velocity, we end with

$$\nu_t = \kappa\, u_*\, y - \nu,$$

where κ is Karmann's constant and y the distance to the wall.

It is possible to derive a one-dimensional eddy-viscosity profile of the tank from the TKE measurements, the friction velocity at the bottom and an estimation of the mean energy-dissipation rate in the tank.

Summary of the turbulent diffusion profile

To summarise the two previous paragraphs the eddy diffusion profile is:

- for $0 < y \leqslant \delta_\nu$,

$$D(y) = \left[\left(\frac{0.2 - 2.5}{\delta_\nu}\right) y + 2.5\right](\kappa\, u_*\, y - \nu)$$

- for $\delta_\nu < y \leq \delta_t$,

$$D(y) = \left[\left(\frac{0.2 - 0.9}{\delta_t - \delta_\nu}\right) y + 0.2 - \left(\frac{0.2 - 0.9}{\delta_t - \delta_\nu}\right)\delta_\nu\right](\kappa\, u_*\, y - \nu)$$

- for $\delta_t < y$,

$$D(y) = 0.9\, \rho_f C_\mu \frac{k^2}{\bar{\epsilon}}.$$

where δ_ν is the viscous boundary layer thickness and δ_t the logarithmic layer thickness.

Inclusion of propagule properties

One thing that has not been taken into account in the calculation of the eddy-diffusion for the tank experiments is the fact that the propagules are coherent particles, and that therefore they cannot always be considered as a simple tracer.

If particles are very small ($d < 0.1\,\mu m$), then they are almost completely carried by the turbulent fluctuations. Therefore, the eddy diffusion for the particles is almost equal to the turbulent diffusion of the fluid [Altunbas et al.(2002)]. This applies especially when turbulent fluctuations are of much larger amplitude than the characteristic sinking velocity of the propagules (i.e., $R_V \ll 0$) which is the case in the tank core flow.

Within the boundary layer, viscosity becomes more important, and the characteristic scales of turbulence and particle eddy-diffusion should be used. The eddy diffusion of the particles is smaller than that of the fluid [Altunbas et al.(2002)].

Transverse velocity fluctuations in turbulent flow affect the transportation of particles. This leads to a difference in the eddy diffusivity of particles and that of the fluid such that [Altunbas et al.(2002)],

$$D_{\mathrm{TP}} = \mu_R D$$

with D the turbulent diffusion of fluid, D_{TP} the turbulent diffusion of the particle and μ_R the particle diffusivity coefficient. Turbulence can result in a sharp increase of the effective diffusion coefficient [Taylor(1921)].

According to Altunbas et al. [Altunbas et al.(2002)], in the case of a turbulent flow in a rough channel the particle diffusivity coefficient μ_R depends mainly on four parameters: the friction velocity of the fluid u_*, the sedimentation velocity of the particles V_p, the Reynolds number of the flow, Re, and the relative roughness of the channel $\left(\frac{\varepsilon}{D}\right.$, with ε the roughness of the channel and D its diameter). Experimental data from Soo and Ihrig [Soo and Ihrig(1960)] determined the particle diffusivity coefficient for an horizontal channel. One of their models that does not take into account the roughness of the channel expresses the particle diffusivity coefficient as,

$$\mu_R = 0.24 \left(\frac{V_p}{u_*}\right)^{1/4}, \ \mathrm{Re}_d \geqslant 2.5$$

$$\mu_R = \kappa(V_p) \left(\frac{V_p}{u_*}\right)^{1/4}, \mathrm{Re}_d < 2.5$$

where $\kappa(V_p)$ is an empirical parameter defined as $\kappa(V_p) = \frac{2.16}{V_p^{1/8}}$ and Re_p is the particle Reynolds number defined from the mean fluid velocity fluid U_m and the particle diameter d as $\mathrm{Re}_p = \frac{U_m d}{\nu}$. The sedimentation velocity of the particles was calculated, assuming that the particles are Stokes particles ($\mathrm{Re} \ll 1$), using the expressions determined by Mednikov [Mednikov(1981)] and by Liu and Agarwal [Liu and Agarwal(1974)],

$$V_p = 6.10^{-4}\, u_* \, \tau_+^2 \ , \ \tau_+ \leqslant 20$$

$$V_p = 0.2\, u_* \ , \ \tau_+ > 20$$

where τ_+ is the dimensionless relaxation time. For Stokes particles of density ρ_p and diameter d_p in a fluid of density ρ_f, the relaxation time is given by $\tau = \frac{1}{18}\frac{\rho_p d_p^2}{\rho_f \nu}$. It can be made dimensionless by using the friction velocity u_*, which gives $\tau_+ = \frac{\tau\, u_*^2}{\nu}$.

Even though the model does not explicitly take into account the roughness of the wall or substrate, u_* (the friction velocity) is representative of the shear stress exerted on the wall by the turbulent flow and would contain information on the nature of the wall. More information on

the properties of the wall are going to be contained by the eddy-viscosity with which the particle diffusivity coefficient has to be associated to form any larger-scale particle dispersion model.

2.5.3 Eddy-diffusion profiles

Turbulent eddy-diffusivity profiles were derived for each of the available PTV measurements of the TKE in the bottom of the tank. The use of a constant turbulent Prandtl number and of the k-epsilon model leads to a mass turbulent diffusivity profile close to a parabola with a maximum where the wakes of both propellers meet and a minimum near the bottom of the tank (Figure 2.11). The eddy-diffusion is sensibly lower in the near-wall region where lower levels of turbulent kinetic energy were measured. Local eddy-diffusivity remains in all cases much larger than sea-water viscosity by an order of 15 to 50.

Little change is observed in the shape of the profiles when the propeller speeds vary. Only small changes in magnitude are recorded with propeller speed. Almost no difference is found between the profiles for propeller speeds of 400 and 500. This is likely not to be realistic and it would be expected that turbulent-diffusivity increases steadily with propeller speed. Whereas the estimation of the rate of energy dissipation $\bar{\epsilon}$ is an averaged value over the tank, the experimental TKE measurements used here are local to the considered slice. It has been shown on similar types of flows [Deshpande and Milton(1998)] that the distribution of the Kolmogorov length scale, and therefore of the rate of energy dissipation, can be highly non-homogeneous, with the largest turbulence dissipation rates confined to a relatively small region near the propellers [Lu et al.(2002)]. Furthermore, it is likely that the energy dissipation rate does not vary homogeneously when propeller speed is increased. In the slice of interest, the rate of energy dissipation should increase slower than rpm^3, which leads to an underestimation of the eddy diffusion.

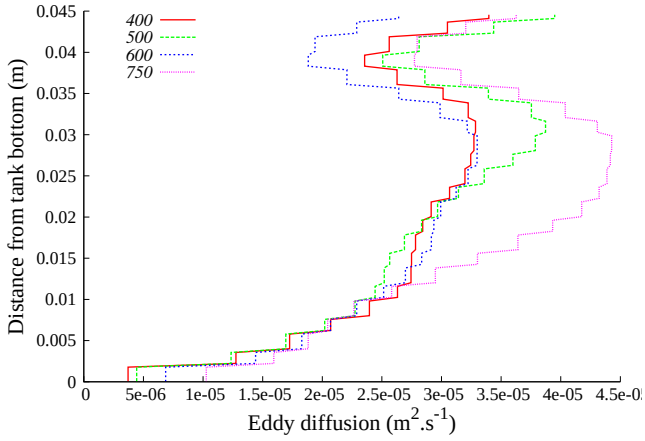

Figure 2.11. Eddy diffusivity profile in the tank without taking into account boundary layer increase in diffusivity.

When the turbulent Prandtl number is modified near the bottom to take into account the change of dynamics due to the importance of viscosity in the boundary layer, a small change in the profile shape can be observed. A decrease in turbulent mixing in the near-bottom region can be seen in Figure 2.12a, with local eddy diffusivity slowly decreasing to become null at the wall.

As stated earlier, the logarithmic profile of the turbulent boundary layer does not stand in the tank flow. The existence of a laminar and a turbulent boundary remains nevertheless true [Oldham et al.(2004)]. The size of the laminar boundary layer can still be calculated as $\delta = 5\ \frac{\nu}{u_*}$ [Tritton(1988)], but the size of the turbulent part of the turbulent boundary layer is not known *a priori*. It was assumed that the turbulent boundary layer extends from the wall until the mean velocity of the flow starts decreasing with the distance to the wall, which to some extent is equivalent to saying that the boundary layer extends until its mean velocity is equal to 0.99 times the velocity of the outer flow.

Within the core flow it is assumed that propagule properties are of little importance and that propagule turbulent diffusivity is equal to mass turbulent-diffusivity. Within the boundary layer, when viscosity effects are more important, the particle diffusivity coefficient μ_R is used to include a propagule/turbulence interaction in the model. This results in a drop in eddy diffusivity in the boundary layer region where viscous sinking becomes far from the dominant mechanism (Figure 2.12b).

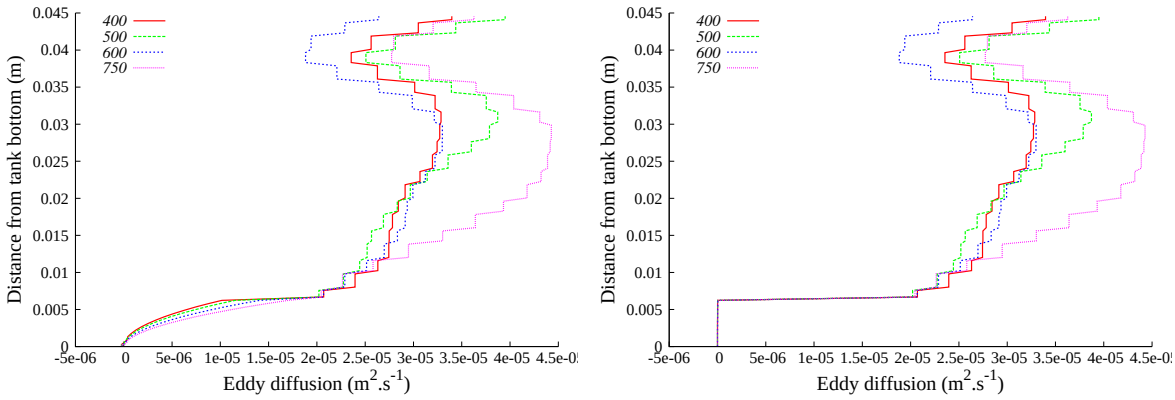

Figure 2.12. Eddy diffusivity profile for a given propagule (*Hormosira banksii* here) without taking into account a boundary layer increase in turbulent-diffusivity(a) and taking into account propagules properties in the boundary-layer (b).

The rather discontinuous shape of the turbulent-diffusion profiles presented here is likely to be well exaggerated; nevertheless, these profiles give a good idea of the order of the transport processes in action in the tank.

2.5.4 Péclet number

More useful information is contained in the Péclet number derived from the various turbulent diffusivity profiles (Tables 2.11 and 2.12), the ratio of the time-scale associated with gravitational sinking to the time-scale associated with turbulent transport.

The time scale associated with Stokes sinking is propagule-dependent and derived from the measured sinking speed of the propagules as

$$T_s = \frac{h}{V_s},$$

where h is the height of the tank.

The time scale associated with turbulent diffusion is given by

$$T_\kappa = \frac{h^2}{\bar{D}},$$

where

$$\bar{D} = \frac{1}{h}\int_0^h D(y)\mathrm{dy}.$$

Therefore, the Péclet number is defined as

$$\mathrm{Pe} = \frac{V_s\, h}{\bar{D}}.$$

High Péclet numbers ($\mathrm{Pe} \ll 1$) denote the preponderance of gravitational sinking over turbulent transport, and propagule sinking should therefore be little affected by turbulence. A low Péclet number ($\mathrm{Pe} \gg 1$) would see turbulent transport dominating the whole process.

Because they depend on the turbulent-diffusivity profile and propagule properties, Péclet numbers have to be calculated for the different types of profile and Stokes velocities envisaged (Tables 2.12, 2.11 and 2.13).

For all three different types of turbulent-diffusivity profiles the Péclet numbers are very similar with most of the variation being due to the differences in Stokes settling speed for the propagules of different species. For example, at 400 rpm, the Péclet number for the slow sinking *Durvillaea antarctica* varies between 0.38 and 0.40 depending on the model, which is almost no variation. For all species, Péclet numbers decrease by about 0.1 when propeller speed increases from 400 to 750 rpm. For given mixing intensity and model, differences between slow sinking *Durvillaea antarctica* and *Fucus gardneri* can be up to 0.2. All Péclet numbers remain overall around 0.3 to 0.6. Such values of the Péclet number indicates that despite a slight domination of turbulence, the time scales associated with turbulent and gravitational transport remain of comparable magnitude.

Species - RPM	400	500	600	750
Durvillaea antarctica	0.38	0.36	0.39	0.31
Hormosira banksii	0.46	0.44	0.48	0.38
Cystophora torulosa	0.43	0.41	0.45	0.35
Pelvetiopsis limitata	0.51	0.49	0.54	0.42
Fucus gardneri	0.55	0.52	0.57	0.45

Table 2.11. Péclet numbers for eddy diffusivity profiles based on the Reynolds analogy.

Species - RPM	400	500	600	750
Durvillaea antarctica	0.40	0.38	0.43	0.33
Hormosira banksii	0.50	0.47	0.52	0.40
Cystophora torulosa	0.46	0.43	0.49	0.37
Pelvetiopsis limitata	0.55	0.52	0.58	0.45
Fucus gardneri	0.59	0.56	0.62	0.48

Table 2.12. Péclet numbers for eddy diffusivity profiles with boundary layer model.

Species - RPM	400	500	600	750
Durvillaea antarctica	0.39	0.37	0.41	0.32
Hormosira banksii	0.48	0.46	0.51	0.39
Cystophora torulosa	0.49	0.42	0.47	0.36
Pelvetiopsis limitata	0.54	0.51	0.56	0.44
Fucus gardneri	0.57	0.54	0.60	0.46

Table 2.13. Péclet numbers for eddy diffusivity profiles with boundary layer and propagule model.

In comparison, the Péclet numbers were also estimated from the mixing time presented in the theoretical model (Table 2.14). The Péclet number predicted by this method are a factor of 5 to 10 smaller than the ones derived from the PTV-based models. The lower values correspond to a higher averaged turbulent diffusion at the scale of the whole tank than at the scale of a slice. Also, turbulent diffusion increases clearly here with propeller speed, which is no surprise given the model formulation.

Unlike for the previous estimations, the time-scale associated with turbulent diffusivity is one order of magnitude smaller than the one associated with Stokes sinking. In that case, the action of gravitational sinking should be negligible compared to the one of turbulent transport. This outcome is fundamentally different to, if not opposite to the conclusions of the other approach.

Species - RPM	400	500	600	750
Durvillaea antarctica	0.082	0.066	0.055	0.044
Hormosira banksii	0.100	0.081	0.067	0.054
Cystophora torulosa	0.093	0.075	0.062	0.050
Pelvetiopsis limitata	0.119	0.095	0.080	0.063
Fucus gardneri	0.112	0.090	0.075	0.060

Table 2.14. Péclet numbers derived from Nienow's mixing time [Nienow(1997)].

For both approaches, the Péclet numbers found here are in the range of Péclet numbers considered in the model of Deleersnijder et al. [Deleersnijder et al.(2006)] (10^{-3} to 10^{2}, see next Chapter). Given the relatively short time scale associated with the mixing time in the tank and the fact that R_V, the ratio of the Stokes sinking speed over the turbulent fluctuation, is much smaller than 1, the Péclet numbers expected here should be much smaller than 1 as well. This is not the case for the estimation made from the TKE, the main drawback of which, is likely to be the local nature of the TKE estimations used here.

It is hard at that stage to be assertive about the worth of these two approaches to evaluate turbulent diffusion. Whereas both are based on proven methods ($k-\epsilon+$ turbulent Prandtl and mixing time), extra assumptions were made to adapt these methods to the measurements. The purely theoretical approach (mixing time) is the one of the two methods which involves the less additional approximations and therefore should be given extra credits. It does not involve propagule properties or explicit boundary layer models, but these did not prove to have a critical influence on the Péclet number.

On an other hand, sinking experiments made with the real propagules (see next Chapter) lead to averaged turbulent sinking speed for the propagules strongly related to the Stokes sinking speed of each species. This certainly cannot be explained from the Péclet numbers derived here, which tend to minimise the importance of gravitational sinking. There is therefore a need for further investigations, possibly in a more direct way (integrated approach) of propagule sinking and determination of the shape of the sinking curves for the different Péclet number found here.

The simplest formulation in terms of mixing time remains for now the most reliable here. It shows that if propagule transport is assumed to be assimilable to mass turbulent-diffusion, turbulent transport is always at least ten times more important than gravitational sinking. Whereas this is true for the core flow, it has to be kept in mind that gravitational sinking remains the dominant process when it come to the last stage of settlement and boundary layer crossing, as indicated on a larger scale domain by Stevens et al. [Stevens et al.(2008)].

2.5.5 Summary

Two approaches have been presented to estimate the relative importance of turbulent transport within the stirred tank. A theoretical approach led to estimation of the mixing time within the tank comparable or much smaller than the time-scale associated with propagule sinking in the tank. This suggests that turbulence can decrease the settling time of some of the propagules to time-scales much shorter than the ones associated with gravitational sinking.

Other estimations of the ratio of turbulent to gravitational transport were derived from the PTV measurements of the turbulent kinetic energy using a $k-\epsilon$ approach. A better knowledge of the tank flow and notably the distribution of the energy dissipation rate over the tank would be required to obtain more credible estimates of the Péclet number from this approach. Boundary layer and propagule properties influences were included in this second approach, both resulting in a drop in the averaged turbulent-diffusion of a propagule. Whereas the model has been evaluated as not reliable here, it showed that the turbulent boundary-layer should have a non-negligible influence on the time-averaged sinking speed measured on the propagules.

The Péclet number is used here to evaluate the relative importance of buoyancy and turbulent transport in average over the whole water-column. A similar quantity, the Rouse number Ro, can be defined for the same comparison but within the turbulent boundary layer [Hendriks et al.(2006)]:

$$\mathrm{Ro} = \frac{V_s}{\kappa\, u_*}.$$

Beside its local meaning at the scale of the water-column, Ro can be seen as a higher bound to the Péclet number associated with propagule sinking in the water column. From the estimations of the friction velocity derived in the first half of this chapter, the Rouse number for propeller speeds ranging between 400 and 750 ranges between 0.3 and 0.09. This tends to support the better suitability here of the circulation model-based estimation of the Péclet number.

It is not straightforward to give an explicit analytical estimation of the Péclet number on a typical rocky shore. Nevertheless, like in the tank, it is smaller than the Rouse number. Stevens et al. [Stevens et al.(2008)] estimated u_* to range between 0.001 and 0.1 $m.s^{-1}$, with the fastest sinking propagule having a Stokes velocity of 0.63 mm.s^{-1}. In the extreme condition of a very quiet sea, the Péclet number parameterising propagule turbulent sinking would be smaller than 1.5. Therefore, the Péclet number is almost always smaller than 1 and turbulent transport almost always dominates over gravitational sinking.

The action of turbulent mixing should substantially increase the settling speed of a significant proportion of the propagules suspended within the tank. In a domain of infinite size, the average action of any diffusion-like process is null and the mean velocity of settling propagule would therefore be their Stokes sinking speed. The diffusion process controls the variance of the sinking process which in the case of low Péclet numbers is large with respect to the time-scale associated with gravitational sinking. Within the stirred tank, the free surface prevents propagules from dispersing too far away from the substrate and "reflects" them [Denny and Shibata(1989)]. This, together with the high turbulent mixing should act to increase propagule sinking for a large part of the population. This tallies with a simple approach to passive larval settlement in an ideal

turbulent logarithmic layer presented by Denny [Denny(1988)], who estimated the mean settlement time of propagules to be reduced down to around ten seconds by turbulent transport (compared to several minutes for gravitational sinking).

It is clear that turbulent transport is the primary mechanism when it comes down to water-column crossing. An important time-scale to evaluate the chances of propagules to be successful at settling is the time-scale associated with their sinking time.

Although the Péclet number presented in this section only presents a scaling of the importance of turbulent transport and gravitational sinking in the core of the tank, these data are related to propagule sinking speed in the following chapter.

Chapter 3
Settlement experiments

3.1 Introduction

The settlement experiments briefly referred to in the general introduction are described here and analysed in details. Propagule settlement experiments were realized within a stirred tank or benthic chamber. Stirred tanks are a convenient alternative, but far less popular, to flumes which have been extensively used to simulate benthic environment (see [Hendriks et al.(2006)] [Nowell and Jumars(1987)] [Muschenheim et al.(1986)]) and study the settlement of diverse micro-organisms (see [Hendriks et al.(2006)] [Gregoire et al.(1996)] [Butman and Grassle(1992)]). Stirred tank flows are quite different from flume flows for which the lower part of the boundary layer can be described by a logarithmic profile [Hendriks et al.(2006)], which is a great asset when it comes to characterising the turbulent boundary layer. It is likely that the less idealised flows generated by stirred tanks are the main reasons why flumes remain often a first choice. It could be argued, however, that for the same reasons stirred tank flows are probably closer to the complexity level of the flows found on rocky shores.

Just like propagule settlement in the intertidal zone which is comprised of a sinking and an attachment phase, the experiments here showed sinking curves made up of a settlement phase and a phase corresponding to an equilibrium between attachment forces and hydrodynamical removal forces. Theoretical models backed by the tank measurements previously described were used to test the experimental data. Propagule adhesiveness was derived from experiments using a particle detachment model.

3.2 Description of the experiments

The objective was to study the influence of different levels of turbulence on the settlement of the zygotes of the five seaweed species described earlier for the stirred tank.

Seaweed propagules were obtained from samples of adult plants collected in the field and left for 24 hours in a fridge at 4°C. Exposing the algae to room temperature instigates the release of their eggs or sperm. These gametes were washed from the algae using filtered seawater. After collection, the male and female gametes were left to fertilise for 15 minutes before being put into

the tank filled with 3 litres of 1 μm filtered seawater. Estimates of the number of propagules used to seed the tank were made by counting the number of propagules in several 0.1 ml samples in a Petri dish using a 100x binocular light microscope. The number of fertilised propagules used in each experiment was between 50,000 and 100,000 per litre of seawater. This ensure a relatively low concentration of propagules in the tank which allows to count them easily. Also, high concentration effects such as enhancement of the viscosity and hydrodynamical interactions between propagules are avoided.

In order to have an homogeneous distribution of propagules at the beginning of experiments, the propagules were gently stirred from the bottom and then re-suspended by stirring the tank at 1000 rpm for 5 seconds.

Four counting areas of 4 mm^2 were chosen on the bottom substrate at 20 mm from the centre of the tank. Using a rigid borescope (Hawkeye Brand), the number of settled propagules were counted at 60, 120, 360, 540, 720, 900, 1200 seconds after the experiment began. The same experiment was renewed for propeller speeds of 250, 300, 350, 400, 500, 600, 750 and 1000 rpm, in five replicates. For each series of runs the same propagules were used. Between each run the propagules were manually re-suspended in the tank so that the initial state in the tank was the same. In order to be sure that the properties of the propagules were not significantly changing over the time scale of a series of runs, the order in which the propagules were exposed to the different turbulent regimes was randomly changed.

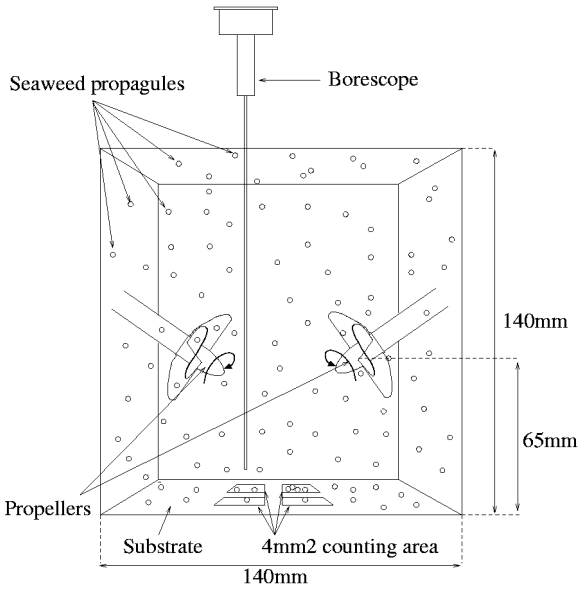

Figure 3.1. Sketch of the settlement experiments using the stirred tank. A borescope was used to count the number of propagules settled on 4 mm^2 areas of substrate for several rotating speeds of the propellers.

3.3 Experimental results

The sinking curves obtained from the experiments described in the previous paragraph (Figure 3.2) needed some post-processing to be comparable, but it was already possible to make some observations. The settling curves appeared to have similar shapes for all the species, which suggests that they all have the same settlement process. The curves certainly have distinct scaling, depending on the amount of stirring exerted in the tank. In no case did propagules remained settled at a propeller speed of 1000 rpm.

At rotating speeds beyond 1000 rpm, the hydrodynamical forces exerted on the propagules at the bottom would be higher than at 1000 rpm and therefore none of the propagules would be able to attach. Experiments run at 0 rpm represent the quietest conditions possible, meaning that the overall range of turbulence regimes covered the whole range of turbulence conditions at which zygotes of the five species could settle successfully.

As all five species settlement curves have similar forms, only the experimental data obtained for *Hormosira banksii* (see Figure 3.3) will be described in detail. For all species, two families of settlement curves have to be distinguished: the ones for which no forcing or energy input is exerted in the tank during the experiments, and the ones involving energy input through stirring. In both cases, the propellers were run at 1000 rpm for 5 seconds before starting the experiments in order to re-suspend the propagules.

3.3.1 Experiments without stirring: Stokes sinking velocities

The top black curve on Figure 3.3, is from the first "no forcing family". The propellers remained turned off during the whole experiment. This curve can be split into two parts: a linear slope and then a threshold or plateau. No mixing is involved in the tank, and therefore, a pure gravity-induced sinking of the zygotes was observed which explains the constant-slope part of the curve. All the seaweed propagules appeared to be sink at approximately the same speed. Because the Stokes sinking velocity (see Chapter 1) depends on the density and diameter of a propagule, slight variations can exist within the propagule population of each species. Nevertheless, the sinking velocity of all propagules should remain within 4% of the average sinking speed (from error in diameter and sinking rate measurements). As the distribution of propagules is effectively homogeneous at $t = 0$, the number of settled zygotes increases uniformly until all propagules have settled. At this moment, the threshold is reached and no more zygotes are sus-

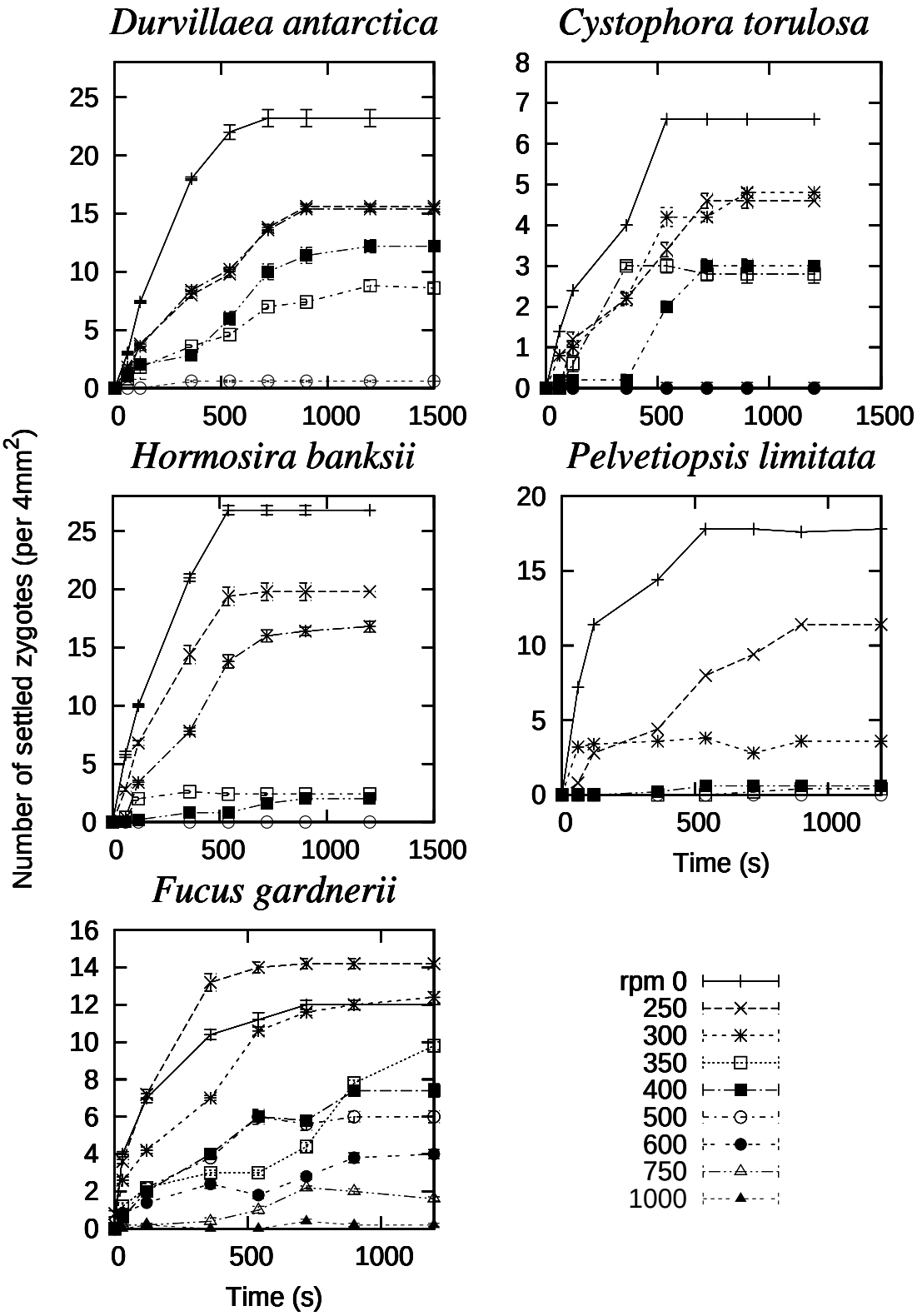

Figure 3.2. Number of settled zygotes per counting area versus time for a whole range of turbulent regimes (propeller speeds) for *Durvillaea antarctica*, *Cystophora torulosa*, *Hormosira banksii*, *Pelvetiopsis limitata* and *Fucus gardneri*.

pended in the tank, and the system stops evolving. In summary, when no mixing is involved, the sinking curves are decomposed into two parts, a linear gravitational sinking followed by a threshold when all the propagules have settled.

The main interest in the "no forcing curves" is that they give an estimate of the Stokes velocity, and therefore the propagule densities, which can be confronted to those obtained using the sinking column (Chapter 1 - Table 1.1). Assuming that all propagules sink at the same speed, the threshold is reached when propagules furthest from the bottom have settled, which means when these have crossed the whole tank (14 cm). An estimation of the sinking velocity can then be made by dividing the height of the tank by the time at threshold.

The sinking velocities found from the tank experiments are summarised in Table 3.1. The times to the threshold were first measured on the curves as the time at which the tangent to the point forming the linear part of the curve intersected with the threshold line. The tangents were drawn by visual inspection. The sinking velocities (as explained in the previous paragraph) are the water height in the tank divided by the time at threshold. The propagule densities are then derived from the sinking velocities using Stokes' Law (Chapter 1). The sinking velocities obtained this way ranged from 0.22 mm.s^{-1} for *Durvillaea antarctica* up to 0.32 mm.s^{-1} for *Fucus gardneri*. The species from Oregon sank faster than those from New Zealand (sinking velocities from 0.22 mm.s^{-1} to 0.27 mm.s^{-1} for the New Zealand species and from 0.30 mm.s^{-1} to 0.32 mm.s^{-1} for Oregon species).

The sinking velocities determined here are of the same order of magnitude as those determined using the column summarised in Table 1.1. Nevertheless, the speeds found using the settling column were globally higher than those measured in the tank (from 0.29 mm.s^{-1} to 0.63 mm.s^{-1} in the column, from 0.22 mm.s^{-1} to 0.32 mm.s^{-1} in the tank). In both case *Durvillaea antarctica* has the slowest sinking velocity and *Pelvetiopsis limitata* the highest. For the three other species, there is no obvious correlation between the sinking velocities found in the two experiments. For example, the zygotes of *Cystophora torulosa* and *Pelvetiopsis limitata*, which according to the settlement column results (Table 1.1) have very similar sinking rates (0.62 and 0.63 mm.s^{-1}), appeared to have different behaviour in the stirred tank. Nevertheless, because of their large diameters, Stokes Law still leads to similar densities for the two species of zygotes.

Table 3.1. Time to reach a threshold of settlement and derived sinking velocity obtained from the stirred tank experiment, along with data from a settling column.

Species	Time to threshold s	Sinking velocity from stirred tank mm.s^{-1}	Sinking velocity from column mm.s^{-1}	Diameter μm	Propagule density g.cm^{-3}
Durvillaea antarctica	630	0.22	0.29	29.3	1.5078
Hormosira banksii	520	0.27	0.44	60.8	1.1621
Cystophora torulosa	570	0.25	0.62	101.0	1.0706
Fucus gardneri	440	0.32	0.37	74.0	1.1346
Pelvetiopsis limitata	460	0.30	0.63	103.0	1.0777

The differences in sinking speeds derived from the two experiments could have several origins:

– the 5 seconds of stirring imposed on the tank before starting the experiments could play a role in the differences recorded. Propagule inertia at the beginning of the experiment might influence settling velocities. A length-scale associated with propagule inertia is the stopping distance [Friedlander and Johnstone(1957)] [Stevens et al.(2008)] defined as

$$d_i = \frac{u_t \, \rho_p \, d_p^2}{18 \, \rho_0 \, \nu}$$

where u_t is a characteristic velocity-scale associated with the turbulence in the core flow. The square-root of the average TKE is used here to derive u_t which leads to an upper limit of the stopping distance of around 0.2 mm, which is very small in comparison with tank size. Particle inertia should therefore have little influence on the variations observed between both experimental devices.

– the mucus that surrounds the propagules might have some influence on settlement rate. In the case of the sinking column a big quantity of mucus and propagules is deposited at the top of the sinking column. The propagules sink through this mucus and then just through seawater. In the stirred tank, zygotes do not sink through the mucus, but likely remain coated with all of its buoyant mucilage during the whole experiment. The presence of a bigger volume of mucous around a propagule would enhance the size of the propagule and reduce its averaged density. An additional $1\mu m$ to the diameter a propagule would induce an increase in the sinking speed of 0.01 to 0.02 mm s^{-1}. This is contrary to the observations. A variation of 10 $g\,\mathrm{cm}^{-3}$ in the total density of a propagule would

result in an increase or decrease of 0.005 to 0.06 mm s^{-1} which is far from negligible. A combination of increase in size and decrease of density could result in variations in settling rate large enough to explain part of the difference from column to stirred tank.

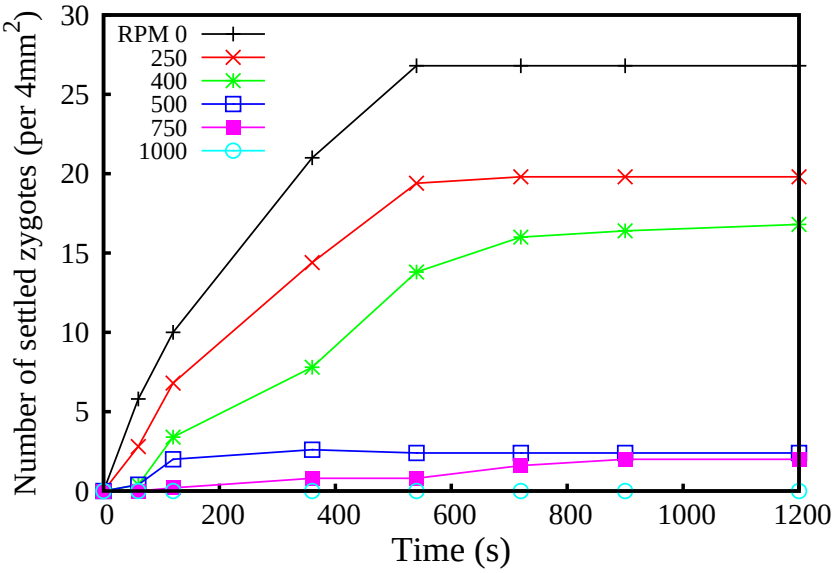

Figure 3.3. Settlement curves for *Hormosira banksii*: Curves show the number of settled zygotes per 4mm^2 area versus time. Each curve corresponds to a stirring regime in the tank from 0 rpm (no stirring) to 1000 rpm.

The propagule properties derived from experiments at 0 rpm will be used in the rest of the thesis rather than the ones from sinking column as they should be the most representative of the propagule–mucous system relevant to the tank experiments.

3.3.2 Experiments with the propellers on

All of the curves beyond the top one on Figure 3.3 belong to the second family of curves, in which the propellers were used during experiments. Except for the highest stirring rates, the results have a similar shape to those obtained when no stirring was involved. The curves can still be separated in two parts, a linear slope and then a threshold.

As before, the linear part corresponds to a progressive settlement of zygotes. When the propellers are turned on, the propagules still make contact with the substrate and some manage to attach. As time passes in the experiment, more propagules have been in contact with the bottom, and more have settled. When propellers are on, the Stokes Law cannot strictly be used to predict or describe the settling of zygotes because the turbulence in the tank should be taken

into account in the sinking process of the propagules. Even if propagule settlement rate is now turbulence-dependent, it still appears as if settlement happens linearly (at a constant rate), at least at low rpm.

The second part of the settlement curves, where turbulent mixing is involved, corresponds to the asymptote. All the experiments were done using the same number of propagules. Therefore, because the asymptotes are much lower when stirring is involved, it appears that not all propagules get to settle. It can be argued that the flow within the tank is highly inhomogeneous and particles are likely to get trapped in low-velocity regions like the corners of the box. However, this is apparently not the case. Zygotes do not get trapped anywhere in the tank, so it can be considered that the number of zygotes relevant to the experiments remains identical regardless of the turbulent regime. Therefore, from a threshold lower than the one found for pure sinking, it can be inferred that not all the propagules have settled at the end of the experiments.

"Threshold" here does not correspond to the state when all the propagules have settled, but to the state when all the propagules that have the ability to settle have settled and the others are still in suspension in the tank. It corresponds to an equilibrium state between the forces that keep the zygotes settled (their stickiness) and the removal forces (hydro-dynamical forces). The threshold can be described as well as the state when all the propagules that are "sticky enough" have settled. The propagules that are not "sticky enough" manage to reach the substrate as well but cannot remain attached and are permanently re-suspended in the tank. This assumes that all the propagules had a chance to meet with the substrate. If all propagules have the same probability of chance of meeting the substrate, it is only a matter of time for all the propagules to do it. When the asymptotic stage is reach, all propagules should have had a chance to attach.

This explains the data obtained for high rotating speeds of the propellers. In these cases, the shear forces exerted at the bottom of the tank are so important that a very small number of zygotes are sticky enough to remain settled on the substrate. Then the linear part of the curves is almost non-existent and most of the propagules remain suspended in the tank during the whole experiment.

The time when the asymptote is reached (time at threshold) and the number of settled zygotes at threshold were determined drawing the tangent to the linear and threshold part of all the experimental settling curves (see Appendix A). The settling rates were calculated by dividing the depth of the tank (140mm) by the time at threshold.

The times at threshold for the New Zealand and the Oregon species were of similar order of magnitude. Except for some specific data points, the time needed to reach the equilibrium state between stickiness and removal forces increases when the speed of the propellers increases, until a point where the number of settled zygotes per area of settlement becomes too low. Then, the measurement errors become significant, and the value at threshold can be considered as too biased to be useful. *Durvillaea antarctica* is the species for which the number of settled zygotes remains reasonably high the longest, and consequently has the largest range of settling rate that can be considered as meaningful. For *Durvillaea antarctica*, as for the other species (except for a few dubious data points), the highest settling rates is for the pure sinking case (0.22 mm.s^{-1}). Then, the settling rate decreases smoothly when the stirring increases (0.16 mm.s^{-1} for 250 rpm, 0.13 mm.s^{-1} for 600 rpm and 0.12 mm.s^{-1} for 750 rpm).

For the five species studied, when turbulence is involved, the settling rate of the propagules does not seem to vary much with time or the concentration of propagules suspended in the tank. The intensity of the stirring has an influence on the sinking of propagules, and slows them down. Despite being lower, the average settling rate of the propagules under turbulent conditions remains comparable to the one of the Stokesian sinking rate, suggesting that the Stokes sinking velocity associated with the propagules remains of importance even when the tank is stirred.

Despite the very complex nature of the experiment which involves complexity at all levels, using propagules of not completely known properties in a complex geometry and turbulent flow, it is quite amazing to find curves that apparently look so simple. This gives hopes for a parametrisation of this problem in terms of a limited number of parameters and the development of a simple model able to explain the settling curves obtained experimentally.

3.3.3 Normalised results

The settlement curves from the different species have very similar shapes, suggesting that all species have fundamentally the same settlement process. A second observation is that two parameters are sufficient to describe the settlement curves :

- the settling rate or average sinking speed of the propagules, V_p. It describes the first part of the curves, the linear slope. This parameter is representative of the way the propagules make contact with the bottom of tank. Assuming that a propagule will attach if it meets the substrate, this parameter describes the way the propagules travel within the tank to reach their settlement area. It is representative of the turbulent (or not) flux of the zygotes to the substrate.

– the number of settled zygotes per counting area at threshold, N_{th}. This parameter can be seen as the concentration of propagules sticky enough to attach and remain attached with the imposed turbulent conditions.

The variability remaining in the system that does not depend on the two parameters previously identified can be checked graphically by non-dimensioning of the results. As the maximum distance to travel for zygotes is 140 mm in all cases, the settling rate parameter is a parameter equivalent to the time at which the threshold starts. Dividing the time scale (x-axis) by the time at threshold would render the results independent of the settling speed parameter. As well, normalising the number of settled zygotes per counting area (y-axis) per the number of settled zygotes per counting area at threshold, would render the results independent of the concentration of zygotes sticky enough in the tank.

After applying the above normalisation to the experimental results, the curves obtained (see Figure 3.4) are all quite similar. Except for *Fucus gardneri* for which there is more variability and the rpm = 400 case for *Pelvetiopsis limitata*, the normalised curves for the other species seem to fit the curve

$$\begin{cases} f(x) = x\,, x \in [0;1[\\ f(x) = 1\,, x \in [1;+\infty[\end{cases}.$$

Two conclusions can be made from Figure 3.4. First, the two quantities, settling rate and number of settled zygotes at threshold, definitely give a good description of the range of settlement behaviour in the settlement experiments. Second, the understanding of each of the two parameters should allow an understanding of the whole settlement process for all species.

The differences observed for *Fucus gardneri*, and in a less important way for *Pelvetiopsis limitata*, are not surprising given the variability in the experimental curves (Figure 3.2). Some of the settlement curves intersect, which clearly shows that the propagules have a more complex behaviour in these cases or the experiments are biased in some way.

The two parameters of the problem are certainly not fully independent as they are related to the same system. Nevertheless, they can be seen as relevant to two different problems. As stated earlier, the mean sinking velocity V_p reflects the ability of propagules to find their way to the substrate through the core tank flow and the boundary layer. It can be seen as a propagule travel/attachment problem, which is likely to depend on the flow dynamics within the tank and near the wall. The number of settled propagules at threshold is governed by an equilibrium state between propagule adhesiveness and removal forces and is indicative of the flow in the vicinity of the substrate.

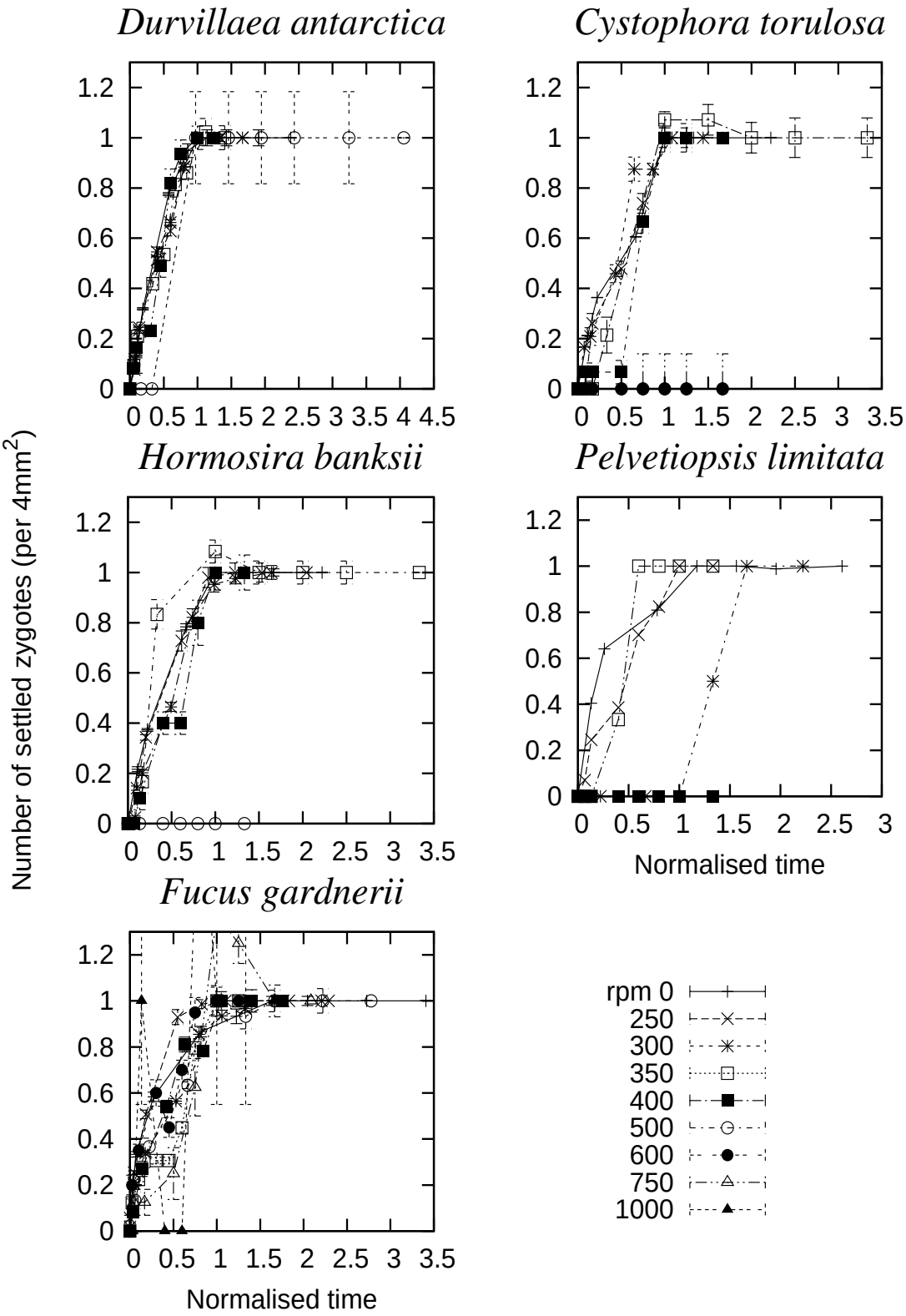

Figure 3.4. Normalised curves of the number of settled zygotes per counting area versus time for a whole range of turbulent regime (propeller speed) for *Durvillaea antarctica*, *Cystophora torulosa*, *Hormosira banksii*, *Pelvetiopsis limitata* and *Fucus gardneri*. The x-axis is normalised by the settling rate found for the experimental curve, and the y-axis by the number of settled propagules at threshold.

The decomposition of the results into two problems is coherent with the decomposition of the settlement problem proposed in the introduction, and sinking and attachment/detachment can be treated separately.

The non-dimensional sinking speed, V_p^*, settling speed normalised by the Stokes velocity, and the non-dimensional number of settled zygotes, N^*, number of zygotes at threshold normalised by the number of zygotes at threshold when no stirring is involved, are used instead of the dimensional data in the following.

Both quantities now have to be related to the problem parameters and characterised separately.

3.4 Turbulent settling rates

Even though the shape of the sinking curves might not be exactly linear, propagule settling can be related to a mean settling speed that depends on propagule and flow properties.

As stated in the introduction, three parameters, the reduced density ratio

$$R_\rho = \frac{\rho_p - \rho_f}{\rho_f},$$

the buoyancy particle Reynolds number

$$\mathrm{Re}_p = \frac{d_p V_s}{\nu}$$

and the ratio of the Stokes sinking speed to the characteristic velocity of the turbulent fluctuations

$$R_V = \frac{V_s}{V_T},$$

similar to the Péclet number defined in Chapter 2, should parametrise the whole problem and therefore lead to a physical model of the settlement process.

Within the range of propeller speeds and propagule properties considered,

- R_ρ varies between 0.47 and 0.046. All propagules are negatively buoyant, with some of them very close to water density.

- Re_p varies between 0.0064 and 0.0307. The buoyancy particle Reynolds number is always far smaller than 1 which means that inertial effects on the propagule are negligible.

- R_V varies between 0.0064 and 0.016. This implies that at any time, the turbulence velocity scale is much bigger than the characteristic velocity of the propagules. Therefore, propagules should be well mixed in the tank.

For the experiments that do not involve any forcing, the slope of the curves or settling rate is given by the Stokesian buoyancy-induced propagules settling speed

$$V_s = \frac{2}{9}\frac{r^2\, g\,(\rho_p - \rho_f)}{\mu_f} = \left(\frac{1}{18}\,\nu\,\mathrm{Re}_p^2\,R_\rho\right)^{1/3},$$

which only depends on Re_p and R_ρ. It is assumed that in this case Stokesian mechanics can be used as Re_p is very small and $R_V = \infty$.

Working on the normalised settling rate $V_p^* = \frac{V_p}{V_s}$ implies that a dependency of the settling on $\left(\mathrm{Re}_p^2\,R_\rho\right)^{1/3}$ is now hidden.

Changing the propeller speed allows one to control R_V. It would therefore be expected that R_V is the main parameter that controls the variations of shape of the settling curves.

Variation of the propeller speed generates turbulent eddies within the tank. Whereas R_V suggests that turbulent transport should dominate propagule dynamics, the measured mean settling velocities remains apparently strongly related to the Stokes sinking velocity.

In order to get an idea of the processes that govern the settlement in the tank, several scenarii can be explored:

- large scale (tank scale) eddies are ensuring efficient mixing at the scale of the tank.

- propagule turbulent sinking can be described using a turbulent drag coefficient that includes turbulent interactions between propagules and turbulence as well as viscous friction.

- propagules behave like a tracer, subject to local (i.e. smaller than tank scale) mass turbulent-diffusion and Stokes sinking.

3.4.1 "Perfect mixing" model

An approach to model the sinking curves is to assume that turbulent mixing ensures homogeneity in the tank at all times. This is equivalent to assuming that propellers ensure a perfect mixing at tank scale. A Lagrangian approach is adopted, with propagules treated in terms of concentration and propagule settlement in terms of flux.

If C_0 is the number of zygotes sufficiently sticky per unit volume in the tank at time $t = 0$, V the total volume of the tank, A the total area of any horizontal section of the tank (and of the bottom of the tank) and $N^*(t)$ the number of settled zygotes per unit area, then the number of zygotes not settled or still in suspension in the tank at time t is given by:

$$C_0\,V - A\,N^*(t)$$

rewritten in terms of concentration, the number of non settled zygotes in the tank per unit volume is

$$C_0 - \frac{A}{V} N^*(t).$$

Assuming uniform turbulence and perfect mixing at any time in the tank, the flux of propagules at the bottom of the tank is

$$V_p\, A\, (C_0 - \frac{A}{V} N^*(t)),$$

with V_p the turbulent settling velocity of the propagules. Propagules are taken out of the problem when they settle; therefore, we have

$$A \frac{d\, N^*(t)}{\mathrm{dt}} = A\, V_p\, (C_0 - \frac{A}{V}\ N^*(t))$$

This leads to the final equation for the number of settled zygotes per unit area

$$\frac{d\, N^*(t)}{\mathrm{dt}} = V_p\, (C_0 - \frac{A}{V} N^*(t)). \tag{3.1}$$

Equation 3.1 with initial condition $N^*(0) = 0$ (no propagule is settled at the beginning of the experiment) can easily be solved. The analytical solution for the number of settled zygotes versus time is

$$N^*(t) = \frac{C_0\, V}{A} (1 - \exp(-\frac{V_p\, A}{V} t)). \tag{3.2}$$

In contrast to the linear slope/threshold description, there is no discontinuity in the settling curves (junction between slope and threshold). The same trends are still observed as $N^*(t)$ converges asymptotically towards the value $y = \frac{C_0\, V}{A} = N^*_{\mathrm{th}}$.

The turbulent settling speed of the propagules, V_p, remains a parameter of the model likely to depend mainly on boundary layer and propagule properties. As well, the horizontal asymptote remains a parameter with N^*_{th} being representative of the number of sufficiently sticky propagules within the tank.

Instead of predictions of the sinking curves from the measured mean sinking velocity, the "perfect mixing" model leads to a description of the sinking curve and a different way of measuring the propagule characteristic sinking velocity. It is interesting to note that in this model, despite a total ruling of the core flow by turbulence, the mean sinking velocity is still going to be controlled by propagule flux through the boundary layer.

Stevens et al. [Stevens et al.(2008)] showed that buoyancy dominates propagules crossing of the boundary-layer, and therefore it would be coherent that the sinking velocities derived from this model remains relatively close to the Stokes sinking velocity. In that respect, the "perfect mixing" model could be in agreement with the experimental mean sinking speeds.

The accuracy of exponential description of the settlement curves was tested by finding the best-fitting function of the shape of Equation 3.2 to the experimental data. The fits were made using the nonlinear Least-square Marquardt-Levenberg algorithm implemented in Gnuplot [Williams and Kelley(1998)]. Two strategies were tried. First, functions of the shape $f(x) = (1 - \exp(-a/0.14\ x))$ with a the only free parameter. Then an additional degree of freedom was allowed for the asymptote using a function of the shape $f(x) = b\ (1 - \exp(-a/0.14\ x))$ with a and b the free parameters.

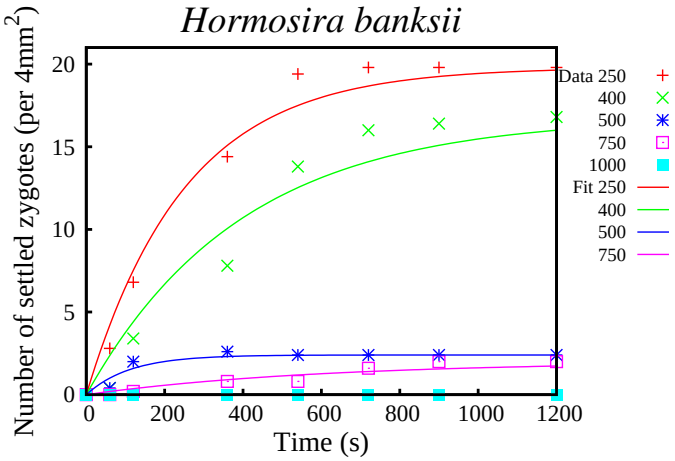

Figure 3.5. Original settlement curves (points) and corresponding fit (plain lines) for *Hormosira banksii*.

An example of the fitting obtained for *Hormosira banksii* is Figure 3.5. Visual inspection seems promising, in most cases the best fits obtained on the data involve non-negligible but reasonable errors (see Appendix B). Asymptotic standard errors for the fits of at least 8% were found for most of the curves, with errors of 15% to 20% being common. Interestingly, better fits were found for functions of the shape $(1 - \mathrm{erf}(a\,x))$ but these could not be reattached to any theoretical model.

The good fits together with the low Péclet estimates made in Chapter 2 support the description of the tank flow proposed in this model with no influence of the core flow itself on the mean sinking velocity of propagules. Description of the settlement curves are down to the sedimentation flux of propagules near the substrate and therefore boundary-layer mechanics. The experimental sinking are independent of the bulk tank flow. This explains also how in such a turbulent environment settling rates are still so close from the propagules' Stokes velocitysupports the description of the tank flow proposed in this model with no influence of the core flow itself on the mean sinking velocity of propagules. Description of the settlement curves are down

to the sedimentation flux of propagules near the substrate and therefore boundary-layer mechanics. The experimental sinking are independent of the bulk tank flow. This explains also how in such a turbulent environment settling rates are still so close from the propagules' Stokes velocity.

The model presented here certainly needs to be refined especially to incorporate a more explicit description of the interactions between the propagules and the turbulence in the near-wall region were the scale of turbulent fluctuations becomes comparable to the Stokes velocity of the propagule. This could be done also by adding a diffusive turbulent flux to the gravitational settling flux of propagules used as boundary condition at the bottom of the tank.

3.4.2 Turbulent-diffusion profile model

From the estimation of the turbulent diffusivity profile (see Chapter 2), an attempt was made to predict the sinking of the seaweed propagules in the stirred tank. This model involves turbulent propagule transport modelled from mass turbulent-diffusivity. A Lagrangian formulation is used that allows the tank to have non-uniform physical properties in space. It is therefore more explicit in terms of physics than the "turbulent mixing" approach described previously.

Model overview

This model is inspired by the work of Deleersnijder [Deleersnijder et al.(2006)] on the residence time of settling particles in the surface mixed layer. They included mathematical modelling of the propagule's sinking and then analysis of the settlement equations as a function of the Péclet number (ratio of the sinking to the turbulent diffusivity of the propagules) defined as

$$\mathrm{Pe} = \frac{V_s\, h}{\bar{D}},$$

with $\bar{D}$ the average of the eddy diffusivity over the tank, i.e.,

$$\bar{D} = \frac{1}{h}\int_0^h D(z)\,\mathrm{dz}.$$

Similar approaches involving an extra-production term (reaction-advection-diffusion models) have been used to study algae growth and bloom [O'Brien et al.(2003)] [Ebert et al.(2001)] or pelagic aggregate sedimentation [Ruiz(1996)]. All of these studies, including Deleersnijder [Deleersnijder et al.(2006)], are made at much larger scales than the stirred tank. At smaller scales, similar equations have been used together with measurement to estimate a turbulent drag coefficient on particles sinking through a turbulent vessel [Brucato et al.(1998)] or to study the influence of bottom roughness on the settlement of planktonic larvae [Eckman(1990)].

One of the terms of the equation that describes the settlement process of the propagules in the tank is a pure sinking term due to Stokesian buoyancy-induced sinking. Assuming that the concentration of sufficiently sticky propagules in the tank depends on the time t and on the distance to the bottom z, this first part of the equation consists of an advection equation where the distribution of propagules is advected toward the bottom at a velocity corresponding to the Stokesian sinking velocity:

$$\frac{\partial C}{\partial t} = V_s \frac{\partial C}{\partial z}.$$

Contrarily to the "perfect mixing" model described in the previous chapter, when some mixing is involved, it is no longer assumed that the concentration of sufficiently sticky propagules is homogeneous in the tank. It depends (as indicated earlier) on the distance to the bottom z and can be written $C(z,t)$.

An alternate approach to the differences between the "perfect mixing" and the turbulent diffusion model is to compare the length scales of the processes involved. By assuming as homogeneous the distribution of the propagules in the tank during the whole experiment, the flux model assumes the mixing time in the tank is small compared to propagule sinking time. The turbulent diffusivity model looks at a settlement process governed by mixing at smaller mixing-scales than the tank.

An extra term is added in the equation to account for turbulent mixing. This is achieved by an eddy diffusivity. Then the final equation is a one-dimensional advection-diffusion equation of the concentration of propagules:

$$\frac{\partial C(z,t)}{\partial t} = V_s \frac{\partial C(z,t)}{\partial z} + \frac{\partial}{\partial z}\left(D(z) \frac{\partial C(z,t)}{\partial z} \right). \tag{3.3}$$

Assuming as before that the propagules are uniformly dispersed within the tank at the beginning of the experiments, the initial condition for the concentration of sufficiently sticky propagules is:

$$C(z,0) = C_0, \forall z \in [0;h]. \tag{3.4}$$

As in [Deleersnijder et al.(2006)] there is no flux of propagules through the air-seawater interface at the top of the tank. Therefore, the first boundary condition is:

$$\left[V_s\, C(z,t) + D(z) \frac{\partial C(z,t)}{\partial z} \right]_{z=h} = 0. \tag{3.5}$$

As well, the flow in the viscous boundary layer near the bottom, where the propagules are settling, is not turbulent. So the turbulent diffusion flux at the bottom of the tank tends to zero

$$\left[D(z) \frac{\partial C(z,t)}{\partial z} \right]_{z=0} = 0. \tag{3.6}$$

The new model is now well-defined and the next challenge is to solve this non-trivial system. Two cases exist:

– The simple case is where I assume that the turbulent diffusion is the same anywhere in the tank and therefore independent of z. If this assumption proves to give good results, it implies that the walls have a limited effect on the sinking stage in the experiment. This assumption has been used before for several studies taking place in the mixed layer of the ocean [O'Brien et al.(2003)] [Ruiz(1996)] [Ebert et al.(2001)], but I am not aware of any other tank study using this assumption. In this case, we get a one dimensional linear partial differential equation, which means development of a theoretical solution is likely.

– The second situation is where the turbulent diffusion depends on the distance from the bottom. This means that the concentration of propagules is given by a non-linear equation, which is difficult to solve analytically. Nevertheless, as we will see later, it is still possible to get useful information from this model.

Relatively simple analytical solutions to the advection-diffusion equation can be derived in the case of a constant eddy-diffusion profile. For more complex profiles, numerical techniques can be used to solve the equation.

Analytical solutions

Constant turbulent-diffusion profile

An analytical solution for the concentration within the tank can be derived in the case of a constant turbulent-diffusion profile. In the case of an impulsive release of a quantity C_0 of tracer at location x_0 in an infinite domain, the solution of the advection-diffusion equation (Figure 3.6) is given by [Crank(1957)]

$$C(z,t) = \frac{C_0}{\sqrt{4\,\pi\,D t}} \exp\left(-\frac{(z-(z_0+V_s\,t))^2}{4\,D\,t} \right).$$

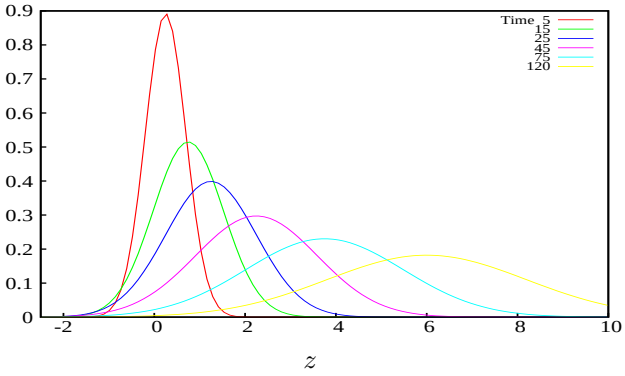

Figure 3.6. Advection-diffusion of a Dirac distribution of tracer where curves at centred on $z = \mathrm{Vs}\,t$.

Given the linear nature of the advection-diffusion equation, superposition can be used to build up a solution for a uniform impulsive release of tracer between z = 0 and z = h. The solution for such a problem still in an infinite domain (Figure 3.7) is

$$C(z,t) = \frac{C_0}{\sqrt{\pi}}\left[\mathrm{erf}\left(\frac{z-u\,t}{\sqrt{4\,D\,t}}\right) - \mathrm{erf}\left(\frac{z-(h+u\,t)}{\sqrt{4\,D\,t}}\right)\right].$$

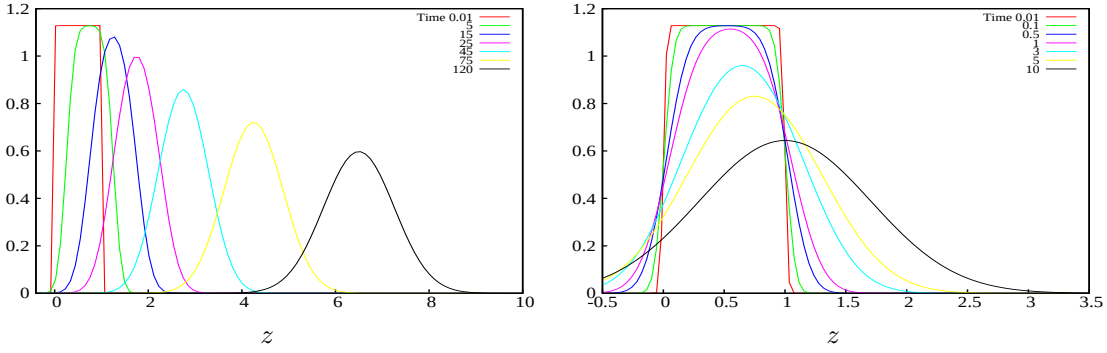

Figure 3.7. Advection-diffusion of a unit wide impulsive distribution of tracer when advection dominates over diffusion (left) and diffusion dominates over advection (right).

To get a solution relevant to the stirred tank, a no-flux boundary condition needs to be applied to account for the free surface at the top of the tank. This can be done by addition of the solution of the symmetrical problem with respect to the wall position (Figure 3.8). For a wall located at z=0, we get

$$C(z,t) = \frac{C_0}{\sqrt{\pi}}\left[\mathrm{erf}\left(\frac{z-u\,t}{\sqrt{4\,D\,t}}\right) - \mathrm{erf}\left(\frac{z-(h+u\,t)}{\sqrt{4\,D\,t}}\right)\right] - \frac{C_0}{\sqrt{\pi}}\left[\mathrm{erf}\left(\frac{z+u\,t}{\sqrt{4\,D\,t}}\right) - \mathrm{erf}\left(\frac{z+(h+u\,t)}{\sqrt{4\,D\,t}}\right)\right]$$

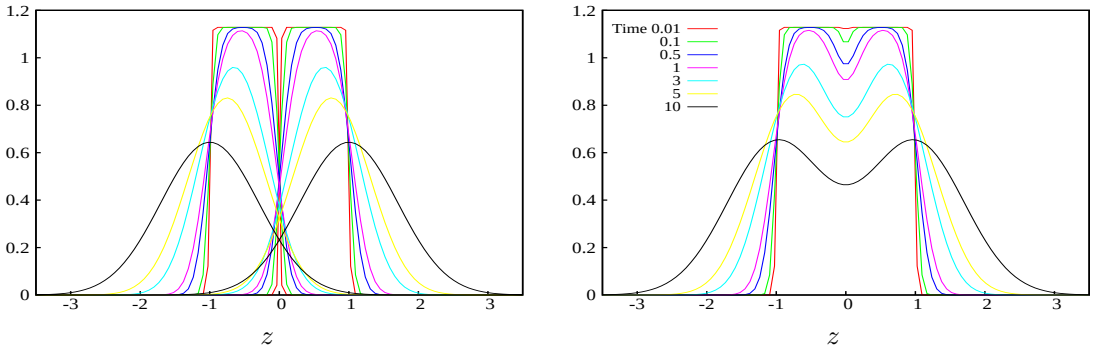

Figure 3.8. A no-flux boundary condition in z=0 can be imposed by solving the symmetrically problem and adding both solutions.

This is as far as we can go with this analytical approach. In the case of the tank, a non-diffusive flux should be imposed at the other end of the tank, which cannot be done easily. One way of doing it would be to consider that the turbulent diffusion profile in the tank is close to parabolic with turbulent diffusion being null at the bottom. Analytical solutions for more com-

plex problems involving spatially variable diffusion profiles or advection velocities have been derived for very specific types of profiles (e. g. [Philip(1994)] [Zoppou and Knight(1997)]) and none is known by us for a constant velocity profile and a parabolic diffusion profile.

Adjoint problem

Deleersnijder et al. [Deleersnijder et al.(2006)] used the adjoint model of Delhez et al. [Delhez et al.(2004)] to solve the adjoint problem to the advection-diffusion equation. The problem can be rewritten in terms of the mean residence time, $\theta(z)$, which corresponds to the mean time a propagule located at the distance z from the bottom at time $t = 0$, will take to reach the bottom.

The total number of propagules suspended in the tank is

$$m(t) = \int_0^h C(t,z)\,\mathrm{dz}.$$

As propagules settle they are removed from the inside of the tank. The number of propagules settling on the substrate at time t can be defined as the derivative of the total number of propagules

$$\frac{d\,m(t)}{\mathrm{dt}} = \int_0^h \frac{\partial}{\partial t} C(t,z)\,\mathrm{dz}$$

as h does not depend on t. By substituting equation 3.3 in the previous equation and applying the boundary conditions, the instantaneous quantity of settling propagules is given by

$$\frac{d\,m(t)}{\mathrm{dt}} = -\,v_s\,C(t,0).$$

From that, the mass-weighted average of the propagules residence time can be defined as:

$$\Theta = -\,\frac{1}{m(0)} \int_{m(0)}^0 t\,\mathrm{dm}. \tag{3.7}$$

Substituting $t' = m(t)$ in equation 3.7, we obtain

$$\Theta = \frac{1}{m(0)} \int_0^\infty m(t)\,\mathrm{dt}.$$

Assuming that $m(0) = 1$, the final expression of the mean residence time is

$$\Theta = \int_0^\infty \int_0^h C(t,z)\,\mathrm{dz}\,\mathrm{dt}.$$

As described in the appendix of [Deleersnijder et al.(2006)], it is possible to extend this method to get a residence time for the propagules located at distance z_0 from the bottom at time $t = 0$. Assuming that $C(0,\, z) = \delta(z - z_0)$ with δ the Dirac distribution and that the time and space integration can be inverted in equation 3.7 (allowed by Fubini's theorem [Folland1999]), then the mean residence time associated with an impulsive release of propagules at distance z_0 from the bottom at time $t = 0$ is given by the expression

$$\theta(z_0) = \int_0^h \int_0^\infty C(t,z)\,\mathrm{dt}.$$

After further transformation described in the appendix of [Deleersnijder et al.(2006)], the final expression for the mean residence time of a propagule, depending on its initial distance to the bottom, is given by

$$\theta(z_0) = \frac{z_0}{v_s} + \frac{1}{v_s}\int_{z_0}^{h} \exp\left[-v_s \int_{z_0}^{\xi} \frac{d\zeta}{D(\zeta)} \right] d\xi. \tag{3.8}$$

The mean residence time of the propagules after non-dimensioning of the problem can be rewritten as

$$\theta(z_0) = z + \int_{z_0}^{1} \exp\left[-\mathrm{Pe} \int_{z_0}^{\xi} \frac{d\zeta}{D(\zeta)} \right] d\,\xi. \tag{3.9}$$

Equations 3.8 and 3.9 involve integrals that admit analytical solutions for simple turbulent-diffusion profiles. In a more general context, a numerical integration has to be performed, which was achieved using a C routine and the Gnu Scientific Library [Galassi et al.(1983)].

Results

The model presented here does not really stand apart from the "perfect mixing" approach, but it includes it in the case of a Péclet number equal to zero. As well, pure gravitational sinking (infinite Péclet number) leads to a mean residence time of $\theta(z) = \frac{z}{v_s}$. Any other Péclet number leads to a mean residence time in between the Stokes sinking time and the residence time associated with perfect mixing.

From Equations 3.8 and 3.9, independent of the turbulence in the stirred vessel, the mean residence time at any distance from the bottom of the tank is found to be higher than the Stokes sinking time of the propagules. Turbulent mixing decreases propagule settling rate, which is in agreement with our observations in the tank.

The residence time for particles released at $z = h$ (top of the box) is always equal to $\frac{h}{v_s}$ independent of the turbulent mixing is involved. This property of the model was already pointed out by Deleersnijder et al. [Deleersnijder et al.(2006)] without further comment.

$\theta(z)$ corresponds to the averaged residence time for particles released in the domain at a distance z from the bottom. In Equations 3.8 and 3.9 the residence time of a propagule released at a distance z_0 from the bottom is independent of the turbulent-diffusion profile between $z = 0$ and $z = z_0$ but depends on the rest of the eddy-diffusion profile. In other words, only the turbulent-diffusion in the parts of tank where not all the propagules go before reaching the bottom have a influence on the mean residence time.

The diffusion process is isotropic and therefore has no influence on the mean settlement time of propagules. This can be illustrated by the solution of the advection-diffusion of a Dirac distribution of tracer (Figure 3.6). The solution is a Gaussian curve whose width is a function of the

diffusion and whose mean position (maximum) is a function of the advection. The mean speed of the tracer patch does not vary with diffusion as the patch diffuses symmetrically around the mean speed. Therefore, in that case the mean-residence time is only dependent on the advection process.

In the case of a Dirac impulse of tracer released at distance z_0 from the bottom, $\theta(z_0)$ is going to be unaffected by the turbulent-diffusion profile extending from the bottom to z_0 as it is an average of the influence of an isotropic process. Nevertheless, the turbulent-diffusion profile extending from z_0 to the top of the tank is only relevant to the propagules that get transported to the upper part of the tank ($z > z_0$), which is only the case for fraction of the propagules. Therefore, all the propagules are not affected by the upper part of the profile and the averaged contribution of the diffusion to the mean residence time is not null anymore.

In the case of propagules released at the top of the tank, they can only go downward, and therefore the mean-contribution of the mixing to the residence time is zero. That explains why the residence time for $z = h$ is always equal to $\frac{h}{V_s}$.

The mean-residence time $\theta(z)$ is therefore not comparable to any of the quantities obtained from the tank's experiments. It should be seen as a quantity relevant to how much particle "re-suspension" in the upper tank affects the propagule sinking.

A time-scale that is more relevant to what can be observed in the tank is the mean residence time of the propagules for an homogeneous initial distribution over the whole tank. For an initial particle distribution of $C(0, z)$, it is given by

$$\Theta = \int_0^h C(0, z)\,\theta(z)\,\mathrm{dz}.$$

In our case, when the initial particle distribution is assumed to be uniform, the mean particle residence time is given by the depth-averaged residence time

$$\Theta = \bar{\theta} = \frac{1}{h}\int_0^h \theta(z)\,\mathrm{dz}\,.$$

While the residence time Θ defined here is not the most detailed quantity, being the average of an average, it is a time-scale characteristic of the settlement-time of the propagules and can be reattached to more concrete concepts by the mean of an estimation of the shape of the settlement curves.

In the simple case, I assume there is constant linear sinking of propagules, then the sinking time of propagules is given by

$$t(z) = \frac{z}{V_p}.$$

From which the mean residence time can be assumed to be

$$\Theta = \int_0^h t(z)\,\mathrm{dz} = \frac{1}{2}\frac{h}{V_p}. \tag{3.10}$$

That way, Θ can be linked to the settling speed of the propagule V_p which is meaningful to compare with or to predict the sinking curves.

Good fits to the experimental curves have been obtained using exponential function as suggested by the "perfect mixing" model. In that case, the number of settled zygotes versus time is given by $N(t) = [1 - \exp(-V_p\,t)]$, with V_p also defined by equation 3.10.

Therefore, rather than using the time-scale Θ, it makes sense to use the velocity scale

$$V_p = \frac{h}{2\,\Theta}$$

to be consistent with previous work.

Residence time

Numerical integration of Equation 3.8 was realized for the turbulent-diffusion profiles presented in the previous chapter. As the $k-$epsilon method led to under-estimation of the turbulent diffusion profiles, only the shape of them was kept and the profiles were rescaled using the estimations of the Péclet number derived from the circulation model (Figure 3.9).

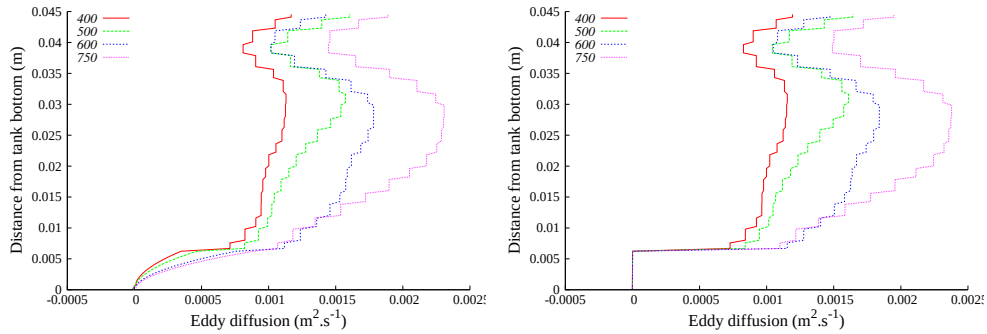

Figure 3.9. Eddy diffusivity profile for *Hormosira banksii* without taking into account boundary layer increase in turbulent-diffusivity(a) and taking into account propagules properties in the boundary-layer (b).

The low Péclet numbers found previously transpose into residence time profiles strongly marked by the predominance of turbulent mixing over gravitational sinking (Figure 3.10). Except in the near-wall area, the residence times are close to $\frac{h}{V_s}$ which is the residence time associated with the perfect mixing case. This is observed independently of the propeller speed (Figure 3.10) or of the propagules of interest (Figure 3.11).

The drop in turbulent-diffusion in the vicinity of the wall imposed through the boundary layer model results in a decrease of the residence time for the corresponding distance to the wall.

This decrease is relatively smooth at first and becomes more and more pronounced closer to the bottom. Nevertheless, turbulent-diffusion is far from negligible, and still dominates over viscous effects until the wall is reached (Figure 3.10).

Inclusion of propagule properties in the boundary layer has a dramatic impact on the associated residence time, with viscous transport taking over turbulent transport in the turbulent boundary layer region. This is the only place where differences can be noticed between the different propeller speeds, with the influence of turbulent diffusion becoming smaller in a smoother way for the highest propeller speeds (Figure 3.10-b).

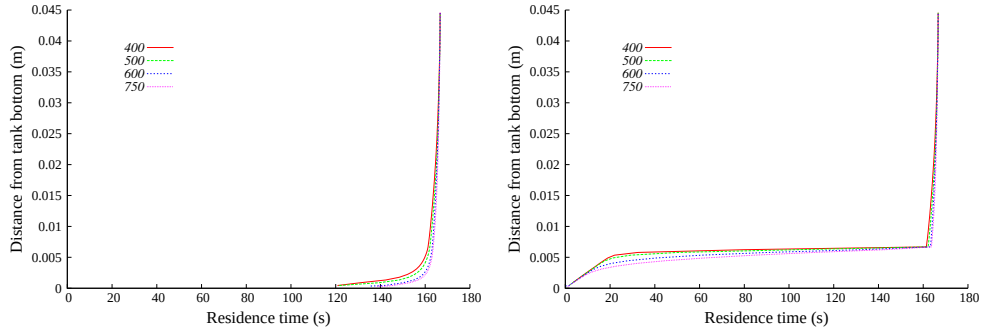

Figure 3.10. Residence time in the tank for turbulent diffusivity profile with (b) and without (a) particle model.

At constant propeller speed, when only the advection velocity varies (Figure 3.11), no major difference can be observed in the shape of the residence time profiles for the different species. The residence time profiles have a different scaling corresponding to the difference of Stokes velocity between propagules. In all cases turbulent transport dominates over gravitational sinking. Only small differences are observable in the boundary layer were small differences were already noticeable when the propeller speed is varied.

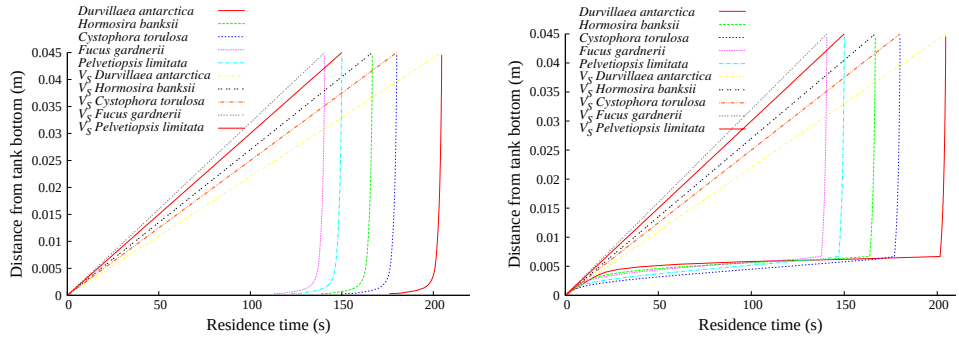

Figure 3.11. Residence time in the tank for turbulent diffusivity profile with particle coefficient in the model with (b) and without (a) particle model. The straight curves correspond to pure Stokes sinking.

It is clear from these profiles that regardless of propeller speed, quasi-homogeneous mixing is ensured within the tank and that the propagule's sinking curves corresponding to the turbulent diffusion profiles used here should therefore be quite close to the ones found for the "perfect mixing" approach (see earlier in the chapter). One major difference nevertheless exists with the turbulent boundary layer where viscous sinking takes over turbulent transport.

Mean sinking times

The mean propagule speeds, V_p, as defined earlier was derived from the integration of the residence time profile in the tank (Figure 3.12). A decrease of 40 to 50% of the characteristic settling speed of the propagules can be observed with respect to pure gravitational sinking. In the case where propagule properties are not taken into account, very little difference can be observed between the different curves. The mean settling velocities here are close to $\frac{V_s}{2}$ which is predicted in the case of Péclet numbers close to zero.

The use of the propagule properties within the turbulent boundary layer creates a difference of around 10% to the mean settling velocities. The influence of propagule dimension is then clearly noticeable and takes over the differences created by the variation in Stokes velocity between the propagules. Bigger propagules tend to be the ones most sensitive to turbulence with lower mean settling speeds (Figure 3.12-b).

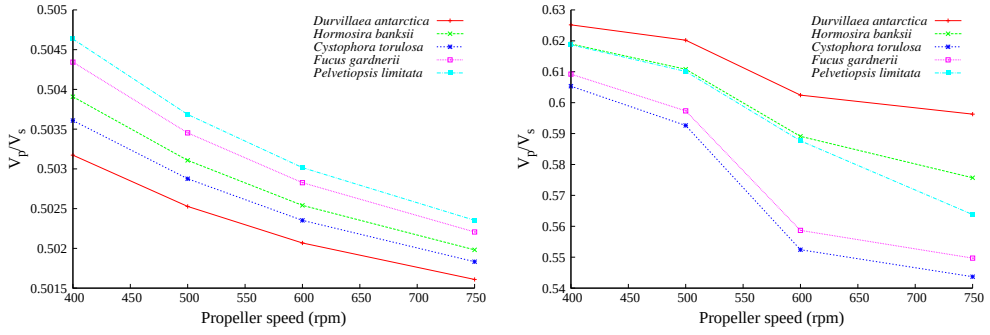

Figure 3.12. Normalised sinkings obtained for the advection-diffusion model versus rpm using turbulent mass diffusivity (a) and particle turbulent diffusivity (b).

The results given by this model do not correspond exactly to the experimental results (Figure 3.13) with higher settling speed recorded in the tank. Nevertheless, it seems to predict the right trends with decreases in velocity close to 30% to 40% observed in the tank. The prediction of the influence of propagule properties are more debatable as no pattern is distinguishable in the experimental data (Figure 3.13).

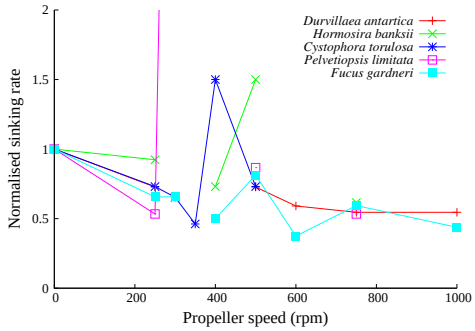

Figure 3.13. Experiment normalised sinking rates versus rpm based on experimental data.

One criteria that has not been tested here is the influence of the shape of the turbulent-diffusion profile on the mean residence time. Deleersnijder et al. [Deleersnijder et al.(2006)] observed that the model had little sensitivity to the shape of the diffusivity profile. For that reason, they suggest that in most cases, a good approximation of the depth-averaged residence time can be obtained directly from the Péclet number as

$$\Theta = \frac{1}{2} + \frac{1}{2 + \mathrm{Pe}}. \tag{3.11}$$

It was tried to fit this curve to the experimental data assuming that the Péclet number is inversely proportional to propeller speed. The best fit was obtained for *Durvillaea antarctica* (asymptotic error of 25%) leading to a Péclet number of 1.9 at 400 rpm which is much higher that what has been predicted (Chapter 2). Given the poor fit obtained from equation 3.11, this approach was not pursued.

The adjoint approach used by Deleersnijder et al. [Deleersnijder et al.(2006)] gives an alternative analytical solution to the advection-diffusion equation. The notion of mean residence time introduced here is not trivial and has to be handled carefully. It was showed that the residence time for an impulse release of tracer at a distance z_0 is independent of the eddy-diffusion profile between z_0 and the bottom. Despite the qualitative explanations developed here from the residence time profile $\theta(z)$, it remains hard to resolve further information about these profiles, as they do not correspond to any real measurable quantity.

Conversely, the depth-averaged residence time, Θ, can be related to the experimental data provided the assumption of the sinking curves' shapes. In that case the model provides a timescale that allows proper scaling of the sinking curves.

Several other types information were extracted from this model:

- the range of Péclet numbers estimated for the tank closely correspond to perfect mixing of the different quantities within the tank, which validates our previous observations on the "perfect mixing" model.

- when mass turbulent-diffusion is used for the transport of propagules, the mean sinking speed of the propagules is always found to be between $\frac{V_s}{2}$ and V_s.

- the addition of a boundary layer in the turbulent-diffusion profile where viscous transport takes over the turbulent one, leads to a non negligible increase in the mean settling velocity. In that case, the mean sinking velocities were closer to the measured ones. Mean sinking velocities were nevertheless still far smaller than the measured ones.

- the model tends to display distinct particle behaviours within the range of parameters tested here, which is not obvious in the experimental curves.

Numerical solution

As it was not possible to investigate the shape of the sinking curves (time evolution) using the adjoint approach, the advection-diffusion equation was solved numerically using the Gerris Flow Solver. Gerris is designed to solve 2D and 3D problems, and would therefore not be recommended as a first choice to solve one-dimensional problems. Nevertheless, it is possible to set up a domain with high resolution in only one direction and use it to solve a one-dimensional problem.

The advection-diffusion problem was solved for parabolic turbulent-diffusion profiles and then for profiles made of a boundary layer (of size BL size) and a region of constant high turbulent-diffusion (Figure 3.14). In both cases, two parameters allowed changes in the shape of the turbulent-diffusion profile. Péclet number and position of the turbulent-diffusion maximum can be imposed for the parabolic profile and Péclet number and u_* for the other profile.

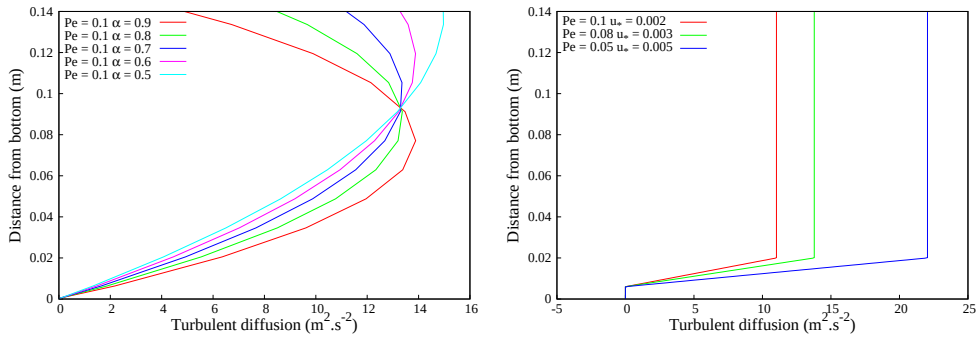

Figure 3.14. Parabolic turbulent-diffusion profile (left) and profile with boundary layer and constant diffusion (right).

One of the main observations is that the profile of the sinking curves is mostly independent of the shape of the turbulent-diffusion profile (Figure 3.15) and therefore the Péclet number is the only parameter to the settling curves. This is still true on average, which is in agreement with Deleersnijder et al. [Deleersnijder et al.(2006)]'s observations.

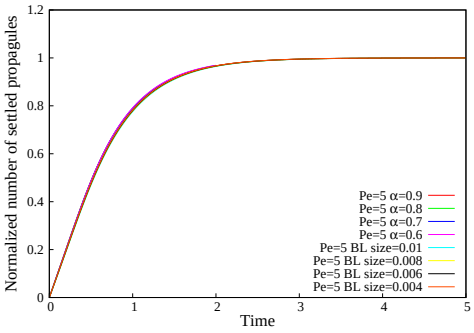

Figure 3.15. Propagules settlement curves from the 1D advection-diffusion model a Péclet of 5 using various shapes of eddy-diffusion profile.

The settlement curves obtained from Gerris can be separated into two groups. The low Péclet number ones (Figure 3.16-a), for which turbulent transport dominates the sinking and the high Péclet (Pe $>$ 1) ones (Figure 3.16-b). For low Péclet numbers, which is the case in the stirred tank, the model predicts that for Péclet numbers lower than 1, the sinking curves become almost independent of the Péclet number. Curves start with a sinking speed (tangent to the origin) close to the Stokes velocity. Propagule deposition decreases progressively when the concentration of propagules within the tank decreases.

For high Péclet numbers (Figure 3.16-b), the curves tend to get closer and closer to the piecewise linear curve corresponding to pure gravitational sinking. Nevertheless, it is still possible to see that they remain Péclet dependent. The mean sinking speed of propagules is found here to increase when the Péclet number increases. In all cases, the mean sinking speed of the propagules is found to be lower than the Stokes sinking speed which is in agreement with what was found using the adjoint model.

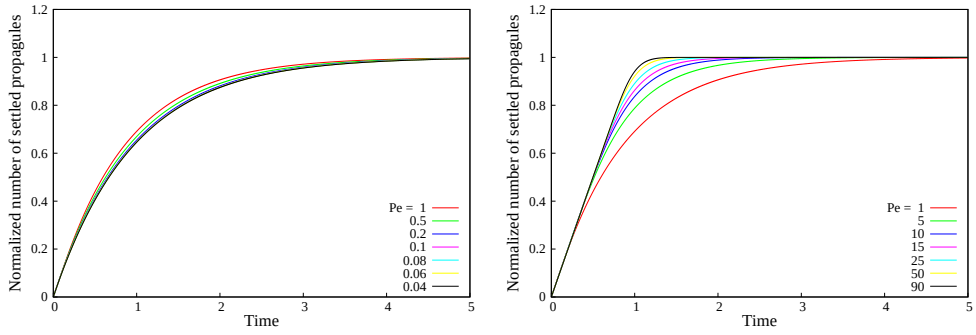

(a) (b)

Figure 3.16. Propagules settlement curves from the 1D advection-diffusion model with a parabolic turbulent-diffusion profile for low Péclet numbers (diffusion dominates on (a)) and high Péclet numbers (gravitational sinking dominates on (a)).

For low Péclet numbers, all the curves are very similar. It was tried to fit an exponential curve to the sinking curves obtained from the Gerris Flow Solver. Excellent agreement was

found independently of the Péclet number (lower or higher than 1). Using $h^2/\bar{D}$ instead of h/V_s for characteristic time-scale for the problem (as turbulent diffusivity dominates over gravitational sinking), the advection-diffusion equation (Equation 3.3) can be rewritten as

$$\frac{\partial C(z,t)}{\partial t} = \mathrm{Pe}\,\frac{\partial C(z,t)}{\partial z} + \frac{\partial^2 C(z,t)}{\partial z^2} \tag{3.12}$$

which for low Péclet numbers reduces to a simple diffusion equation whose solution is an exponential. This gives credence to the assumption made with the adjoint model that the sinking curves were exponential. As well, this is in agreement with the simple "perfect mixing" presented earlier.

3.4.3 Discussion

The observations from tank characterisation and experimental data showing that propagule settling velocity are strongly influenced by the propagules properties and that the turbulence levels within the tank are such that turbulence should dominate propagule transport in the bulk of the tank were confronted using two models.

Assuming that mass turbulent-diffusion can be used to account for the turbulent transport of the propagules, the influence of the Péclet number and of the profile of turbulent-diffusion within the tank was investigated using a one-dimensional advection-diffusion Lagrangian approach. The Péclet number was found to be the relevant parameter, with the shape of the turbulent diffusion profile being of little importance. Within the range of Péclet number corresponding to the sinking experiments, the bulk of the tank is homogeneously mixed. Sinking is therefore possible to describe with the $(1 - \exp(-a\,x))$ function solution of the "perfect mixing" model. It remains to explain the better fits obtained using the function $\mathrm{erf}(a\,x)$.

It was showed that slightly different Péclet numbers can be found if propagule properties are taken into account without the boundary layer instead of using mass turbulent-diffusion. It follows that higher mean sinking speeds were found in that case. These were closer to the ones observed experimentally.

The influence of the turbulent boundary-layer on what was designed to be "turbulent sinking through the core of the tank" was most-likely under-estimated. The "perfect-mixing" approach initially showed that in the case of total dominance of the turbulence in the core flow, the mean propagule sinking speed still depends mainly on the boundary conditions at the bottom of the tank. In a first time, it was assumed appropriate to impose the Stokes velocity as a boundary condition as in the viscous sub-layer. While this is likely to be a good model for an ideal viscous sub-layer, it does not include the influence of the turbulent boundary-layer on propagule depos-

ition. The boundary condition applied to the problem should therefore not be the Stokes sinking speed but a sinking velocity representative of the sinking of the propagules within the whole boundary-layer.

Eddy-diffusion is therefore not likely to be relevant to the description of the settlement curves, and the friction velocity should be used instead. More discussions on the propagule settling flux are in the general discussion.

3.5 Asymptotes and propagule adhesiveness

The asymptotic settlement state reached at the end of each experiment corresponds to an equilibrium state between the stickiness (mucous adhesiveness and propagule weight) of the propagules and the removal hydrodynamical-forces. Solid particle detachment theory is used to evaluate the involved forces and derive an estimation of propagule adhesiveness.

3.5.1 Threshold versus RPM

By definition, the friction velocity, u_*, is proportional to the square-root of the shear stress in the boundary layer and therefore directly representative of the stress undergone by settled propagules. It was shown in Chapter 2 that the friction velocity is proportional to propeller speed which makes the rough data of the number of settled zygotes at threshold as a function of propeller speed worth a description (Figure 3.17). On Figure 3.17, the number of settled propagules at threshold is normalised by the number of settled propagules that settles in the absence of stirring, which is representative of the total number of propagules in the tank. For all species, the number of settled propagules decreases when propeller speed increases. As well, for all of them no propagule manages to attached successfully at rotating speeds of 1000 rpm.

Differences were observed with *Durvillaea antarctica*, which had a substantial number of its propagules still attached at a rotating speed of about 800 rpm, whereas *Hormosira banksii* and *Pelvetiopsis limitata* barely had any propagules settled at a rotating speed of 500 rpm. This is consistent with observations in the field where *Durvillaea antarctica* is found in the highly exposed part of the rocky shore and *Hormosira banksii* in more sheltered areas.

For a given species, it can be assumed that:

- all propagules have the same adhesion mechanism
- all propagules have a characteristic adhesiveness
- all propagules have the same probability to reach the substrate in the best conditions allowed by the flow

All three factors can potentially have an influence on the meaning of the observed asymptotes. The threshold data allow to compare asymptotic settlement states i.e. at times long enough so that propagules have had a chance to settle. Therefore the probability to have a chance to settle is 1 at threshold, which implies that only propagule adhesiveness and adhesion mechanism are left.

If some propagules can settle, then the adhesion mechanism should allow all of them to settle within a long enough time, this only if the process is adhesiveness-independent. The number of zygotes counted at threshold should therefore mainly be representative of the adhesiveness of the propagules.

A direct correlation exists between slope steepness and propagule removal rate in Figure 3.17. A steep slope corresponds to the detachment or absence of settlement of a large number of propagules when propeller speed is increased from the speed of the latest data-point to the next one.

These curves were "derived" at intervals of 100 rpm to calculate the proportion of the total population of propagules that get detached when the propeller speed is increased from the lower to the upper rotating speed covered in the interval. Given the proportionality existing between propeller speed and bottom stress, the derived histograms can be seen as the stickiness distribution within a propagules population (Figure 3.18). Figure 3.18 contains the same information as Figure 3.17 but, nevertheless, it is believed that the notion of stickiness distribution is of interest and observations are much easier to resolve with the format of Figure 3.18.

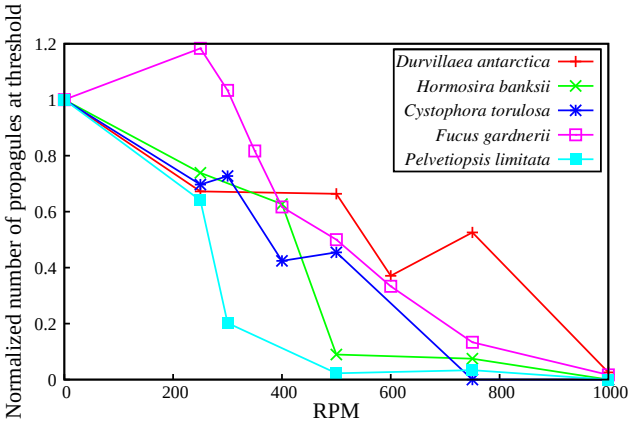

Figure 3.17. Normalised number of propagule per counting area at threshold versus the propellers' speed in RPM.

From Figure 3.18 it can be seen that for all species but Fucus, 30% of the propagules get detached or cannot settle when the propellers speed is increased from 0 to 200 rpm. Despite 30% being quite a significant part of the total population, this range of rpm does not correspond

to a critical value for any of the three species. These 30% are most likely the non-viable propagules, the ones that have been damaged when they have been removed from the substrate to be re-suspended, or that have not been fertilised or are otherwise defective.

Hormosira banksii and *Pelvetiopsis limitata* have similar stickiness distributions, with one main peak corresponding to a 100 rpm window within which more than half of the propagule population starts being unable to settle. Then the remaining 20% of the total population still manage to settle past the peak, and can stand up to an increase of a further 200 rpm. Characteristic propeller speeds for the removal of *Pelvetiopsis limitata* are between 200 and 300 rpm. For *Hormosira banksii*, most propagules become unable to settle for speeds between 400 and 500. *Fucus gardneri* has a similar peak around 200 to 300 rpm but almost 45% of the propagules can still settle past 300 rpm.

Durvillaea antarctica and *Cystophora torulosa* have different stickiness distributions than the three other species in two different ways. Both species are able to settle in more turbulent conditions, especially *Durvillaea antarctica* for which 20% of the zygotes still settled at 900 rpm. The second specificity of these species' stickiness distributions is that they contain two peaks. This might be associated with the tendency propagules can have to clump into groups of up to 4 propagules in low velocity flows, as observed on by Schiel and Taylor [Taylor et al.(2009)], which is likely to have an influence on their settlement ability.

3.5.2 *In situ* bottom shear stress

The ability of the different zygotes to settle given the turbulent conditions imposed in the tank has now been described qualitatively and quantitatively in terms of "tank units" (rpm). *Durvillaea antarctica*, the species found in the most extreme environment, has the ability to settle in the most turbulent flows.

Expression of the data in terms of "more standard units" is now required to allow comparisons with other systems, such as the intertidal zone. This can be done in terms of friction velocity.

The methods used to relate propeller speed to the friction velocity were explored in the previous chapter. As the friction velocity was only determined for propeller speeds of 400, 500, 600 and 750 rpm, simple extrapolation techniques were used to extend the estimation to the whole 0 to 1000 rpm range. The maximum friction velocity corresponding to 1000 rpm, over which no settlement was found, is of 0.0116 ms^{-1}.

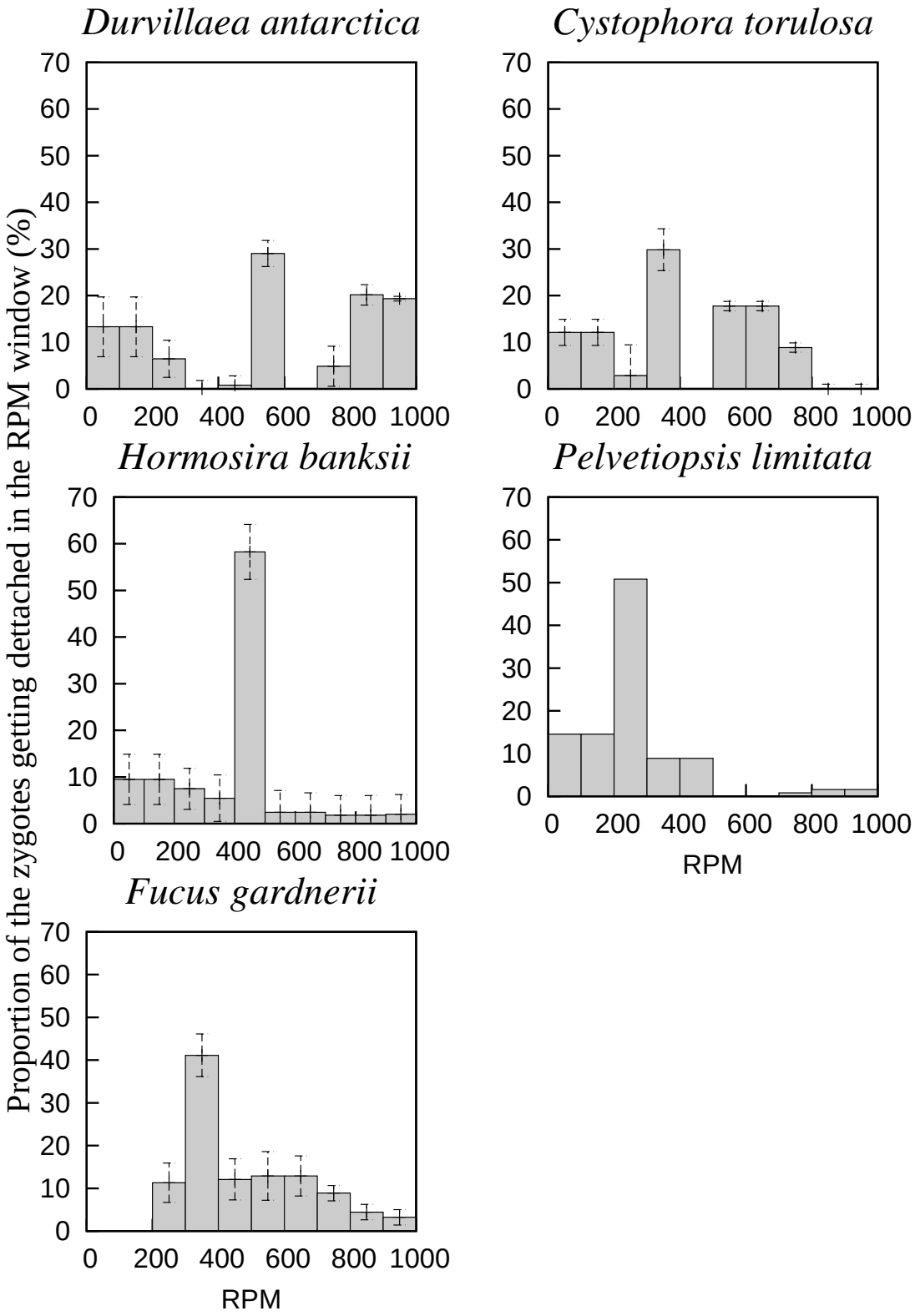

Figure 3.18. Proportion of the zygotes that gets detached from the substrate if the rotating speed is increased from the lower to the upper end of each interval covered by the histogram bar.

The peaks observed in the stickiness distribution are transposed in terms of friction velocity in Table 3.2. Both species from Oregon, *Fucus gardneri* and *Pelvetiopsis limitata* were sticky enough to withstand friction velocity up to around 0.005 $m.s^{-1}$, whereas New Zealand species are adapted to more demanding conditions and were able to settle under a friction velocity of around 0.006 $m.s^{-1}$ for the "less efficient" species.

Table 3.2. Ranges of friction velocities ($\mathrm{mm}.s^{-1}$) within which a significant part of the propagules population becomes unable to settle.

Species	Peak 1	Peak 2
Durvillaea antarctica	6.8 - 7.7	9.7 - 11.6
Cystophora torulosa	5.8 - 6.8	7.7 - 9.7
Hormosira banksii	5.8 - 6.8	xxx
Fucus gardneri	4.4 - 5.8	xxx
Pelvetiopsis limitata	4.4 - 5.8	xxx

The friction velocities in the natural environment can be estimated in the idealised context of shallow water waves travelling over the sea bed as done by Stevens et al. [Stevens et al.(2008)]. The bottom shear stress can be expressed using a skin friction drag approach [Reidenbach et al.(2006)] as

$$\tau = \rho_f \, u_*^2 = \rho_f C_f u_\infty^2,$$

where u_∞ is the outer flow speed and C_f an empirically determined skin friction drag coefficient. The outer velocity u_∞ is estimated from wave orbital motion,

$$u_\infty = \frac{H}{2}\sqrt{\frac{g}{\mathrm{Depth}}},$$

where H is the wave-height, g the gravity and Depth is the water depth.

The skin drag coefficient C_f is taken equal to 0.01 but in reality is a function of the roughness of the substrate [Reidenbach et al.(2006)].

Friction velocity as a function of the wave climate (wave height and water depth) was estimated (Figure 3.19). The range of friction velocities estimated to be relevant to propagule settlement in the tank (0 to 0.0115 $m.s^{-1}$) corresponds in the intertidal zone (depth from 1 to 4 meters) to wave heights ranging between 0 and 0.12 m. This can be considered as very calm conditions for the intertidal.

In their estimation of the friction velocity for wave hindcast, Stevens et al. [Stevens et al.(2008)] showed that u_* ranges between 0.001 and 0.1 $m\,s^{-1}$ which shows that there is a window of time when conditions are calm enough for settlement according to our critical u_*.

The requirement of calm conditions suggested by the tank measurements is consistent with the known tendency of some seaweed species to release their zygotes when the conditions are calm [Taylor et al.(2009)]. This shows that despite being provided with a complex adhesiveness mucous, seaweed zygotes still need the wave conditions to be favourable to be able to settle on a proper substrate.

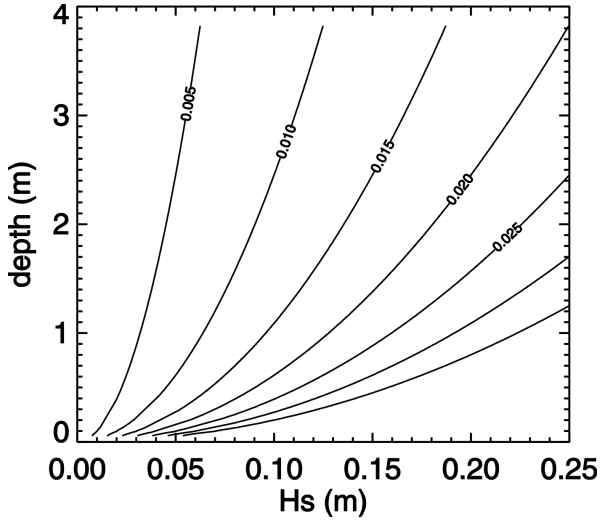

Figure 3.19. Friction velocity u_* as a function of wave height (H_s) and water depth.

3.5.3 Removal forces

Numerous models have been developed to describe the detachment or re-suspension of deformable solid propagules in turbulent shear flows [Soltani and Ahmadi(2001)] [Johnson et al.(1971)] [Derjaguin et al.(1997)] [Tsai et al.(1991)] [Burdick et al.(2001)] in response to hydrodynamical forces. Particles are considered as deformable spheres. In most models, contact between particles and a substrate is not point-based but occurs on a circular area. These models are based on a mechanical approach to the problem, with the detachment criteria based on removal forces exceeding adhesion forces (Figure 3.20) and on the physical properties of the particles (diameter, density, Young modulus, Poisson ratio for deformable particles).

Adhesion forces can relate to chemical bonds [Cooper et al.(2001)], electrostatic forces [Burdick et al.(2001)], gravity forces. Often, however, they are only the inter-molecular Van der Walls forces given by

$$\boldsymbol{F}_a = \frac{A\,d}{12\,h^2}\left(1+\frac{2\,a}{h\,d}\right)$$

where A is the system-dependent Hamaker constant, h the particle-surface separation distance, a the contact radius and d the particle diameter.

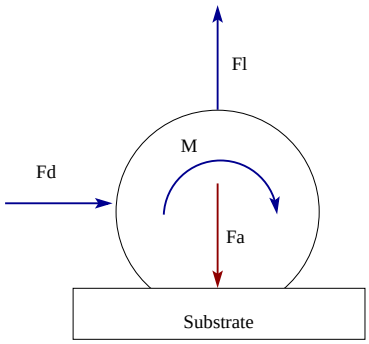

Figure 3.20. Summary of the forces on a particle. The particle experiences hydrodynamical forces: the lift force $\boldsymbol{F}_l$, the drag force $\boldsymbol{F}d$ and the surface stresses moment $\boldsymbol{M}$. Attachment is ensured by the adhesion forces $\boldsymbol{F}_a$.

Stokes Flow

In the case of a laminar flow or for small particle Reynolds numbers, hydrodynamical forces can be expressed using a modified Stokes Law. The drag force, parallel to the substrate, in the stream-wise direction can be expressed as

$$\boldsymbol{F}_d = 1.7009\,3\,\pi\,\mu_f\,d_p\,V_p,$$

where V_p is the fluid velocity at the centre of the particle and μ_f is the fluid dynamic viscosity.

The lift force, in the direction perpendicular to the attachment surface is given by

$$\boldsymbol{F}_l = 1.615\,\mu_f\,d_p^2\left(\frac{\rho_f}{\mu_f}\frac{d\,u}{d\,z}\bigg|_{z=d/2}\right)^{1/2} V_p,$$

where ρ is the fluid density, u the fluid velocity parallel to the surface and z the direction normal to the surface.

Finally the moment of surface stress is given by

$$\boldsymbol{M} = 0.943993\,2\,\pi\,\mu_f\,d_p^2\,V_p.$$

The constants 1.70093, 1.615 and 0.943993 are correction factors for the wall effects and can be found in [ONeill(1968)].

Turbulent flow

In the case of a near wall turbulent flow, hydrodynamical forces can be expressed as functions of the friction velocity u_*. Soltani and Ahmadi [Soltani and Ahmadi(2001)] derived a model taking into account vortical motion in near-wall turbulence. This approach led to hydrodynamical forces slightly higher than those purely based on laminar viscous sub-layer theory in turbulent flow. In that case, drag forces are given by

$$\boldsymbol{F}_d = \frac{2.9\,\pi\,\rho_f\,d_p^2\,u_*^2}{C}$$

where C is the Cunningham correction factor.

Lift force and moment of surface stress are expressed as

$$\boldsymbol{F}_l = 0.975\,\rho_f\,\frac{(d_p\,u_*)^3}{\nu_f}$$

and

$$\boldsymbol{M} = \frac{1.07\,\pi\,\rho_f\,u_*^2\,d_p^3}{C}.$$

Turbulence burst

Both previous estimations of hydrodynamical forces are based either on a laminar flow or on averaged flow properties. It has been suggested that particle detachment in a turbulent flow is governed by the peaks in Reynolds stress associated with turbulent burst or inrush near the substrate [Cleaver and Yate(1973)].

From this observation, Cleaver and Yates [Cleaver and Yate(1973)] developed a particle resuspension model based on the lift force arising from turbulent bursts. Soltani and Ahmadi [Soltani and Ahmadi(2001)] adapted this idea to their detachment model basing their estimation on the velocity experienced by the particles on approximations of the r.m.s. stream-wise velocity for near-wall turbulent flow.

The main outcome of this model was that critical shear velocities predicted by the burst/inrush model are about 40% lower than those predicted by the viscous sublayer approach.

Adhesive forces

In the case of seaweed propagules, two types of adhesive forces are keeping the propagule on its substrate. One is the propagule weight,

$$\boldsymbol{W}_p = (\rho_p - \rho_f)\,\frac{\pi}{6}\,d_p^3\,g,$$

the other is the stickiness of its mucilage, A_ρ, which is the main unknown of the problem.

Hydrodynamical forces magnitude

The critical friction velocities determined earlier correspond to the mean value of the turbulent bottom shear-stress. The mean removal forces experienced by the propagules in that case should therefore be possible to predict using the turbulent flow formulation of the drag, lift and moment of surface stress. In the perspective of the evaluation of the mucilage adhesiveness, one should not consider the mean critical u_* but a corrected u_* that takes into account turbulence burst and inrush. Following the conclusion of Soltani and Ahmadi [Soltani and Ahmadi(2001)] that the critical shear velocity predicted by their burst/inrush model is about 40% lower than that predicted by the turbulent flow approach, the real critical u_* corresponding to mucous adhesiveness should be higher than the critical mean u_*. Evaluation of the forces on the propagules are therefore made using the turbulent flow formulation and applying a correction for

the 40% difference due to turbulent bursts (Table 3.3). The Cunningham factor is taken equal to 1 given the size of the propagules (See [Davies(1945)]).

Table 3.3. Total hydrodynamical forces experienced by the propagule at critical u_*.

	Drag force ($\mathrm{kg}\,m\,s^{-2}$)		Lift force ($\mathrm{kg}\,m\,s^{-2}$)		Moment ($\mathrm{kg}\,m^2\,s^{-2}$)	
Species	Peak 1	Peak 2	Peak 1	Peak 2	Peak 1	Peak 2
Durvillaea	1.0 - 1.3e-9	2.1 - 3.0e-9	3.6 - 5.3e-11	1.1 - 1.8e-10	1.1 - 1.4e-14	2.3 - 3.2e-14
Hormosira	3.2 - 4.4e-9	5.7 - 9.0e-9	2.0 - 3.3e-10	4.7 - 9.4e-10	7.2 - 9.9e-14	1.3 - 2.0e-13
Cystophora	0.9 - 1.2e-8	xxx	0.9 - 1.5e-9	xxx	3.3 - 4.6e-13	xxx
Fucus	2.7 - 4.8e-9	xxx	1.6 - 3.6e-10	xxx	0.8 - 1.3e-13	xxx
Pelvetiopsis	5.3 - 9.2e-9	xxx	4.3 - 9.8e-10	xxx	2.0 - 3.5e-13	xxx

Critical drag forces are found to be at least ten times higher than lift forces most of the time. No comparison is possible with moment here, given the different nature of the quantity. The species which undergoes the strongest forces is *Cystophora torulosa*, mainly due to the large size of its propagules. This is not surprising as it can be noticed that the drag force is a function of the friction particle Reynolds number to the square and the lift of Re_{p*} cubed.

Comparison of the magnitude of these forces with propagule weight (Table 3.4) shows that, whereas the critical total drag force is about ten times higher than propagule weight, propagule weight is always comparable to lift force.

Table 3.4. Propagule weight obtained from the densities derived from propagule sinking when propellers are off.

Species	Propagule weight ($\mathrm{kg}\,m\,s^{-2}$)
Durvillaea antarctica	6.25e-11
Hormosira banksii	1.59e-10
Cystophora torulosa	2.4e-10
Fucus gardneri	2.3e-10
Pelvetiopsis limitata	3.0e-10

3.5.4 Propagule detachment

From estimation of the hydrodynamical forces on the propagules, detachment criteria are derived using Newton's second law of motion [Newtown(1687)], with the two equations based on a force balance leading to the sliding (parallel to substrate) and lifting (perpendicular to substrate) criterion and the moment balance leading to the rolling criterion.

Independently of the formulation of hydrodynamical forces, rolling was found to be the mechanism governing the particle detachment process [Burdick et al.(2001)] [Soltani and Ahmadi(2001)], with sliding coming second. In both cases, the drag is generally the

dominating force [Soltani and Ahmadi(2001)]. The rolling mechanism is the most complex to quantify as it depends strongly on lever effects and therefore on the contact area between substrate and the mucilage/propagule system and on the roughness of the substrate.

Given the little information known about deformation of the propagule themselves and of their mucilage, it is hard to evaluate the contact radius between substrate and propagules. A study on the settlement process of the green alga *Enteromorpha* by Callow et al. [Callow et al.(2000)] shows atomic force microscopy pictures of settled spores of green alga surrounded by a gel-like pad of adhesive substance. Even though mucilage volume is believed to be smaller for our species, it suggests that it should significantly increase the contact surface between substrate and propagule and then have the strongest impact on the rolling criteria through decreasing lever effects. This suggests that propagule detachment can be considered as mainly based on the drag equation and sliding criteria.

Also, it was suggested that turbulent bursts occurring in the viscous sublayer could create high increases in the lift force experienced by particles and that the lift force could be responsible for particle dislodgement [Cleaver and Yate(1973)]. It was proved experimentally later that turbulent bursts are not significantly involved in particle re-entrainement and when they are, the drag force dominates the process [Yung et al.(1989)].

Sliding criteria

The sliding criterion assumes that propagules can be considered as dislodged when the drag force overcomes mucous adherence to the substrate. Mucous adherence was chosen to be expressed as an adhesion force per unit area and is therefore proportional to the contact area between propagule and substrate.

As drawn on Figure 3.20, adhesive forces are usually represented as normal to the substrate. A common approach to model the transverse component of adhesive forces is to consider a friction coefficient, k_A, linking directly transverse and normal components [Burdick et al.(2001)]. The sliding criteria can then be expressed as

$$F_d > (F_a - F_l)\, k_A.$$

k_A should be directly related to the properties of the mucilage. The adhesion can be split into the weight of the propagule and its stickiness, which in the case of a contact area of radius r_c leads to the sliding criterion

$$F_d > (W_p + \pi\ r_c^2\, A_p - F_l)\, k_A.$$

We have only one equation for three unknowns (A_p, k_A and r_c) and therefore need to make further assumptions to be able to evaluate one of the three quantities. r_c is bound to be of the order of the size of the propagule and therefore we will replace r_c by the propagule radius $\frac{d_p}{2}$. Just like r_c, k_A is strongly dependent on completely unknown properties of the propagules. We have no idea *a priori* about the value of k_A and for now will take it to be equal to one. This leads to the simplified sliding criterion

$$F_d > W_p + \frac{\pi}{4} d_p^2 A_p - F_l.$$

Detachment corresponds to the situation when both members of the inequality are equal and the propagule adhesiveness per unit area can be expressed as

$$A_p = \frac{4}{\pi d_p^2} (F_d + F_l - W_p).$$

The estimates of mucous adhesiveness are summarised in Table 3.5. Propagule adhesiveness is almost directly proportional to the critical friction velocity. Reasonably small differences are found between species (up to a factor 3) except in the case of the second peak for *Durvillaea antarctica* and *Hormosira banksii*. It can be noticed that the ratio between stickiness at peak 1 and at peak 2 is not far from 4. This would be consistent with the assumption made earlier that one of the peaks could be representative of propagules clumped together as a pack of 4 occupying an area four times larger than a single propagule.

Table 3.5. Propagule adhesiveness in $\mathrm{kg}\, m^{-1}\, s^{-2}$ estimates from the sliding criteria.

Species	Peak 1	Peak 2
Durvillaea antarctica	1.49 - 1.94	3.17 - 4.61
Hormosira banksii	1.12 - 1.58	2.06 - 3.37
Cystophora torulosa	1.19 - 1.68	xxx
Fucus gardneri	0.62 - 1.14	xxx
Pelvetiopsis limitata	0.65 - 1.19	xxx

3.5.5 Propagule characteristics

It is interesting to see that in this approach, propagule size and weight is of little relevance to remaining attached or detaching. Whereas the hydrodynamical forces scale with the friction particle Reynolds number, Re_{*p}, which shows that the total magnitude of the hydrodynamical forces is strongly dependent on propagule size as well as on flow, this becomes of little importance when considering the total force balance. The total drag force depends on propagule surface, but so does the adhesion strength and this cancels out the dependence in size.

The lift force is dependent on propagule diameter cubed and therefore its ratio to adhesive strength is still size-dependent. Nevertheless, lift force more or less cancels particle weight at detachment. This makes propagule density and size of little influence on the detachment criteria.

Therefore, the mucous adhesiveness A_p seems to be the only important propagule property relevant to propagule detachment.

This conclusion can be made only within the context of this simple model. It is possible, and even likely, that the coarse expressions of the contact radius of propagules with the substrate and the one of the mucous friction coefficient are much more complex and can hide dependency with propagule geometry.

3.5.6 Summary

A mechanistic approach to propagule detachment was developed based mainly on solid particle removal theory. Whereas in the introduction four non-dimensional numbers (R_ρ, Re_{*p}, R_σ and R_r) were introduced as the main parameters, our proposed answer to the problem remains fundamentally independent of propagule size and density and therefore would take little advantage of the use of these non-dimensional numbers.

Proportionality was almost found between u_* at detachment within the tank and mucous adhesiveness. The adhesiveness of the different species was established. It shows basically that the stickiest propagules can settle in the most extreme environment, but only during calm conditions, and accordingly *Durvillaea antarctica* was found to be the stickiest species.

Two characteristic values were found for the stickiness of *Durvillaea antarctica* and *Cystophora torulosa*. I assume that one of these peaks can be associated with the propagules tending to clump together. As there is little chance that this would affect the properties of the propagule's glue, clumping must allow the propagules to share a wider adhesiveness area for a reduced exposition to hydrodynamical removal which appears in our data as an enhance stickiness ability.

One observation that needs pointing out is that weight and lift force are almost equivalent at detachment. One of the key assumption of the whole study is that the studied seaweed zygotes are sticky. From this assumption it comes that if lift and weight forces are compensating each other, then the propagule is still firmly attached. If removal can occur at the condition that the lift force overcomes the weight, then it would mean that the main role of mucous would be to increase the contact area between propagule and substrate in order to prevent propagule rolling and increase the friction resisting to drag removal forces. While this is unlikely, this detail is

worth being stressed. This shows as well that even if the drag force is responsible for particle removal, then when a particle is removed the lift it experiences should be strong enough to re-suspend it.

Comparison with values of the friction velocity estimates *in situ* showed that the success of propagule attachment is strongly dependent on the wave climate. Several hours of calm sea are required for a propagule in the vicinity of a suitable substrate to perform the last stage of its settlement.

Chapter 4
Tank Flow Modelling

4.1 Introduction

Measurements were made within the experimental stirred tank that allowed estimate the averaged key physical parameters characterising propagule settlement experiments. Beside the three-dimensional nature of the flow that has been so far left aside, it is known that most stirred tanks exhibit large-scale instabilities [Sheng et al.(1998)]. These certainly play an important role in mixing, but must also be responsible for recurring increases of the bottom shear-stress and therefore might govern the detachment of the propagules. A deeper and more detailed understanding of the tank flow would therefore be of great importance in the context of the study of both turbulent sinking and attachment/detachment.

This can be realized through the setting up of a computational fluid dynamics (CFD) model of the tank flow. Several CFD studies of stirred tank can be found in the literature (e.g. [Sheng et al.(1998)] [Micale et al.(2000)] [Yoon et al.(2003)] [Lu et al.(2002)]), mainly for tank flows generated by a Rushton turbine (e.g. [Micale et al.(2000)] [Yoon et al.(2003)] [Lu et al.(2002)]). In most cases, stirred tank flows are fully turbulent over the entire volume [Yoon et al.(2003)] and therefore the use of a turbulence model is required. The majority of numerical studies of stirred tanks in the literature are based on the Reynolds averaged Navier-Stokes (RANS) equations [Yoon et al.(2003)]. These provide a description of the tank flow in terms of a mean velocity field, with all the turbulent fluctuations being modelled. Given the importance of the dynamics of the large-scale structures and their unsteadiness, several attempts have been made more recently to model stirred tank flow using Large-Eddy simulation based on spectral [Yoon et al.(2003)] or Lattice Boltzmann methods [Lu et al.(2002)] [Eggels(1996)].

The following describes a modelling of the stirred tank using the Gerris Flow Solver. A two-dimensional model is first setup to investigate possibilities of model calibration, simple propeller modelling and computation of the hydro-dynamical forces experienced by a settled propagule. Prior to the setup of a three-dimensional model, the question of turbulence modelling was addressed. Attempts at validating a recent LES model (Shear-Improved Smagorinsky model [Leveque et al.(2007)]) in the context of a lid-driven cavity flow are discussed. A brief illustration of the three-dimensional model is then made.

4.2 Turbulence modelling

A key issue to be addressed prior to setting up the computationally very demanding 3D simulation is that of turbulence closure. One can often not afford to resolve all the scales of a flow, especially using a desktop computer. In that respect, techniques have been designed so that only part of turbulent flow needs to be solved and the rest of it can be modelled.

4.2.1 Turbulence

"*Turbulence is like pornography - difficult to define but you know it when you see it*" - Hugo Fisher.

It is not really possible to give a precise definition of turbulence, but it is possible to make a list of some of its properties [Tennekes and Lumley(1972)]. Turbulent flows occur at high Reynolds numbers where inertia overcomes viscosity. Turbulent flows are irregular, diffusive, mostly 3-dimensional and dissipative.

A key property of turbulence is the wide range of length scales it involves, from scales of the dimensions of the flow field to the smallest scales where the energy of the flow is dissipated into heat by diffusive action of molecular viscosity. The degeneration of the small-scale fluctuations from large to diffusive scales is due to the nonlinear terms in the equations of motions where energy is extracted from the mean flow to sustain turbulence.

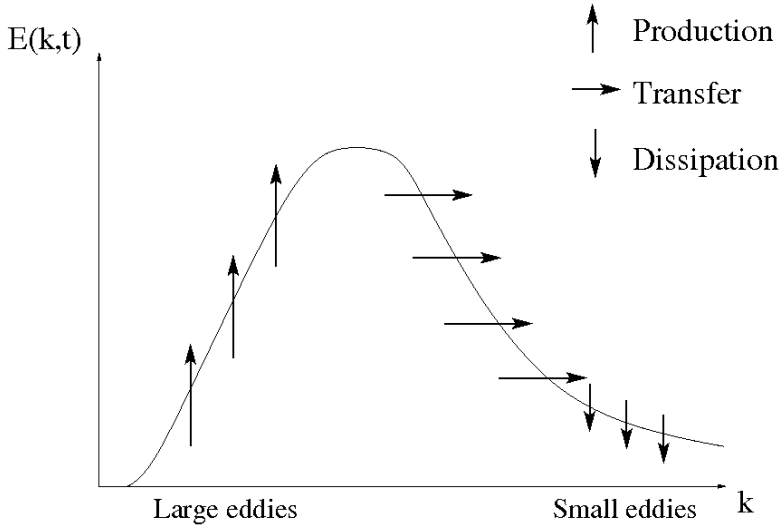

Figure 4.1. Turbulence energy spectrum as a function of the wave number

The different scales that can be found in a turbulent flow can be split in three different families, as summarised by the turbulent energy spectrum in Figure 4.1 [Caltagirone(2004)]:

- The large scales at which kinetic energy is produced mainly through interaction with the boundaries. The presence of boundaries leads to the formation of shear layers due to the

viscosity of the fluid (for a viscous fluid, the velocity of the fluid is equal to the velocity of the domain boundaries). This implies the presence of transverse velocity gradients and therefore the production of vorticity. Other mechanisms like wave breaking can be responsible as well for the production of turbulence.

- The intermediate scales where the energy cascade or inertial range takes place. The kinetic energy is transmitted from the large scales to the small scales by vortex stretching. Vortices can get stretched by the presence of a strain-rate field. Mass conservation implies that the radius of a vortex decreases if it is stretched, which would happen if its vorticity is in the direction of a positive strain rate (See Figure 4.2). Because angular momentum is also conserved, the vorticity in the direction of a positive strain rate is amplified. For the same reason the opposite result is obtained if the strain rate is negative. This way vortices can interact with each other and energy can be transmitted at smaller scales.

  Furthermore, there is a back-scatter energy cascade where energy is transmitted from small to large scales by a vortex-merging mechanism (fusion of two vortices of the same size and of almost parallel axes that occurs when the two vortices are within a critical distance of each other. Vortex merging is principally a 2-dimensional process) .

- The small scales at which the kinetic energy is dissipated into heat through molecular viscosity. Energy is dissipated through the work done by the viscous stresses resisting the deformation of the fluid.

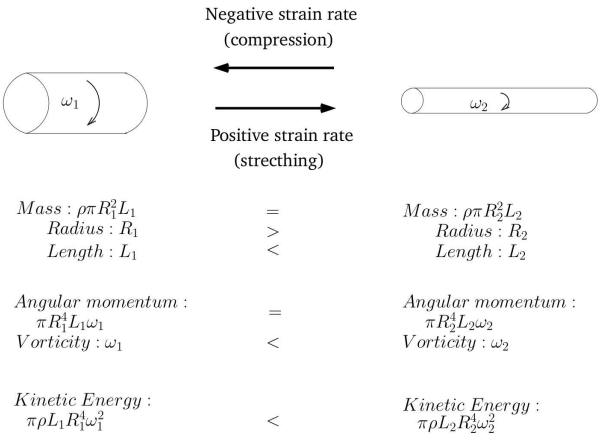

Figure 4.2. Vortex stretching or compression allows a transfer of kinetic energy from bigger to smaller scales.

Because they are of the size of the geometric dimension of the flow, the length scale of the large scales does not vary with the Reynolds number. Conversely, the size of small scales varies

with the properties of the flow. At high Reynolds number, the influence of viscous effects becomes very small compared to inertial effects. The inability of the viscosity to dissipate the energy generated at large scales is balanced by the generation through nonlinear terms of scales small enough to be affected by viscosity [Tennekes and Lumley(1972)]. Therefore, the higher the Reynolds number, the more turbulent the flow is, the smaller the smallest scales are.

The size of the smallest scales in a turbulent flow can be estimated using Kolmogorov's 1941 theory [Kolmogorov(1941)]. He introduced the idea that the smallest scales of turbulence are universal and depend only on the energy dissipation rate ϵ (in m^2s^{-3}) and the kinematic viscosity of the fluid ν (in m^2s^{-1}). The smallest length scale in a turbulent flow, or, Kolmogorov micro-scale, η, is given by:

$$\eta \sim \left(\frac{\nu^3}{\epsilon}\right)^{1/4}. \tag{4.1}$$

Similarly, Kolmogorov's time and velocity scales are:

$$\tau_\eta \sim \left(\frac{\nu}{\epsilon}\right)^{1/2} \text{ and } u_\eta \sim (\nu\epsilon)^{1/4}.$$

The rate of energy dissipation, ϵ, is of the order of [Roberts and Webster(2001)]

$$\epsilon \sim \frac{\tilde{u}^3}{l}, \tag{4.2}$$

where l represents the size of the largest eddies and is called "integral scale" and $\tilde{u}$ the standard deviation of the velocity field. It is apparent that the rate of energy dissipation that occurs at small scales depends on the production at large scale. This turbulence energy cascade adjusts itself so that the energy created in the system at large scales can be dissipated at small scales.

Combining equation 4.1 and 4.2, the scale relation between the Kolmogorov length scale and the integral scale is given by:

$$\frac{\eta}{l} \sim \left(\frac{\tilde{u}\,l}{\nu}\right)^{-3/4} = \mathrm{Re}^{-3/4}.$$

Similarly,

$$\frac{\tau_\eta \tilde{u}}{l} \sim \left(\frac{\tilde{u}\,l}{\nu}\right)^{-1/2} = \mathrm{Re}^{-1/2} \text{ and } \frac{u_\eta}{\tilde{u}} \sim \left(\frac{\tilde{u}\,l}{\nu}\right)^{-1/4} = \mathrm{Re}^{-1/4}.$$

These relations confirm that the length, time and velocity scales of the smallest eddies depend directly on the Reynolds number. The larger the Reynolds number is, the smaller those three micro-scales are.

4.2.2 Direct Numerical Simulation

As explained in the previous paragraph, turbulent flows are very complex to describe (even to define) and involve many different energy transfer processes, as well as many different scales.

Nevertheless, it is believed that turbulent flows can be described by the Navier-Stokes equation of motion [Tennekes and Lumley(1972)]

$$\rho\left(\frac{\partial \boldsymbol{u}}{\partial t}+\boldsymbol{u}.\nabla\boldsymbol{u}\right)=-\nabla p+\nabla.(\mu(\nabla\boldsymbol{u}+\nabla^T\boldsymbol{u})).$$

Unfortunately, the Navier-Stokes equation admits analytical solutions only in very specific configurations. In three-dimensions, the existence of a unique smooth solution remains to be proved [Devlin(2002)], and there is no exact theoretical solution for any turbulent flow. For these reasons, numerical methods have to be used to solve turbulent flows.

As turbulence is inherent to the Navier-Stokes equations, a good code solving these equations should provide an accurate representation of any turbulent flow. To resolve a turbulent flow accurately using a Navier-Stokes solver, the main constraint is to use a mesh refined enough to solve the smallest eddies of the flow down to the Kolmogorov scale and a time step suitable for these small eddies.

Solving the full Navier-Stokes equation down to the smallest eddies of turbulence is called Direct Numerical Simulation or DNS.

Practically, DNS gives solutions that are believed to be very close to reality, but due to the fact that the Kolmogorov time and length scales decrease quite dramatically when the Reynolds number of a flow increases, the meshes required to solve a turbulent flow become quickly huge and overcome the computer resources actually available. As well, because the energy cascade in the flow is governed by the vortex stretching mechanism which is a three-dimensional mechanism, there are only a few marginal cases for which making two-dimensional simulations leads to meaningful results. In conclusion, it is only possible to use DNS in a limited range of cases involving a simple geometry and reasonably small Reynolds numbers.

4.2.3 Turbulence modelling

As the use of DNS is non-realistic to solve most turbulent flows, several techniques have been designed to model turbulence with varying success. Among them, two families can be distinguished [Caltagirone(2004)]:

- the methods based on statistical modelling, like the Reynolds Averaged Navier-Stokes equations (RANS). In this method, the velocity and pressure fields are decomposed into a mean (time averaged) and fluctuating field. After averaging the Navier-Stokes equations,

a new term representing the turbulent constraints or Reynolds constraints appears in the equations. This term has to be modelled using closure schemes, often resulting in the evaluation of a turbulent viscosity term, like the $k-\varepsilon$ turbulence model or RNG (Renormalization Group) turbulence model [Wilcox(2006)].

- Large Eddy Simulation methods (LES). The idea of LES is to resolve the large scales of a flow using DNS, and then to model the unresolved scales using a subgrid-scale model [Lesieur and Metais(1996)]. This family of models is based on Kolmogorov's theory [Kolmogorov(1941)] of self-similarity of small eddies, which says that smaller eddies have a universal character and therefore should be possible to model.

Large Eddy Simulation

The first step in LES is to separate large and small scales. Practically, the large scales (or resolved scales) are often the ones that the size of the mesh is resolving, and the small ones are the scales smaller than the mesh size. This is equivalent to applying a filter on the full Navier-Stokes equations. The large-scale component of the velocity field can be defined by the filtering operation [Germano et al.(1991)] [Piomelli(1993)]:

$$\bar{u_i}(X) = \int_{\Omega} \bar{G}\,(X, X')\, u_i(X')\, \boldsymbol{d}X',$$

with Ω the entire flow domain. The length scale associated with $\bar{G}$ is the filter width $\bar{\Delta}$.

Applying this filter to the dimensionless Navier-Stokes equations for an incompressible fluid leads to the set of filtered equations:

$$\begin{cases} \dfrac{\partial\,\bar{u}_i}{\partial t} + \dfrac{\partial\,(\bar{u}_i\,\bar{u}_j)}{\partial x_j} = -\dfrac{\partial \bar{P}}{\partial x_i} + \dfrac{1}{\mathrm{Re}}\dfrac{\partial^2\,\bar{u}_i}{\partial x_i\,\partial x_j} - \dfrac{\partial\,\tau_{\mathrm{ij}}}{\partial x_j} \\ \dfrac{\partial\,\bar{u}_i}{\partial x_i} \end{cases},$$

with τ_{ij} the subgrid-scale Reynolds stress term

$$\tau_{\mathrm{ij}} = \overline{u_i\,u_j} - \bar{u}_i\,\bar{u}_j.$$

The main challenge in LES is to model accurately this subgrid-scale stress.

A simple model for the SGS stress, and probably the most well known and popular one, is the Smagorinsky model [Smagorinsky(1963)], which assumes that the SGS stress can be modelled as an additional dissipation term. Therefore, an eddy-viscosity, ν_t, is introduced. Smagorinsky's eddy viscosity model can be summarised as:

$$\tau_{\mathrm{ij}} - \frac{\delta_{\mathrm{ij}}}{3}\,\tau_{\mathrm{kk}} = -\,2\,\nu_t\,(X,t)\,\bar{S}_{\mathrm{ij}} = -\,2(C_S\,\bar{\Delta})^2\,|\bar{S}\,|\,\bar{S}_{\mathrm{ij}}, \text{where } \bar{S}_{\mathrm{ij}} = \frac{1}{2}\left(\frac{\partial\,\bar{u}_i}{\partial\,x_j} + \frac{\partial\,\bar{u}_j}{\partial\,x_i}\right),$$

with δ_{ij} Kronecker's delta, C_S the non-dimensional Smagorinsky constant and $|\bar{S}| = \sqrt{2\,\bar{S}_{ij}\,\bar{S}_{ij}}$ is the magnitude of the resolved rate-of-strain tensor. This practically means that to use the Smagorinsky model with a Navier-Stokes solver, one replaces the viscosity of the fluid by the sum of its viscosity and the eddy-viscosity

$$\nu_t = (C_s\,\bar{\Delta})^2|\bar{S}|. \tag{4.3}$$

The Smagorinsky "constant" C_S often depends on the geometry of the studied flow. One commonly used value determined by Lilly [Lilly(1966)] using Kolmogorov-like arguments, is $C_S \sim 0.165$. In most cases, the value of C_S is found to be between 0.1 and 0.2.

Despite its huge popularity, the Smagorinsky model is known to give good results in only a very limited number of cases. Except for buoyancy-induced turbulence, the Smagorinsky model has proved to be successful mainly in modelling relatively simple flows at rather low Reynolds numbers [Ferziger(1998)].

The drawbacks of the Smagorinsky model are that the model [Zang et al.(1993)] :

- requires a flow-dependent input model coefficient C_s.
- predicts incorrect asymptotic behaviour near a wall or in laminar flow, because it assumes that turbulence is isotropic which is not the case near boundaries.
- does not allow subgrid-scale energy back-scatter to the resolved scales, as it is modelled as an always positive viscosity term.
- assumes the principal axes of the subgrid-scale tensor are aligned with those of the resolved strain rate tensor.

In my case, the major problem is likely to be the fact that the Smagorinsky model struggles when dealing with wall-bounded flows. The eddy-viscosity remains very high near the walls which induces too much damping. Nevertheless, the Gerris Flow Solver allows very fine refinement near the boundary and a coarser mesh further from the walls. Therefore, the Smagorinsky model combined with DNS resolution of the viscous boundary layer next to the wall should lead to useful results. Using an adaptive mesh compatible with the thickness of the viscous boundary layer should not imply any change in the formulation of the Smagorinsky model, but, as the eddy-viscosity ν_t is proportional to the size of the cells (Equation 4.3) its magnitude should significantly decrease in the very refined cells near the walls.

Improvements in the approach since Smagorinsky (1963) [Smagorinsky(1963)] include the van Driest damping function [vanDriest(1956)]. VanDriest attempted to correct for the effect of anisotropy of turbulence next to the boundaries by adding a damping function in the definition of the Smagorinsky constant C_S [vanDriest(1956)]. The modified Smagorinsky constant is

$$C_s'(y) = [C_s \bar{\Delta} (1 - e^{-y^+/A})]^2$$

with C_s being the standard Smagorinsky constant (0.165 according to Lilly [Lilly(1966)]), y^+ the non-dimensional distance from the wall and $A = 25$ the van Driest constant.

The non-dimensional distance from the wall y^+ is defined as $y^+ = \frac{u_* y}{\nu}$ with u_* the wall shear or friction velocity. By choosing this definition for y^+, van Driest's approach ensures that information on the distance from the wall (y), the viscous forces (ν) and the inertial forces (u_*) are taken into account.

The idea of using the van Driest damping function is appealing as its formulation is quite simple. Nevertheless, it requires the calculation of the wall shear velocity u_* which is the velocity scale derived from the wall shear stress

$$\tau_w = \mu \left(\frac{\partial u}{\partial y} \right)_{y=0}$$

with μ the dynamic viscosity of the fluid, u the flow velocity parallel to the wall and y the distance to the wall. A good approximation of the wall shear velocity u_* would be possible to obtain either by using a refinement that allows the viscous boundary layer near the wall to be resolved, or by using a boundary layer model.

Other families of methods exist to model the SGS terms in LES. Bardina [Bardina et al.(1983)] proposed the scale-similarity model based on similarity between large and small scales. Unlike the Smagorinsky model, it does not involve any turbulent viscosity concept. It does not assume that the SGS and the resolved strain tensor are aligned. It was found that the scale similarity model does not dissipate energy, but combining this model with the Smagorinsky model gave good results in the case of a turbulent channel flow [Zang et al.(1993)]. This model proved sometimes to be unstable as it does not dissipate energy but allows SGS energy back-scatter to the large scale.

Yakhot et al. [Yakhot et al.(1989)] proposed a SGS model based on their renormalization group theory. This model naturally insures that the stress goes to zero near solid boundaries. Yakhot et al. [Yakhot et al.(1989)], however, needed to tune their model in the near-wall region to properly take into account the anisotropy of the small scales.

Germano et al. [Germano et al.(1991)] and Piomelli et al. [Piomelli(1993)] proposed models based on improvements to the Smagorinsky model. Their dynamic subgrid-scale eddy viscosity model, or dynamic Smagorinsky model (DSM), use the eddy viscosity concept but introduce a dynamic Smagorinsky constant that is evaluated at each time step in each cell of the domain. Germano and Piomelli's dynamic SGS model, uses an additional filter coarser than just the grid filter usually used in the Smagorinsky model (test filter). From the expressions of the subgrid stress for the grid-filtered equations

$$\tau_{\mathrm{ij}} = \overline{u_i\, u_j} - \bar{u}_i\, \bar{u}_j,$$

the subgrid stress for the other filter

$$T_{\mathrm{ij}} = \widetilde{\bar{u}_i\, \bar{u}_j} - \tilde{\bar{u}}_i\, \tilde{\bar{u}}_j,$$

and the resolved turbulent stress

$$\mathcal{L}_{\mathrm{ij}} = \widetilde{\bar{u}_i\, \bar{u}_j} - \tilde{\bar{u}}_i\, \tilde{\bar{u}}_j,$$

we get the relation

$$\mathcal{L}_{\mathrm{ij}} = T_{\mathrm{ij}} - \tilde{\tau}_{\mathrm{ij}}.$$

The resolved turbulent stress $\mathcal{L}_{\mathrm{ij}}$, which quantifies the contribution to the turbulent stress by the scales whose length is between grid and test filters, can be evaluated. From this resolved stress and the formulation of the Smagorinsky model on both grids, we get

$$\mathcal{L}_{\mathrm{ij}} - \frac{\delta_{\mathrm{ij}}}{3}\mathcal{L}_{\mathrm{kk}} = -2\,C(X,t)\left(\tilde{\bar{\Delta}}^2\,|\tilde{\bar{S}}\,|\,\tilde{\bar{S}}_{\mathrm{ij}} - \bar{\Delta}^2|\tilde{\bar{S}}\,|\tilde{\bar{S}}_{\mathrm{ij}}\right). \tag{4.4}$$

As equation 4.4 represents five independent equations and only one unknown, the system is over-determined and no value of $C(X,\,t)$ can be chosen that is the solution of all of them [Lilly(1992)]. Germano[Germano et al.(1991)] approximated $C(X,\,t)$ using spatial-average techniques as

$$C(X,t) = -\frac{1}{2}\,\frac{\left\langle \mathcal{L}_{\mathrm{ij}}\,\bar{S}_{\mathrm{kl}}\right\rangle}{\tilde{\bar{\Delta}}^2\left\langle |\tilde{\bar{S}}\,|\,\tilde{\bar{S}}_{\mathrm{mn}}\,\bar{S}_{\mathrm{mn}}\right\rangle - \bar{\Delta}^2\left\langle |\tilde{\bar{S}}\,|\,\tilde{\bar{S}}_{\mathrm{pq}}\,\bar{S}_{\mathrm{pq}}\right\rangle}, \tag{4.5}$$

with $\langle\,\rangle$ an average over a plane parallel to the wall.

The dynamic subgrid-scale eddy-viscosity model has been applied successfully to a variety of turbulent flows involving solid boundaries [Vreman et al.(1994)] (see [Germano et al.(1991)] [Piomelli(1993)] [Moin et al.(1991)] [El-Hady et al.(1993)]) and seem to deal well with most of the drawbacks of Smagorinsky's model. The only common problem remaining from Smagorinsky's model is that the DSM requires that the principal axes of the SGS tensor are aligned

with those of the strain rate tensor [Zang et al.(1993)], a problem that is tackled in Zang et al.'s dynamic mixed subgrid-scale model [Zang et al.(1993)], which is a mixed model between the DSM and Bardina et al.'s [Bardina et al.(1983)] scale similarity model.

The dynamic Smagorinsky models remain non-trivial to implement as they require spatial filters to get the test-filtered velocity field and of either a space-averaging algorithm, or a least-square algorithm to solve equation 4.4. It is of particular interest in our case to look at those methods with successful simulation of flows with geometry and Reynolds numbers similar to the ones I am interested in (lid-driven cavity at Reynolds numbers of 3200, 7500 and 10000 by Zang et al. [Zang et al.(1993)]).

Implementing a dynamic Smagorinsky model in the Gerris flow solver would be very tempting as it is suitable to make simulations of many different types of turbulent flows which would be coherent with Gerris' versatility. Nevertheless, such an implementation is beyond the present scope, especially as it requires the use of spatial filters. However, questions about filtering and adaptive meshes have to be answered as well. Using this type of approach in Gerris would still be a very exciting perspective for the future.

Another approach to LES is the Shear Improved Smagorinsky Model by Leveque, Toshi et al. [Leveque et al.(2007)]. The main attraction of this method is that potentially either spatial or time-averaging can be used. Our preference is time-averaging which requires more storage capacity, but which is much simpler to implement. The Shear Improved Smagorinsky Model, as most of the methods previously described, is derived from the Smagorinsky model and still involves the use of an eddy viscosity. Just like Germano's DSM it used an eddy viscosity that depends on space and time, which in some ways makes it a dynamic Smagorinsky model as well. The main difference is that in this model the Smagorinsky constant C_s (See equation 4.3) does not depend on time or space, but the magnitude of a space or time average of the resolved rate of strain tensor or mean shear $|\langle \bar{S} \rangle|$ is subtracted from the magnitude of the resolved rate of strain tensor $|\bar{S}|$. In this way anisotropic turbulence and wall bounded turbulence are taken into account. The theory behind this model can be found in [Toschi et al.(2000)]. When the turbulence is isotropic, the mean shear $|\langle \bar{S} \rangle|$ is equal to zero and the Shear Improved Smagorinsky Model is equivalent to Smagorinsky's model. The eddy viscosity in this model is formulated as

$$\nu_t = (\bar{\Delta}\, C_S)^2\, (|\bar{S}| - |\langle \bar{S} \rangle|). \tag{4.6}$$

The Shear-Improved Smagorinsky Model has been tested on plane channel flows [Leveque et al.(2007)] and on backward-facing step flows [Toschi et al.(2006)]. Tests on plane

channel flows showed that the model was able to resolve near-wall turbulence and the comparisons made with DNS simulations were satisfactory. The backward-facing step flow tests provided opportunities to study the performance of the model when dealing with a more complex geometry. The quality of the average profiles and low order statistics obtained using the Shear Improved Smagorinsky Model were found to be acceptable with respect to experimental data and almost identical to the ones obtained using dynamic Smagorinsky models [Toschi et al.(2006)].

The main issue that remains to be addressed is to define a proper way to deal with temporally non-stationary flows and whether this is possible. Solving this problem likely involves being able to find a proper way to average the resolved rate of strain tensor. This might only be possible through space-averaging techniques. Furthermore, the model needs more testing regarding its performances with very coarse resolution [Toschi et al.(2006)].

This recent development looks very exciting and suitable to be applied in Gerris reasonably quickly. The tests run with backward-facing step give me confidence on the suitability of the model to our problem as the Reynolds number used in this tests were high. The ability of the model to deal with geometry of the test (sharp angles) corresponds to something definitely needed for stirred tank simulations. One point that remains is whether the SISM behaves well in the case of a pure time-averaging of the mean SGS tensor. It is likely that time-averaging techniques are well-suited only for turbulent flows that exhibit a strong mean flow and quite steady large-scale dynamics, which is not the case in stirred tanks. Nevertheless, it can be hoped that the correction applied by the mean SGS term can make the model more accurate than the standard Smagorinsky one without requiring empirical tuning. If that proved to be the case, the SISM model would become a useful alternative to the standard Smagorinsky model. Details about the implementation of the model in the Gerris Flow Solver can be found in Appendix C.

Benchmark test case: Lid-driven cavity

A benchmark test case suitable for this work is the lid-driven cavity test. DNS results of lid-driven cavities at various Reynolds numbers have been published. Ghia [Ghia et al.(1982)] published DNS results for a two dimensional lid-driven cavity at Re = 1000 using a vorticity stream function formulation of the Navier-Stokes function. More two dimensional DNS results were published by Erturk [Erturk(2005)]. Deshpande and Shankar [Deshpande and Shankar(1994)] used a finite-difference Navier-Stokes solver to make three dimensional simulations of lid-driven cavity flow at Reynolds numbers of 3200 and 10000. Spectral methods were developed by Botella and Peyret [Botella1998]. Bouffanais et al. [Bouffanais et al.(2006)] published DNS res-

ults from a spectral element method for high Reynolds numbers. The number of results that can be considered as reliable is quite large and therefore, it has been and remains a very convenient test case to validate a model.

The lid-driven cavity test consists in a cubic or rectangular tank filled with a fluid. The boundary conditions on all the directions except for the top are wall boundary conditions, i.e., the velocity is equal to zero on the solid surface. At the top, the fluid is dragged along horizontally at a given velocity U by an "infinite lid" that would be sliding over the tank (Figure 4.3). Practically, a belt can be used to replace the "infinite lid" [Stevens and Imberger(1996)].

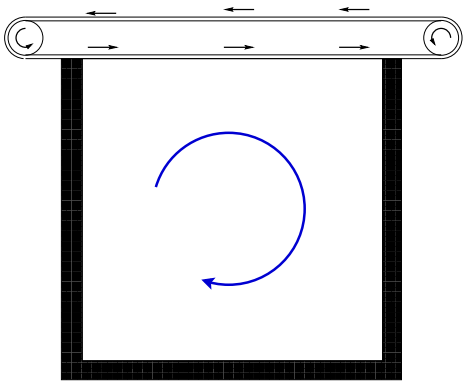

Figure 4.3. Lid driven cavity setup. Cavitation is sustained by horizontal entrainment of the fluid at the top of the box.

Lid-driven cavities have been studied extensively from an experimental and numerical point of view [Shankar and Deshpande(2000)]. The popularity of this problem can be explained by the simplicity of its design, but equally by the number of applications it has in the environmental or the industrial domain.

Lid-driven cavities have been used as a simplified model of many manufacturing devices, such as short blade coater or flexible blade coater used for the production of high-grade paper or photographic films, or devices used for melt-spinning for the formation of continuous metal ribbons of micro-crystalline material [Aidun et al.(1991)]. Lid-driven cavity flows have been associated with several mixing devices used in the plastic and food industry [van der Meer et al.(1992)]. Such flows have also been studied in order to suppress or reduce the noise associated with wheel-well cavity and inter-wheel gap on planes [Povitsky(2001)].

Lid-driven cavity flows can be found in nature and have been used to model urban canyons [DeLaFuente2003]. Stevens and Imberger studied the response of a stratified lake to the action of a wind stress as a rectangular cavity forced at the top by a belt [Stevens and Imberger(1996)].

With respect to this PhD work, lid-driven cavity flow could fit into two different contexts:

- At large scale, this problem is very similar to the one of the stirred tank. Both experiments involve a wall-bounded flow in a rectangular box. Despite the fact that both experiments are stirred by different mechanisms, they both imply large scale eddies of about the size of the tank and smaller structures forming in the corner. Obviously, given the flow regimes imposed in the stirred tank, it is only the turbulent regime for the lid-driven cavity that should be considered in this case.

- At a much smaller scale, microhabitats [Abelson and Denny(1997)], very small cavities in the substrate where propagules could potentially get trapped could be modelled as lid-driven cavities. In this case, the geometrical similarities would probably not be as good as the one we have in the stirred tank case, but the forcing of the system would be more likely to be well represented as a lid (channel-driven cavity flow).

Other important features of the lid-driven cavity test are the fact that it is well-studied. Good experimental results have been published in the literature, the best-known being by Prasad and Koseff [Prasad and Koseff(1998)] for Reynolds numbers of 3200 and 10000 observed a using a laser-Doppler velocimetry system.

Despite being very simple in appearance, lid-driven cavity flows are of interest from a fluid mechanical point of view and can even be considered as a complex and very challenging problem. At low cavity Reynolds number, they present a complex structure with a large eddy in the middle of the cavity and smaller eddies in the corners. The structure of the flow at a given Reynolds number in the laminar regime depends on the aspect ratio of the box used as a cavity.

Transition from laminar flow to turbulence in lid-driven cavity flows has also been studied extensively numerically [Goodrich et al.(1990)] [Shen(1990)] [Auteri et al.(2002)] [Peng et al.(2003)]. The first Hopf bifurcation has been localised for Reynolds numbers around 8500 in most papers. First a transition from laminar flow to periodic flow is observed. Then, with the increase of the Reynolds number, some additional modes appear until the flow eventually becomes completely chaotic or turbulent.

At very high cavity Reynolds numbers, when the flow is fully turbulent, stable eddies no longer form. Cavity flows are particularly interesting for turbulence modelling because they involve an inhomogeneous repartition of the turbulence in the tank. The turbulent regions close to the centre of the cavity host mainly isotropic turbulence, while those closer to the wall host highly anisotropic turbulence, and ultimately there is a viscous sub-layer on the wall. All those

characteristics of the turbulent flow in a cavity work together to make this experiment very appropriate to validate turbulence models [Jordan and Ragab(1994)] [Zang et al.(1993)] [Habisreutinger et al.(2007)] [Popiolek et al.(2006)].

2D simulations

A DNS of a two-dimensional cavity already existed in the Gerris test suite, with comparison to the DNS results published by Ghia [Ghia et al.(1982)].

One of the main topics of interest regarding two-dimensional cavity flow is transition to turbulence and the Hopf bifurcations that shift the flow slowly from laminar, then into periodic oscillation and finally into a fully chaotic flow. This can be illustrated by the detail of the total energy in the cavity, as plotted on Figure 4.4, for Reynolds numbers of 1000 (laminar), 11500 (periodic) and 14000 (pseudo-periodic). The first Hopf bifurcation was found to be around a Reynolds number of 8500 with the periodic mode extending to about 12000.

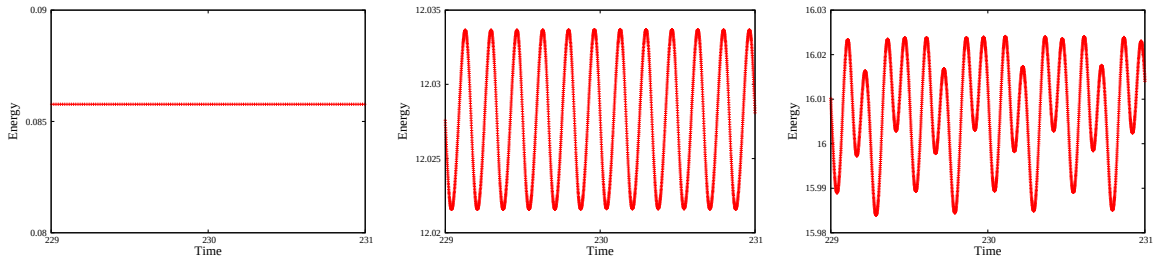

Re 1000 Re 11500 Re 14000

Figure 4.4. Detail of the variation of the total energy in the cavity for flow Reynolds numbers of 1000, 11500 and 14000.

The large-scale structure of the flow becomes more complex for higher Reynolds numbers (Figure 4.5) with the formation of an increasing number of smaller unstable eddies in the corners or in the near wall region.

Re 1000 Re 11500 Re 14000

Figure 4.5. Vorticity field and streamlines at time 300 in a 2D lid-driven cavity for Reynolds numbers of 1000, 11500 and 14000.

3D simulations

The 3D simulations made with Gerris were at first dedicated to turbulent cavity flows at a Reynolds of 10000. The choice of this Reynolds number was motivated by the available experimental data by Prasad and Koseff [Prasad and Koseff(1998)] and the DNS data by Deshpande and Shankar [Deshpande and Shankar(1994)] or Verstappen and Veldman [Verstappen1994]. Furthermore, 10000 is the lowest Reynolds number for which the cavity flow is turbulent and DNS results are available. It was of particular importance to use the lowest Reynolds number possible because three-dimensional calculations are very expensive and still fairly hard to achieve on a desktop computer. The use of a relatively low Reynolds number allows the size of the Kolmogorov length-scale to be maximised.

The DNS data by Deshpande and Shankar [Deshpande and Shankar(1994)] provide an ideal framework to evaluate the performance of the SISM model and the range of comparisons between experience and DNS over mean velocity profiles, punctual time series and spectra allow a comparison of the most important properties of the flow. Gerris simulations were designed so that each of the graphs that can be found in (Deshpande and Shankar,1994) [Deshpande and Shankar(1994)] would be regenerated and compared with the LES-SISM results from the Gerris Flow Solver.

Ideally, it was planned to realize a DNS simulation of the cavity flow at Re 10000 and then use the mean SGS tensor obtained from the DNS simulations to run the SISM model. This would have allowed us not to have to worry about the convergence of the mean SGS tensor. Performances would have been checked using the Smagorinsky-Lilly constant, C_s, in the expression of the eddy viscosity

$$(\bar{\Delta}\, C_S)^2\, (|\bar{S}\,| - |\langle \bar{S}\,\rangle|).$$

An eventual tuning of C_s could have been realized. Then, a convergence study of the mean SGS tensor, $|\langle \bar{S}\,\rangle|$, as a live averaging would have been possible. The different averaging strategies would have been compared leading to the identification of the best strategy. All this, depending on whether a simple time-averaging of the SGS tensor is a good way to obtain $|\langle \bar{S}\,\rangle|$.

Such work represents a massive amount of computing time, especially given the fact that all anisotropic eddies still need to be resolved directly. In that respect, the lid-driven cavity flow is very demanding because the smallest non-isotropic eddies are usually due to the presence of wall boundary layer and the whole flow here is surrounded by walls. It would have been possible to consider the classic benchmark test of the channel flow [Moin and Kim(1982)] [Jeanmart and Winckelmans(2002)], but tests were already realized by another Gerris user.

Calculations started on single processors did not succeed because of the conjunction of technical problems, their long duration and an over-evaluation of the characteristic time-scale of the flow. As most of this work was realized near the end of this PhD, the only opportunity I had to complete a whole run was given to us by the Norwegian Metacenter for Computational Science (NOTUR) thanks to Dr. Haarward Holm. The simulation was parallelised and run on one of the NOTUR's linux cluster (Stallo).

After familiarisation with parallel computing, queue system and performance assessment of Stallo it was found that problems were regularly encountered when the simulation was running on more than a node at a time. A single node on Stallo contained up to 8 processors, and the use of the cluster provided quite a gain in time. Only this single run is reported here.

Deshpande and Shankar [Deshpande and Shankar(1994)] realized their DNS simulation of the cavity flow at Re 10000 using a Cartesian grid with refinement $84 \times 84 \times 84$, which almost solves the flow down to Kolmogorov scales everywhere in the domain [Deshpande and Milton(1998)]. Such a resolution is slightly coarser than $2^7 \times 2^7 \times 2^7$ which is a resolution down to level 7 in Gerris. The mesh used for the LES simulation was refined down to level 7 near the wall and then progressively coarsened to level 5 ($32 \times 32 \times 32$) in the core of the cavity.

The mean stress tensor was averaged within an averaging window of time-scale T corresponding to the characteristic length scale of the flow as stated by Deshpande and Shankar [Deshpande and Shankar(1994)] using the Gerris syntax:

```
GfsEventSum { istart = 6 istep = 1 } (0.061*t+1.)*dx("U")-0.061*SSxx SSxx
```

where $0.061 = \frac{1}{T}$. This is equivalent to

$$\left\langle \bar{S} \right\rangle^{n+1} = \frac{(t^n - 0.061\,\Delta t)\left\langle \bar{S} \right\rangle^n + (1 + 0.061)\,\Delta t\,\bar{S}^{\,n+1}}{t^n + \Delta t}.$$

The mean SGS tensor was fed back into the turbulence model after 40 time units, which was long enough to avoid instability. The simulation was started from the velocity field obtained in a previous run which is closer to the established flow than fluid at rest. It was arbitrarily decided for this trial to run the model for about 1 time, the characteristic time-scale of the problem, before starting the averaging from the different quantities.

This proved to be far too short for the model to converge toward a constant mean SGS tensor and for the energy of the system to reach a state of turbulent equilibrium. The energy of the system was still distinctly decreasing at the end of the simulation, whereas the spatial average norm of the SGS tensors was still increasing sharply. This is consistent with the velocity traces along the (x,0,0) axis (Figure 4.6) which are significantly higher than the DNS results from Deshpande and Shankar [Deshpande and Shankar(1994)].

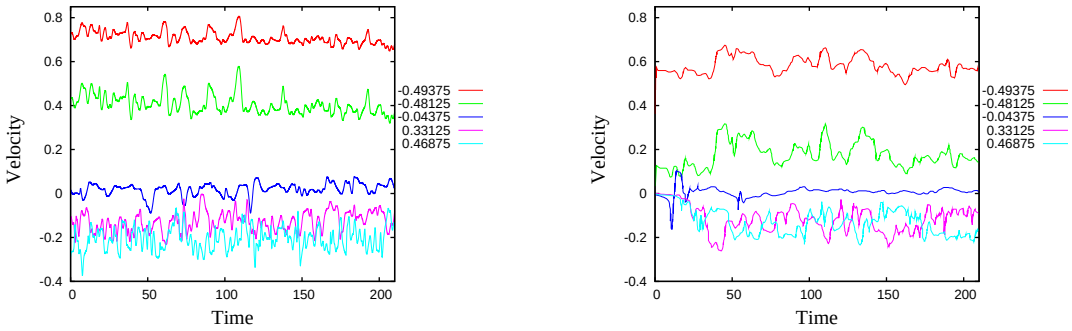

Gerris SISM Deshpande and Shankar[Deshpande and Shankar(1994)]

Figure 4.6. Time traces of the y component of the velocity field at five different locations on the (x,0,0) axis.

Approximately the same thing can be observed on the mean velocity profiles along the X and the Y axis (Figure 4.7). The mean velocity profiles obtained from the model have the right shape but are of much higher amplitude.

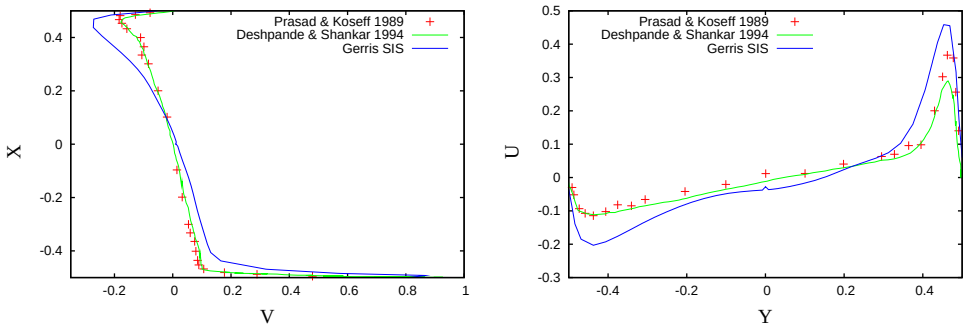

Figure 4.7. Mean velocity profile along the X and Y axis in the plan of symmetry of the cavity.

Spectra (Figure 4.8) show good comparison with most of the significant frequency matching between Gerris SISM simulations and DNS or experimental data. Nevertheless, there is more energy in the inertial range especially compared to the DNS data.

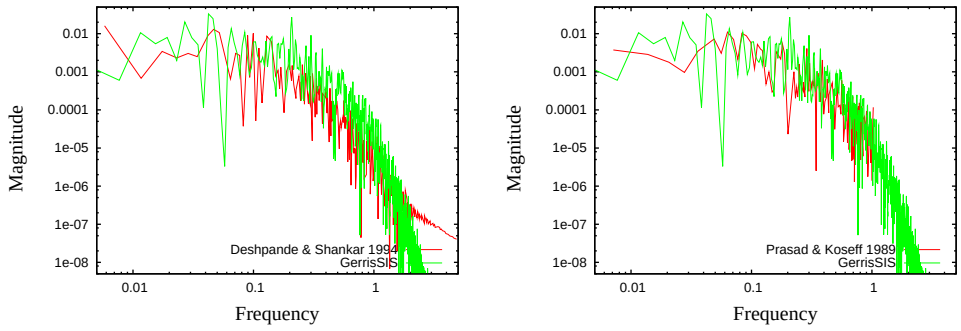

Comparison with DNS Comparison with experiment

Figure 4.8. Power spectra at the point (0.466, 0,0), comparison with numerical data by Deshpande and Shankar [Deshpande and Shankar(1994)] and experimental data by Prasad and Koseff [Prasad and Koseff(1998)].

It is hard to make any conclusion from these results. It is obvious that they represent only part of the work that should be done to give a verdict on the usefulness of the SISM method with time-averaged mean SGS tensor. The model does not seem to behave wrongly so far, but unlike the standard Smagorinsky model seems to create too little dissipation in the near wall area. Nevertheless, the trend observed in the energy fluctuation show that dissipation is still increasing in the tank.

Most of the technical work necessary to assess the performance of the SISM on the 3D lid-driven cavity has been done. The main problem remains to find enough computational time to realize DNS calculations to feed back into the model.

4.3 Two-dimensional model

4.3.1 Numerical model

Geometry setup

It is not expected that the free surface at the top of the tank is of great importance for the dynamics of the flow within the tank, and therefore the tank was modelled as a cubic box with no-slip boundary conditions ($\boldsymbol{u} = 0$) applied to all its walls.

Grid

The choice of the resolution used within the tank should be dictated by the size of the smallest eddies. The tank flow is globally turbulent and therefore the resolution should ideally be down to Kolmogorov's length scale in the core flow, and the viscous sub-layer near the walls should be resolved. It was decided to use the adaptivity of the mesh only to increase the resolution in the near-wall area where the smallest anisotropic structures should be. A uniform Cartesian grid was used to solve the core flow.

From the estimation of u_* obtained in the previous section, the viscous boundary layer should be around 1 mm thick for the highest flow speed of interest. In that case, in most flow regimes, a resolution down to $\Delta x = \frac{1}{2^8} 150 = 0.58\text{mm}$ is sufficient near the walls.

Estimation of the averaged Kolmogorov length scale within the tank can be made from the estimation of the mean energy dissipation rate in a stirred tank given by Nienow

[Nienow(1997)]. The mean energy dissipation rate $\bar{\epsilon}$ can be expressed as

$$\bar{\epsilon} = \frac{P_0 N^3 D^5}{V}$$

where P_0 is the power number of the propeller which can be taken as equal to 1.70 for a pitch blade turbine [Jaworski et al.(1996)], N the propeller speed, D the propeller diameter and V the tank volume. Therefore, for two propellers

$$\bar{\epsilon} = \frac{2 \times 1.70 \left(\frac{\text{rpm}}{60}\right)^3 0.03^5}{0.065^3} = 1.393E^{-9}\,\text{rpm}^3$$

The Kolmogorov micro-scale is then given by

$$\bar{\eta} \equiv \left(\frac{\nu^3}{\bar{\epsilon}}\right)^{1/4} = 0.00562\,\frac{1}{(\text{rpm})^{3/4}}. \tag{4.7}$$

From equation 4.7, the Kolmogorov scale is estimated to vary from 0.18 mm to 0.03 mm when the propeller speed varies from 100 to 1000 rpm (Table 4.1), which in all cases is even smaller than boundary layer size. These estimations are of the same order of magnitude as the ones given by Yoon et al. [Yoon et al.(2003)]. Resolving such small length-scales would require the use of a mesh refined down to level 11 to 13 (2048 × 2048 to 8192 × 8192 in 2D) which is not reasonable for a high-powered Desktop computer.

Table 4.1. Estimated Kolmogorov length in the tank.

rpm	100	250	500	750	1000
$\bar{\eta}$ (mm)	0.178	0.089	0.053	0.039	0.032
Level of resolution needed	11	12	12	13	13

For that reason, turbulence modelling should be used and the grid needs to be set up for the Large Eddy Simulation approach (See earlier in the Chapter). The Smagorinsky or Shear-Improved Smagorinsky are both based on the eddy-viscosity concept and assume that the modelled turbulent eddies are isotropic. Therefore, the mesh needs to be set up in order to resolve all the anisotropic structures. Typically, the smallest coherent anisotropic eddies can be found near the walls, and they scale with the distance from the wall in wall units. For that reason, the use of a mesh refinement level allowing the resolution of the viscous-sublayer in the vicinity of the wall allows resolution of the smallest anisotropic scales. Consequently, the mesh was refined down to level 9 near the wall and then coarsened to level 7 in the core flow.

To measure the hydrodynamical forces experienced by the propagules, the substrate area where the number of settled propagules was counted on the experimental tank, was refined down to level 13 and a static solid sphere was placed near the substrate (Figure 4.9).

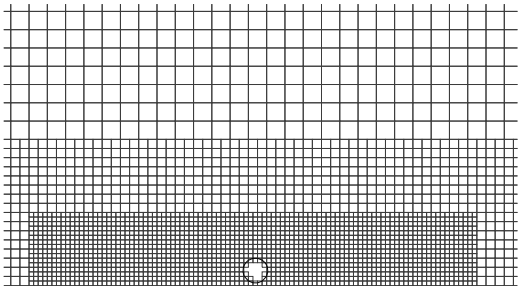

Figure 4.9. Adaptive refinement on the settlement area around a static solid propagule.

Propeller modelling

In the context of Rushton turbine (impeller commonly used in industrial blending devices [Sheng et al.(1998)]) modelling, two main approaches to stirring were found. One is to make experimental measurements of the flow coming out of the turbine and use them as boundary conditions (e.g. [Sheng et al.(1998)]). A second approach is to model impeller flow as the sum of a jet (momentum source), a circumferential flow and a component representative of the tip vortices generated by the impeller's blade [Yoon et al.(2001)].

Propellers here are modelled as sources of momentum in 2-D, and sources of momentum and vorticity in 3-D. This is mainly equivalent to the jet component used by Yoon et al. [Yoon et al.(2003)]. To some extent, this could be seen as similar to the approach used by Jimenez et al. [Jimenez et al.(2008)] or reported by Vermeer et al. [Vermeer et al.(2003)] to model wind turbines, except that the propellers are accelerating the flow whereas the wind turbines are absorbing energy. A drag coefficient is determined from the geometry of the turbine (size, blade shape and angle), then the turbine is modelled as a disk where the total force exerted by the turbine on the surrounding flow is uniformly distributed.

Several approaches were examined regarding propeller shape and input velocity:

- the simplest approach consists of having a well-refined disk of thickness 0.002 in non-dimensional units. The choice of thickness of the disk does not correspond to any physical length-scale, but is simply thin while being thick enough to be well-represented on the chosen mesh. The disk corresponds to a uniform constant source of velocity.

- a routine was written to regulate the source of velocity using the total amount of kinetic energy in the tank. A maximum intensity was set up for the velocity source as well as a targeted total amount of kinetic energy for the tank. Source intensity was changed if necessary to keep the kinetic energy constant around the desired value. It proved to be hard to control the large

variations in kinetic energy over time due to turbulent fluctuations in the tank, and the method was dropped.

- a constant velocity was imposed within the propeller area instead of imposing a source. This can be done using a momentum source term whose intensity is defined as the difference between the local velocity and the desired velocity.

The simplest approach with constant sources of velocity was used for most of the work, assuming that the system would reach a turbulent equilibrium between the constant input of energy from the tank and energy dissipation within the tank. The approach with regulation of the propeller input from the local velocity presented interesting features, such as the possibility to impose an explicit velocity scale, but could lead to unstable simulations.

The magnitude of the required velocity source was first evaluated from the propeller's shape and rotation speed. This did not compare well with a review of the propeller literature. For that reason, the velocity input was tuned to get the desired flow (See next paragraph).

It would have been possible to predict the velocity source from a simple propeller efficiency model. Nienow [Nienow(1997)] reports that the flow just away from the blades of an impeller is proportional to its speed (N in rotation per s) and its diameter (D) to the power of three

$$Q = F_l N D^3$$

where F_l is the dimensionless flow number that is about 0.73 for a pitch blade turbine [Jaworski et al.(1996)]. This has been successfully used to model stirred benthic chambers [Oldham et al.(2004)] and can be adapted to modelling of this stirred tank.

4.3.2 Model calibration

The flow within the tank is characterised by three dimensional quantities which are the tank size, L, seawater kinematic viscosity, ν, and a velocity scale representative of the propeller speed, u_0. According to Vaschy-Buckingham [Vaschy(1892)] [Buckingham(1914)]'s Pi theorem, the tank flow can be characterised by a single non-dimensional parameter, the Reynolds number.

Proper calibration of the model must ensure that the Reynolds number in the numerical model is the same as the one in reality.

$$\mathrm{Re}_{\mathrm{model}} = \mathrm{Re}_{\mathrm{reality}}$$

The main challenge in the tank calibration lies in the fact that no known velocity scale is explicitly imposed on the tank in reality (propeller flow speed is not known) which makes it harder

to ensure Reynolds similarity between the real tank and its model. Proper Reynolds number scaling should produce proper turbulence scaling [Hendriks et al.(2006)].

Ideally, from the perspective of the settlement experiments, it would have been preferred to use the friction velocity u_* for the reference velocity scale but given the variability found in my estimation of u_* in the previous chapter, this approach would not be reliable. Also, given the uncertainty of the measurements of the friction velocities, it is of a greater interest to calibrate the model with a different velocity scale and directly output measurements of the shear stress in the propagule settlement area.

Another velocity scale linked to turbulence that could be used is the square-root of the average of the TKE within the tank, or within the slice of the tank where the PTV measurements were realized. Nevertheless, the use of a turbulence model implies that part of the turbulent fluctuations are modelled and therefore would be missing in the computation of the TKE.

I chose to use a velocity scale derived from the total kinetic energy within the measurement slice for reference length scale:

$$u_0 = \sqrt{2\,\mathrm{KE}_{\mathrm{slice}}}.$$

The Gerris Flow Solver solves the non-dimensional Navier-Stokes equations, and therefore the problem had to be non-dimensionalised. The reference length-scale for the whole problem is chosen to be the tank length which is 140 mm in reality. The kinematic viscosity which is $1.004.10^{-6} m^2 s^{-1}$ for seawater is taken to be equal to 0.0001. Therefore, if the non-dimensional quantities are noted with a *,

$$u_0^* = \frac{L\,u_0}{\nu}\,\frac{\nu^*}{L^*} = \frac{L\,\nu^*}{\nu\,L^*} u_0.$$

Table 4.2. Non-dimensional velocity reference for the different rotating speeds of the propellers.

rpm	400	500	600	750
KE ($\mathrm{mm}^2 s^{-1}$)	200	265	409	589
u_0 ($\mathrm{mm}\,s^{-1}$)	20.0	23.0	28.6	34.3
$\bar{u_0}$	0.30	0.34	0.43	0.51

u_0 is a mean quantity and has to be averaged over a suitable time scale to be representative of the mean velocity. The mean velocity fields obtained from PTV correspond to a time averaged (over a 33 *s*econds window), and therefore the velocity field was averaged over similar or longer time scales before the kinetic energy of the mean field was calculated.

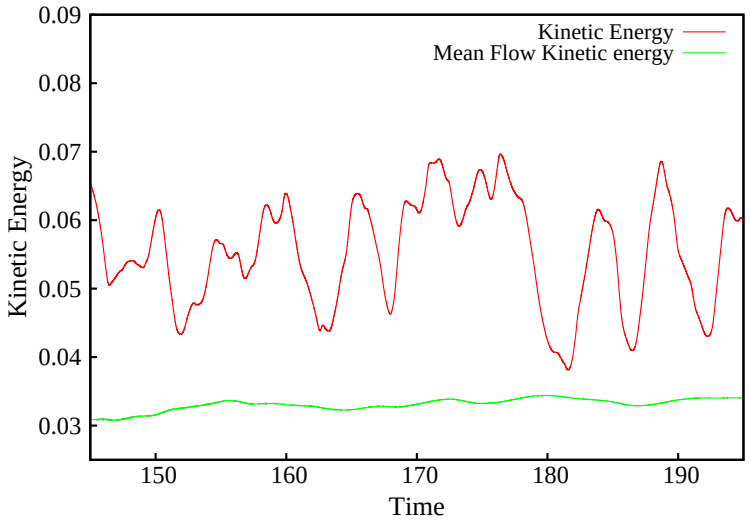

Figure 4.10. Evolution of the non-dimensional instantaneous KE (red) and of the mean velocity field KE (green) within the tank for a unit velocity inflow through the propellers.

Simulations have usually been run in two parts. First the model was run without a particle for 100 time units to quickly get the established regime. Half a day to a whole day was needed to realize this first run on a 3 GHz Intel Xeon CPU. Then, the particle was added, the settlement area was further refined and the model was run for another 100 time units (around 5 days of calculations).

4.3.3 Results

Recall of PTV data

Model validation was achieved using the PTV and ADV data taken in the tank. Mean flow structure (Figure 4.11) is obviously the most straightforward way to get a qualitative evaluation of the model's behaviour. In this case, it is based on the PTV measurement realized on a single slice of the tank for several propeller speeds.

As recalled from Chapter 2, the mean flow observed in the slice of interest contains a whole eddy in the bottom right corner (on the side where the propeller is the closest to the bottom). The flow is strongly asymmetrical, with most of the kinetic energy located in the central left and left corner parts of the slice. A second eddy is partly present in the top left corner of the slice, where the only upward flow is located. The influence of both propellers looks similar as two jets collide in the slice. The bottom right corner is a region of lower energy with possibly a second coherent structure hidden in the corner.

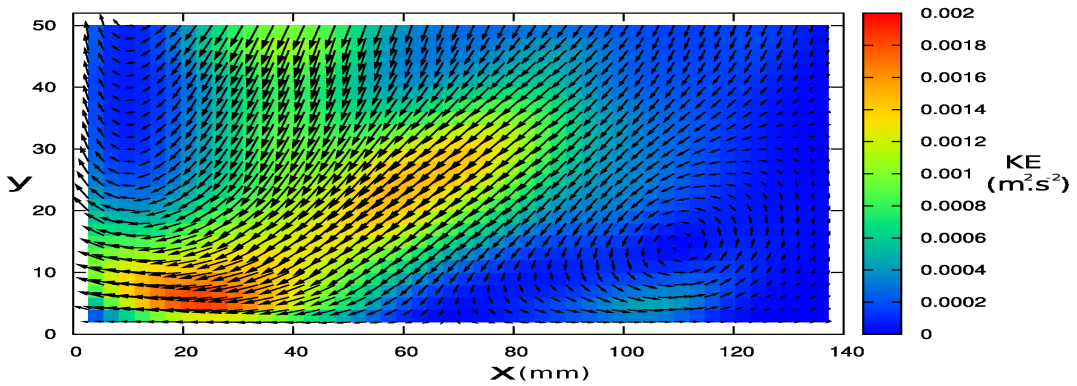

Figure 4.11. Plot of the PTV instantaneous velocity field and kinetic energy ($m^2\ s^{-2}$) for propeller speed of 600.

Quantitative calibration can be resolved from the measurements of the kinetic energy extracted from the PTV measurements. This will be discussed later in this section.

More quantitative and qualitative validation can be done from the ADV measurements. Local energy spectra can be generated from velocity time series and compared with numerical spectra derived from the models. Repartition of energy by frequency can be observed and turbulence structure (Kolmogorov length-scale and inertial range) can be checked. This is especially relevant for 3D simulations, as described in the next section.

Preliminary 3D simulations

Preliminary simulations were first realized at low resolution and Reynolds number. These cannot be considered as final results but illustrate well the behaviour of the 3D model and the reason why the constant velocity source representation of the propellers was first adopted.

These simulations were realized using the constant velocity source representation of the propellers. The Reynolds number of the flow is low enough that the simulation remains laminar and converges toward a steady state. This is, of course, not representative of the range of Reynolds numbers where settlement experiments were made. Nevertheless, this remains in the range of Reynolds numbers where a simulation can run in around 24 hours on a desktop computer. That way, it remains affordable to "experiment" with the different parameters.

Figure 4.12 shows plots of the vorticity (colours) and velocity (arrows) fields at steady state for Reynolds numbers of 500, 900 and 1500, where the Reynolds number is based on the magnitude of the velocity source.

It can be seen that despite the crudeness of the model the velocity field at steady state presents numerous common features with the mean velocity field observed in the PTV measurements including,

- a main closed recirculation at the bottom right of the slice;

- location of most of the vorticity in the middle left of the slice;

- main upward flow at the left of the slice;

- presence of a stagnation point close to the middle of the bottom.

Several differences can be noticed as well:

- upward flow on the right;

- very limited influence of the right hand propeller;

- the higher the Reynolds number the further the global flow shape is from the PTV records.

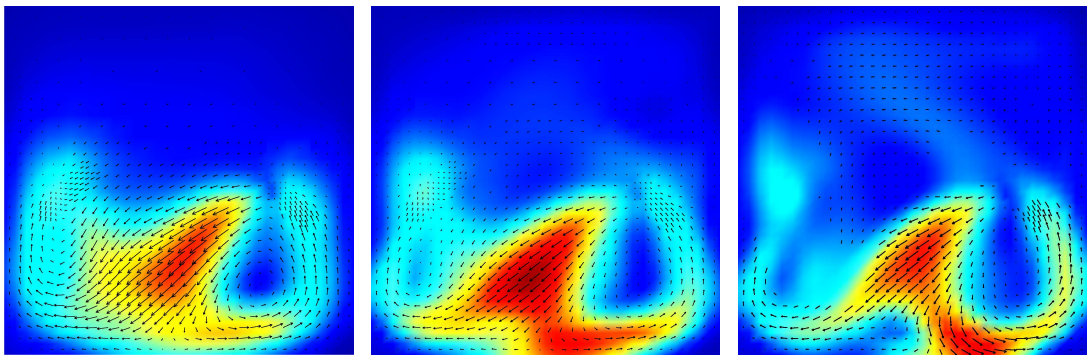

Figure 4.12. Velocity field in a full cross section of the tank at steady state on 3D simulations, at low Reynolds number with propellers modelled as constant velocity inputs. From left to right Re = 500, 900 and 1500, with Re based on the amplitude of the velocity source.

These three plots (Figure 4.12) show promising behaviour of the 3-dimensional model, and denote the potentially good behaviour of the constant velocity source propeller model.

Given the reasonable quantitative results obtained in this configuration, it was initially decided to keep working with this propeller representation. It was also envisaged to superimpose a source of solid body rotation to the velocity source to add more vorticity to the flow. Several different ratios of rotation over momentum source were simulated, without any obvious conclusion resolved from them.

Initial setup

I used faster 2D modelling to consider a range of issues. These simulations need to be be placed in context by the limited possibility to realize 3D simulations (mainly because of computational reasons).

The results presented in the 2D section are mainly focused on the bottom half of the tank corresponding to PTV measurements. Only one plot of the whole tank is presented here (Figure 4.13), showing the action of the propellers on the fluid at rest. Vorticity is generated on the

edge of the propeller blades due to the gradient of velocity between the fluid at rest and the propelled fluid. It can be noticed that both propellers are not at the same height, to reproduce a geometry as similar as possible to reality. It was very tempting to make the assumption that both propellers were located symmetrically and only solve the flow for half of the box using a symmetry boundary condition in the middle of the tank. This would have accelerated the simulations by a factor of two. Nevertheless, the PTV data show strong asymmetry of the large scale circulation, which is of interest for validation purposes. With a high enough level of confidence in the propeller model, it is possible to generate all the physical data of interest from a symmetrical tank model.

It also has to be kept in mind that most of the 2-dimensional work was done with the ultimate aim of evaluating the relevance and feasibility of several modelling/calibration ideas before working with a fully three-dimensional model. For that reason, no turbulence model was used here. Two-dimensional and three-dimensional turbulence are fundamentally different mechanisms [Canuto(2000)] and most efforts in that direction were exclusively dedicated to the 3D model.

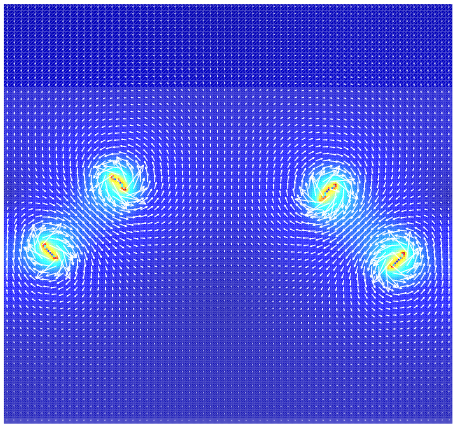

Figure 4.13. 2D tank at the start of the simulation after projection of the velocity field.

Constant source versus regulated source - velocity source intensity

Models using propellers modelled as constant or regulated sources of momentum were tuned until the desired level of mean kinetic energy in the bottom section of the tank was reached.

For the constant source approach, simulations were run for velocity sources of 0.5, 1, 1.5 and 2 in non-dimensional units. This was found to be representative of the range of flow of interest (0 to 1000 rpm). Correspondence in terms of Reynolds number or propeller speed is in table 4.4, with the two extreme propeller inputs 0.5 and 2 being equivalent to propeller speeds of 315 and 810.

It is of interest to compare these with a characteristic velocity scale derived from Nienow's [Nienow(1997)] estimation of the flow off the blades of a propeller. From the propeller discharge

$$Q = F_l N D^3$$

in $m^3 s^{-1}$, the velocity associated with the propeller can be estimated as

$$u_p = \frac{4Q}{\pi D^2} = \frac{4 F_l \mathrm{ND}}{\pi},$$

which corresponds to the division of Q by the propeller area. Globally, such an approach leads to characteristic velocities around two times higher than those obtained from propeller tuning. This is hardly surprising as the use of a constant source of momentum implies that a constant amount of energy is supplied to the system, whereas propeller stirring efficiency is related to the background velocity much more like the regulated source modelling of the propellers. As well, Nienow's approach is fully three-dimensional whereas this one is two-dimensional.

Table 4.3. Characteristics of the PTV data and non-dimensional equivalent propeller characteristic velocity derived from Nienow's [Nienow(1997)] estimation of the flow off the blades of a propeller.

rpm	u_0 $(m\,s^{-1})$	Re	u_* $(m\,s^{-1})$	$\overline{u_p}$
400	0.01415	1973	0.0058	2.52
500	0.01630	2273	0.0069	3.15
600	0.02023	2821	0.0077	3.78
750	0.02427	3384	0.0092	4.72

Table 4.4. Characteristics of the numerical simulations and their equivalent in rpm and friction velocity for the constant input propeller model.

Propeller input	$\bar{u_0}$	Re	rpm	u_* $(m\,s^{-1})$
0.5	0.145	1450	315	0.0046
1	0.173	1730	375	0.0055
1.5	0.259	2590	560	0.0074
2	0.374	3740	810	0.0098

The regulated source modelling of the propeller, which should be equivalent to forcing the flow through the propellers to be constant, was found to behave well at relatively low Reynolds numbers (Table 4.5) equivalent to the range of 0 to 250 rpm. For higher Reynolds numbers, the model became unstable, with high variations in the mean flow and no stabilisation of the mean flow energy. Proportionality was not maintained between propeller characteristic velocity and mean kinetic energy in the tank.

Table 4.5. Characteristics of the numerical simulations and their equivalent in rpm and friction velocity for the regulated input propeller model.

Propeller input	$\bar{u_0}$	Re	rpm	$u_* \ (m\,s^{-1})$
0.2	0.075	750	165	0.0023
0.4	0.085	850	185	0.0026
0.6	0.115	1150	250	0.0035
1	0.109	1090	235	0.0033
3	0.327	3270	705	0.0088
4	0.235	2350	505	0.0070

Besides their use in the estimation of a reference velocity scale in the tank, the kinetic energy records (Figure 4.10) confirm the turbulent nature of the flow in all the simulations. This can seem to be an insignificant observation but nevertheless, 2 dimensional and 3 dimensional turbulence are fundamentally different mechanisms. Therefore, transition to turbulence does not happen around the same Reynolds numbers for a 3-D problem and its 2-D equivalent (around 7402 in 2D [Peng et al.(2003)] and around 6000 in 3-D [Shankar and Deshpande(2000)]). Such observations have been made in the case of transition to turbulence in a lid-driven cavity problem, which presents many similarities with the tank problem.

Mean velocity field

Comparisons between both constant and regulated source models can only be made at low Reynolds numbers because of the inability of the regulated source model to come to a turbulent equilibrium state at high stirring rates.

The two scenarii that should be the closest are Figure 4.14-a-1 and 4.14-b-3 (375 and 250 rpm respectively). In both cases, mean flow patterns are not identical to those observed by PTV but do present similarities. The main recirculation on the right side of the tank is present in both cases but a second smaller eddy can also be observed in both. The main upward flow region is in both cases located near the left wall area. This upward flow is actually part of a developing main eddy of about the size of the tank, still slightly off-centred towards the left of the tank. In all cases, there is a small eddy in the bottom left corner. The main differences between PTV measurements and CFD lie in the central area of the slice where the forcing tank-size eddy replaces the two propeller-induced jets observed experimentally. This can also been observed in the kinetic energy plot where most of the mean kinetic energy is located within the downward and upward part of this mean eddy instead of being more spread out in the middle part of the slice.

For higher Reynolds numbers (constant velocity source approach) the main central eddy develops and becomes increasingly stronger, constraining the corner eddy to become smaller. Most of the mean kinetic energy is found in a ring located at the periphery of the main central eddy and going through the location of the right-hand propeller and passing between the left propeller and the left wall. The main eddy is rotating clockwise due to the asymmetrical disposition of the propellers, with the propeller the closest to the bottom (right) dominating the flow. Both propellers feed kinetic energy into the main ring, the right by inputting momentum in the ring and the left by exerting a sucking effect.

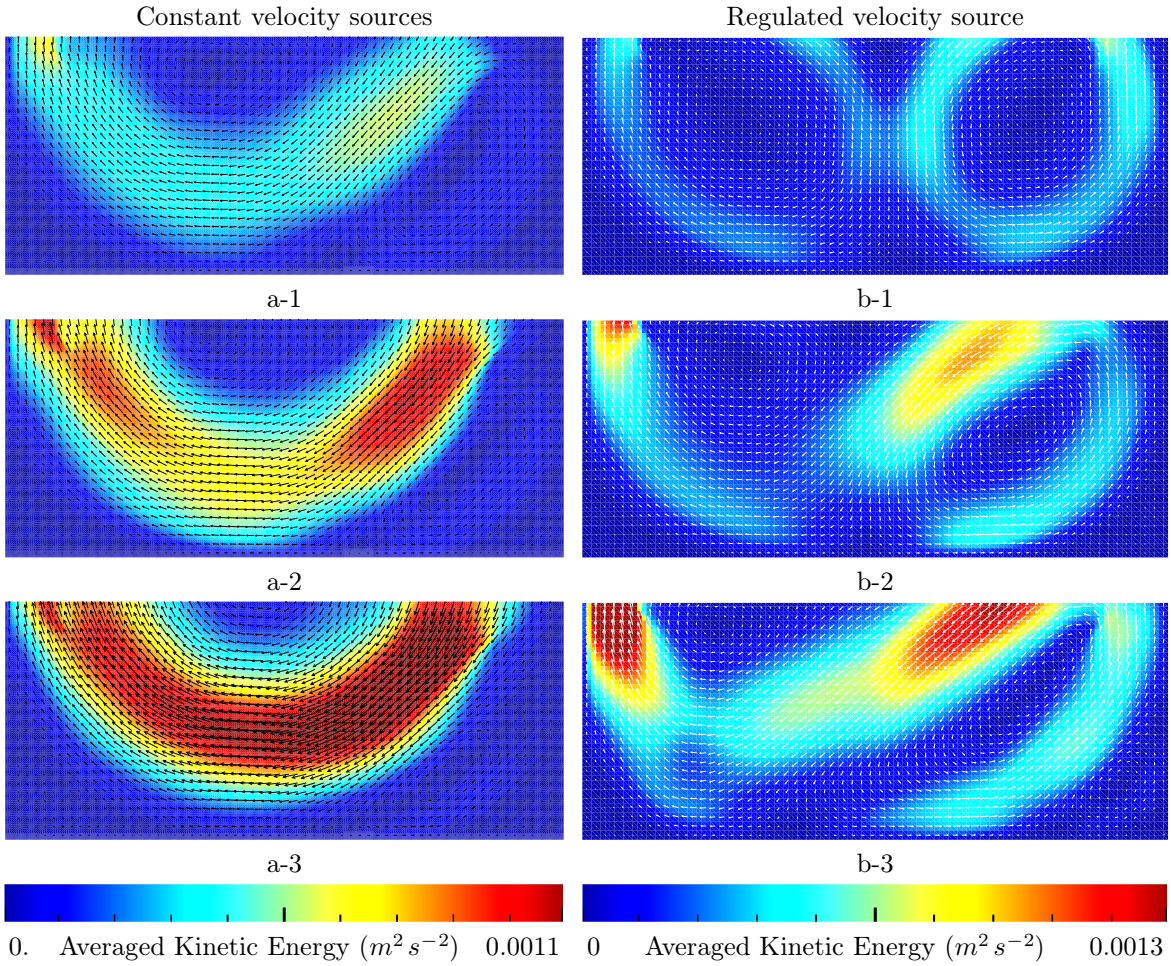

Figure 4.14. Plot of the mean velocity field and Kinetic energy. The left column plots are for propeller modelled as constant velocity source (rpm 375 (a-1), 560 (a-2) and 810 (a-3)). The right column plots are for propeller modelled as regulated velocity source (rpm 165 (b-1), 185 (b-2) and 250 (b-3)).

It is clear that there are significant differences between the tank dynamics from the model results and PTV measurements. These can be explained by even more fundamental reasons than the fact that the slice where the simulation is made should not contain the propellers. Figure 4.11 shows that the desired velocity field should be mainly directed downward and that most of

the energy is contained in the downward flow. This simple observation is incompatible with mass conservation, which imposes the sum of the upward fluxes to be equal to the sum of the downward ones for an incompressible fluid. This explains the ring observed at high propeller speed.

At low Reynolds numbers, the propeller discharge is not strong enough for any of the propellers to dictate the whole tank dynamics and two main eddies, each driven by one of the propellers, forms in the slice (Figure 4.14-b-1). When the propeller speed is increased, the asymmetry in propeller position becomes important and the right propeller shifts the whole flow towards the ring structure observed at high Reynolds numbers.

The formation of the central tank-size eddy also corresponds to transition to instability of the regulated source propeller model. When the main eddy forms, the mean flow around the left propeller should keep going upwards, which is opposite to the velocity imposed for the left propeller. Propeller feedback is then amplified to keep the local velocity at the desired value, and so on until the system becomes unstable.

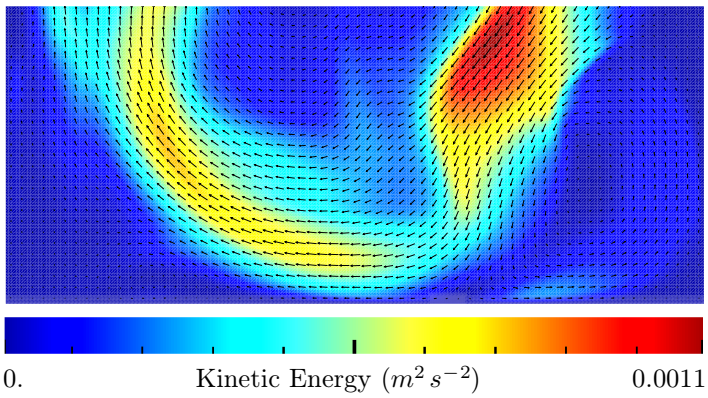

Figure 4.15. Plot of the instantaneous velocity field and Kinetic energy for propeller input of 2.

In conclusion, the dynamics of the slice is explicably different to what is observed in reality, although showing the same asymmetry and the right corner-eddy. This is nevertheless not related to the way propellers were modelled but rather to the two-dimensional nature of the model.

There appears to be very little difference between the two approaches to propeller modelling presented here at low Reynolds numbers. The unstable nature of the regulated source model makes it impossible to examine high Reynolds number scenarios and suggests it is not a good choice for three-dimensional modelling. From now, only the constant source approach is used to model the propellers.

Bottom shear-stress

Because it is known that the dynamics of the 2-D model is different to reality, it is of interest to examine the mean-bottom shear stress and more particularly the derived friction velocity to assess the calibration of the model.

Bottom friction is far from evenly distributed (Figure 4.16) with a clear maximum located where the tank-size eddy and the right corner eddy are tangential to the bottom (i.e., where the near-bottom flow is quasi-horizontal). This corresponds to the region where the settlement area was located.

For all simulations, a linear profile growing with the distance from the bottom can be observed for the mean velocity field. This confirms that the resolution used for the simulation is high enough and that boundary layers are properly resolved.

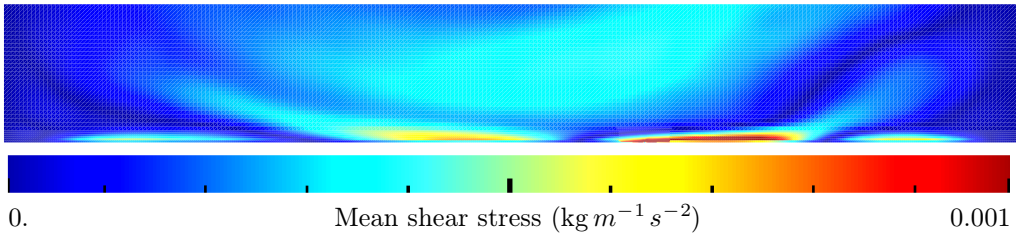

Figure 4.16. Mean shear stress distribution at the bottom of the tank for propeller input of 2.

The friction velocity at the bottom of the tank can be derived from the mean bottom stress velocity field using (See general introduction)

$$u_* = \mu_f \left(\frac{\partial \bar{u}}{\partial y} \right).$$

This was calculated in the settlement area and on average over the whole bottom (Table 4.6) leading to reasonably low mean friction velocities, about three times lower than the experimental ones in the settlement area. Only small variations of the mean bottom shear stress are observed, but the maximum of the bottom stress does increase with propeller speed.

Table 4.6. Friction velocity derived from the model with propellers as constant sources.

Propeller input	u_* in settlement area (mm s^{-1})	mean u_* (mm s^{-1})	max u_* (mm s^{-1})
0.5	1.3	0.8	1.6
1	2.2	1.1	2.5
1.5	2.0	1.1	2.3
2	2.7	1.3	3.0

Particle lift and drag

After calibration of the kinetic energy within the slice, a static solid propagule was added near the bottom of the tank at a place corresponding to the settlement area used in the tank experiments (Figure 4.17). Only one size of particle was tested in three different flow regimes (93 μm of diameter).

As expected, even when stirring is at its maximum, the flow around the particle remains laminar (Figure 4.17) and close to a Stokes flow around the particle.

Pressure and viscous forces on the propagule were calculated and added to get the drag and lift forces experienced by the particle.

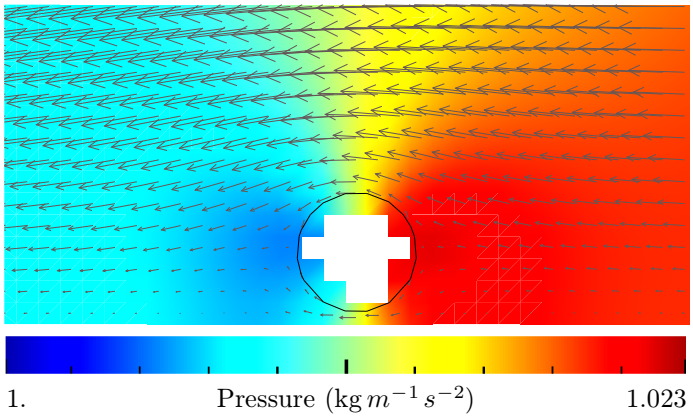

Figure 4.17. Velocity field around the particle (white area) with pressure field at the background for propeller input of 2.

Because they are derived from 2D simulations, hydrodynamical forces are representative of the force experienced by a cylinder of unit length and had to be rescaled to be consistent with the spherical shape of particles.

Furthermore, the turbulent nature of the flow implies large variations in drag and lift over time, and regular turbulent bursts are therefore experienced by the particle (Figures 4.18 and 4.19). Whereas a clear increase in the drag and lift is seen when the propeller speed is increased from 1, there is very little difference between 1.5 and 2. Shorter and more powerful bursts of turbulence occur at high propeller speeds.

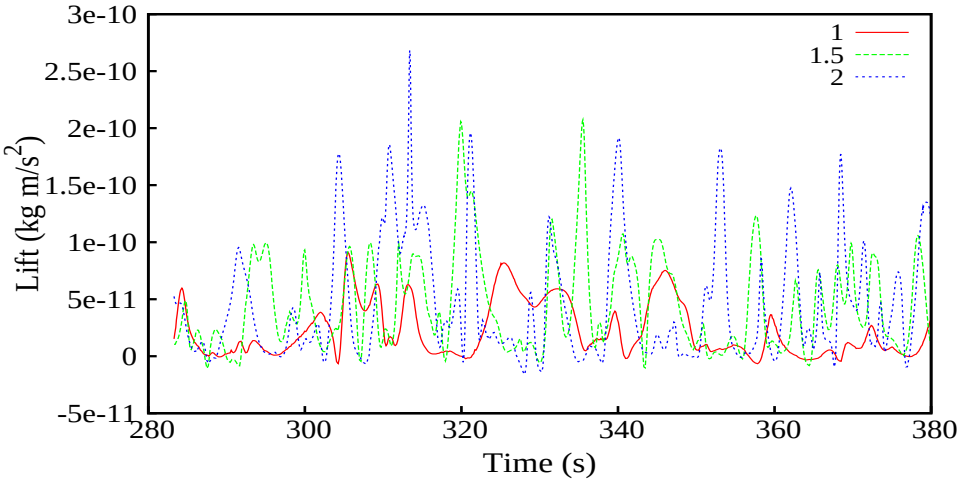

Figure 4.18. Lift force on the particle for propeller constant velocity sources of 1, 1.5 and 2.

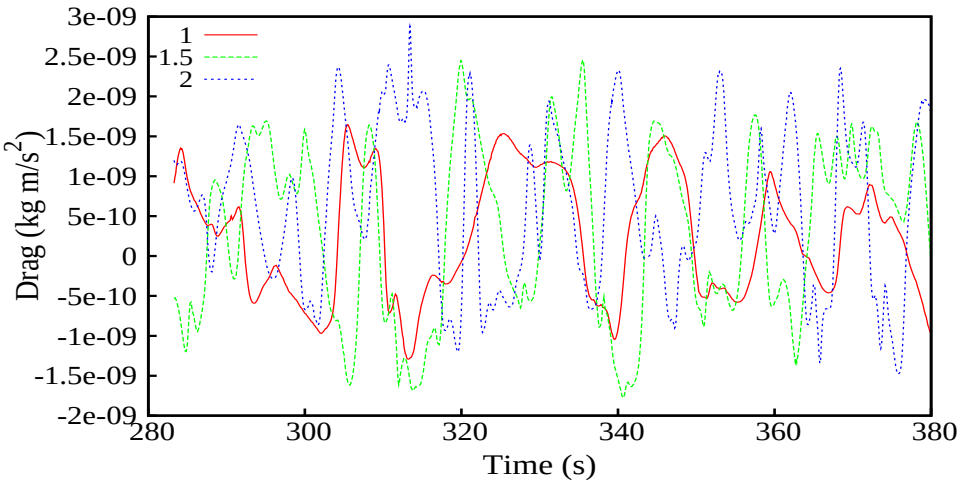

Figure 4.19. Drag force on the particle for propeller constant velocity sources of 1, 1.5 and 2.

Statistics on the drag and lift forces given by the model match those of the graphical observations, particularly showing very little difference between hydrodynamical forces for propeller velocity sources of 1.5 and 2 (Table 4.7). This can be explained by the proximity of the settlement area to a stagnation point.

Table 4.7. Statistics on particle drag and lift forces from the model in kg ms^{-2}.

Propeller input	Mean Drag	Mean Lift	Max Drag	Max Lift	Stdev Drag	Stdev Lift
0.5	3.15e-10	4.23e-12	8.98e-10	2.52e-11	1.80e-10	4.38e-12
1	6.72e-10	2.20e-11	1.61e-9	8.87e-11	3.96e-10	2.24e-11
1.5	9.71e-10	4.41e-11	2.40e-9	2.02e-10	5.11e-10	3.97e-11
2	9.48e-10	4.56e-11	2.81e-9	2.63e-10	6.29e-10	4.95e-11

Estimation of the mean drag and lift experienced by a solid spherical particle near a smooth wall can be found in the literature [Soltani and Ahmadi(2001)] [Burdick et al.(2001)] and used for comparison with the CFD model. In the case of a laminar flow (small particle Reynolds numbers), hydrodynamical forces can be expressed using a modified Stokes Law. The drag force, parallel to the substrate, in the streamwise direction [Burdick et al.(2001)] :

$$\boldsymbol{F}_d = 1.7009\,3\,\pi\,\mu\,d\,V_p = 2.5514\,\pi\rho\,d^2\,u_*^2$$

where V_p is the fluid velocity at the centre of the particle and μ is the fluid viscosity.

Similarly, the lift force, in the direction perpendicular to the attachment surface [Burdick et al.(2001)]

$$\boldsymbol{F}_l = 1.615\,\mu\,d^2\left(\frac{\rho}{\mu}\frac{d\,u}{d\,z}\bigg|_{z=d/2}\right)^{1/2} V_p = 0.8075\,\rho\,d^3\frac{u_*^3}{\nu}.$$

where ρ is the fluid density, u the fluid velocity parallel to the surface and z the direction

normal to the surface.

In the case of a near-wall turbulent flow, hydrodynamical forces can be expressed as a function of the friction velocity u_*. Soltani and Ahmadi [Soltani and Ahmadi(2001)] derived a model taking into account vortical motion in near-wall turbulence. This approach led to hydrodynamical forces slightly higher than those of models purely based on laminar viscous sublayer theory in turbulent flow. In that case, the drag force is given by

$$\boldsymbol{F}_d = \frac{2.9\,\pi\,\rho\,d^2\,u_*^2}{C}$$

where C is the Cunningham correction factor, which can be taken as equal to 1 for propagules of this size (See [Davies(1945)]).

Lift force and moment of surface stress are expressed as

$$\boldsymbol{F}_l = 0.975\,\rho\,\nu^2\left(\frac{d\,u_*}{\nu}\right)^3.$$

Globally, Stokes or turbulent lift and drag estimations from the friction velocity lead to drag and lift values much higher than those given by the model (Table 4.8).

Table 4.8. Estimation of the mean drag and lift from theoretical Stokes and turbulent formulas. The estimations are based on the friction velocity measured on the real tank.

Propeller input	Stokes drag ($\mathrm{kg\,m\,s^{-2}}$)	Turbulent drag ($\mathrm{kg\,m\,s^{-2}}$)	Stokes lift ($\mathrm{kg\,m\,s^{-2}}$)	Turbulent lift ($\mathrm{kg\,m\,s^{-2}}$)
0.5	1.71e-9	1.50e-9	7.79e-11	6.45e-11
1	2.46e-9	2.16e-9	1.34e-10	1.11e-10
1.5	4.45e-9	3.91e-9	3.27e-10	2.71e-10
2	7.80e-9	6.86e-9	7.60e-10	6.30e-10

The friction velocity corresponding to the drag and lift forces given by the model can be estimated from the ratio of mean lift to mean drag using the theoretical Stokes and turbulent formulas cited earlier.

From Stokes drag and lift,

$$u_* = 0.106409\,\frac{F_l}{F_d}$$

and from the turbulent drag

$$u_* = 0.1006175\frac{F_l}{F_d}$$

which leads to the friction velocities summarised in Table 4.9. Although the friction velocity is found to be roughly proportional to propeller speed for propeller velocity ranging from 0.5 to 1.5, less difference is found when propeller velocity is increased from 1.5 to 2. Again, the friction velocities estimated from the mean drag and lift experienced by the propagule are smaller than the ones expected from the PTV measurements. Nevertheless, these are close to the double of

those obtained from the bottom stress predicted by the model.

It can be considered that the relevant friction velocity for the model that should be compared to the "real" value is the one estimated from the drag/lift model. Indeed, the one derived from the bottom stress is derived from the mean velocity field and is likely to be as biased as the friction velocities derived from the logarithmic profile approach in Chapter 2. Conversely, the one obtained from the Stokes drag is a real measure of the mean intensity of the bottom stress.

Table 4.9. Friction velocity near the settlement area estimated from the theoretical models.

Propeller input	u_* from Stokes drag and lift (ms^{-1})	u_* from turbulent drag and lift (ms^{-1})
0.5	0.0014	0.0013
1	0.0035	0.0033
1.5	0.0048	0.0043
2	0.0051	0.0048

Drag and lift outputs are of interest because of the estimation of the amplitude of the removal forces they provide, but also because they show the frequency and the duration of their extremes. Both could be of importance in the context of propagule settlement. Although propagules can perform definitive attachment (thanks to the growth rhizoids) over time-scales much larger than the settlement experiments, it is possible that initial attachment requires a short period of relatively calm conditions near the substrate. The length of the hydrodynamical force extremes could be of importance depending on the properties of the mucilage. It can be thought that the mucilage has elastic properties and deforms first before breaking.

The outputs presented here are for a spherical propagule. Despite the importance of its adhesiveness properties, mucous is likely to induce a reduction of the hydrodynamical forces experienced by the propagules (Figure 4.20). This should be considered and would principally affect the norm of the detachment forces. Indeed, the frequency and duration of the peaks of drag and lift are related to the large-scale dynamics in the tank and therefore independent of the shape of the propagules.

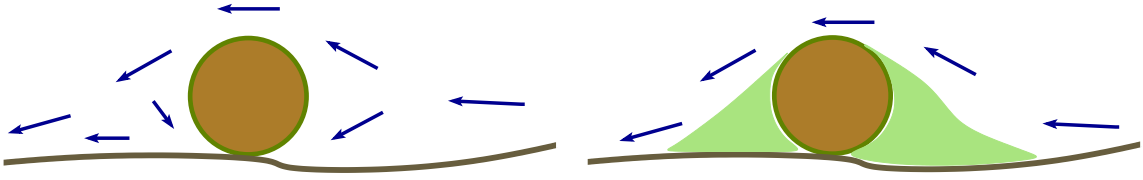

Figure 4.20. Mucilage could have a dramatic influence on the hydrodynamical forces experienced by the propagules.

Conclusions about the 2D model

The two-dimensional model presented here behaves well. The three-dimensional nature of the tank flow is mainly responsible for the lack of a satisfying correlation between measured data and the numerical model.

This section displays some of the possibilities offered by the Gerris Flow Solver:

- use of the adaptive mesh to resolve the dynamics around a 90 μm particle within a 14x14 cm tank;

- modelling of propellers as a velocity source;

- calculation of the hydrodynamical forces experienced by a solid object.

Estimations of the frictional velocity at the bottom of the tank by various means led to smaller values than those expected from experiments. This is somewhat surprising as the ring structure of the flow is *a priori* compatible with the friction velocity estimates obtained from Oldham et al.'s [Oldham et al.(2004)] circulation approach.

The non-appearance of the 3D circulation in the 2D model means it provides poor estimates of bottom friction. It does, however, provide an interesting perspective on the frequency and the magnitude of the lift and drag forces experienced by the propagules attached on their substrate.

4.4 Three-dimensional model

A single high-resolution run of the three-dimensional tank model was made using a standard Smagorinsky model. As it is a single run, it is not sought here to demonstrate any of the properties of the domain, but rather to briefly illustrate it.

The propellers are modelled as a constant source of velocity of magnitude 1, which from the slice-averaged kinetic-energy (Figure 4.21) should be equivalent to a propeller speed of around 220 rpm, which is much lower than what was obtained in 2D from a similar velocity input. In all cases, the flow here is fully turbulent.

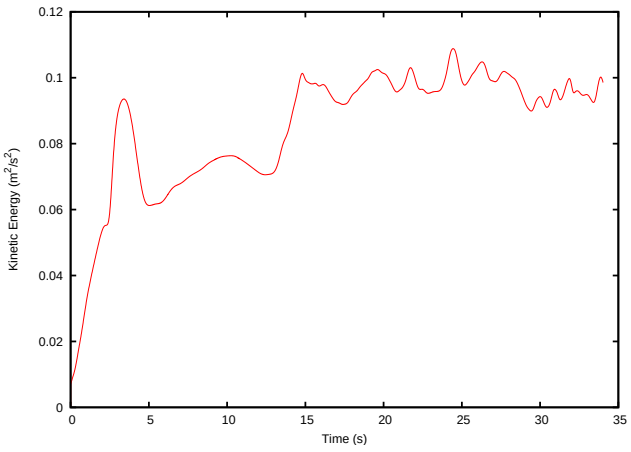

Figure 4.21. Evolution of the slice-averaged kinetic energy in the 3D tank with time.

The "central" slice of the tank is clearly dominated by the propeller discharge flow (Figure 4.22) with most of the kinetic energy located there. Strong interactions between both propellers can be observed near the bottom of the tank where small eddies are generated due to the presence of high velocity gradients. In contrast, the corners host much smaller velocities with almost no apparent coherent structures.

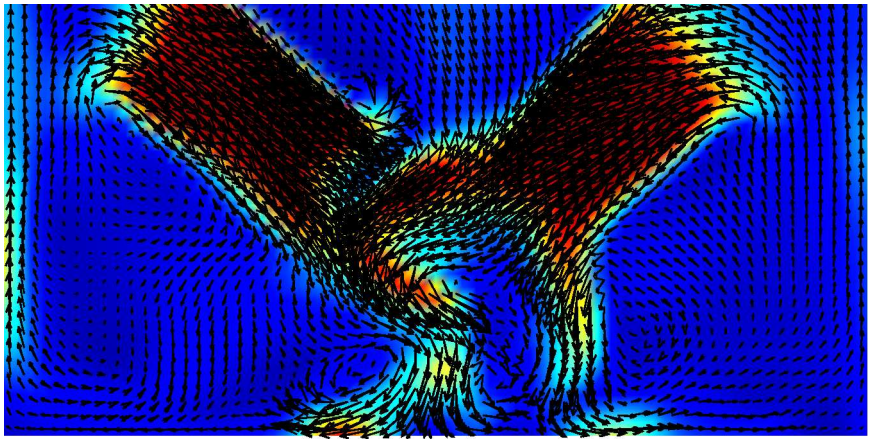

Figure 4.22. Instantaneous velocity (arrows) and kinetic energy (color) in the middle of the tank.

The mean velocity is surprisingly symmetrical (Figure 4.23). It is hardly possible to see any influence of propeller position on the mean velocity field. This results in two quasi-symmetrical eddies in each corner. A high level of kinetic energy can be observed at the bottom of the tank for the mean flow, which was not observable in the instantaneous plots. This does not mean that the flow at the bottom of the tank contains far more energy than the bulk flow. This is likely to show that the flow at the bottom is mainly in a single direction, whereas flow in the bulk of the tank (except for the propeller region) hosts more isotropic turbulence.

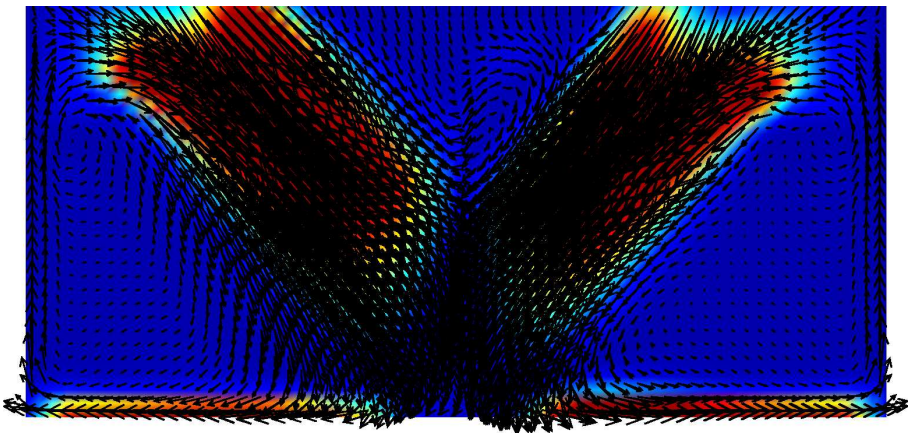

Figure 4.23. Averaged velocity (arrows) and kinetic energy (color) in the middle of the tank.

Propeller flow is hardly noticeable on the instantaneous velocity field in the slice of the tank where PTV measurements were made (Figure 4.24). The slice does not seem to host any stable large eddy (Figure 4.25). The global level of energy in the slice is far smaller than in the central slice where propellers are located. This is likely to show that despite the turbulent flow observed in the tank, the Reynolds number of the simulation is lower than the one estimated from the kinetic energy. This is likely to be caused by the high mean velocity found near the bottom of the tank.

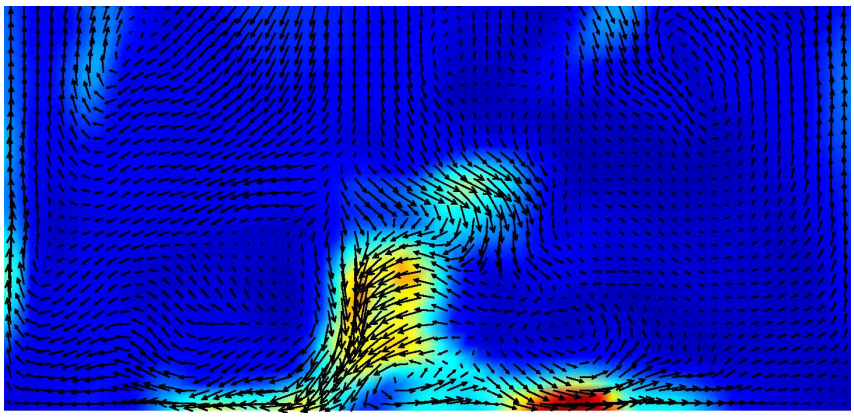

Figure 4.24. Instantaneous velocity (arrows) and kinetic energy (color) in the slice where PTV measurement were made.

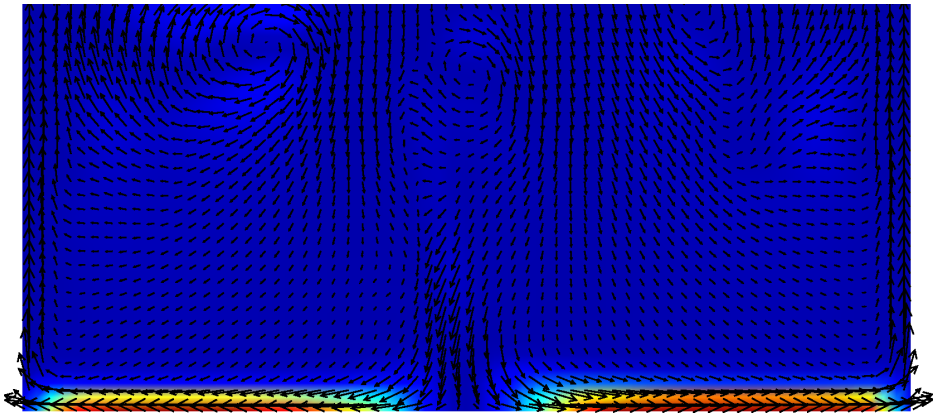

Figure 4.25. Averaged velocity (arrows) and kinetic energy (colours) in the slice where PTV measurement were made.

The instantaneous bottom shear stress can be extracted from the simulations (Figure 4.26). As observed in the lift and drag plots from the 2D model, the bottom shear stress is highly inhomogeneously distributed in time and in space. Most of the peaks in bottom shear stress seem to be located in the central area of the bottom, but nevertheless, high peaks can be seen closer to the tank wall.

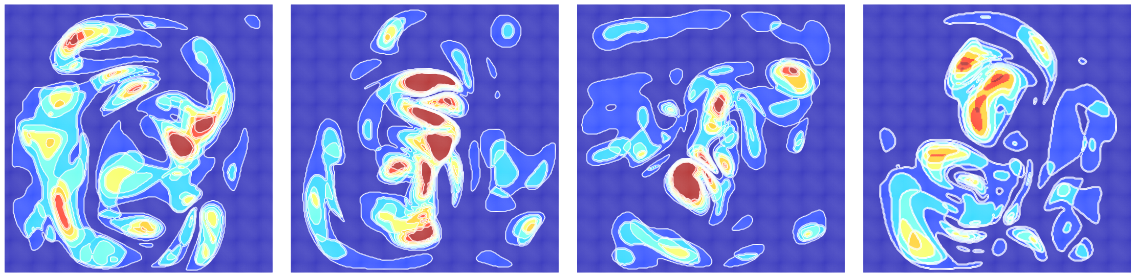

Figure 4.26. Instantaneous snapshots of the bottom shear stress at times 28, 30, 32, and 34 over the whole area of the tank (left to right).

Concerns remain about the large scale dynamics obtained from the 3D tank model. These can potentially be caused by the calibration method used here. Despite the limited number of runs realized in 3D, it would be worth changing the calibration method to adopt a propeller-oriented one as done by Yoon et al [Yoon et al.(2003)].

It is interesting to see that the mean velocity field obtained for very low Reynolds numbers (earlier in the chapter) is qualitatively much closer from the PTV observations than the present simulation. Beside the calibration method, the problem of turbulence modelling still needs to be tackled. The standard Smagorinsky model used here is known to be far too dissipative near walls which obviously are key to the tank flow. Despite the enhanced mesh refinement used to limit the influence of the subgrid-scale model in that area, it is possible that the Smagorinsky model still induces too much dissipation near walls resulting in the thicker boundary layers.

4.5 Summary

A model of the stirred tank using the Gerris Flow Solver was reported. A two-dimensional model was first set up to investigate possibilities of model calibration using a Reynolds number based on a velocity scale defined from the mean kinetic energy in the slice of interest. For an equivalent kinetic energy level, fundamentally different large scale dynamics were found. This was attributed mainly to the three-dimensional nature of the flow, leading to the conclusion that two-dimensional models are likely to be of limited use in describing the stirred tank. For an equivalent kinetic energy level, lower bottom stress was found.

The ability of the Gerris Flow Solver to handle multi-scale flows was demonstrated by inserting a propagule within the viscous boundary layer and outputting the hydrodynamical forces experienced by the propagule. The velocity profile around the propagule was found to be close to linear showing that the boundary layer was well-resolved. The influence of turbulence bursts on the propagule was clearly observed.

While the two-dimensional nature of the model limits the behaviour of the simulations, it would be of interest to consider a different way of calibrating the model. Successful propeller models have been found in the literature since the simulations were made; even though they have been designed for Rushton turbines, it would of interest to experiment with them.

A review of Large Eddy Simulation models made as a preamble to the three-dimensional model, highlighted the usefulness of the fairly recent Shear-Improved Smagorinsky model [Toschi et al.(2006)]. Like most of the improved-Smagorinsky models, the SISM incorporates information about the larger scales of the flow. The main difference between the most popular methods is that potentially the correction terms can be computed by time-averaging instead of spatial filtering, which makes the method far easier to implement and cheaper in terms of computation time.

It was decided to experiment with the SISM on the lid-driven cavity test for technical reasons as well as because of the similarities existing between cavity flow and stirred tank geometry and micro-cavities.

Parallelisation of the simulation over several runs on one of the NOTUR's computer clusters suggests there is much to be generated from this approach.

If parametrised well, the SISM could lead to good results in the case of flows with stable large-scale dynamics. This is not the case for stirred tanks and it is likely to be only a good alternative to the standard Smagorinsky model.

The development of the three-dimensional model has generated several possibilities and it is likely that in its actual state the model will be hard to calibrate because excessively demanding in terms of computational power. It would make sense to consider that the problem is symmetrical which would allow a reasonable reduction in the size of the problem. This would still be a problem, however, as the real tank is not symmetrical and the large-scale unsteady dynamics are likely to be very different.

Chapter 5
Numerical modelling of solid/fluid inter action

5.1 Introduction

Propagules are often viewed as Lagrangian particles, advected by a given velocity field. This way the flow is independent of particle motion and particles are carried by the flow like a tracer. This approach proves convenient for the study of dispersion of particles (e.g. [Lanzani and Tamponi(1995)] [Stohl et al.(1998)]), drifters (e.g. [Garraffo et al.(2001)]) or sediments (e.g. [Lane(2003)] [Gidhagen et al.(1989)]). The similarity between all these problems is that limited attention is given to the particles properties as most of the time the scales of motion are all far bigger than the scale of the particles themselves.

The problem of algae settlement on the rocky shore or in an experimental stirred tank, as stated earlier is a multi-scale problem. For many aspects of the problem, especially those which occur far enough away from the substrate, the use of Lagrangian particles is feasible.

For the last stage of the settlement, when the propagules approach the substrate and enter the boundary-layer, the dynamics of the propagule itself is of importance and the application of Lagrangian particle models become unsuitable. In that case, feedback from the propagules to the flow or a fully reciprocal fluid/solid interaction is desirable. The use of solid/fluid interaction models allows the capture of the hydrodynamics forces acting on the propagules more accurately than with drag and lift models where the forces are derived from a flow free of particles. Potentially, proper particle deformation models can be used at the same time allowing the representation of the propagules to go far beyond the diameter/density characterisation.

However important particle/flow interactions are at small scale, the dynamics of the background flow, derived from the flow at larger scales remains of great importance. The study at the propagule scales is of great interest, but being able to link the propagule scale to large scale parameters is even more useful. In that perspective, the use of a computational fluid dynamics code using adaptive mesh is an asset. This is even more important because unlike in the previous chapter where the geometry of the problem was well defined (tank with settlement area needing a better resolution), the modelling of "real particles" is even more ambitious as not only very small scales need to be resolved, but these regions of fine-scale resolution are moving. Adaptivity of the mesh in space and time offered by the Gerris Flow Solver is therefore a great asset for this problem. It was therefore decided to implement a solid/fluid interaction model in the Gerris Flow Solver.

5.1.1 Solid/Fluid interactions

Many problems in many domains (engineering [Murman et al.(2003)] [Aftosmis et al.(2000)], biomechanics [Peskin(1977)] [Peskin(1972)] [Wang and Fogelson(1999)]) involve moving solids or boundaries, and therefore numerous models have been developed to represent solid/fluid interaction in fluid dynamics codes. It is hard to sort these models into families in a clear and simple manner as several aspects of a solid/fluid interaction model can be key to the properties of the whole scheme. Depending on the main focus or novelty of each method, it is usually presented as belonging to a class of method named after the way the grid, interface tracking, interface/fluid interaction or equations discretisation are treated. Therefore each scheme usually belongs to several families of methods.

Importance of the grid

The nature of the mesh is a key point for solid/fluid interaction as it is directly related to the way the solid objects are represented. Three types of grids can be found: conforming, non conforming and hybrids (see Figure 5.1).

Conforming grids (Figure 5.1-a) fit the solid object, allowing a precise discretisation of the fluid domain. This implies that at each time-step, when the position of the solid object changes, the mesh or at least part of it has to be regenerated to follow it. The main advantage is that the solid boundaries coincide with the faces of the cells neighbouring the solid object. Separation between solid and fluid is well defined and the Navier-Stokes equations can be discretised on the grid in the same manner as when no moving boundary is involved.

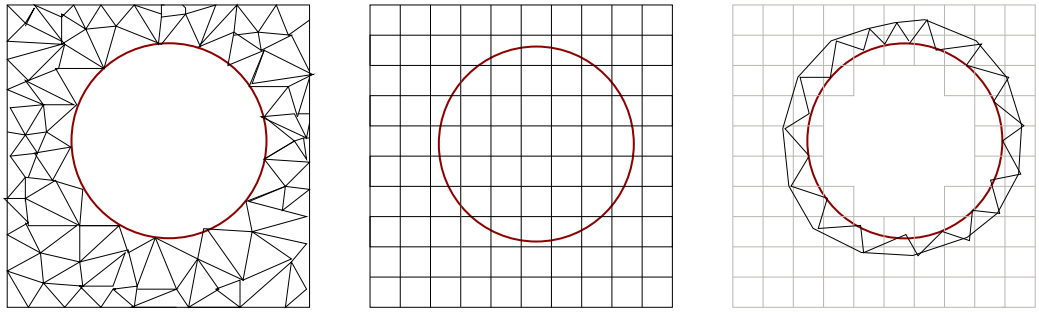

(a) (b) (c)

Figure 5.1. From left to right illustration of conforming, non-conforming and hybrid grids with a cylindrical solid object.

Non-conforming grids are typically structured grids (Cartesian grids for example). The grid does not change in time and has no reason to be suited to the shape of the boundary. Boundary and interface are completely independent. It that case, the distinction between fluid and solid domains is not as clear as for conforming grids as the cells crossed by the solid interface are partly fluid and partly solid. Consequently the discretisation of the equations near the interface has to be adapted to the way the solid boundary intersects with the grid. Besides that, very little work on the mesh is needed.

Hybrid methods, like Delanaye et al.'s hybrid-Cartesian grid method [Delanaye et al.(1999)] are more marginal and involve two coupled meshes. A thin conforming mesh surrounds the solid boundary while the whole fluid domain is discretised on a structured grid. The moving boundary conditions are applied on the fitting grid and then propagated to the whole fluid domain through the coupling between the two grids. In that case mesh and boundary fit well together, and very little mesh has to be updated when the object moves. Most of the difficulties lie in the implementation of the coupling between both grids.

With its quadtree/octree structure the Gerris Flow Solver is clearly part of the non-conforming grid codes. Implementing a hybrid method in Gerris would be possible but is not a first choice as the quadtree/octree grid is one of the specificities of the code.

Interface tracking

Closely related to the choice of the mesh is the representation and tracking of the interface.

Three main categories of interface tracking methods exist [Singha and Shy(2007)]:

- Lagrangian methods for which the fluid equations are discretised on a grid that adapts to the position of the moving interface. They are body-fitted grid approaches with the interface as boundary.

- Eulerian methods: the interface and fluid are defined on the same stationary grid. The interface is therefore defined implicitly. Eulerian methods include the volume of fluid or level-set approaches.

- Eulerian-Lagrangian methods like the front-tracking approach track the interface using a set of markers moving passively on a stationary grid.

A volume of fluid method (VOF) is already implemented in Gerris to deal with fluid-fluid interfaces but does not use the GTS library dedicated to the representation of the solid objects as triangulated surfaces.

My approach falls into the Eulerian-Lagrangian method category with, as for Singh et al. [Singha and Shy(2007)], the solid interface represented as a triangulated surface and the Navier-Stokes equations solved on a fixed quadtree/octree grid. The main difference with this method is that solid objects are seen as rigid solid objects, and therefore each solid object is treated as a single entity and not as a cloud of triangle nodes.

Interface interaction with the fluid

For Eulerian-Lagrangian methods, several approaches exist when it comes to dealing with the action of a moving interfaces. Some codes treat boundaries as membranes, others as proper solid boundaries with Dirichlet boundary conditions. The main difference between these two approaches is that, in the first case (membrane) both fluid and solid domains are discretised on the same grid and the solid object is represented as an interface separating the two phases. In the second approach, only the fluid domain is discretised and the solid objects appear as boundaries of the fluid domain.

Among codes based on conforming or hybrid grids this second method makes the most sense as the solid interface already matches the grid. For non-conforming grid codes like the Gerris Flow Solver, membrane methods are the most common option. These methods are among the most popular ones and have been used extensively in the past. In membrane methods, the solid interface is generally represented by a set of Lagrangian points. The no-slip boundary condition on the solid surface is then enforced in the fluid equation through a set of boundary forces. The two major approaches for membranes are the Immersed Boundary method (IB) of Peskin [Peskin(1972)] [Peskin(2002)] and the Immersed Interface (II) method of Leveque and Li [Leveque and Li(1994)] [Leveque and Li(1997)].

For both IB and II methods the analytical problem's formulation is the same. The incompressible Navier-Stokes,

$$\begin{aligned} &\rho\left(\frac{\partial}{\partial t}\boldsymbol{u}+\boldsymbol{u}.\nabla\boldsymbol{u}\right)=-\nabla p+\mu\,\Delta\boldsymbol{u}+\boldsymbol{F} \\ &\nabla.\boldsymbol{u}=0 \end{aligned},$$

with boundary conditions,

$$\boldsymbol{u}|_{\partial\Omega(t)} = \boldsymbol{u}_b,$$

on the outer boundary of the domain are solved on the whole (solid+fluid) domain. The solid interface only appears through the solid force $\boldsymbol{F}$. The solid interface force, $\boldsymbol{F}$, is a singular force linked to the force strength of the membrane in curvilinear coordinate $\boldsymbol{f}(s,t)$ by

$$\boldsymbol{F}(\boldsymbol{x},t) = \int_{\Gamma(t)} \boldsymbol{f}(s,t)\,\delta(\boldsymbol{x}-\boldsymbol{X}(s,t))\,\mathrm{ds} \tag{5.1}$$

where $\boldsymbol{X}(s,t)$ is the arc-length parametrisation of the solid interface $\Gamma(t)$ and δ the Dirac distribution. The motion of the membrane is linked to the fluid's velocity field by the motion equation

$$\frac{\partial}{\partial t}\boldsymbol{X}(s,t) = \boldsymbol{u}(\boldsymbol{X},t) = \int_{\Omega(t)} \boldsymbol{u}(\boldsymbol{x},t)\,\delta(\boldsymbol{x}-\boldsymbol{X}(s,t))\,d\boldsymbol{x}.$$

The difference between immersed boundary and immersed interface methods lies in the way the solid forces term of the Navier-Stokes equations, $\boldsymbol{F}$, is discretised.

In the IB method the interface is smoothed out and the solid interface force is applied as a volume force term. This is equivalent to adding a source term to the Navier-Stokes equations. This artificial thickening of the interface prevents the method from being more than first order and requires the use of small time-steps [Le et al.(2006)]. Nevertheless, this approach has been very popular with many variants developed since the original paper of Peskin [Mittal and Iaccarino(2005)]. Among them, the feedback force method from Goldstein et al. [Goldstein et al.(1993)] and the direct-forcing one by Mohd-Yusof [Mohd-Yusof(1996)] improves the IB method by offering the possibility to impose the motion of the solid objects (by opposition to a solid object carried by the flow). Overall, the main reasons for such a success of the immersed boundary method is its ability to deal with complex boundaries and its simplicity of implementation [Le et al.(2006)].

The II method is more complex to implement as the interface forces are incorporated straight into the discretisation of the Navier-Stokes equations as "jump conditions" on the velocity, velocity derivatives, pressure and pressure derivatives across the interface. This way the surface nature of the interface forces is respected. As well as the IB method, the immersed interface method has been extensively used and from its original formulation for elliptic equations has been extended to Stokes flows [Leveque and Li(1997)] and Navier-Stokes equations [Lee(2003)] [Li and Lai(2001)] [Li and Wang(2003)]. It is reported to be second order accurate in time [Le et al.(2006)] and deal successfully with complex geometries.

An other approach is that of Udaykumar et al. [Udaykumar et al.(2001)] [Ye et al.(1999)] which does not treat solid objects as a forcing term in the Navier-Stokes equations. Udaykumar et al. have implemented moving boundaries in a code using a conservative finite-volume formulation. At each time step, the intersection of the solid surface with the Cartesian grid is reshaped into body-fitted trapezoidal shape control volumes. Solid fluxes are computed and added to the control-volumes according to solid boundary displacement. That way the solid interface is represented by the changes of shape of the mesh and the computed solid fluxes. Their method belongs to the Cartesian cut-cell approaches. The formulation of the Navier-Stokes equations for this method is

$$\begin{array}{l} \rho\left(\dfrac{\partial}{\partial t}\boldsymbol{u}+\boldsymbol{u}.\nabla\boldsymbol{u}\right)=-\nabla p+\mu\,\Delta\boldsymbol{u} \\ \nabla.\boldsymbol{u}=0 \end{array},$$

with for boundary conditions,

$$\begin{array}{l} \boldsymbol{u}|_{\partial\Omega(t)}=\boldsymbol{u}_b \\ \boldsymbol{u}|_{\Gamma(t)}=\boldsymbol{u}_s \end{array},$$

where $\boldsymbol{u}_s$ is the velocity of the solid. Here, solid boundaries only appear as boundary conditions and in the fact that the domain $\Omega(t)$ is time dependent.

The main drawback of this method is that many configurations have to be taken into account regarding the geometry of the control-volume and therefore the fluxes calculation due to the different possibilities of mesh/solid interface intersection. Nevertheless, good results have been obtained with second order convergence.

Despite not being able to deal with moving objects, the static version of the Gerris Flow Solver can already deal with embedded static solid objects [Popinet(2003)]. Theses objects are triangulated surfaces (GTS surfaces from the Gnu Triangulated Surface Library) and the intersections between mesh and surfaces are dealt with using functions from the GTS Library [Popinet(1999)]. As most of the routines needed to intersect mesh and solid interfaces are already available, the most natural approach for the implementation of moving boundaries in Gerris is the Cartesian cut cell approach close to the one by Udaykumar at al. [Udaykumar et al.(2001)] [Ye et al.(1999)].

Conservative Finite-volume formulation

The main argument for the use of the Cartesian cut-cell approach is that it is well-suited for finite-volume formulation of the Navier-Stokes equations and therefore adapted to the implementation of a fully conservative method. Immersed boundary methods have been used as well with finite volume codes but techniques like mass sources/sinks [Kim et al.(2001)] had to be used to ensure exact mass conservation near the interface. Additionally, the static version of the Gerris Flow Solver already uses control-volumes restructuring near solid interfaces [Quirk(1994)] [Popinet(2003)]. which only needs to be adapted to moving boundaries.

Because of its complexity of implementation due to the numerous geometrical configurations that have to be taken into account, finite-element or finite-difference methods have for a long time been preferred to finite-volume ones for incompressible Navier-Stokes solvers with Lagrangian-Eulerian moving solid boundaries.

Several implementations for compressible fluids [Lesoinne and Farhat(1996)] [Wang and Bayyuk(1998)] or magneto-hydrodynamics equations [Tan(2007)] can be found in the literature, but Udaykumar et al. [Udaykumar et al.(1996)] and Ye et al. [Ye et al.(1999)] provide the only finite-volume solid moving boundary code for the two-dimensional incompressible Navier-Stokes I am aware of published before 2000.

Recently, several solid/fluid interaction models based on finite-volume methods were reported (e.g. [Taira and Colonius(2007)] [Choi et al.(2007)] [Kim et al.(2001)] [Wu and Wang(2007)]), but none of them is fully conservative. Efforts have been made to alleviate the computationally expensive nature of the Cartesian cut-cell approach by adapting the IB approach to finite-volume formulation (e.g. [Kim et al.(2001)] [Choi et al.(2007)] [Singha and Shy(2007)]).

This work is the first conservative implementation of a finite-volume Cartesian cut-cell solid/fluid interaction model with quadtree/octree adaptive refinement. As well, the method works in both 2D and 3D, which makes it unique.

5.1.2 The Gerris Flow Solver

The Gerris Flow Solver is an open source finite volume code that solves the incompressible Navier-Stokes equations. One of the main features of the Gerris Flow Solver is the use of a quadtree/octree adaptive mesh with velocity and pressure collocated at the centre of the cells.

The different numerical schemes used by the Gerris Flow Solver are given in the development of a time-step:

- Prediction of the face-centred (MAC) velocities at time $t^{n+1/2}$ using a Godunov type scheme:

$$u_d^{\star,n+1/2} = u^n + \left[\frac{\Delta x}{2} - \frac{\Delta t}{2} v_d^n\right] \partial_d u^n - \frac{\Delta t}{2}\, v_{\perp d}^n\, \partial_{\perp d}\, u^n - \frac{\Delta t}{2} \nabla p^n$$

  where $u_d^{\star,n+1/2}$ is the predicted face velocity field at time $t^{n+1/2}$, $(u^n,\ v^n)$ is the cell-centred velocity field at time t^n, (u_d^n, v_d^n) is the face-centred velocity field at time t^n for a face of direction d, p^n the centred pressure field at time t^n, $\perp d$ is the direction perpendicular to d, Δx is the size of the cell and Δt the time-step. A simple upwind criteria is then used to select the face velocity [Popinet(2003)].

- Projection of the MAC velocities on the divergence-free space. Using the Hodge decomposition, the predicted velocity field $u^{\star,n+1/2}$ can be decomposed in a divergence-free component $u^{\star\star}$ and a correction term $\nabla\phi$, which is computed by solving the Poisson equation

$$\nabla.\boldsymbol{u}^\star = \nabla.(\nabla\phi).$$

  The Poisson equation is solved using a multi-grid Poisson solver.

- Calculation of advection fluxes using the corrected face-velocities $u_d^{\star\star,n+1/2}$.

$$\int_t^{t+\Delta t} \int_{\Omega(t)} \boldsymbol{u}.\nabla\boldsymbol{u}\,\mathrm{dv}\,\mathrm{dt} = \sum_d \boldsymbol{u}_d^{\star\star,n+1/2}\,(\boldsymbol{u}_d^{\star\star,n+1/2}.\boldsymbol{n}_d)$$

  where n_d is the normal to the cell face in direction d.

- Calculation and addition of the diffusion fluxes using a semi-implicit Crank-Nicholson type scheme:

$$\frac{\boldsymbol{u}^{n+1} - u^{\star\star}}{\Delta t} = (1-\beta)\big(\nabla.\big(\nabla\boldsymbol{u} + \nabla^T\boldsymbol{u}\big)\big)^n + \beta\big(\nabla.\big(\nabla\boldsymbol{u} + \nabla^T\boldsymbol{u}\big)\big)^{n+1}$$

  where β controls the implicitness of the scheme. The default value is 0.5 for a semi-implicit scheme. An Helmholtz equation is solved using multi-grid-acceleration.

- Mesh adaptation. The mesh is refined and/or coarsened locally depending on the adaptivity criteria. The new cells are initialised by interpolation of the existing ones.

- Approximate projection of the face-centred velocity field obtained by interpolation of the centred velocities. The corrections calculated by solving a Poisson equation with the multi-grid solver are applied on the centred velocity field.

5.1.3 Notations

a streamwise distance from cylinder to centre of one of the wake's vortices

b distance between the centre of both wake vortices

d cylinder diameter

$_d$ direction

f vortex shedding frequency

l wake length

$\boldsymbol{n}$ normal to the boundary

p pressure field

t the time

$\boldsymbol{u}$ velocity field

$\boldsymbol{u}^*$ predicted velocity field

$\boldsymbol{u}^{**}$ corrected velocity field

u_d normal velocity on the direction d face of a cell

t^n time at the beginning of a time-step

$t^{n+1/2}$ time at half the time-step

t^{n+1} time at the end of a time-step

C_d drag coefficient

C_l lift coefficient

D^n diffusion operator matrix at time t^n

Re Reynolds number

$\mathrm{S_d}^{\,\mathrm{n+1}}$ fluid surface of a cell face at time t^{n+1}

St Strouhal number

T tracer field

V^n fluid fraction of the control volume at the beginning of the time-step

V^{n+1} fluid fraction of the control volume at the end of the time-step

X spatial coordinates

$\delta(x)$ Dirac function

λ cylinder diameter to channel width ratio

ρ fluid density

μ fluid dynamic viscosity

Δt length of the time-step

Δx cell size

Φ correction term

$\Omega(t)$ control-volume

$\partial\,\Omega(t)$ control-volume boundary

$\partial\Omega_f(t)$ fluid part of the control volume boundary

$\partial\Omega_s(t)$ solid part of the control volume boundary

∇ the nabla operator

^{T} transposition operator

$\frac{\partial}{\partial n}$ normal derivative

5.2 Mesh update

The first step in the implementation of moving boundaries in the Gerris Flow Solver is to adapt the mesh to moving objects.

The Gerris Flow Solver is based on a Quadtree/Octree adaptive mesh [Popinet(2003)] [Khokhlov(1998)] (Figure 5.2). The Quadtree architecture is based on a square root-cell of level 0 which includes the whole domain. The square root-cell is recursively refined following criteria imposed by the user until the desired mesh is obtained. The number of subdivisions realised to get to the size of a cell is called the level of the cell (the size of a cell is therefore $1/2^{\text{level}}$).

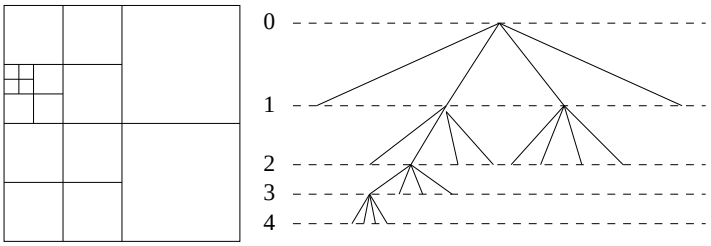

Figure 5.2. Illustration of a quadtree mesh and its tree representation.

Figure 5.3 shows a quadtree mesh around a circular solid with high refinement near the boundary and low refinement further away. This picture illustrates the use of spatial adaptivity with quadtree meshes. More importantly, this shows that the mesh only exists in the fluid regions of the domain; in the solid region all the cells have been destroyed. Only the cells adjacent to the solid (containing the solid interface) are not completely filled with fluid (from now on called mixed-cells).

Figure 5.3 shows a mesh at its the highest possible resolution. When going up in the quadtree, the resolution becomes coarser and more and more solid is then contained in the boundary cells, until the root cell is reached which includes the whole solid object. For this reason, even if the solid cells do not exist it is still potentially possible to refine the quadtree mesh to create a cell of any size smaller than the solid anywhere in the solid.

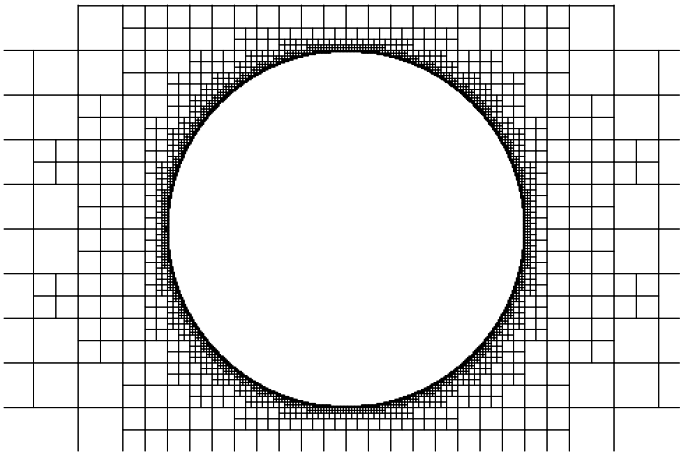

Figure 5.3. Quadtree adaptive mesh around a circular solid.

Moving objects imply moving interfaces. Pieces of interface are then moving out of mixed cells (which become a fluid cell) to go in the solid domain, and the original mixed-cell becomes a fully fluid cell. Furthermore, pieces of interface move from being mixed cells to a fully fluid cell, the first one becoming part of the solid and the second one becoming a mixed cell. When a piece of interface moves into the solid, the quadtree has to be refined in order to transform this part of the solid domain into a new mixed cell (or just new cell - see figure 5.4). When a mixed cell is cleared of the interface and becomes part of the solid, then the cell has to be destroyed (Figure 5.4).

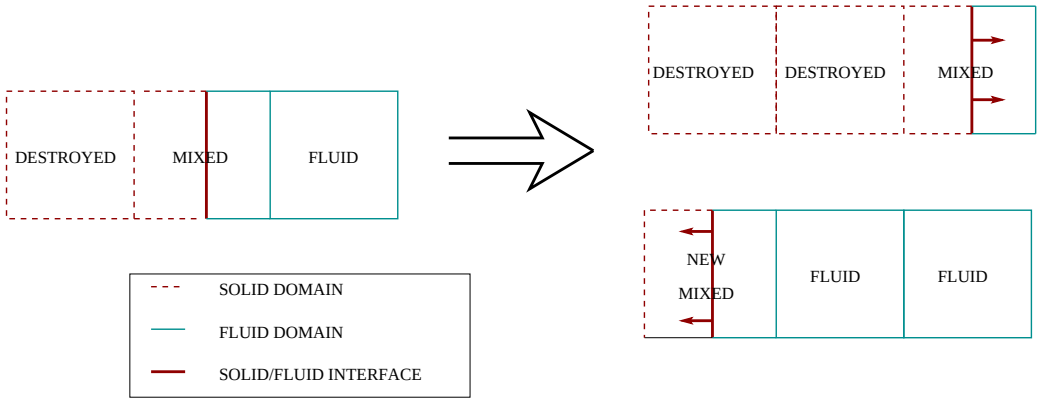

Figure 5.4. Depending on the direction the solid/fluid interface is moving, cells have to be destroyed or new cells created.

The constant creation and destruction of cells are the two main consequences on the mesh imposed by the presence of moving boundary. Ensuring that interface refinement is achieved is of secondary importance.

5.2.1 General algorithm

In the static-boundaries version of Gerris, the quadtree mesh is generated once at the beginning of the simulation. The mesh is generated from the root to the highest level of refinement using the refinement criteria defined in the parameter file, for example the distance to an interface. Then solid boundaries are intersected with the mesh and the solid fraction and face fractions are calculated for all the mixed cells. Finally, all the solid cells are marked and destroyed, then the simulation can start.

After this point, the mesh will still change but only through the adaptivity routines and only within the fluid domain. The solid interface is not re-meshed during the simulation.

For moving boundaries, as the solid and fluid domains are not static anymore, parts of the mesh-generation routines have to be employed during the simulation. At each time-step the interface is moved. Then, starting from the root of the quadtree, all the cells that are intersecting with the solid surface are traversed. If they are conveniently refined then nothing changes. If they need to be further refined and cells to be created then this can be done using the standard mesh refinement routines. After creating the new cells, the solid fractions are reinitialised and the solid cells are marked and destroyed as previously explained.

Two more fundamental questions have to be taken into account when creating or destroying cells. When a cell is destroyed, it still contains some fluid that is supposed to leave this cell within the time-step, which therefore has to be redistributed. The initialisation of the new cells is the second problem.

5.2.2 Redistribution of the destroyed-cells content

Cells that get destroyed during solid boundary motion need the momentum and tracer quantities they contain to be kept within the fluid domain. These quantities have to be redistributed to neighbouring cells to ensure full conservation of mass and tracers. The quantities are part of the solid advection flux that will be introduced later on.

As part of the advection-scheme, a cell-merging algorithm ensures that each mixed cell whose fluid fraction is smaller than 0.5 is merged to one of its neighbours [Quirk(1994)]. Advection fluxes are then treated together for both merged cells.

By imposing the right CFL condition, it is possible to ensure that any cell that gets destroyed is merged to another cell. As both cells are sharing their advection fluxes it is natural to redistribute the content of a cell that gets destroyed to the cell with which it is merged. This is done just before the cell gets destroyed.

As the changes of volume of the mixed cells has to be taken into account during the advection, the volume of the destroyed cell is added to the volume of its merging partner.

Volume and quantities have to be carefully dimensioned to take into account of the eventual difference of size between neighbours due to the adaptive mesh.

5.2.3 New fluid cells

When the structures of the new fluid cells have been created, the cell needs to be initialised properly.

The different quantities that have to be initialised are:

– Velocity: Two strategies can be used. One approach is to use an extrapolation of the velocity field higher in the quadtree to get an estimation of the velocity in the cell. The extrapolation is the same as the one used to initialise the new cells created when the mesh gets refined in the static-boundary code. The second approach is to set up the fluid velocity in the cell to the velocity of the solid boundary intersecting with it.

  The choice of initialisation velocity is important for the precision of the scheme. Nevertheless, the choice of a random value would not result in a momentum leak or source (see tracer field). The main consequence of an inappropriate choice of this velocity would be a degradation of the pressure field through the correction (projection) of the velocity field.

  In the latest version of the code the initialising is done using the velocity of the solid boundary. Both approaches have their legitimacy. As the solid interface is moving in the fluid towards solid direction an extrapolation of the velocity field at time t^n would be appropriate as the velocity field would be estimated from upwind information. The use of the velocity of the solid remains nevertheless the first choice solution given the no-slip boundary condition generally applied on the solid boundary.

– Pressure: Pressure is different from the other variables as it is not a conserved quantity. Pressure cannot be defined from a boundary value and has to be initialised from the existing pressure field. The initialising routine from the adaptive refinement toolbox is used to set the pressure field in a new cell.

– Tracer: As for momentum, local conservation is ensured independently of the initialising value. This can be demonstrated by integration of the time-dependent advection equation for a tracer quantity T.

$$\int_t^{t+\Delta t} \int_{\Omega(t)} \frac{\partial T(X,t)}{\partial t} + \boldsymbol{u}(X,t).\nabla T(X,t)\,\mathrm{dv}\,\mathrm{dt} = 0,$$

leads to

$$V^{n+1}T^{n+1} = V^n T^n - \frac{1}{\Delta t}\int_t^{t+\Delta t}\int_{\Omega(t)} \boldsymbol{u}(x,t).\nabla T(X,t)\,\mathrm{dv}\,\mathrm{dt}, \tag{5.2}$$

where V^n (resp. V^{n+1}) is the cell volume at time t^n (resp. $t^{n+1} = t + \Delta t$). For any new cell, V^n is null (there is no fluid in the cell at time t^n). The tracer fluxes being locally conservative, conservation is independent of T^n.

The same interpolation routine as the one used for the pressure is used to initialise the tracer field.

– Old Fraction: Old_fraction is a variable used to store the value of the fluid fraction at the previous time-step. As the new cells were fully solid during the previous time step, the old fraction is set to 0.

5.3 Projection Scheme/Divergence

Now that the structural modifications of the code have been exposed, the implementation of moving solid boundaries in the Navier-Stokes solver is detailed in the next paragraphs.

The implementation is exposed in three parts. The most basic form of the equation,

$$\begin{cases} \dfrac{\partial \boldsymbol{u}}{\partial t}(X,t) = -\nabla p(X,t) \\ \nabla.\boldsymbol{u}(X,t) = 0 \end{cases} \tag{5.3}$$

is first treated while advection and diffusion schemes are detailed in separated paragraphs.

5.3.1 Local formulation

The incompressible Navier-Stokes equations are solved in Gerris using a classical fractional step projection method [Popinet(2003)] [Chorin(1968)] [Peyret and Taylor(1983)] [Brown et al.(2001)]. The velocity field is updated using the pressure field obtained through the reinforcement of the incompressibility constraint,

$$\nabla.\boldsymbol{u}(X,t) = 0,\ X \in \Omega(t), t \in [0;+\infty[\tag{5.4}$$

where $\boldsymbol{u}$ is the velocity field, $\Omega(t)$ is the fluid domain and t is time.

The incompressibility constraint is enforced twice per time step. First, the predicted MAC (face-centred) velocities are projected on the divergence-free space prior to an eventual momentum advection. The second projection is an approximate projection of the cell-centred velocity field at the end of the time step, before the advection of the tracers.

Both projections are made solving a Poisson equation with homogeneous Dirichlet boundary conditions. This Poisson equation is derived from the Hodge decomposition of the velocity field before projection. The velocity field before projection $\boldsymbol{u}^\star$ can be decomposed into a non-divergent part $\boldsymbol{u}$ plus a correction term $\nabla\Phi$

$$\boldsymbol{u}^\star(X,t) = \boldsymbol{u}(X,t) + \nabla\Phi(X,t) \tag{5.5}$$

with $\nabla.\boldsymbol{u}(X,t) = 0$ and $\boldsymbol{u}(X,t).\boldsymbol{n}(X,t) = 0$ on $\partial\Omega(t)$ the solid wall boundary of $\Omega(t)$. Taking the divergence of (5.5) we get the Poisson equation

$$\Delta\Phi(X,t) = \nabla.\boldsymbol{u}^\star(X,t) \tag{5.6}$$

with $\frac{\partial\Phi}{\partial n}(X,t) = \boldsymbol{u}^\star(X,t).\boldsymbol{n}(X,t)$ on $\partial\Omega(t)$ which is then solved using a multi-grid Poisson solver [Minion(1996)]. The non-divergent velocity field after correction is given by

$$\boldsymbol{u}(X,t) = \boldsymbol{u}^\star(X,t) - \nabla\Phi(X,t).$$

One of the properties of prediction-correction type schemes is that the correction term ϕ is more than only a correction to the velocity field. It is the pressure as well [Popinet(2003)]. That way, velocity and pressure are implicitly coupled.

Solving equation 5.3 resides therefore mainly in the resolution of the Poisson problem that ensures that the velocity field remains non-divergent.

5.3.2 Integral formulation

The Poisson equation (5.6) with homogeneous Dirichlet boundary conditions is solved using the multi-grid Poisson solver implemented in the Gerris Flow Solver. The finite-volume formulation of the problem is obtained through integration of the Poisson equation (5.6) over all the control-volumes of the domain:

$$\int_t^{t+\Delta t}\int_{\Omega(t)} \Delta\Phi(X,t)\,\mathrm{dv}\,\mathrm{dt} = \int_t^{t+\Delta t}\int_{\Omega(t)} \nabla.\boldsymbol{u}^\star(X,t)\,\mathrm{dv}\,\mathrm{dt}, \tag{5.7}$$

where $\Omega(t)$ is a control-volume.

As Gerris is based on a quad-tree/oct-tree mesh, a control-volume, $\Omega(t)$ is typically a square/cubic cell eventually intersected by one or several solid boundaries. $\partial\Omega(t)$, the boundary of the control volume is made of fluid (connections with another control volume) and solid parts (intersection with a static or moving solid- see figure 5.5). $\partial\Omega_f(t)$ refers to the fluid part of the control volume boundary and $\partial\Omega_s(t)$ to its solid part.

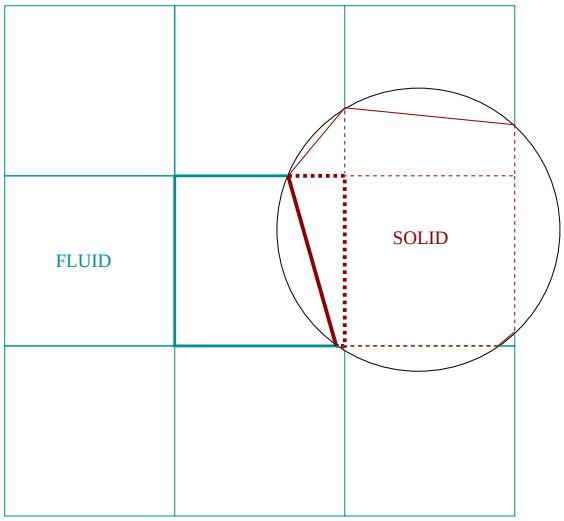

Figure 5.5. Control volume with a boundary made of a fluid part $\partial\Omega_f$ in light blue and a solid part $\partial\Omega_s$ in dark red.

When working with solid moving boundaries, only the right hand-side of the Poisson equation (5.7) is different to the static boundary formulation. The integral of the right hand side of equation (5.6) over a control volume in space $\Omega(t)$ and time [t ; t + Δt],

$$\int_t^{t+\Delta t}\int_{\Omega(t)} \nabla.\boldsymbol{u}^\star(X,t)\,\mathrm{dv}\,\mathrm{dt}$$

can be formulated in terms of fluxes using Gauss-Ostrogradsky's theorem [Arfken(1985)]:

$$\int_t^{t+\Delta t}\int_{\Omega(t)} \nabla.\boldsymbol{u}^\star(X,t)\,\mathrm{dv}\,\mathrm{dt} = \int_t^{t+\Delta t}\int_{\partial\Omega(t)} \boldsymbol{u}^\star(X,n).\boldsymbol{n}(X,t)\,\mathrm{ds}\,\mathrm{dt}.$$

$\partial\Omega(t)$ is then decomposed in its solid and fluid parts, respectively $\partial\Omega_s(t)$ and $\partial\Omega_f(t)$,

$$= \int_t^{t+\Delta t}\int_{\partial\Omega_f(t)} \boldsymbol{u}^\star(X,n).\boldsymbol{n}(X,t)\,\mathrm{ds}\,\mathrm{dt} + \int_t^{t+\Delta t}\int_{\partial\Omega_s(t)} \boldsymbol{u}^\star(X,n).\boldsymbol{n}(X,t)\,\mathrm{ds}\,\mathrm{dt}.$$

When only dealing with static solid boundaries the $\partial\Omega_s(t)$ term is equal to 0, and $\partial\Omega_f(t)$is time independent for t in $[t; t + \Delta t]$. The implementation of solid moving boundary conditions in the projection algorithm requires the addition of the « solid flux » term to the right hand side of the equation and to take into account the change of shape of the control volume.

5.3.3 Numerical scheme

The Gerris Flow Solver was originally designed to deal only with static solid boundaries, so there was no solid flux to take into account in the calculation of the divergence. Therefore, the integral of the fluid fluxes over the fluid boundary of the control volume was discretised as the sum of the products of the normal component of the velocities on the faces times the fluid surface fraction on the face (Figure 5.6-1):

$$\int_t^{t+\Delta t}\int_{\Omega(t)} \nabla.\boldsymbol{u}^\star(X,t)\,\mathrm{dv}\,\mathrm{dt} = \int_t^{t+\Delta t}\int_{\Omega_f(t)} \nabla.\boldsymbol{u}^\star(X,t)\,\mathrm{dv}\,\mathrm{dt} = \Delta t\sum_d S_d\,u_d^\star \tag{5.8}$$

with d the directions of the faces of the control-volume (4 directions in 2D, 6 in 3D), S_d the fluid surface of the face in direction d, $u_d^\star$ the normal velocity at the centre of the face and Δt the length of the time step.

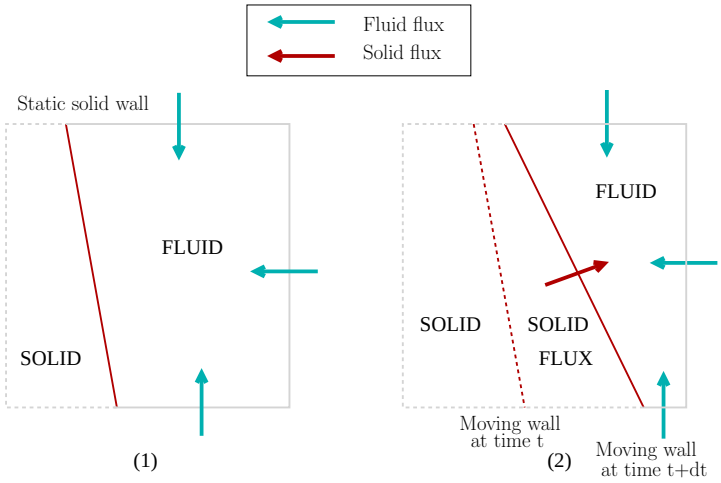

Figure 5.6. Fluid and solid fluxes on the faces of a control volume in the case of a static solid boundary (1) and of a moving solid boundary (2).

Solid flux

The solid flux induced by the presence of a moving boundary is fairly easy to compute when adopting a geometrical point of view. The solid flux is nothing else but the area drawn in the control volume by the solid boundary over the time step. This corresponds as well to the difference between the fluid fraction (proportion of fluid in the cell relative to the volume of the whole cell) of the cell at time t and time $t + \Delta t$. On Figure 5.6.2, it corresponds to the areas between the position of the solid interface at time t and the position at time $t + \Delta t$. From a computational perspective, it means that the volume fraction at time t has to be stored in each cell so that the difference in volume fraction can be computed.

This geometrical approach is particularly well-suited to a conservative finite-volume formulation as it implies that the only errors introduced in the numerical scheme when computing the solid fluxes are due to the discretisation of the solid surface or object on the quadtree/octree grid. As the solid object moves, it is very likely that it is not going to intersect exactly the same way with the mesh, and therefore it will not have exactly the same shape at each time step, which is a source of error. This inaccuracy is inherent to the type of description of the solid interface used by Gerris (see later in the Chapter). The use of a proper adaptive refinement along the solid interface helps to reduce this error when necessary.

Fluid fluxes

The expression of fluid fluxes is not as straightforward as it was in the static boundary case (Equation 5.8). It is exactly the same for the control-volumes that do not contain the moving solid interface. For the other ones, that are changing shape within the time-step, three different configurations have to be taken into account (Figure 5.7):

- Simple mixed cell. The most common and simplest case is represented on Figure 5.6-2 or Figure 5.7.a. The solid boundary remains within the control volume for the whole time step $[t; t + \Delta t]$, therefore the control volume considered exists and changes shape during the whole time step. A first order estimation of the fluid flux is the sum of the velocities on the face times the fluid surfaces of the faces at time t^{n+1} (Equation 5.9). In the case of the MAC projection, the face velocities at time $t^{n+1/2}$ are still used, without any modification being made to the prediction scheme. In the case of the approximate projection, the face velocities are still the average of the cell-centred velocities obtained at the end of the time step.

$$\text{Fluid flux} = \sum_d {S_d}^{n+1} u_d^\star \tag{5.9}$$

- The case of a new fluid cell (Figure 5.7-b). This configuration involves two control volumes that cannot be treated separately. Because of the solid interface's displacement, new fluid cells and therefore new control-volumes have to be created. One problem with new control-volumes is that, because of the discrete nature of the code, they can only be created at the beginning of a time-step and therefore exist during the whole time-step, whereas in reality they should only exist during part of this time-step. The main consequence is that fluxes in this cell are going to be dimensionalised by the length of the whole time-step instead of the real existence time of the cell within the time step. Consequently, this new control volume has to be handled in a specific way.

To overcome this issue, the new control-volume can be merged with one of its neighbouring control volumes that exists during the whole time step. This way the whole control volume exists and is supposed to exist during the whole time-step.

The design of the Poisson solver allows only separate cells to be treated at a time. This restriction implies that if the fluid fluxes are computed for a group of merged cells, then the cells have to regain their independence before applying the Poisson solver. For that reason, the divergence, once calculated for both cells together (Equation 5.10), has to be distributed between these two cells.

The total divergence is calculated as a sum of the fluid and solid fluxes for both cells:

$$\begin{aligned} \text{Divergence(total)} &= \text{Divergence(new cell)} + \text{Divergence(merged cell)} \\ &= \text{Fluid fluxes(new cell)} + \text{Fluid fluxes(merged cell)} \\ &\quad + \text{Solid flux(new cell)} + \text{Solid flux(merged cell)} \\ &= (\sum_d S_d\, u_d^\star)\,(\text{new cell}) + (\sum_d S_d\, u_d^\star)(\text{merged cell}) \\ &\quad + \Delta V(\text{new cell}) + \Delta V(\text{merged cell}) \end{aligned} \tag{5.10}$$

with S_d the face fluid fraction of the cells, $u_d^\star$ the normal predicted velocity on the direction d face of a cell and ΔV the variation of fluid fraction over a time-step.

The total divergence can be seen as a quantity that can be distributed on the group of cells. Any distribution of the divergence over the new cell and its merged cell ensures conservation at the scale of the block of cells. An appropriate distribution could ensure conservation at the scale of the cell. The optimal distribution is not at all obvious to formulate and requires the use of other data (old face fluid fractions, information on the neighbours, etc). It was decided to distribute the divergence according to the size of the cells, as:

$$\text{Final Divergence(new cell)} = \frac{V(\text{new cell})}{V(\text{new cell}) + V(\text{merged cell})}\ \text{Divergence(total)}$$

$$\text{Final Divergence(merged cell)} = \frac{V(\text{merged cell})}{V(\text{new cell}) + V(\text{merged cell})}\ \text{Divergence(total)}$$

.

- Case of a cell that disappears (Figure 5.7-c). The third and last configuration involves cells that disappear and become fully solid. At time t, they still contain some fluid but at $t + \Delta t$ they have been destroyed. Obviously, the fluid contained in these cells has to be redistributed. This case has already been discussed on the mesh-update section. As for the previous case, the control-volume is extended by merging of the cell with one of its neighbours.

Unlike in the previous case, the divergence does not have to be distributed between the merged cells, because at the end of the time step there is only one cell left. As the quantities within the cell have been distributed to its merge partner during the mesh-update, the computation of the fluid fluxes is exactly the same as for the first case (see Equation 5.9).

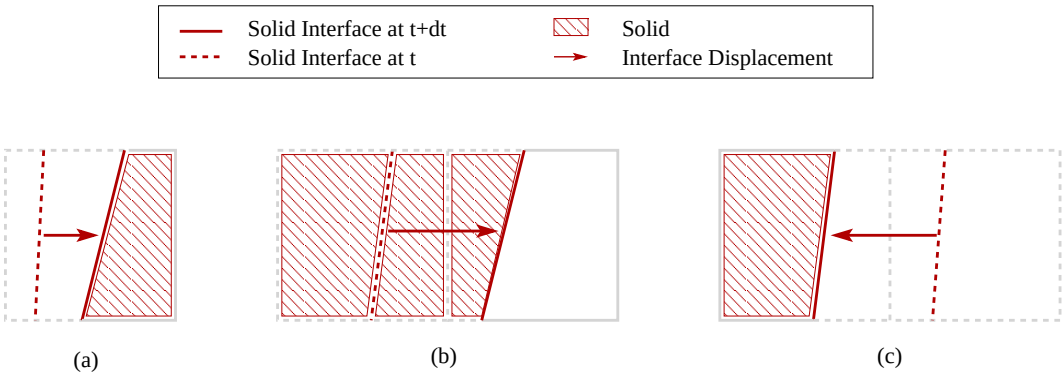

Figure 5.7. The 3 cases of solid interface displacement. (a) The solid interface moves within a control volume. (b) The solid interface moves out of the control volume and a new control volume has to be created. (c) The solid interface moves in a fully fluid control volume and the neighbouring control volume becomes fully solid.

5.3.4 Approximate projection

In contrast to the MAC-projection, which is key to the conservative properties of the whole scheme and therefore needs computation of the exact solid fluxes, the approximate projection can be seen as an instantaneous projection of the velocity field at time t^{n+1}. In this case, the solid flux can simply be computed as the product of the solid interface length times the normal component of the velocity at the solid interface.

Only the geometry at time t^{n+1} is considered and therefore there is no destroyed or new cell to take into account.

5.4 Advection Scheme

Gerris uses a predictor-corrector advection scheme. Advection fluxes are computed from the predicted face velocities after projection. Face velocities are predicted at time $t^{n+1/2}$ using a second-order Godunov method. The predicted velocities are then projected using a multi-grid Poisson solver. These face-centred velocities are then used to compute the advection fluxes on the cell faces.

The advection scheme for static boundaries can be summarised with the case of a tracer $T(X,t)$ advected by a velocity field $\boldsymbol{u}(X,t)$. The tracer advection equation can be written in a conservative form as

$$\frac{\partial T(X,t)}{\partial t} + \nabla(\boldsymbol{u}(X,t).T(X,t)) = 0,\ X \in D, t \in [0;+\infty[.$$

The integration over a control-volume $\Omega \times [t: t+\Delta t]$, gives

$$\int_t^{t+\Delta t} \int_\Omega \frac{\partial T(X,t)}{\partial t}\,\mathrm{dvdt} + \int_t^{t+\Delta t} \int_\Omega \nabla(\boldsymbol{u}(X,t).T(X,t))\,\mathrm{dv\,dt} = 0.$$

Applying the Green-Ostrogradsky's theorem to the second term leads to

$$\int_t^{t+\Delta t} \int_\Omega \frac{\partial T(X,t)}{\partial t}\mathrm{dvdt} + \int_t^{t+\Delta t} \int_{\partial\Omega} T(X,t)\,\boldsymbol{u}(X,t).\boldsymbol{n}(X,t)\,\mathrm{dsdt} = 0,$$

where $\boldsymbol{n}(X,\ t)$ is the normal to the control-volume boundary. The second term, or advection term can be discretised as the sum of the fluid flux on each face of the cell:

$$\int_t^{t+\Delta t} \int_{\partial\Omega} T(X,t)\,\boldsymbol{u}(X,t).\boldsymbol{n}(X,t)\,\mathrm{dsdt} = \Delta t \sum_d {T_d}^{n+1/2} {S_d}^{n+1}\, {u_d}^{n+1/2}.$$

5.4.1 Merged cells

Besides the numerical discretisation of the advection equation, one interesting feature of the advection scheme in the Gerris Flow Solver is the use of cell merging for CFL reasons.

The CFL number $\left(\frac{u\,\Delta t}{\Delta x}\right)$ is set up so that anywhere in the domain the fluid cannot move from more than the length of a cell within a time-step. This way the quantity of fluid that enters a cell during a time-step should not exceed its volume. If this limit is exceeded the cell overflows and the code becomes unstable. When a solid object is present in the domain, its discretisation leads to the creation of mixed-cells sometimes containing only a small fraction of fluid, depending on the way solid and mesh intersect. As the length of the time-step is proportional to the size of the smallest cell in the domain to satisfy the CFL condition, this could potentially make the time-step very small.

For that reason, each mixed cell whose fluid fraction is less than 0.5 (less than half filled with fluid) is merged with at least one of its neighbours to form a control-volume with a fluid fraction higher than 0.5 (Figure 5.8). When it is ensured that each control-volume has a volume fraction of at least 0.5, the CFL criteria is independent of the way the mesh and the solid boundary intersect.

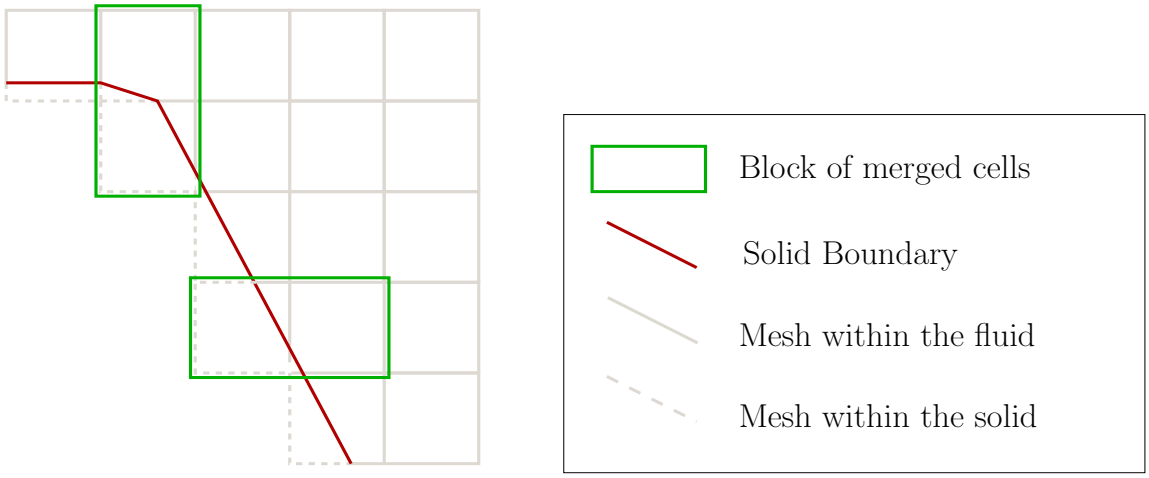

Figure 5.8. Cells whose fluid fraction is less than 0.5 (which are more than half in the solid) are merged with one of their neighbours.

For this merging algorithm to work properly with moving boundaries it has to be ensured that the CFL number is smaller than 0.5. Then, only merged cells can be destroyed within a time-step (see mesh update section).

Cell merging is a very convenient solution to the CFL problem induced by mixed cells; nevertheless it raises the question of the redistribution of the total advection flux within a group of merged cells. Indeed, no distinction is made at first between the fluxes entering both cells and they are treated in common. Despite being merged during the advection process, both cells still remain independent as the total flux can be redistributed differently in each cell and diffusion and pressure terms are not merged. The flux redistribution problem will be dealt with at the end of the advection section.

5.4.2 Advection with moving boundaries - theory

Now moving boundaries are introduced, control-volumes are time-dependent which means that some extra terms appear when integrating the local equation.

Let us consider again a tracer $T(X,t)$ with X in the domain $D(t)$ and t the time. The tracer T is advected by a non-divergent velocity field $\boldsymbol{u}(X,\,t)$ defined in the same domain $D(t)$. The local advection of the tracer T can be written in conservative form as

$$\frac{\partial T(X,t)}{\partial t} + \nabla(\boldsymbol{u}(X,t).T(X,t)) = 0,\, X \in D(t), t \in [0;+\infty[.$$

integration over a control-volume $\Omega(t) \times [t: t + \Delta t]$, gives

$$\int_t^{t+\Delta t} \int_{\Omega(t)} \frac{\partial T(X,t)}{\partial t} \,\mathrm{dvdt} + \int_t^{t+\Delta t} \int_{\Omega(t)} \nabla(\boldsymbol{u}(X,t).T(X,t)) \,\mathrm{dv}\,\mathrm{dt} = 0, \tag{5.11}$$

for which the time derivative has to be taken out of the integration bracket.

Theorem 5.1. *If A(X,t) is a scalar function then*

$$\frac{d}{\mathrm{dt}} \int_{\Omega(t)} A(X,t) \,\mathrm{dv} = \int_{\Omega(t)} \frac{\partial A(X,t)}{\partial t} \,\mathrm{dv} + \int_{\partial\Omega(t)} A(X,t)\, \boldsymbol{v}(X,t).\boldsymbol{n}(X,t) \,\mathrm{ds}$$

with v(X,t) the velocity of the boundary $\partial\Omega(t)$.

Applying Theorem 5.1 to the first term of equation (5.11) and the Green-Ostogradsky's theorem to the second term leads to

$$\int_t^{t+\Delta t} \frac{d}{\mathrm{dt}} \int_{\Omega(t)} T(X,\ t)\ \mathrm{dvdt}\ +\quad \int_t^{t+\Delta t} \int_{\partial\Omega(t)} T(X,\ t)\,(\boldsymbol{u}(X,\ t)\ -\ \boldsymbol{v}(X,\ t)).\boldsymbol{n}(X,\ t)\ \mathrm{dsdt}\ =$$
$$0. \tag{5.12}$$

Comparing equation (5.12) to the integral of the local tracer advection equation over a control volume without moving solid boundaries,

$$\int_t^{t+\Delta t} \frac{d}{\mathrm{dt}} \int_{\Omega} T(X,t) \,\mathrm{dvdt} + \int_t^{t+\Delta t} \int_{\partial\Omega} T(X,t)\, \boldsymbol{u}(X,t).\boldsymbol{n}(X,t) \,\mathrm{dsdt} = 0, \tag{5.13}$$

two differences can be noticed. When solid moving boundaries are involved, the control volume $\Omega(t)$ depends on the time t and the velocity of the boundary of the control volume $\boldsymbol{v}(X,\, t)$ has to be taken into account in the calculation of the advection fluxes.

After time integration the time derivative term of equation 5.12 depends on the geometry of the control-volume at time t and $t + \Delta t$:

$$\int_t^{t+\Delta t} \frac{d}{\mathrm{dt}} \int_{\Omega(t)} T(X,t) \,\mathrm{dvdt} = \int_{\Omega(t+\Delta t)} T(X, t+\Delta t) \,\mathrm{dv} - \int_{\Omega(t)} T(X,t) \,\mathrm{dvdt}.$$

As the fluid fraction at time t is already stored for computation of the solid fluxes, it can be reused as to calculate with this term.

The advection term,

$$\int_t^{t+\Delta t} \int_{\partial\Omega(t)} T(X,t)\,(\boldsymbol{u}(X,t) - \boldsymbol{v}(X,t)).\boldsymbol{n}(X,t) \,\mathrm{dsdt},$$

depends on the time-dependent geometry of the control volume. Whereas with the time derivative term, where the geometry was important only at time t and $t + \Delta t$, now its evolution over the whole time-step is important .

The boundary $\partial\Omega(t)$ of the control volume $\Omega(t)$ can be separated into its fluid part $\partial\Omega_f(t)$ (virtual frontier) and its solid part $\partial\Omega_s(t)$ (Figure 5.5), just like for the divergence scheme. In the original case with only a static solid boundary, the solid flux term was equal to zero, as there is no flux through the solid boundary, and the advection term was integrated in the following way:

$$\int_{\partial\Omega} T(X,t)\,\boldsymbol{u}(X,t).\boldsymbol{n}(X,t)\,\mathrm{ds} = \int_{\partial\Omega_f} T(X,t)\,\boldsymbol{u}(X,t).\boldsymbol{n}(X,t)\,\mathrm{ds}.$$

For solid moving boundaries,

$$\int_{\partial\Omega(t)} T(X,t)\,(\boldsymbol{u}(X,t)-\boldsymbol{v}(X,t)).\boldsymbol{n}(X,t)\,\mathrm{ds} =$$

$$\int_{\partial\Omega_f(t)} T(X,t)\,(\boldsymbol{u}(X,t)-\boldsymbol{v}(X,t)).\boldsymbol{n}(X,t)\,\mathrm{ds} + \int_{\partial\Omega_s(t)} T(X,t)\,(\boldsymbol{u}(X,t)-\boldsymbol{v}(X,t)).\boldsymbol{n}(X,t)\,\mathrm{ds}. \tag{5.14}$$

The velocity of the fluid boundary $\boldsymbol{v}(X,\ t)$ on $\partial\Omega_f(t)$ is equal to zero as it is a "virtual" boundary that corresponds to the limits of the quadtree/octree cell that are fluid. On the solid boundary $\partial\Omega_s(t)$, a no-slip boundary condition is applied, the velocity of the fluid is the same as the velocity of the solid boundary. Therefore, on $\partial\Omega_s(t)$, $\boldsymbol{u}(X,\ t) = \boldsymbol{v}(X,\ t)$ which implies that there is no contribution from the solid to the advective fluxes. After introducing these boundary conditions in equation (5.14), we get

$$\int_{\partial\Omega(t)} T(X,t)\,(\boldsymbol{u}(X,t)-\boldsymbol{v}(X,t)).\boldsymbol{n}(X,t)\,\mathrm{ds} = \int_{\partial\Omega_f(t)} T(X,t)\,\boldsymbol{u}(X,t).\boldsymbol{n}(X,t)\,\mathrm{ds}. \tag{5.15}$$

The final integrated tracer advection equation for moving solid boundaries is

$$\int_{\Omega(t+\Delta t)} T(X,t+\Delta t)\,\mathrm{dv} - \int_{\Omega(t)} T(X,t)\,\mathrm{dvdt} + \int_t^{t+\Delta t}\int_{\partial\Omega_f(t)} T(X,t)\,\boldsymbol{u}(X,t).\boldsymbol{n}(X,t)\,\mathrm{dsdt} = 0$$

This equation shows that the implementation of moving solid boundaries in the advection scheme of The Gerris Flow Solver only requires a change to the integration scheme so that it takes into account the changes of shape and volume of the control-volume $\Omega(t)$. The velocity of the solid boundaries does not have to be directly taken into account in the advection scheme. It is only involved through the topological changes of the fluid domain.

Advection and divergence schemes cannot be seen as independent entities as the divergence scheme ensures that the advection schemes will be fully conservative. Therefore, despite the fact that no solid flux is explicitly used in the advection algorithm, solid flux does exist but is taken into account beforehand during the projection of the face velocities.

In contrast to a tracer advection equation, the advection equation for momentum,

$$\frac{\partial\,\boldsymbol{u}(X,t)}{\partial t} + \boldsymbol{u}(X,t).\nabla\boldsymbol{u}(X,t) = 0, X \in D(t), t \in [0;+\infty[$$

is non-linear. It is nevertheless treated as three scalar linear advection equations on each component of the momentum. No difference exists from a theoretical point of view between scalar and vector quantities. The final integrated equation for momentum advection is

$$\int_{\Omega(t+\Delta t)} \boldsymbol{u}(X,t+\Delta t)\,\mathrm{dv} - \int_{\Omega(t)} \boldsymbol{u}(X,t)\,\mathrm{dvdt} + \int_t^{t+\Delta t} \int_{\partial\Omega_f(t)} \boldsymbol{u}(X,t)(\boldsymbol{u}(X,t).\boldsymbol{n}(X,t))\mathrm{dsdt} = 0.$$

As for static boundaries, momentum can still be advected using the same routines as the ones used for tracer advection, with each component being advected separately.

5.4.3 Numerical scheme

The control-volume $\Omega(t)$ over which the advection equation is integrated can be a fully-fluid cell, a mixed cell or a block of merged cells. Depending on the type of cell, fluxes are not going to be added exactly the same way to the cells. Nevertheless, advection fluxes are going to be calculated using the same method and the overall idea is identical.

Advective fluxes,

$$\int_t^{t+\Delta t} \int_{\partial\Omega_f(t)} T(X,t)(\boldsymbol{u}(X,t).\boldsymbol{n}(X,t))\mathrm{dsdt}$$

depend on the geometry of the control volume, on the velocity field and on the tracer field. As said earlier, the velocity field used to perform the advection is the face-centred velocity field at mid-time-step and the tracer field is the face-centred tracer field at time $t^{n+1/2}$.

The control-volumes used to calculate the advection fluxes are the control-volumes at time $t+\Delta t$. This way the new cells have already been created and the old cells have been destroyed and their fluid fraction re-distributed.

The discretisation of the advection term is given by

$$\Delta t \sum_d T_d^{n+1/2} {S_d}^{n+1} u_d^{n+1/2}.$$

Unlike the static boundary case, where the advective fluxes are fully expressed at $t^{n+1/2}$, here the face fractions are evaluated at $t+\Delta t$. This is nevertheless first order in time.

The time derivative is discretised as

$$\Delta t \frac{V^{n+1}T^{n+1} - V^n T^n}{\Delta t}$$

which leads to the final expression of the advection algorithm for a non-merged cell:

$$V^{n+1}T^{n+1} = V^n T^n + \Delta t \sum_d T_d^{n+1/2} {S_d}^{n+1} u_d^{n+1/2}.$$

Redistribution between merged cells

Now the "normal cell" case has been depicted. Merged cells (new cell + neighbour(s)) are dealt with slightly differently. The initial quantities are still the same and fluxes are still calculated the same way, but now both are distributed differently between the merged cells

This redistribution can be done in an arbitrary way, but some redistribution strategies give more sensible or accurate results than others.

So far three strategies have been implemented in the Gerris Flow Solver:

– The coarsest one consists of adding together the content of all the merged cells with the total advection flux, and then the total quantity is redistributed according to the volume fraction of each cells. That can been written as

$$V_i^{n+1} T_i^{n+1} = \frac{\mathrm{Vi}^{n+1}}{\sum_j V_j^{n+1}} \left(\sum_j V_j^n T_j^n + \sum_j \mathrm{Flux}_j^{n+\frac{1}{2}} \right)$$

with T_i^n the value of the a scalar quantity (for example tracer) in the cell i at time t^n, V_i^n the volume fraction of cell i at time t^n and Flux_i the flux of tracer through the fluid boundaries of cell i. This corresponds to an averaging of all the quantities and fluxes, and leads to a uniform value of the tracer field within the block of merged cells.

– the second redistribution [Quirk(1994)] is an averaging as well but only of the fluxes and not of the quantities. The weighting used to redistribute the fluxes is still the same, i.e. the size of the cell.

$$V_i^{n+1} T_i^{n+1} = V_i^n T_i^n + \frac{\mathrm{Vi}^{n+1}}{\sum_j V_j^{n+1}} \left(\sum_j \mathrm{Flux}_j^{n+\frac{1}{2}} \right)$$

This strategy leads to a non-uniform repartition of the quantities in the group of merged cells. Nevertheless, as the fluxes are all averaged prior to the redistribution, all the information regarding the spatial origins of the advection fluxes is lost.

– the third strategy which is the one used most of the time in the Gerris Flow Solver, redistributes part of the fluxes to the cells to which they belong, and then the rest is arbitrary redistributed using the volume fraction for weighting. The redistribution works in two steps. First, if the cell is a big cell(fluid fraction > 0.5), then its whole flux goes into the cell:

$$V_i^{n+1} T_i^* = V_i^n T_i^n + \mathrm{Flux}_i^{n+\frac{1}{2}}$$

if the cell is small, only part of its flux goes into the cell. The fraction of the flux let into the cell, is equal to the ratio of the size of the small cell to half the size of a cell (limit size for a small cell). This should prevent cell overflow.

$$V_i^{n+1} T_i^* = V_i^n T_i^n + \frac{V_i^{n+1}}{0.5} \mathrm{Flux}_i^{n+\frac{1}{2}}$$

Then the remaining flux $\sum_{\text{small cells}} (1 - \frac{V_i^{n+1}}{0.5}) \text{Flux}_i^{n+\frac{1}{2}}$ is redistributed, and the final redistribution is

$$V_i^{n+1} T_i^{n+1} = V_i^n T_i^n + \text{Flux}_i^{n+\frac{1}{2}} + \frac{V_i^{n+1}}{\sum_j V_j^{n+1}} \left(\sum_{\text{small cells}} (1 - \frac{V_i^{n+1}}{0.5}) \text{Flux}_i^{n+\frac{1}{2}} \right)$$

if it is a big cell or

$$V_i^{n+1} T_i^{n+1} = V_i^n T_i^n + \frac{V_i^{n+1}}{0.5} \text{Flux}_i^{n+\frac{1}{2}} + \frac{V_i^{n+1}}{\sum_j V_{\text{jl}}^{n+1}} \left(\sum_{\text{small cells}} (1 - \frac{V_i^{n+1}}{0.5}) \text{Flux}_i^{n+\frac{1}{2}} \right)$$

if i is a small cell.

This third redistribution strategy is far more satisfying than the two previous ones. Nevertheless, part of the flux is still redistributed arbitrarily. This means that no matter how good this redistribution algorithm is, it does not provide the correct advection of a constant tracer field (only the first algorithm was working in this configuration).

As explained earlier the merging algorithm deals well with CFL problems. It is now clear that it is also very convenient for dealing with time-dependent control-volumes. Nevertheless, it is not completely clear at this stage what the influence of cell-merging will be on a solid/fluid simulation. Despite the use of the first strategy (total average) to redistribute fluxes and quantities seeming to be the coarsest, it will be used at first because it makes it easier theoretically to predict the content of the cells after advection. Doing so is bound to introduce more numerical viscosity but only in the direction of the neighbour with which the new cell is merged.

5.5 Diffusion Scheme

The Gerris Flow Solver was first designed as an incompressible Euler equation solver [Popinet(2003)]. It was then extended to a full Navier-Stokes equation solver by adding two diffusion algorithms, an implicit to semi-implicit one and an explicit one.

The fully to semi-implicit diffusion scheme is based on the multi-grid solver (SourceDiffusion and SourceViscosity) and involves the solving of an Helmholtz equation. The default scheme is the semi-implicit Cranck-Nicholson diffusion scheme. The explicit diffusion scheme is less complex and treat the diffusion terms as source terms.

For both diffusion schemes, two branches exist, SourceDiffusion and SourceViscosity. SourceDiffusion is designed to deal with fluid of constant viscosity (Newtonian), while SourceViscosity can deal with any law imposed on the viscosity. The practical difference between these two schemes is that SourceViscosity takes into account the cross-terms that appear when the viscosity is not constant.

5.5.1 Theory

Let us consider the diffusion of a tracer or scalar quantity T. The diffusion equation for a tracer is written as

$$\frac{\partial T}{\partial t}(X,t) = \nabla.(\mu\,\nabla T(X,t)), \tag{5.16}$$

where μ is the viscosity.

Equation 5.16, has to be integrated over a control-volume $\Omega(t)\times[t\colon t+\Delta t]$,

$$\int_t^{t+\Delta t}\int_{\Omega(t)}\frac{\partial T}{\partial t}(X,t)\mathrm{dv}\,\mathrm{dt} = \int_t^{t+\Delta t}\int_{\Omega(t)}\nabla.(\mu\,\nabla T(X,t))\mathrm{dv}\,\mathrm{dt}$$

which can be rewritten in term of gradient fluxes as

$$\int_t^{t+\Delta t}\int_{\Omega(t)}\frac{\partial T}{\partial t}(X,t)\mathrm{dv}\,\mathrm{dt} = \int_t^{t+\Delta t}\int_{\partial\Omega(t)}\mu\,\nabla T(X,t).\boldsymbol{n}(X,t)\mathrm{ds}\,\mathrm{dt},$$

where $\boldsymbol{n}$ is the normal to the control-volume surface $\partial\Omega(t)$.

As for the advection scheme, the fluxes can be separated into solid and fluid parts,

$$\int_t^{t+\Delta t}\int_{\partial\Omega(t)}\mu\,\nabla T(X,t).\boldsymbol{n}(X,t)\mathrm{ds}\,\mathrm{dt} =$$
$$\int_t^{t+\Delta t}\int_{\partial\Omega_f(t)}\mu\,\nabla T(X,t).\boldsymbol{n}(X,t)\mathrm{ds}\,\mathrm{dt} + \int_t^{t+\Delta t}\int_{\partial\Omega_s(t)}\mu\nabla T(X,t).\boldsymbol{n}(X,t)\mathrm{ds}\,\mathrm{dt},$$

where $\partial\Omega_f(t)$ is the fluid part of the boundary and $\partial\Omega_s(t)$ is the solid part.

Clearly the main difference between a simulation involving static or moving objects is the time dependence of the control-volume geometry. In the case of a tracer, boundary conditions on the solid surfaces are unchanged. No extra term appears in the equations as the eventuality of having a non-null flux of tracer on solid boundary was already considered in the static case. Therefore, no changes are required to have a first-order diffusion scheme working for moving boundaries.

5.5.2 Numerical scheme

Two key words can be used in Gerris to set up the diffusion of a tracer: SourceDiffusion and SourceDiffusionExplicit.

- The semi-to-fully implicit diffusion term, SourceDiffusion, (depending on the choice of the β parameter) can be expressed as,

$$\frac{\partial T}{\partial t} = \beta\left[\nabla.(D\nabla T)\right]^{t=t^{n+1}} + (1.-\beta)\left[\nabla.(D\nabla T)\right]^{t=t^n}.$$

For $\beta=1$, we have a fully implicit backward Euler scheme, and for $\beta=1/2$, a Cranck-Nicholson one. The implicitness of the scheme implies that a linear system has to be solved (Helmholtz equation type).

After integration and discretisation, we get

$$\frac{T_{\mathrm{ij}}^{n+1} - T_{\mathrm{ij}}^{n}}{\Delta t} = \beta \boldsymbol{D}^{n+1} T_{\mathrm{ij}}^{n+1} + (1. - \beta)\, \boldsymbol{D}^{n} T_{\mathrm{ij}}^{n}, \tag{5.17}$$

where $\boldsymbol{D}^n$ is a matrix for the diffusion operator. Equation 5.17 can be rearranged to be written as a matrix times the tracer field at time $n+1$ equal to a vector which only depends on the tracer field at time n

$$(I - \Delta t \beta \boldsymbol{D}^{n+1}) T_{\mathrm{ij}}^{n+1} = (I + \Delta t (1. - \beta)\, \boldsymbol{D}^{n}) T_{\mathrm{ij}}^{n}.$$

This system is solved using an iterative algorithm. In Gerris, it is solved using a multi-grid-Jacobi method.

- the explicit scheme, SourceDiffusionExplicit, is the equivalent of SourceDiffusion for $\beta = 0$. No Helmholtz equation has to be solved as the contribution of the diffusion term to the velocity field can be explicitly computed from the velocity field at time t^n. In this, the diffusion is expressed as a source term. This scheme is much simpler to implement, but is stable only for $\Delta t < \frac{\Delta x^2}{\nu}$. Furthermore, it does not deal with solid boundaries which makes it of little relevance to the moving boundary problem.

The use of the semi-implicit scheme is something not obvious at all for moving boundaries. The semi-implicit formulation involves gradient fluxes to be computed at time t^n and t^{n+1}, which correspond to two different geometries. For this reasons, β was chosen to be equal to one and therefore the diffusion scheme to be fully implicit for simulations involving moving boundaries.

5.5.3 Momentum

For momentum , the diffusion term in its general form

$$\nabla \cdot \Big(\frac{\mu}{2} \big(\nabla \boldsymbol{u} + \nabla^T \boldsymbol{u} \big) \Big) \tag{5.18}$$

involves crossed terms. A diffusion equation for momentum is not always equivalent to three scalar diffusion equations. Another major difference is the type of boundary conditions on solid boundaries which are most of the time Dirichlet boundary condition, with the fluid velocity equal to the solid velocity on the boundary:

$$\boldsymbol{u}|_{\partial \Omega_s} = \boldsymbol{v}_s$$

where $\boldsymbol{v}_s$ is the solid object velocity. The flux of velocity gradient on the walls

$$\int_t^{t+\mathrm{dt}} \int_{\partial \Omega_s(t)} \frac{\mu}{2} \big(\nabla \boldsymbol{u} + \nabla^T \boldsymbol{u} \big) . \boldsymbol{n} \, \mathrm{ds}\, \mathrm{dt}$$

is most of the time not equal to zero (for static boundaries as well) and has to be computed from the velocity on the solid interface and the velocity field near the interface. Despite these differences, only the change of geometry matters to evolve from static to moving boundaries. The use of the diffusion scheme designed for the solid boundary should lead to a first order diffusion scheme for moving boundaries.

5.5.4 Momentum diffusion - numerical scheme

Two key words can be used in Gerris to set up the diffusion of momentum: SourceViscosity and SourceViscosityExplicit.

- as SourceDiffusion, SourceViscosity consist in a semi to fully implicit diffusion term depending on the choice of the β parameter,

$$\frac{\partial U}{\partial t} = \beta \Big[\nabla . \Big(\frac{\mu}{2} \big(\nabla \boldsymbol{u} + \nabla^T \boldsymbol{u} \big) \Big) \Big]^{t=t^{n+1}} + (1. - \beta) \Big[\nabla . \Big(\frac{\mu}{2} \big(\nabla \boldsymbol{u} + \nabla^T \boldsymbol{u} \big) \Big) \Big]^{t=t^n}.$$

- SourceViscosityExplicit is also, an explicit formulation of the diffusion as a source term.

From a practical point of view, both explicit diffusion schemes did not need any work to be used with moving objects. The only thing needed was to specify the proper Dirichlet boundary conditions on the velocity on the solid object in the simulation file. Until now (in the divergence and advection scheme), the boundary conditions on the walls were not required, as the solid fluxes were computed from the difference in fluid fraction in the mixed cells.

For the same reasons as for the tracer, β is taken as equal to zero. The implicit diffusion schemes only needed structural modifications of the static version to ensure that the right hand term of the Helmholtz equation takes into account the modifications made in the advection scheme.

5.6 Simple tests

Simple tests were first realised to study the behaviour of the new solid/fluid interaction method under controlled conditions. The first series of tests is of very little interest from a physical point of view but allows an illustration of the different types of errors realised by the code.

Two discretisation of the advection terms have been considered. At first, the advection fluxes were computed using the geometry at time t^{n+1} (first order method):

$$\int_t^{t+\mathrm{dt}} \int_{\partial\Omega(t)} \boldsymbol{u}.(\boldsymbol{u}.\boldsymbol{n}) \, \mathrm{ds} \, \mathrm{dt} = \sum_d S_d^{n+1} \, \boldsymbol{u}_d^{n+1/2} \, u_d^{n+1/2}$$

Only the first tests are realized with the first order method to illustrate the different sources of error more clearly. Then, all the tests were done with the advection fluxes computed with the geometry at time $t^{n+1/2}$ (second order method) :

$$\int_t^{t+\mathrm{dt}} \int_{\partial\Omega(t)} \boldsymbol{u}.(\boldsymbol{u}.\boldsymbol{n})\,\mathrm{ds}\,\mathrm{dt} = \sum_d S_d^{n+1/2}\,\boldsymbol{u}_d^{n+1/2}\,u_d^{n+1/2}.$$

5.6.1 Advection term computed with the geometry at time t^{n+1}

The different sources of error

Different sources of errors have been found in the moving boundary implementation in Gerris. Some of these errors are linked directly to the moving-boundary scheme, and others are linked to the interaction of the moving-boundary scheme with other parts of the code.

To facilitate the discussion of the following tests, it is useful to introduce and describe the different sources of error. For more convenience, the three main causes of error are numbered from type 1 to type 3 error:

- Error of type 1: for any method errors are due to the way the equations are discretised. In finite volume methods, most of those errors are in the way fluxes are computed. Gerris uses a prediction-correction algorithm to compute the fluxes. The prediction part of the algorithm is unchanged compared to the static boundary version of Gerris. The correction part, or projection algorithm, is where the main differences are and where additional error terms appear. One major additional cause of errors here comes from the computation of fluid fluxes from the geometry at time t^{n+1}. In contrast, the solid fluxes are computed as the differences of the solid fractions at t^{n+1} and t^n. They are therefore geometrically exacts, but more important, they are not computed in a consistent way with respect to the way the fluid fluxes are.

Computing the solid fluxes this way is required to keep the scheme conservative. Figure 5.9 gives a good summary of the fluxes calculation (Equation 5.19) for a wall translating at uniform speed U in a fluid at the same speed. The lack of consistency between solid and fluid fluxes, with the solid fluxes being computed using the time integral of the geometry over the whole time step and the fluid fluxes being computed from the geometry at the end of the time-step, induced errors in the computation of the fluxes.

$$\begin{aligned}\int_t^{t+\mathrm{dt}} \int_{\partial\Omega(t)} \boldsymbol{u}.\boldsymbol{n}\,\mathrm{ds}\,\mathrm{dt} &= \int_t^{t+\mathrm{dt}} \int_{\partial\Omega_s(t)} \boldsymbol{u}.\boldsymbol{n}\,\mathrm{ds}\,\mathrm{dt} + \int_t^{t+\mathrm{dt}} \int_{\partial\Omega f(t)} \boldsymbol{u}.\boldsymbol{n}\,\mathrm{ds}\,\mathrm{dt} \\ &= \Delta V + \sum_d S_d^{n+1}\,\boldsymbol{u}_d^{n+1/2}\,u_d^{n+1/2}\end{aligned} \quad . \tag{5.19}$$

A consistent formulation of the solid flux would have been to express it as the product of the solid interface length at time t^{n+1}, the normal component velocity of the solid boundary. In this way, solid and fluid fluxes would have exactly compensated, but mass conservation (which is more important) would not have been ensured.

It has to be pointed that this error is not present in all configurations. For example, Figure 5.10 shows a configuration where the solid and the fluid fluxes are of equal magnitude but opposite signs. This configuration does not allow any errors to be made in the x direction and the errors in the y direction would compensate each other. These considerations are true only for a steady uniform flow, the situation would much more complex for a different flow.

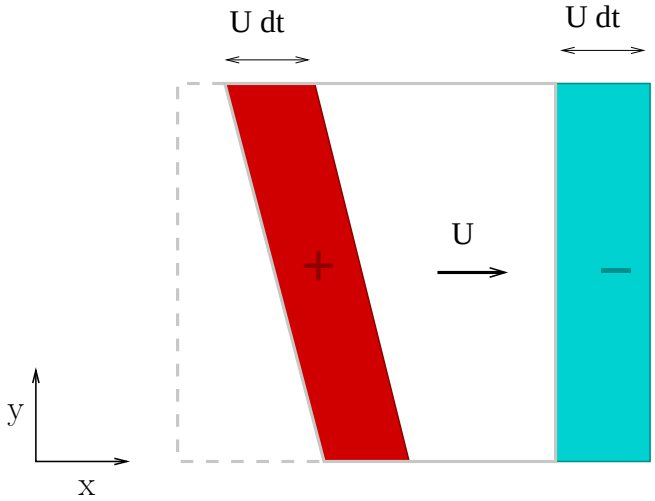

Figure 5.10. Fluxes in a cell from a wall translating at uniform speed U in a fluid a speed U. Positive and negative fluid fluxes are in blue, solid flux is in red. In this case the sum of the solid and fluid fluxes is equal to zero.

As will be seen later, this source of error sometimes gets compensated but only in specific configurations. On Figure 5.9, the error is time-step dependent and should be consistent with the first order in time accuracy expected for the scheme. If the cell is refined, the total error on the divergence calculation should still remain the same.

- Error of type 2: Another source of error is the way solid objects are represented in Gerris. At first, solid objects are defined as GTS surfaces or implicit surfaces. Then, they are introduced in the simulation and intersected with the grid. All the points where the solid surface intersects the grid are linked together with segments (plane surfaces in 3D), which gives the "true" shape of the solid surface used by the code. Depending on its position on the mesh a circular object will not be discretised the same way (Figure 5.11).

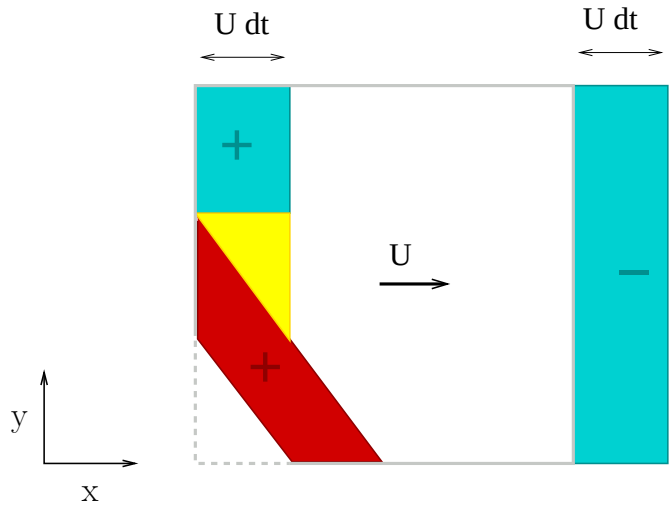

Figure 5.9. Fluxes in a cell from a wall translating at uniform speed U in a fluid a speed U. In blue are the fluid fluxes computed as the product of the face fraction at the end of the time-step times the velocity on the face. In red is the positive solid flux computed as the difference of volume fraction in the cell between the beginning and the end of the time step. In yellow is the missing part of the flux. This missing part is due to the fact that the geometry is evolving within a time-step which is not taken into account.

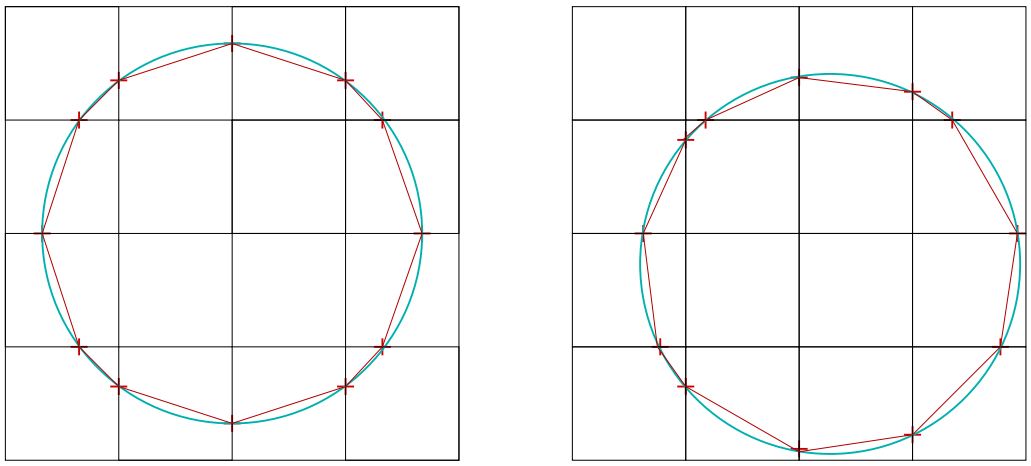

Figure 5.11. Representation in Gerris (dark red) of a circular object (light blue) for two positions in the mesh. The real object keeps the same shape, but its Gerris representation changes.

For static boundaries we get one approximation of the shape of the solid object at the start of the simulation and then keep working with it. For moving boundaries, moving objects are constantly being re-discretised and therefore keep changing shape. For an object translating uniformly we could even say that its shape is oscillating around an "average position".

The use of a more refined grid gives a better representation of the object and induces less fluctuations (in amplitude) when it is displaced.

- Error of type 3: the redistribution of the flux for disappearing cells cleared by the moving boundaries induces some errors. The fluid contained in the cells that are disappearing is arbitrarily redistributed to the cell with which they are merged. The merging algorithm being the same as the ones used for the advection algorithm, no particular criteria except for the size of the cells is used to choose the neighbours with which the future destroyed cells are merged. This results in error in the repartition of the divergence inducing errors in the velocity field.

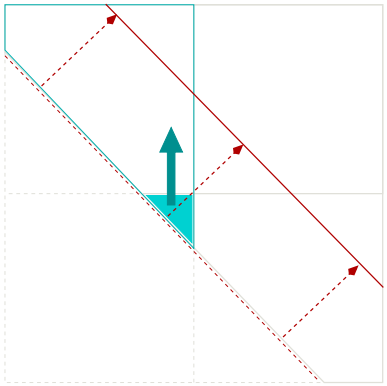

Figure 5.12. When the solid interface (dark red) move so that the bottom left cell becomes fully solid, the fluid that was inside the cell is redistributed to the cell with which it is merged (merged block in light blue).

The redistribution of fluid to the neighbour with which the cell is merged is illustrated in Figure 5.12. The redistribution acts like a flux that is in a direction different to the one that should have been imposed by the moving interface (red dashed arrows). The advection scheme makes use of the cell-merging algorithm for CFL and stability reasons; redistributing the fluid this way ensures that the scheme is locally conservative.

The three sources of errors that have just been described are the main ones for implementation of the moving boundaries using the geometry at time t^{n+1} to compute the advection fluxes. The list is not exhaustive, especially as the main sources of errors can interact with the merging and divergence-redistribution algorithm.

Translating wall

The simplest test cases that can possibly be used are moving walls translating at a uniform speed with a uniform flow. For a domain of finite size, two main configurations are possible. One is when the domain is expanding with the wall moving in the direction fluid to solid, the other is the domain shrinking with the wall moving in the direction solid to fluid.

In both cases, the velocity field should not change at all, the right velocity should be predicted by the prediction algorithm, and the divergence of the velocity field before projected should always be equal to zero. Both cases involve merged cells, but one involves the creation of cells and the other the destruction of cells.

The velocity field used in the case of the shrinking case (Figure 5.13) is

$$\begin{array}{l} U_0 = \cos(18_\circ) \\ V_0 = \sin(18_\circ) \end{array} . \tag{5.20}$$

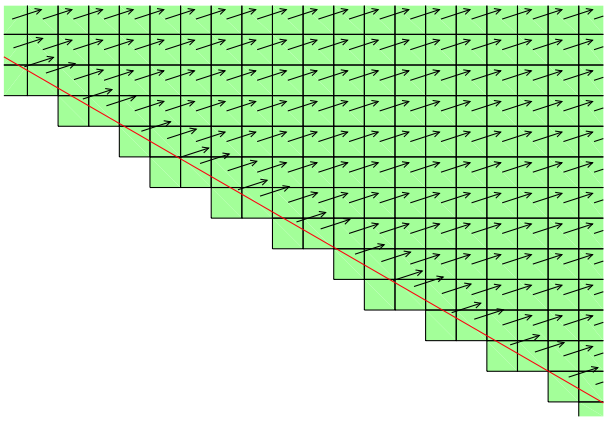

Figure 5.13. Wall moving at the same speed as the fluid. In this case, the domain is going to become smaller and smaller until all the cells have disappeared.

The simulation is run for an arbitrary 0.025 time units (more than 100 time steps in all cases) for resolutions from 4 to 8 level of refinement and time-steps from 0.0002 to 0.00000625. I mainly focused on the errors on the velocity field.

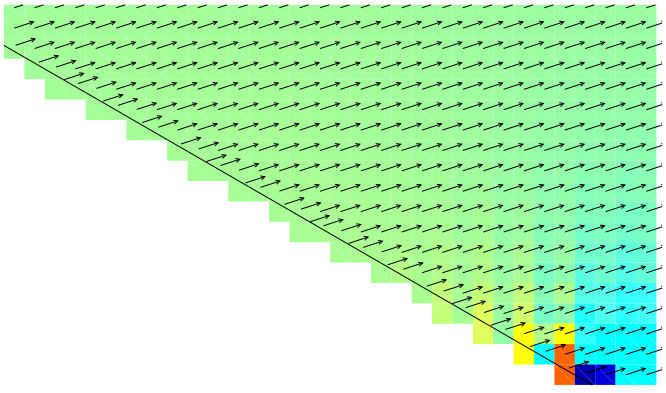

Figure 5.14. Error in the norm of the velocity field at the end of the test. Error are between -2% (dark blue) and +2% (dark red) of the velocity magnitude. Simulation parameters: 5 levels of refinements, time-step of 0.0002, length of the simulation 0.025.

The main errors encountered are those of type 1 due to the different nature between the fluid and the solid fluxes, which cause a wrong estimation of the divergence. The representation of the geometry is exact and the redistribution of the "destroyed cell flux" between merged cells is of little importance as it could be seen as a part of the solid flux. In Figure 5.14, it looks like errors are only made in the bottom corner where the interface is intersecting with the domain's boundary. In fact, errors are made along the whole interface as shown on Figure 5.15-a, but the distribution of the divergence within the groups of merged cells (in yellow on Figure 5.15-a) allows to get a better divergence field. In this case, the errors in divergence completely cancel out except for one cell at the bottom right that is not merged with another mixed cell, as there is none free because of the domain boundary.

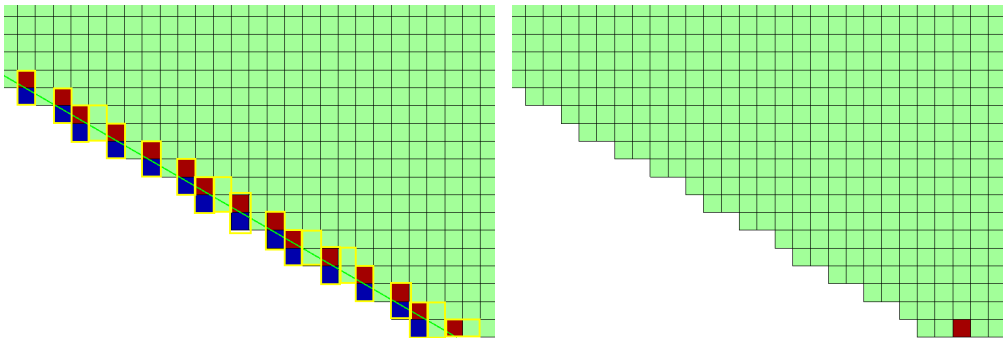

(a) (b)

Figure 5.15. Figure a shows the total flux or divergence before distributing the divergence between groups merged cells at time t=0. All the green cells have a total flux of zero. The red and blue ones are have the same amplitude but opposite signs. The merged cells groups are delimited in yellow. Figure b shows the distribution of divergence in the domain after spreading of the divergence over the merged cells blocks.

The "wrong" calculation of the divergence in this bottom cell is the cause for all the errors seen in Figure 5.14. Errors slowly propagates to the whole domain but remain of relatively small amplitude (around 2% of the mean flow). The presence of an outflow boundary condition next to the error source probably helps the errors to remain small.

The evolution in time of the error on the velocity field was computed in norm 1, 2 and infinite (Figure 5.16) are plotted. The "instantaneous norms" are defined as

$$\begin{aligned}
\|\text{error}\|_1(\boldsymbol{u})(t) &= \frac{1}{\sum_i V_i}\sum_i V_i\sqrt{(u-u_0)_i^2+(v-v_0)_i^2} \\
\|\text{error}\|_2(\boldsymbol{u})(t) &= \sqrt{\frac{1}{\sum_i V_i}\sum_i V_i\,(u-u_0)_i^2+(v-v_0)_i^2}\ , \\
\|\text{error}\|_\infty(\boldsymbol{u})(t) &= \max_i \sqrt{(u-u_0)_i^2+(v-v_0)_i^2}
\end{aligned}$$

where V_i is the volume of cell i and (u_0, v_0) is the exact solution.

When dealing with objects that change shape due to reconstruction errors, a time-averaged norm is used. The solid object's representation depends on the position of the object on the mesh, and is periodic. The time length over which the average is realized corresponds to the time the solid boundary takes to move of a whole cell ($U\Delta t = \Delta x$). This choice of the length scale allows us to take into account all the different shapes of the solid object.

After time averaging, the final definitions of the norms used are

$$\begin{aligned}
\|\text{Error}\|_1(\boldsymbol{u}) &= \frac{1}{\sum_j \Delta t_j}\left(\Delta t_j \|\text{error}\|_1(\boldsymbol{u})(t_j)\right) \\
\|\text{Error}\|_2(\boldsymbol{u}) &= \frac{1}{\sum_j \Delta t_j}\left(\sqrt{\Delta t_j \left(\|\text{error}\|_2(\boldsymbol{u})(t_j)\right)^2}\right) . \\
\|\text{Error}\|_\infty(\boldsymbol{u}) &= \max_{t_j}\left(\|\text{error}\|_\infty(\boldsymbol{u})(t_j)\right)
\end{aligned} \tag{5.21}$$

The error in the velocity field is relatively steady in time. For a level of refinement of 5, the error on the whole domain is between 1e-5 and 1e-6 (Figure 5.16), which is small from a general point of view but quite big for such a simple case. The mesh dependence of the error clearly appears through periodic drops in error corresponding to the way the bottom of the wall (only region where error is generated) intersects with the mesh.

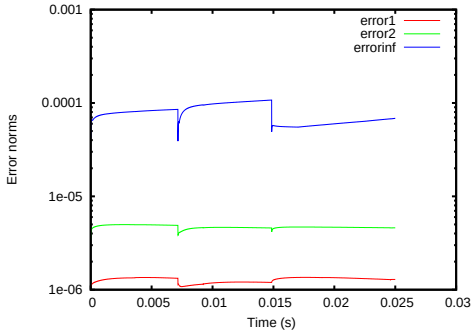

Figure 5.16. Plot of the error on the velocity versus the time for the wall moving at speed 1. Norms 1 (red), 2 (green) and ∞ (blue) are displayed.

First order convergence in time is observed for all norms when varying the time-step (Figure 5.17), and increasing the resolution for a constant time-step does not bring any improvements (Figure 5.18). Mesh refinement only spreads the same amount of error in more cells without changing its total magnitude. Meanwhile, the errors are made only in the cells traversed by the wall, that is in a region of smaller area, which explains why the infinite norm is increasing with resolution.

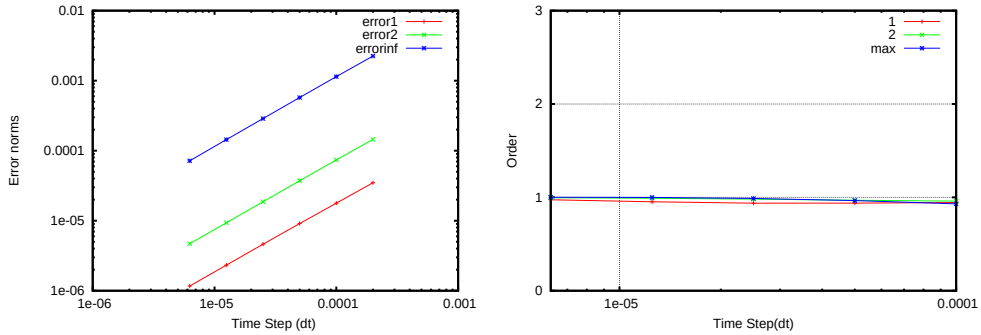

(a) (b)

Figure 5.17. (a)- Error on the velocity field for the wall moving at speed 1 for 6 values of dt. (b) - Order of the scheme in time for a moving wall.

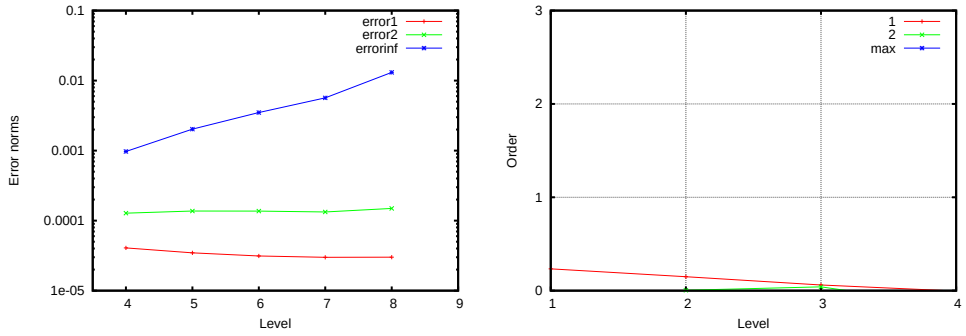

(a) (b)

Figure 5.18. a- Error on the velocity field for the wall moving at speed 1 for 5 levels of refinement. b - Order of the scheme in space for a moving wall.

First order in time has been demonstrated when advection fluxes are discretised on the geometry at time $t^{n+!}$. It has also been shown as well that in this case most of the errors (type 1 and 3) do compensate because of the moving wall configuration. Nevertheless, it is clear that the method is strongly geometry-dependent. The scheme used here can be improved by considering the geometry at time $t^{n+1/2}$ for the computation of advection fluxes. This way, solid and fluid fluxes are coherent within the hypothesis of a linear displacement of the interface. Errors of type 1 and 3 would not exist anymore in this kind of configuration. For that reason, the numerical scheme was improved to reconstruct the geometry at half the time-step. Only this improved approach is used in the rest of the chapter.

5.6.2 Advection term computed with the geometry at time $t^{n+1/2}$

In the same spirit, several tests with translating objects in a uniform velocity field have been realised with only the advection scheme and the projections on.

Translating hexagon

The idea behind the hexagon test case is to use a solid object whose discretisation on the mesh is almost exact. As Gerris cannot deal with solid faces coinciding with the frontier of the mesh's cells, only the top and bottom of the hexagon are not going to be exactly represented. Nevertheless, it is possible to scale the hexagon so that the top and bottom face are as close as possible to coincide with the mesh and therefore the reconstruction error is minimised. This test aims at assessing the way the code deals with straight lines in both cases of an interface moving in the solid to fluid direction or fluid to solid (when cells appear or get destroyed). The influence and importance of the error on the representation of solid objects in Gerris will be addressed in the next section.

The hexagon test case involves an hexagonal solid object translating in a fluid at uniform speed. Quantities as momentum or any tracer should not vary with time. As well, the velocity and fields should remain unchanged during the whole simulation.

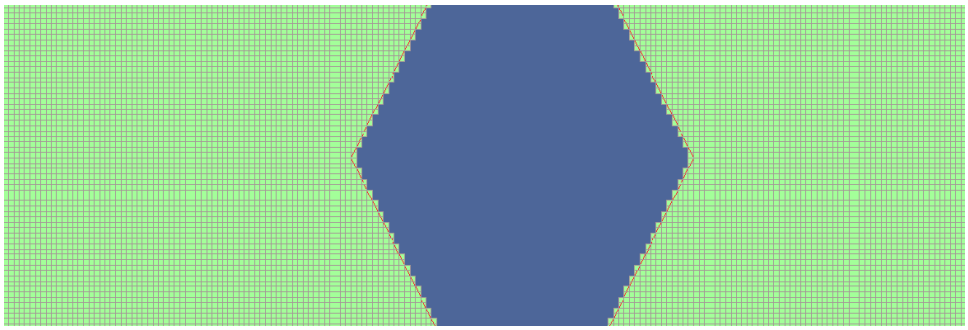

Figure 5.19. Hexagon translating in a moving fluid with uniform velocity field.

The mass conservation results are shown on Figure 5.20. The total quantity of tracer (Figure 5.20) does not vary at all or the variation are down to the tolerance set up on the projection of the face-centred velocity, which is down to 10^{-7} here. The Gerris and the solid/fluid algorithm being based on a finite-volume approach the scheme should be fully conservative which is the case here. Mass does not vary in the domain only if the volume of the solid objects contained within the simulation domain does not vary. This point will be addressed later on in this test section.

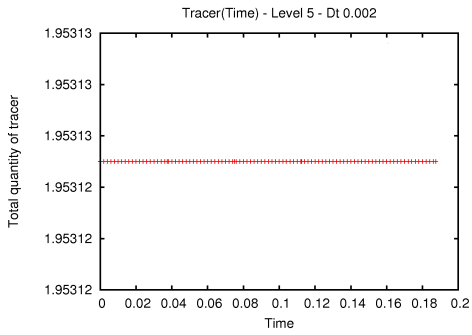

Figure 5.20. Evolution of the total quantity of tracer in the domain with time for the hexagon test-case.

The geographical repartition of error on the velocity field is displayed on Figure 5.21. Only the area where the error in norm 2 is higher than 1% are coloured in red. Most of the error is located on the top and bottom right corners of the hexagon. This is not a surprise as reconstruction errors (type 2) are expected for both top and both bottom corners. The fact that only for the corners on the right hand-side the error gets higher than 1% must come from the fact that as the hexagon translates from right to left, errors are more likely to accumulate in front of the object.

For a mesh refined down to level 8, with the geometry of the hexagon optimised so that the reconstruction errors are the minimum ones for level 8, it is possible to see on Figure 5.22, that again most of the error is localised near the top and bottom corners of the hexagon. The region in red is the where the local error is higher than 0.01% compare to the theoretical solution. It shows that very little error is generated on the face of the hexagon where the fluxes should be estimated exactly.

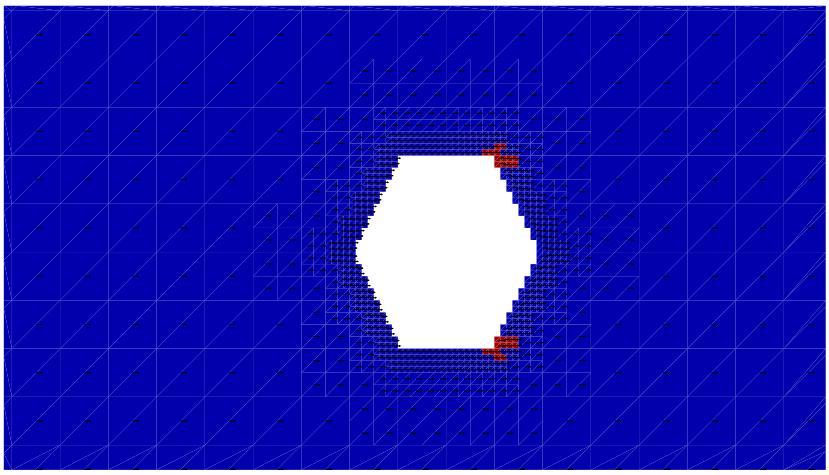

Figure 5.21. In red is the area where at the end of the simulation the norm 2 of the error on the momentum is higher than 1%.

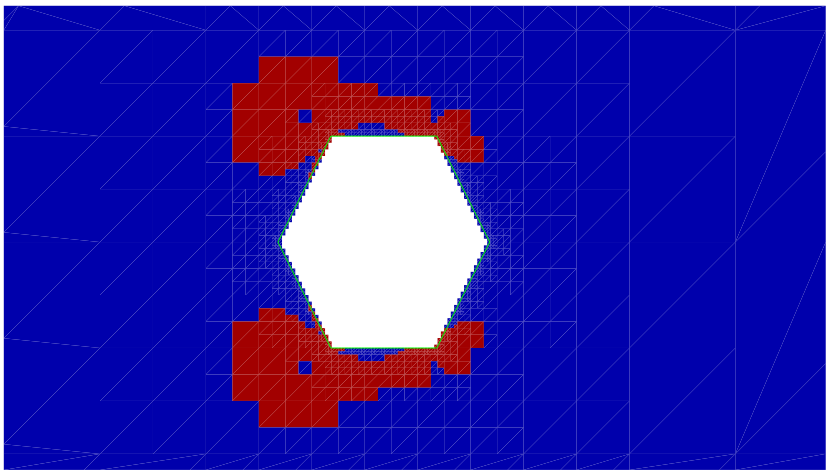

Figure 5.22. In red is the area where at the end of the simulation the norm 2 of the error on the momentum is higher than 0.01%. The refinement at the solid interface is down to level 8 and the error at the corner is reduced to its minimum.

When different time steps are used (Figure 5.23), the error decreases very quickly as the time step is reduced, and the order of convergence with the time-step is close to two.

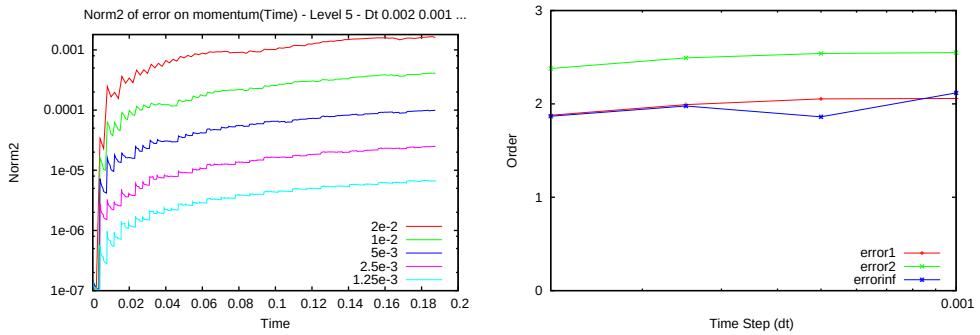

(a) (b)

Figure 5.23. (a) Evolution of momentum with time for a translated hexagon. Each curve correspond to a different time step. (b) Order of convergence in time for the velocity field for a translating hexagon.

Conversely, the global error increases when the mesh is refined (Figure 5.24). This is mainly due to the error in reconstruction of the corners. When the mesh is refined, the error of reconstruction does not increase in absolute, but as the volume of the cells is divided by four, the reconstruction errors increase relatively to the size of the cells (Figure 5.25), inducing more correction from the Poisson solver and therefore bigger errors.

In other tests made using the geometry at time t^{n+1} to compute the advection fluxes, the errors made in the estimation of the divergence were much higher. It was observed several times that for large enough errors the number of iterations required by the Poisson solver to convergence would be big enough that the error would spread to the whole domain.

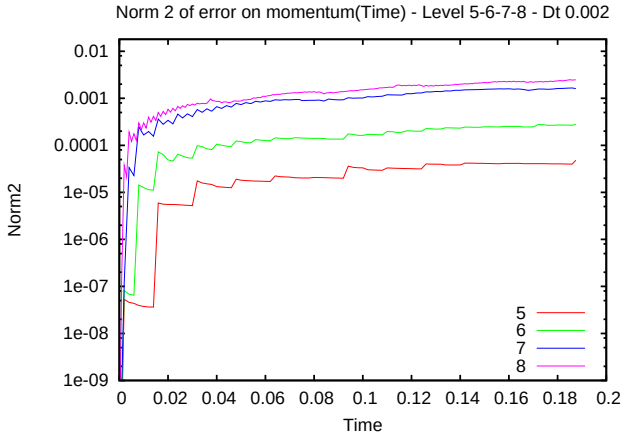

Figure 5.24. Evolution of momentum with time for a translated hexagon. Each curve corresponds to a different refinement of the mesh.

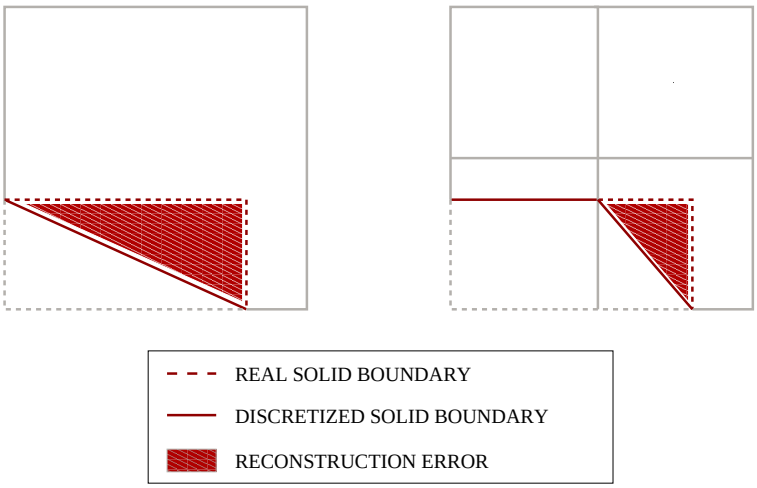

Figure 5.25. Discretisation of the same solid object on meshes of different sizes. On the finest mesh the reconstruction error is smaller in absolute but bigger relatively to cell size.

I have shown through this test case that the advection scheme is conservative. The code behaves well when dealing with straight lines. Reconstruction errors are the main obstacle to getting a very good solution, as they do not compensate and tend to slowly spread away. Also, reconstruction errors seem to prevent the code from converging in space. This does not seem to be the case for time convergence.

Translating square

A translating square was chosen to go further into the understanding of solid objects having a variable geometry in time. The setup is identical to the previous test case except for the shape of the solid object, which is a square (Figure 5.26). This time again, only the advection scheme is on.

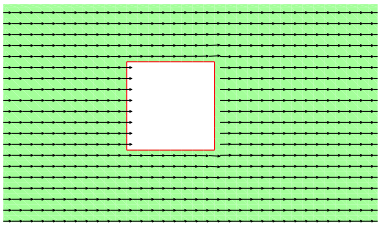

Figure 5.26. Square translating in a uniform velocity field at constant speed.

I expect no divergence errors induced by the calculation of the fluxes around the square. The only source of error should be the solid object changing shape at each time step when it is re-discretised on the mesh. Only the four corners of the square are not well represented in Gerris (Figure 5.27) as they get truncated.

The way the square is truncated (i.e. intersected with the mesh) can be controlled through the size or scaling of the square object. Gerris does not accept solid objects whose geometry overlaps with the mesh, and therefore it is not possible to design a test with no reconstruction error at all. Using a square of size 1, a scaling of 0.25 would allow no reconstruction error (coincides with the mesh at level 2). Scaling from 0.2625 to 0.3 is used for the test, ensuring increasing truncation errors (Figure 5.27).

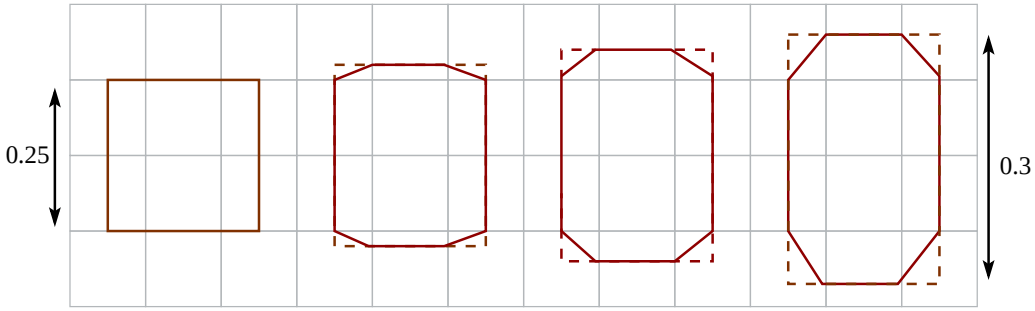

Figure 5.27. Illustration of the term "scaling" used in this section. It corresponds to how much a unit square is re-sized. For 0.25, the square matches with the mesh (left) which means it is exactly represented in the code. The scaling gets bigger from left to right, and the reconstruction error as well.

These small reconstruction errors add themselves to the simulation at each time step. Figure 5.28, makes a summary of the causes and contributions to the reconstruction error. From top to bottom, first the difference between the "real object" i.e. the GTS surface, and the discretised object is shown. Second, the difference between the "real solid flux" and the solid flux computed by Gerris is drawn. It is clear that a non-negligible error is made each time the interface moves. Finally, it has to be noted that the reconstruction error is not a constant source of error in time. It depends on the object/mesh configuration. As illustrated at the bottom of Figure 5.28, when

one of the corners of the square moves from one cell to another, a peak of error occurs all at once. In the cell left by the corner, the object comes back to an accurate representation of the "real geometry". This means that a term equivalent (but of opposite sign) to all the errors accumulated while the corner was in the cell is added during this time-step. Meanwhile, the usual reconstruction error is still present in the cell where the corner currently is. In the case of a corner moving forward (resp. backward), the constant reconstruction error realised at each time step leads to an underestimation (resp. overestimation) of the solid fluxes.

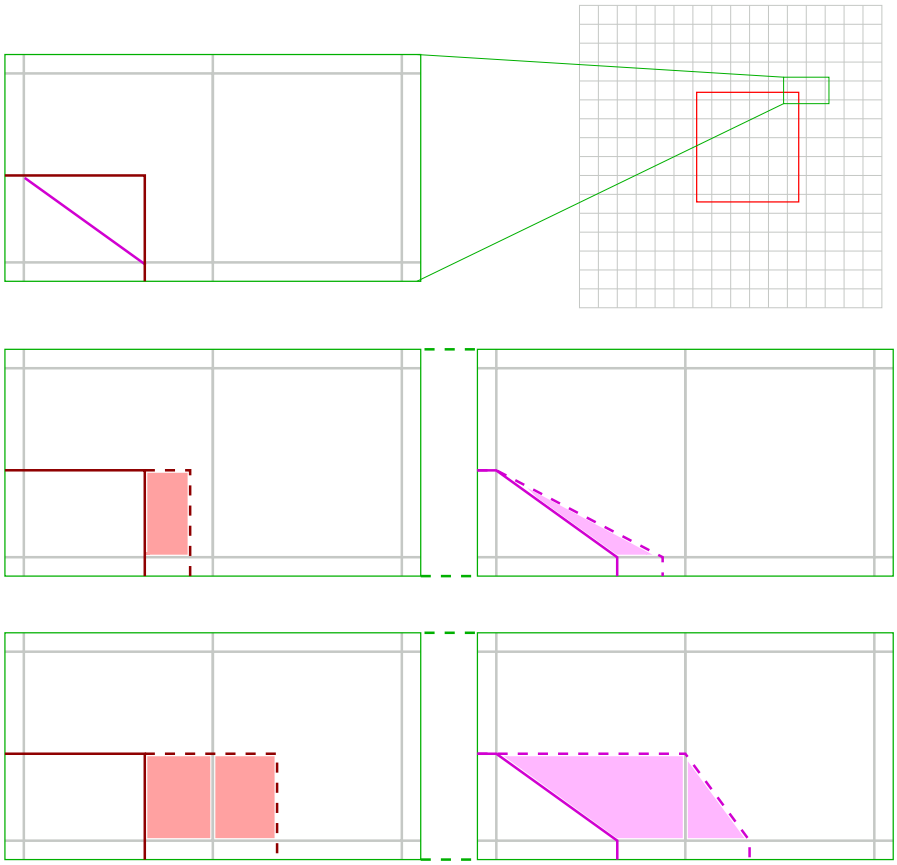

Figure 5.28. Illustration of the difference between the "real" solid (red - left column) object and its discretisation (purple - right column). For a square only the corners are not well represented, as a straight line joins the two points where the solid intersects with the mesh (see top). This also induces a difference in solid flux (see middle) as it is computed from the difference in fluid fraction in the cells at time n and n+1. There is a jump in solid flux when the corner is changing cell (see bottom) as the interface representation goes back instantly to its exact form.

The peaks of error in solid flux can be seen on the plots of the norm2 of the error on the velocity field (Figure 5.29). Errors of reconstruction do tend to compensate, but the overall error still grows in time.

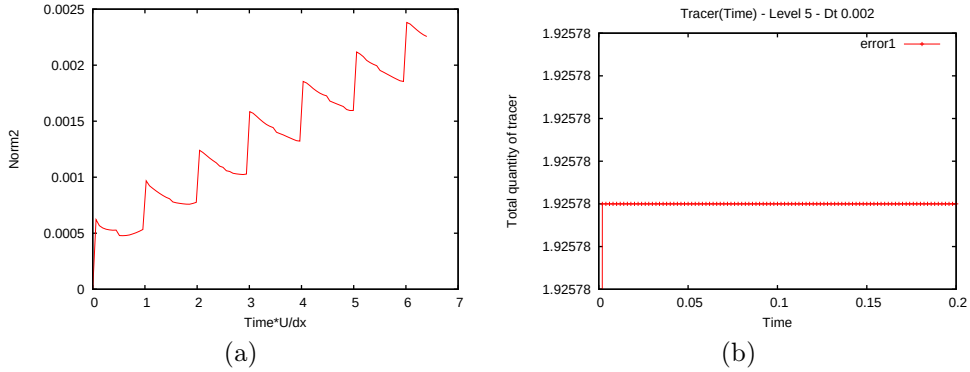

(a) (b)

Figure 5.29. (a) Evolution of the norm2 error on the velocity with time for a translated square. (b) Evolution of the total quantity of tracer in the domain with time for a translated square.

In contrast with the translating hexagon test, the square case does not converge with the use of a smaller time-step. Smaller time-steps tend to generate bigger peaks of error associated with the solid interface entering a new cell (Figure 5.30). The reconstruction errors that generates the peak of error is mostly independent of the time-step. Therefore, when the time-step is diminished, the same error happens within a shorter period of time, which explains the bigger peaks.

If, as claimed, the only existing error comes from the reconstruction of the corners, it should be possible by changing the scaling of the square to make the error becomes as small as desired. This was checked (Figure 5.30-a) and gave satisfying results. It was checked that when the tuning of the object's scaling is good enough, reconstruction errors get smaller than the Poisson solver errors (which depend on the imposed tolerance). Ultimately, these errors can be made smaller than machine precision.

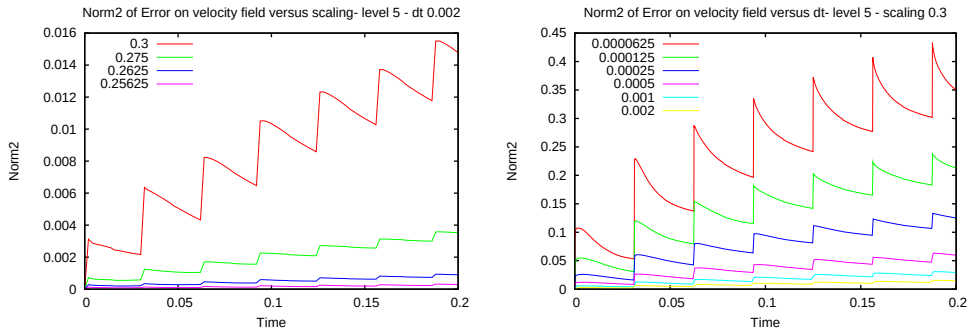

(a) (b)

Figure 5.30. (a) Evolution of the global error on the velocity for a translated square for different scaling of the square. A scaling of 0.25 would correspond to no reconstruction error. (b) Evolution of the global error on the velocity for a translated square versus time-step.

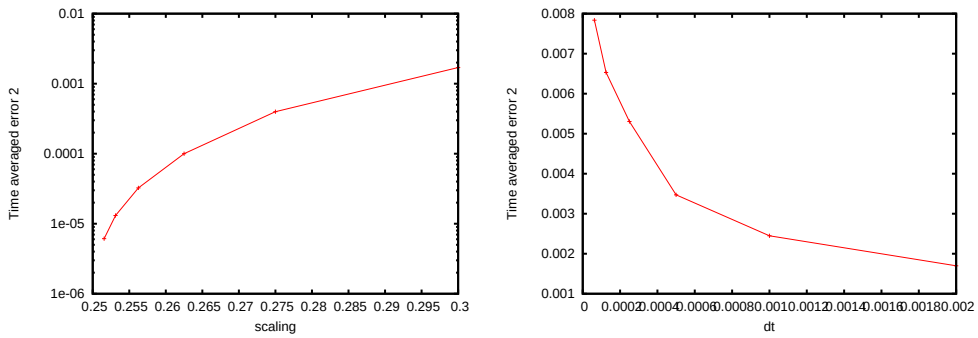

(a) (b)

Figure 5.31. (a) Time average of the global error on the velocity field for a translated square versus scaling of the square. A scaling of 0.25 would correspond to no reconstruction error. (b) Time average of the global error on the velocity field for a translated square versus time-step.

The geographical repartition of the error is very similar to the one observed for the translating hexagon, with most of the error located around the corners. The error is largest for the front corner (more than 1% in Figure 5.32).

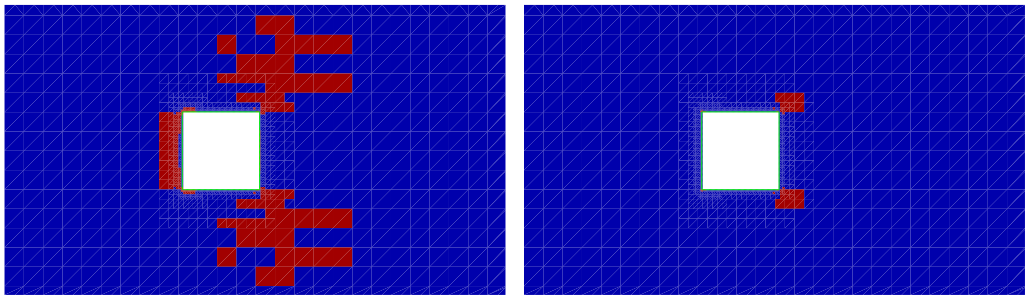

(a) (b)

Figure 5.32. In red are the areas of the domain where the error on the u component of the velocity field is more than 0.1% (a) and 1% (b). An adaptive mesh refined down to level 8 was used.

This test emphasises the role played by reconstruction errors and corners in general. Because interface curvature at the corner is not continuous, corners are known to be the reason for many problems for most codes including static problem. It has been shown that the total error in this problem can be directly related to the truncation error at the corners of the square.

Lid-driven cavity

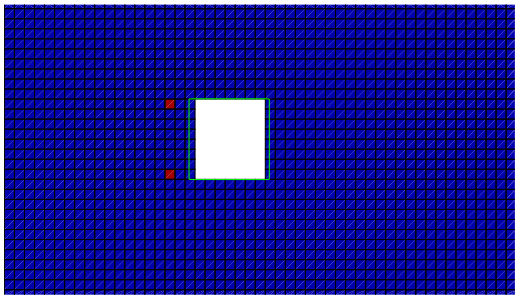

Figure 5.33. In red are the areas of the domain where the error on the u component of the velocity field is more than 0.1% for a Cartesian mesh.

The idea of the lid-driven cavity test is to compare solutions for a lid-driven cavity flow (see previous chapter) for a cavity driven by a Dirichlet boundary condition on the velocity of the top part of the domain and a cavity driven by a moving solid translating at the same speed.

The simulations were made for a Reynolds number of 10000 and a uniform mesh of resolution 64×64. The steady state is considered as reached when the difference between the velocity field ten time-steps apart is smaller than 0.00001.

It can be seen in the Gerris test suite [Popinet(2001b)] that the static version of the code compares very well with the benchmark results by Ghia et al. [Ghia et al.(1982)]. Similar comparisons are realised using a moving boundary. Figure 5.34 shows that the moving version of Gerris agrees very well with the results by Ghia et al. The results from the moving version look very similar to the ones of the test suite.

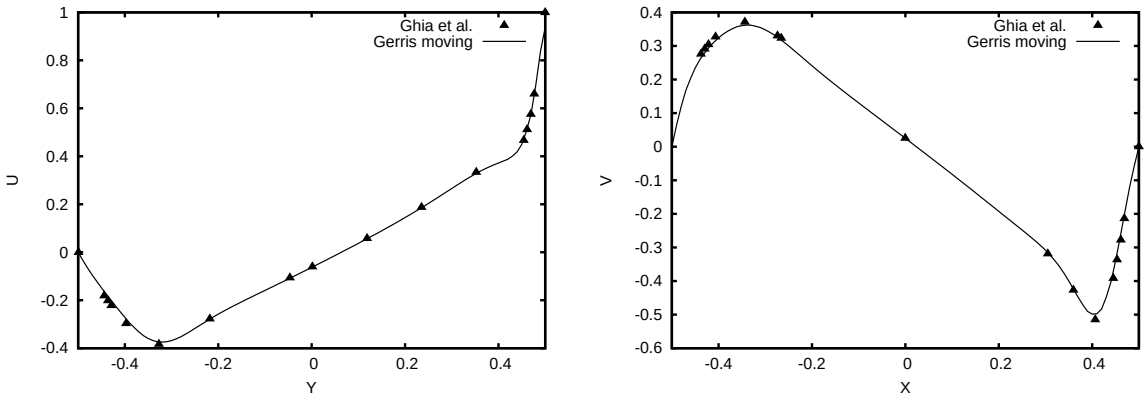

Figure 5.34. Comparison between benchmark test by Ghia et al.[Ghia et al.(1982)] and results with Gerris moving. (a) Vertical profile of the x-component of the velocity on the centre-line of the cavity. (b) Horizontal profile of the y-component of the velocity on the centre-line of the cavity.

The static and moving versions do not actually give exactly the same results. Figure 5.35 shows the difference between the cross-section velocities given by both models. The difference goes up to 0.007 (several percent).

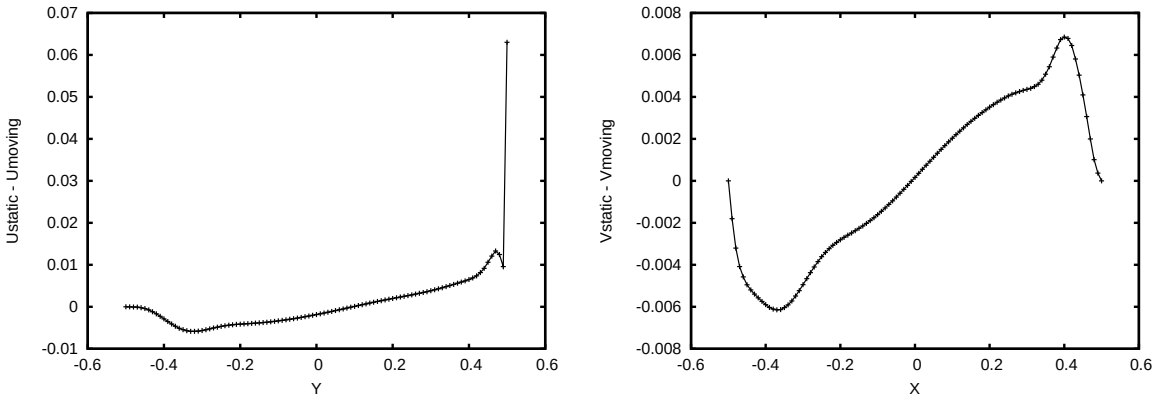

Figure 5.35. Difference between the results of the static and moving Gerris code for the cross-sections of the cavity displayed in Figure 5.34.

The results of the lid-driven cavity using a moving boundary, despite not being identical to the calculation with the static code, can be considered as a success. This test is not very strong on the code as there is no solid flux involved in the simulation. Nevertheless, it shows that the diffusion scheme seems to be working reasonably well with solid boundary forcing a fluid.

5.7 Flow past a cylinder

The flow past a cylinder is a classical benchmark for the validation of solid/fluid interaction models for static [Taira and Colonius(2007)] [Le et al.(2006)] [Lai and Peskin(2000)] [Kim et al.(2001)] [LimaESilva et al.(2003)] [Marella et al.(2005)] [Saiki and Biringen(1996)] [Zhang and Zheng(2007)] as well as moving [Taira and Colonius(2007)] [Le et al.(2006)] [Marella et al.(2005)] boundaries. Its geometrical simplicity and dependence on a limited number of parameters makes it easy to set up and therefore to compare results with other published data. This simplicity is only apparent as the problem involves complex physics and transitions from laminar to turbulent regimes. This explains the abundance of experimental data for this setup which is a great asset for validation [Coutanceau and Bouard(1977)] [Roshko(1953)].

In 2D, the geometry consists of a channel with slip boundary conditions on the wall (i.e. the velocity component normal to the wall is equal to zero and the viscous stress tangential to the wall is null). On one end of the channel a constant inflow boundary condition (Dirichlet boundary condition normal to the boundary) is imposed and an outflow boundary condition at the other end (zero normal derivative at the boundary). A solid cylinder is placed in the channel at equal distances from the walls of the channel. The boundary conditions on the cylinder's contours are no-slip boundary conditions (i.e. the norm of the velocity at the interface is equal to zero).

The full incompressible Navier-Stokes equations are solved on the whole domain.

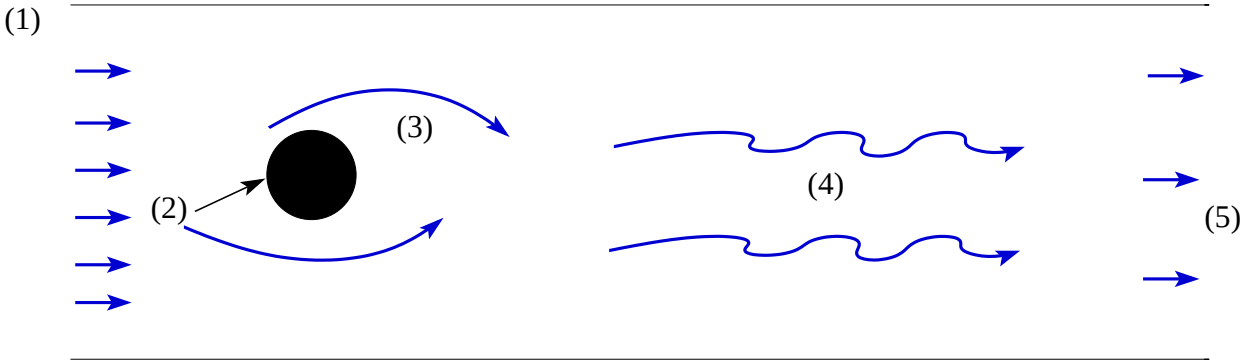

Figure 5.36. Sketch of the 2D setup for the flow past a cylinder. The flow takes place within a channel. (1) Upstream inflow boundary condition (2) Cylinder (3) Recirculation region (4) Downstream wake (5) Outflow boundary condition.

The three dimensional parameters describing the flow around a cylinder, the diameter of the cylinder d, the inflow velocity u_0 and the kinematic viscosity of the fluid ν can be put together into a single parameter, the Reynolds number, defined as

$$\mathrm{Re} = \frac{u_0\, d}{\nu}.$$

The Reynolds number is representative of the importance of the inertial effects to the viscous effects and therefore is used to characterised the different flow regimes observed around the cylinder from laminar to chaotic (see streamlines for regimes from laminar to turbulent in Figure 5.37).

Despite not being mentioned as often as the Reynolds number, a second parameter is relevant to this problem, λ the ratio between the diameter of the cylinder and the width of the channel. It is rarely mentioned in papers and can be calculated most of the time from the dimensions of the channel or the computational domain. It has nevertheless quite a strong influence on the problem, as shown in the parametric study by Coutanceau and Bouard [Coutanceau and Bouard(1977)]. For all the simulations realized except the ones for which it is mentioned, λ is 0.125.

Two regimes are considered, the laminar regime for Reynolds numbers from 0 to 45 and part of the periodic, vortex shedding regime for Reynolds numbers from 200 to 450. The 45–200 Reynolds range was skipped, even though it would have been interesting to determine the Reynolds number for which transition to vortex shedding occurs, for two reasons. First, there exists an empirical formula which links the frequency of vortex shedding to the Reynolds number, (Equation 5.22) which is considered to hold true for the range $250 < \mathrm{Re} < 200000$, that is of use to make comparisons. Secondly, the smaller the Reynolds number, the lower the frequency of vortex shedding. Therefore, to measure the frequency, simulations need to be longer. This is not a problem for a static cylinder, but for a moving one, as it means that the domain needs to be longer which has direct consequences on the computation time. Only Reynolds numbers less than to 450 were considered because, the higher the Reynolds number the thinner the viscous boundary layer near the cylinder, and then the more resolution is needed, which makes the simulation more expensive to realise (we are doing direct numerical simulations of the problem).

The choice of quite a narrow range of Reynolds number to test the code is not believed to be a problem as most of the codes found in the literature are validated in the same range of Reynolds numbers and usually on two values of the Reynolds number per regime.

5.7.1 Static Cylinder

Static cylinder -Laminar regime - Re 0 to 45

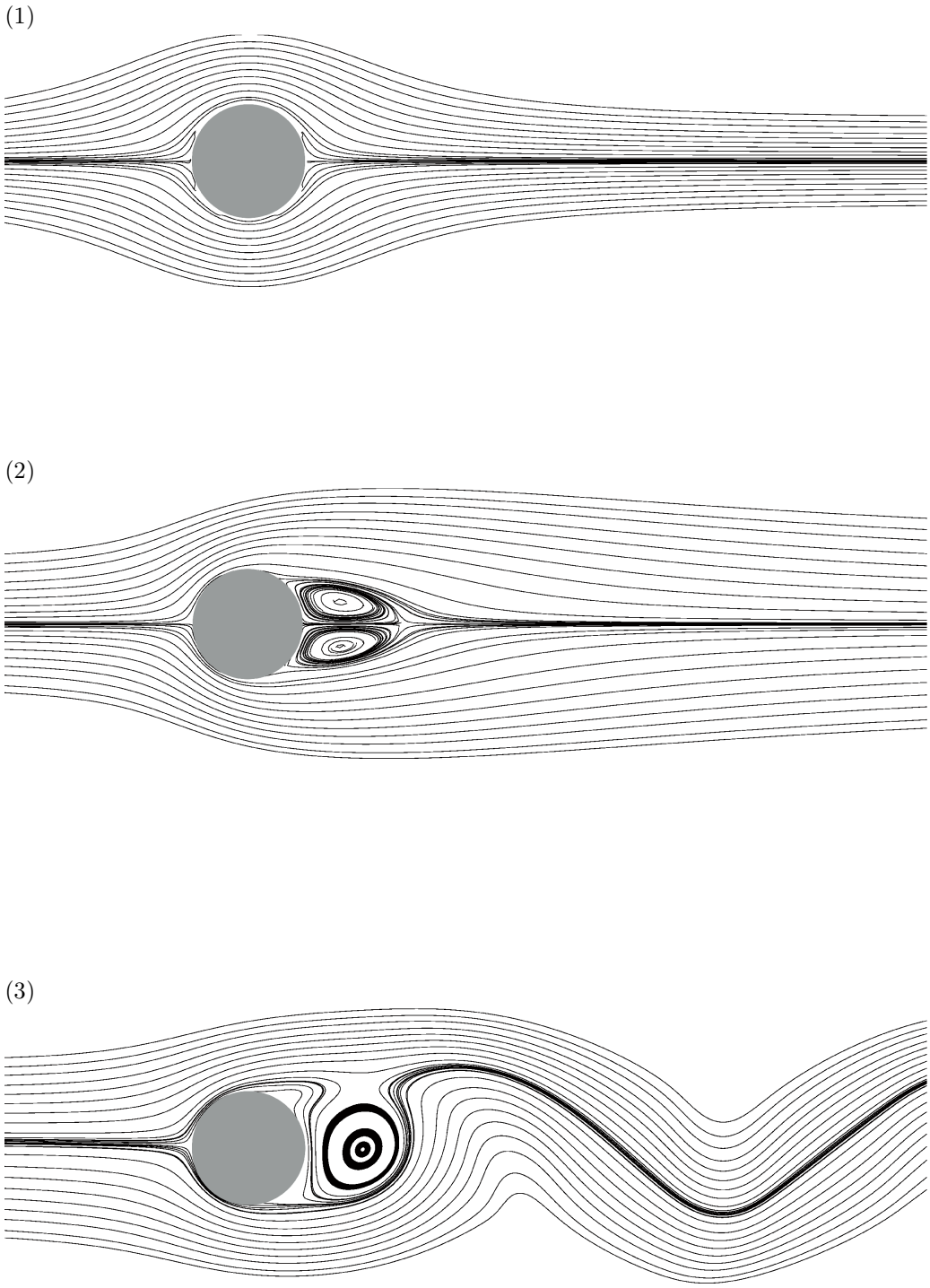

Figure 5.37. Streamlines for the flow over a static cylinder at Re 0 (1), 20 (2) and 200 (2).

The laminar regime for the flow past a cylinder is considered to range from a Reynolds number of 0 (for a theoretical fluid of infinite viscosity - Figure 5.37) to values of about 90 [Tritton(1988)]. Instabilities are observable at Reynolds numbers lower than 90, with the periodic wake first appearing at Reynolds numbers of about 40 [Bloor(1964)]. Nevertheless, for low Reynolds numbers the flow can be considered as laminar everywhere [Bloor(1964)].

In the laminar regime, the flow detaches from the cylinder to form a pair of recirculating eddies in the cylinder's wake. During the transitional regime, these symmetrical recirculations grow until reaching a stable state when the flow is fully developed. The physical characteristics of the recirculation are controlled by the Reynolds number and λ. For a constant value of λ, the length of the recirculating region grows proportionally with the Reynolds number (Figure 5.38).

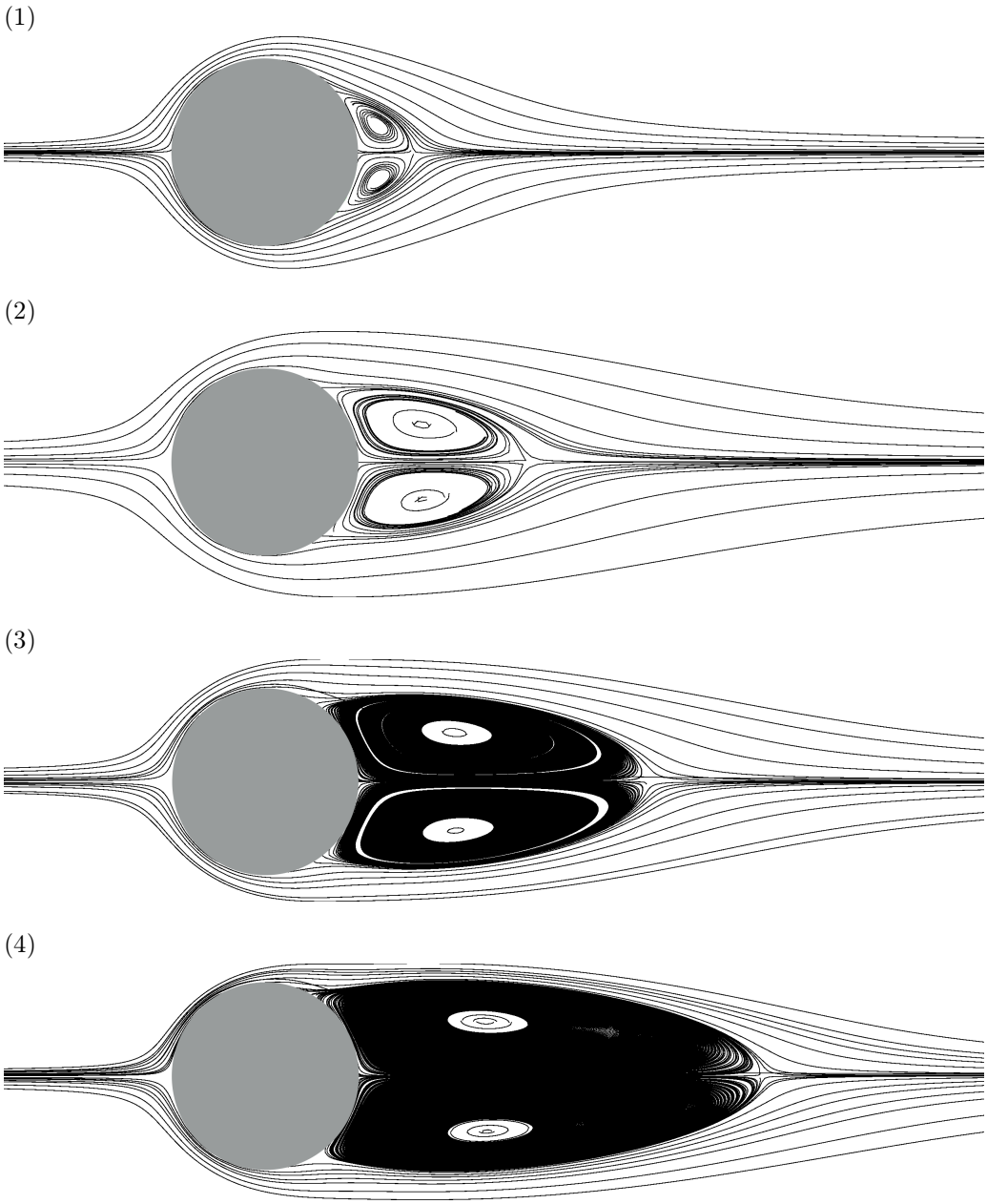

Figure 5.38. Streamlines for a flow behind a static cylinder for Re 10 (1), 20 (2), 30 (3) and 40 (4).

The shear created by the viscous friction of the fluid on the cylinder's surface generates vorticity. Two zones of high vorticity are created at the top (negative) and bottom (positive) of the cylinder. Vorticity isolines for Reynolds numbers of 20 and 40 are displayed in Figure 5.39. The higher the Reynolds number, the further away the same isoline extends.

The two stagnation points can be observed on the front and back of the cylinder, on the axis of symmetry of the problem. Most vorticity isolines start near the front stagnation point and end near one of the detachment points on the top or bottom of the cylinder. For higher Reynolds numbers one can see that some vorticity isolines are at the back of the cylinder between the back stagnation point and the two detachment points.

A region of high pressure exists at the front of the cylinder where the inflow meets with the solid surface (Figure 5.40). The two recirculations in the wake of the cylinder form regions of low pressure where the flow accelerates past the cylinder.

The simulated vorticity and pressure fields are qualitatively very similar to that found in the literature. A quantitative assessment of these simulations is necessary and can be done through measuring several parameters. A common approach is the measurement of the physical characteristics of the cylinder's wake from the streamlines (Figure 5.41).

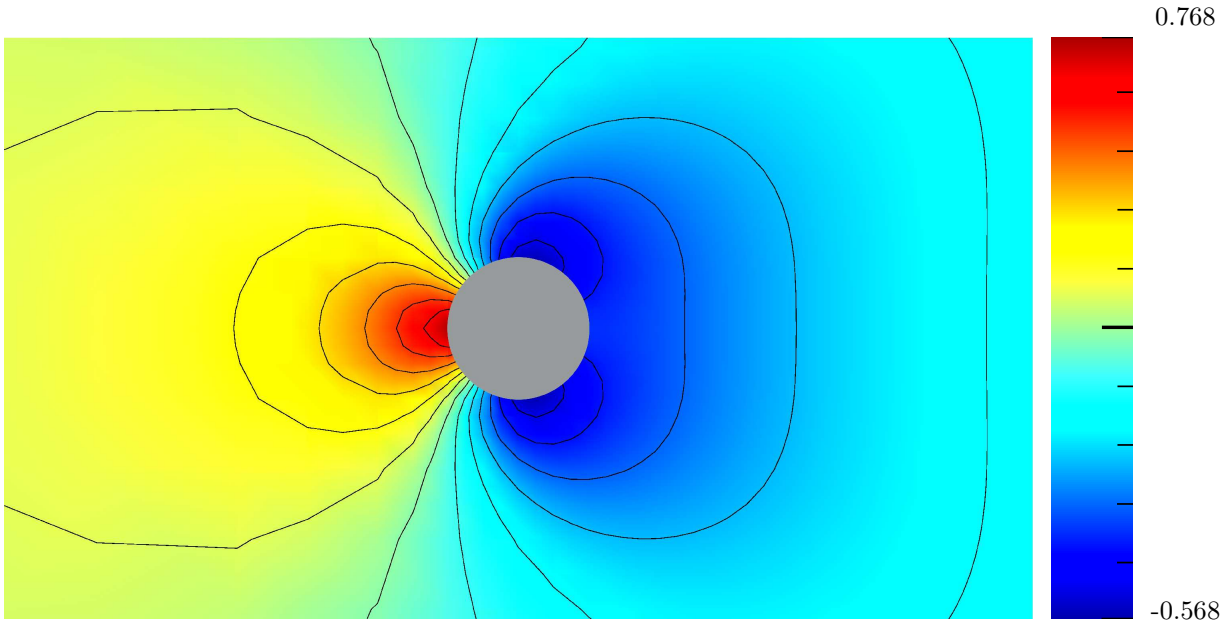

Figure 5.40. Pressure field around the static cylinder for Re 20.

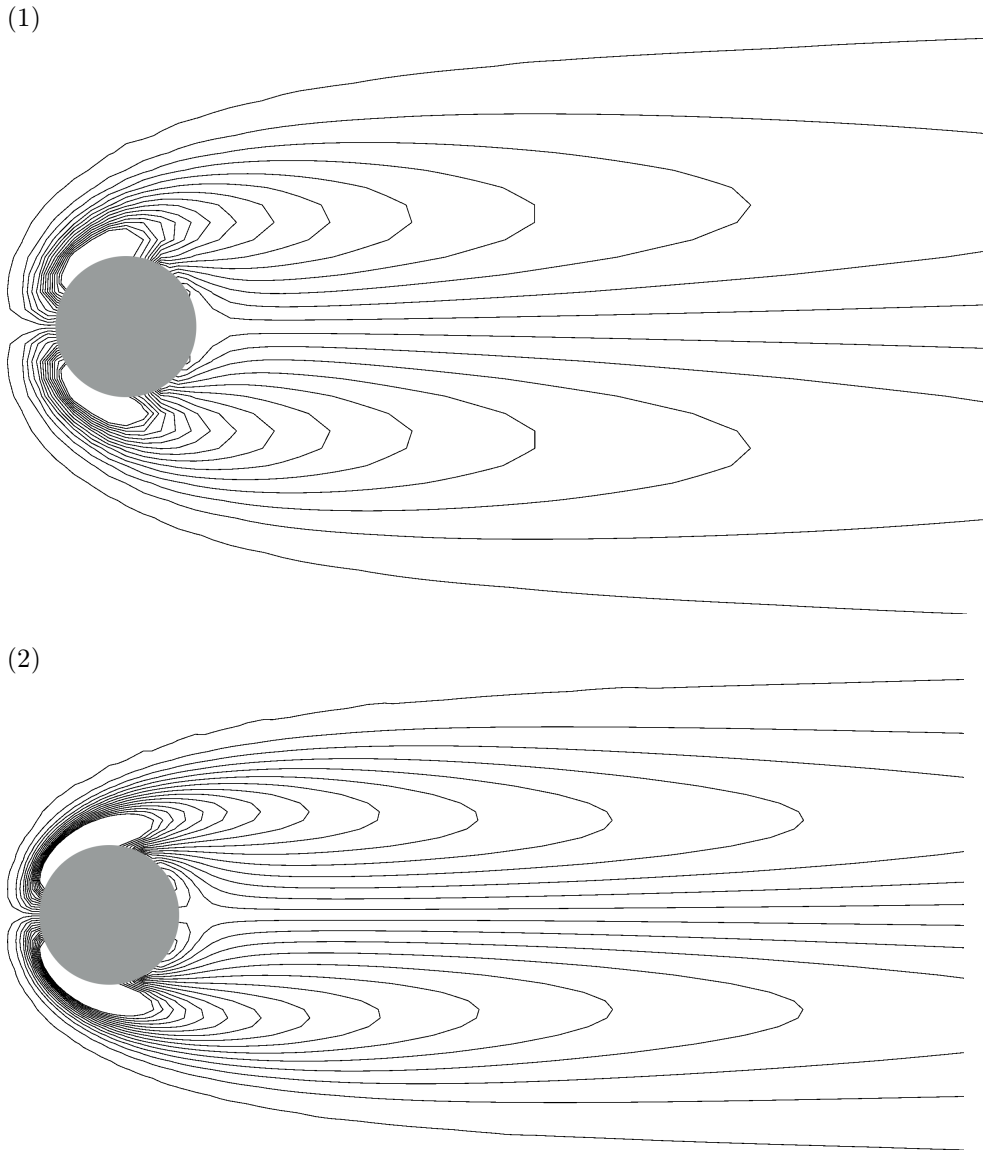

Figure 5.39. Isolines of vorticity for Re 20 (1) and 40 (2). Each figures contains 30 isolines going from -30 s^{-1} to 30 s^{-1}.

The length of the closed wakes (Parameter l in Figure 5.41) were measured for Reynolds numbers from 5 to 45 for simulations realized in a domain of size 5x1 with $\lambda = 0.125$ and a resolution down to level 8 ($1/2^8$) on the solid boundary of the cylinder. Mesh adaptivity was used on the vorticity field down to level 7. l can be defined as the distance from the cylinder to the point where the x component of the velocity changes sign. It was obtained from outputs of the stream-wise component of the velocity on the cross-section corresponding to the symmetry axis of the problem.

The values of l obtained using the static version of Gerris seem to be linearly dependant on the Reynolds number (Figure 5.42). Despite this and results found in other papers [Coutanceau and Bouard(1977)], no analytical formulation of the closed wake length was found in the literature.

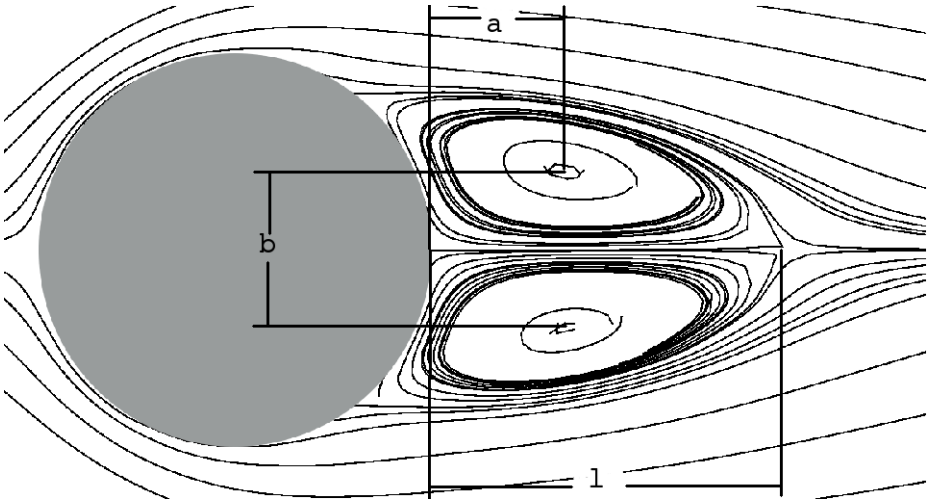

Figure 5.41. Definition of the characteristic dimensions of the laminar wake.

Comparison with experimental data from Coutanceau and Bouard [Coutanceau and Bouard(1977)] are plotted on Figure 5.42 as well as two numerical results. There is a good agreement between the numerical results and the simulation realized using Gerris. More results collected in the literature have been put together in Table D.1 in the moving cylinder section and the results obtained for the static cylinder are comparable. Nevertheless, it is only a rough comparison, as not many of these simulations are identical. For all of them, the Reynolds number of the flow is clearly identified but the size of the domain and the boundary conditions (on which the λ parameter depends) varies a lot between the different publications. Although the size of the domain and the boundary conditions are always specified in the description of the problem, it is not often that those ones are explicitly interpreted in term of the λ parameter, which is unfortunate, especially as Coutanceau and Bouard [Coutanceau and Bouard(1977)] explicitly demonstrated the importance of this parameter.

Usually large domains (compared to cylinder size) are required to minimise the effects of the boundaries. For most of the results reported in Table D.1, λ was calculated from the geometry described in the paper. Outflow boundary conditions for top and bottom were considered as an infinitely wide domain, therefore $\lambda = 0$ in this case.

Table 5.1. Characteristic dimensions of the wake behind a static cylinder obtained with Gerris for the flow behind a static cylinder with $\lambda = 0.125$.

Re	l/d	a/d	b/d	C_d
10	0.268	0.109	0.279	3.68
15	0.591	0.244	0.352	2.96
20	0.908	0.348	0.424	2.57
25	1.211	0.440	0.478	2.32
30	1.522	0.532	0.522	2.14
35	1.824	0.603	0.551	2.00
40	2.130	0.690	0.578	1.89
45	2.420	0.777	0.603	1.81

Despite the wide range of λ parameters that can be found in the literature, very little variation can be observed regarding the size of the wake obtained. For example, at a Reynolds number of 20, most values for l are between 0.92 and 0.93, and for values of λ ranging from 0 to 0.0625. Simulations were run for a Reynolds number of 20 for four values of λ (0.0125, 0.0625, 0.03125 and 0.015625) to investigate the influence of λ on the wake. Very little difference was noticed in the physical characteristics of the wake (Table 5.2), with the two extreme values recorded for wakes of 0.908 and 0.939, which in all cases remains comparable to the values found in other papers.

This remark regarding the importance of λ in the parametrisation of the problem is surprising as it contradicts the observation by Coutanceau and Bouard [Coutanceau and Bouard(1977)] showing important variation of l when λ varies (from 0.60 for λ = 0.12 to 0.93 for $\lambda = 0$). This might be explained by the different natures of the boundary conditions between their experiments and the numerical simulations. Indeed, working with a real fluid, the conditions applied on Coutanceau and Bouard's channel were proper wall conditions (no slip) whereas for numerical simulations, when wall are used (i.e. when $\lambda \neq 0$), slip boundary conditions are applied.

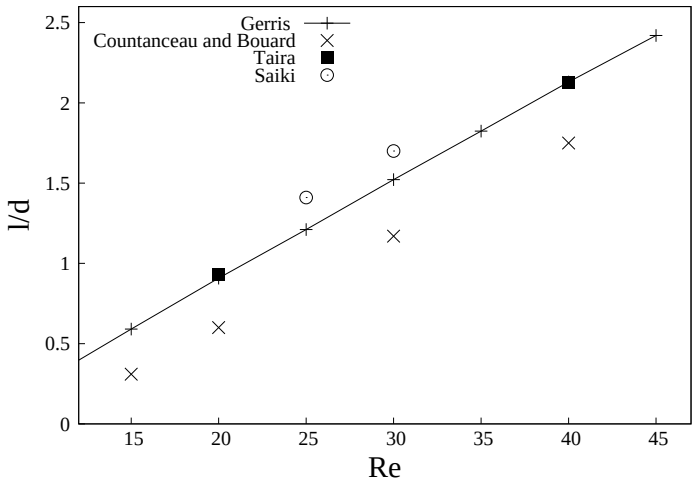

Figure 5.42. Length of the wake behind the static cylinder.

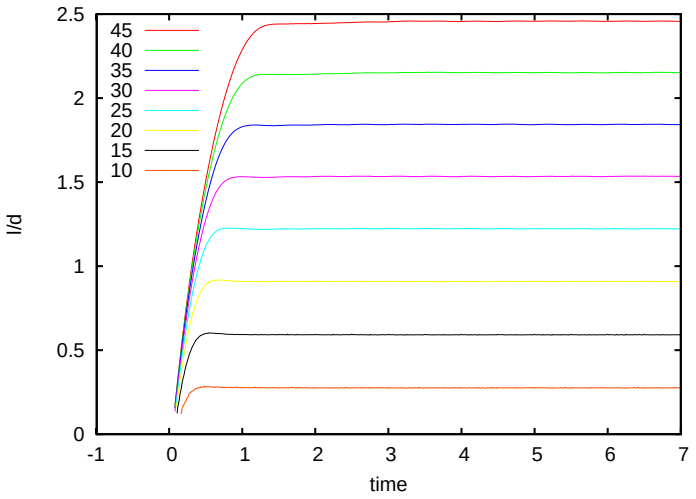

Figure 5.43. Evolution of the size of the wake behind a moving cylinder with time for Reynolds numbers from 10 to 45.

Two other characteristics of the recirculation that are often measured are the x coordinate of the centre of the recirculations and the distance between the centres (resp. a and b on Figure 5.41). The values measured for these parameters are summarised in Table 5.1. As for l, a and b did not seem to be very sensitive to λ and were comparable to the ones reported in Table D.1.

Table 5.2. Characteristic dimensions of the wake behind a static cylinder obtained with Gerris for the flow behind a static cylinder at Re 20.

λ	l/d	a/d	b/d	C_d
0.125	0.908	0.348	0.424	2.57
0.0625	0.939	0.351	0.433	2.28
0.03125	0.929	0.351	0.434	2.16
0.015625	0.915	0.346	0.432	2.11

The hydrodynamical forces experienced by the cylinder (pressure forces and viscous stress) are another characteristic quantity of the problem. The stream-wise and transverse components of these forces are often referred to in terms of drag coefficient (C_d) and lift coefficient (C_l).

C_d is defined as

$$C_d = \frac{F_x}{\rho u_0^2 (d/2)}$$

and C_l as

$$C_l = \frac{F_y}{\rho u_0^2 (d/2)}$$

where F_x is the integral of the stream-wise component of the pressure forces and viscous stress over the surface of the cylinder, and F_y the traverse one. In the laminar case, the problem remains symmetrical which implies that $C_l = 0$.

The drag coefficients stabilises when the flow becomes steady (Figure 5.44) but noise remains, so an average over the last 3 time units was taken to determine the drag coefficients at steadiness.

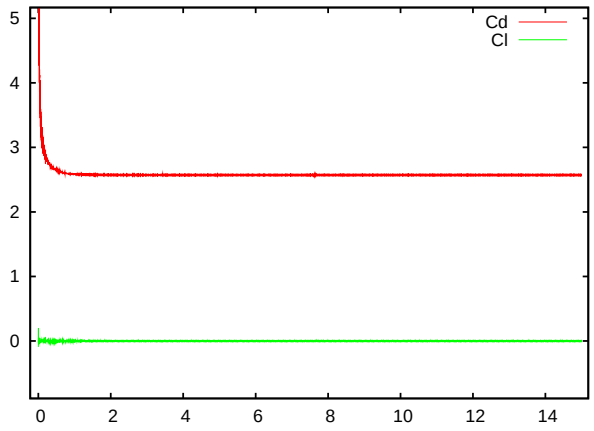

Figure 5.44. Drag coefficient versus time for Re 20.

Unlike for the characteristics of the wake, significant differences were noticed with published values, where drag coefficients around 2.1 are mainly reported for a Reynolds number of 20, against a drag coefficient of 2.57 obtained by Gerris.

The ratio cylinder diameter to size of the channel used for all these simulations was large compared to those of most published numerical results, so an investigation of the influence of λ on simulations is required. Simulations of a flow past a cylinder at a Reynolds number of 20 were run for values of λ of 0.125 (current), 0.0625, 0.03125 and 0.0156325.

Convergence of the drag coefficient is observed when λ becomes close to zero (Figure 5.45). By extrapolation of the values of the drag coefficient found for λ equal 0.125 (current), 0.0625, 0.03125 and 0.0156325, it is possible to determine the drag coefficient for $\lambda = 0$ which is 2.07 here. Running a simulation using outflow boundary conditions instead of the channel's slip boundary conditions to mimic an infinite domain gives a value of 2.06 for the drag coefficient. In both cases, C_d is now in the range of values expected from the literature.

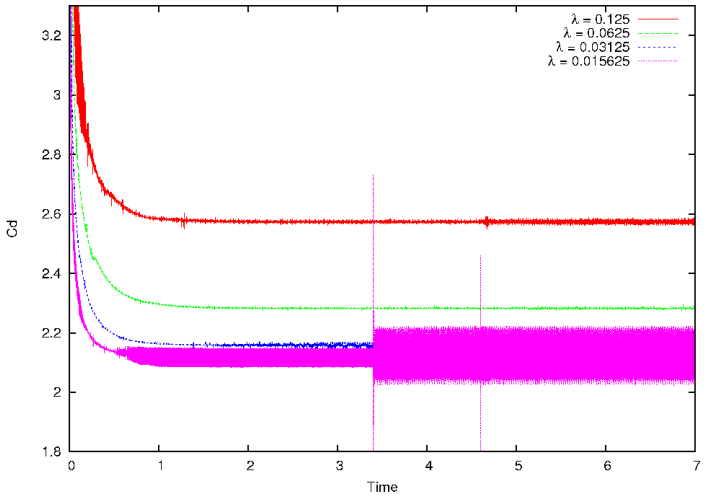

Figure 5.45. Drag coefficient versus time for four different values of the cylinder size to channel width ratio λ.

Static cylinder - Bénard-Von Kàrmann vortex Street Re 200-450

For higher Reynolds numbers, instabilities grow and the wake behind the cylinder becomes unstable. Vortices of alternate polarity form and detach periodically at the back of the cylinder forming the well known Bénard-Von Kàrmann vortex street [Benard(1908)] [Karmann(1912)].

The vortex shedding occurring behind the obstacle can be characterised by its frequency and by a non-dimensional number, the Strouhal number defined as

$$S_t = \frac{f\,d}{u_0},$$

where f is the frequency of shedding of the vortices, d the diameter of the cylinder and u_0 the inflow velocity at the domain boundary.

The vortex-shedding frequency increases as with the Reynolds number as illustrated in Figure 5.46. Roshko [Roshko(1953)] determined an empirical relationship between Reynolds and Strouhal number as

$$S_t = 0.212\,(1 - \frac{12.7}{\mathrm{Re}}). \tag{5.22}$$

The simulations setup was identical to the laminar case. Convergence was obtained for a resolution of level 9 on the solid interface and down to level 8 in the wake. The mesh was adapted in time according to the gradient of vorticity in order to resolve the vortices sufficiently (Figure 5.47) without wasting much computational time on the unimportant parts of the domain.

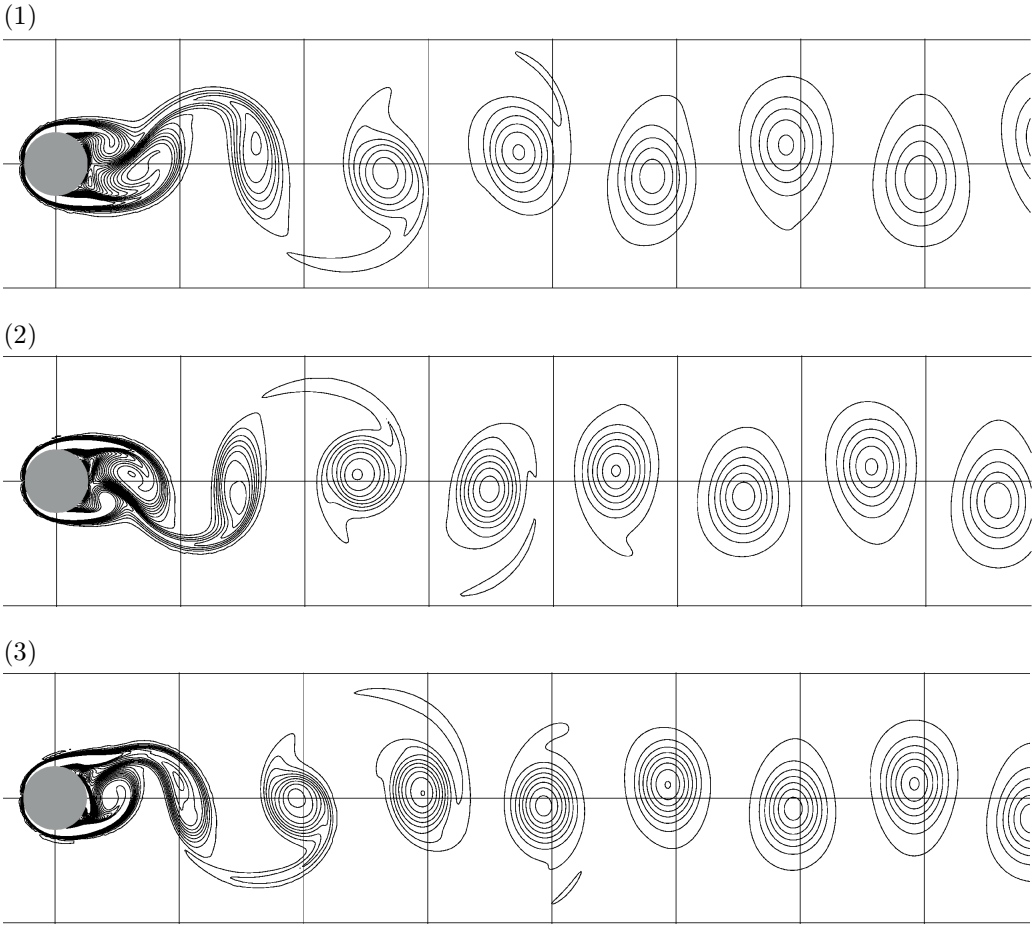

Figure 5.46. Vorticity isolines from the flow behind a static cylinder from Reynolds numbers of 250 (1), 350 (2) and 450 (3).

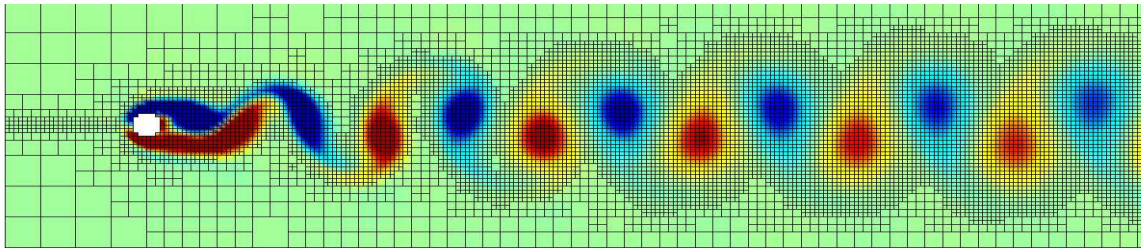

Figure 5.47. Use of the adaptive quadtree mesh to simulation the Benard-Von Karmann vortex street. Vorticity field for Re160.

The characteristics of the vortex street were calculated for a high ($\lambda = 0.125$) and a low ($\lambda = 0.025$) cylinder size to channel width ratio (Table 5.3). Good agreement is found with respect ot established results for a Reynolds number of 200, with larger but reasonnable differences found for higher Reynolds number (Figure 5.48 Figure 5.49). The largest difference with published results are found for the drag coefficient which is hardly surprising given its higher sensitivity to λ.

Table 5.3. Characteristics of the Von Karmann vortex street obtained with the static version of Gerris.

	$\lambda = 0.125$		$\lambda = 0.025$	
Re	S_t	C_d	S_t	C_d
150			0.185	
200			0.198	
250	0.216	1.513	0.204	
300	0.221	1.550	0.210	
350	0.224	1.569	0.214	1.423
400	0.228	1.590	0.220	1.443
450	0.231	1.609	0.221	
500			0.224	1.464

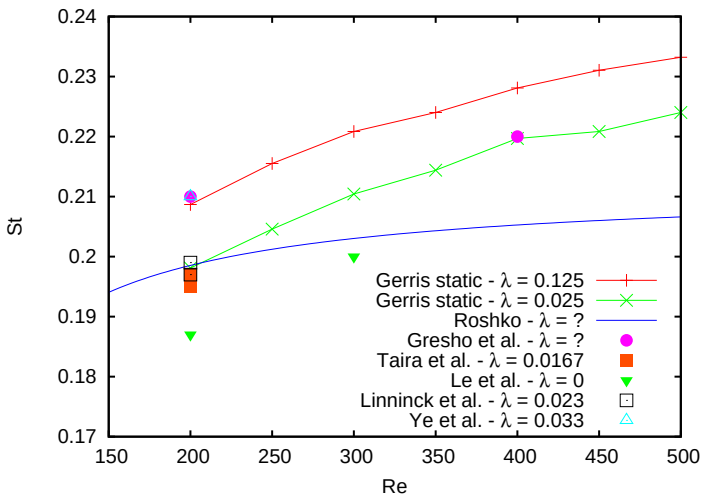

Figure 5.48. Strouhal number versus Reynolds number for Gerris and published results.

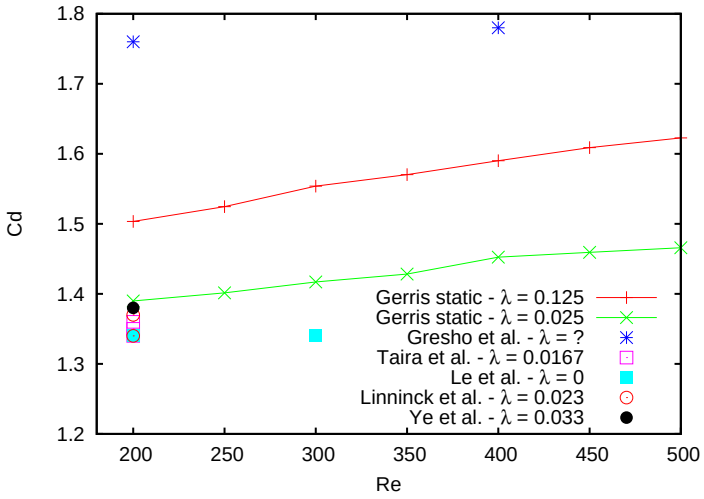

Figure 5.49. Drag coefficient versus Reynolds number for Gerris and published results.

5.7.2 Cylinder translating in a fluid at rest

As suggested by Coutanceau and Bouard [Coutanceau and Bouard(1977)], the problem of a cylinder translating in a fluid at rest is equivalent to the problem of a flow past a static cylinder.

It has been demonstrated that the Gerris Flow Solver accurately computes a flow past a cylinder for a wide range of Reynolds numbers. Comparisons between the static and moving solid boundary problem using Gerris are a good way of testing the performance of the solid/fluid interaction scheme just implemented in Gerris.

The test of the translating cylinder uses most features of the moving boundary model, with the moving object going through the whole domain. The modified advection and diffusion schemes are both involved and key to the problem, especially as the main parameter is the Reynolds number, which is the ratio of inertial to viscous effects.

The moving boundary part is very similar to the static cylinder one with the use of the same geometry, refinement criteria and both laminar and vortex-shedding regime being tested. The choice of the boundary condition was found to be of particular importance and is discussed in this section.

Moving cylinder - Laminar regime - Re 0 to 45

The first set of simulations is realized using a domain of size 8×1 with a cylinder of diameter 0.125. The domain is slightly bigger than the one used in the static case to allow the cylinder to move for a long enough time. The cylinder moves from 0.5 space units from one end of the domain to 0.5 space units from the other end of the domain (i.e. the simulation lasts for 7 time units). The constant inflow boundary condition used for the flow past a static cylinder is turned into an outflow boundary condition. The cylinder's motion is impulsively started at the beginning of the simulation.

The characteristics of the wake (Figure 5.41) after 7 time units are shown in Table 5.4 and their length is plotted in Figure 5.50. Whereas wake sizes remain in the range defined by the experiments by Coutanceau and Bouard [Coutanceau and Bouard(1977)], they are noticeably smaller than the ones found using the static version of the code.

As the length of the wake is proportional to the Reynolds number, it was first supposed that these differences could originate from a high numerical viscosity of the new moving boundary scheme. The use of higher refinement and smaller time step proved this hypothesis wrong. The results displayed in Table 5.4 and Figure 5.50 are the converged solution of the moving cylinder previously described.

Table 5.4. Characteristics of the cylinder wake for outflow boundary conditions at both ends of the domain.

Re	l/d	a/d	b/d
10	0.175	0.058	0.253
15	0.462	0.200	0.324
20	0.683	0.267	0.376
30	1.394	0.328	0.569
40	1.895	0.628	0.551

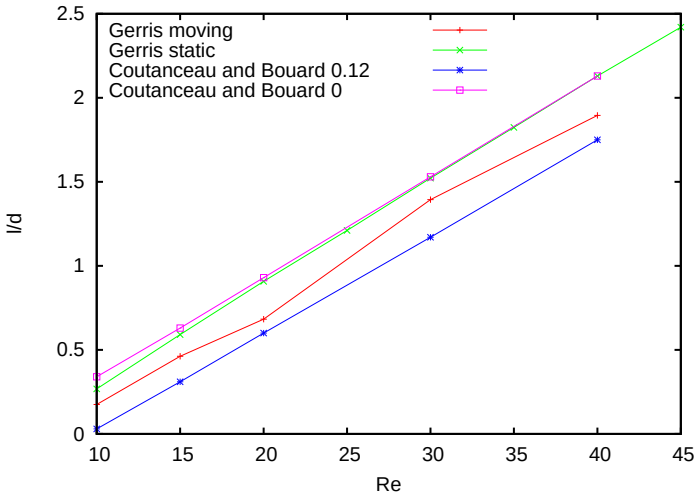

Figure 5.50. Length of the cylinder wake normalised by the cylinder diameter versus the Reynolds number for outflow boundary conditions at both end of the domain. The results by Coutanceau and Bouard are for $\lambda = 0.12$ and 0. The Gerris simulation are for $\lambda = 0.125$.

Influence of the geometry

A closer look at the evolution of wake length with time for a Reynolds number of 20 (Figure 5.51) shows that the recirculation quickly reaches a size comparable to the static solution but never stabilises. The closer the cylinder gets from the other end of the domain, the smaller the size of the recirculation. This suggests that the problem solved is constantly changing with the position of the cylinder in the channel and is therefore geometry-dependent.

Several domain lengths were tested to confirm the influence of the domain size on the size of the wake of cylinder (Figure 5.51). Once normalised, the evolution of wake length with time is very similar. For large domains the curves are almost identical, meaning that the recirculation size at the start and the end of the simulation are the same. The decrease in size of it being inversely proportional to the length of the domain. For smaller simulation domains, the start and end wake characteristics are not quite similar for the different domains, but, nevertheless, the decrease in size of the recirculation is similar to all the other curves.

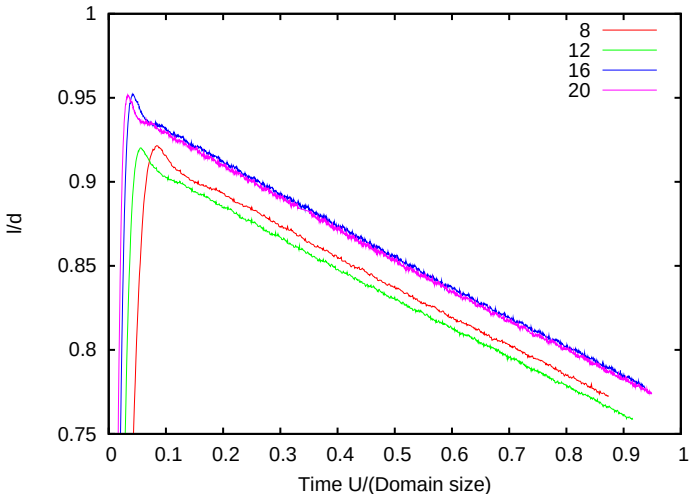

Figure 5.51. Size of the wake versus normalised time behind a moving cylinder with outflow boundary conditions at both ends of the domain for 4 different domain lengths.

In addition, the influence of cylinder location within the domain at the beginning of the simulation was investigated through four runs in a 1×20 domain with the cylinder starting at different locations (Figure 5.52). As in the previous run, the decrease of the recirculation size during the cylinder's progression seems to be domain-dependent and does not depend on the influence of the starting location of the cylinder. The wake size at the start and end of the simulation varies between the different simulations without following any apparent rule.

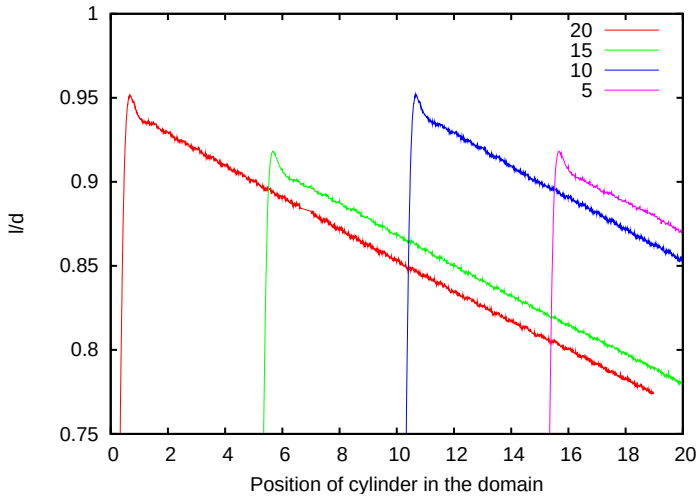

Figure 5.52. Size of the wake versus normalised time behind a moving cylinder with outflow boundary conditions at both end of the domain for 4 different a starting positions of the cylinder within a 1 x 20 domain.

It has been shown that the solution of the problem solved by the moving boundary code is geometry-dependent and can be directly related to the domain size. In all cases there is no coherence between the results obtained using the static code. The static and moving problems have thus to be different.

Dirichlet boundary condition

The main difference between the two problems lies in the boundary condition at the left of the domain. The inflow boundary condition in the static case was turned into an outflow condition in the moving one. The inflow boundary condition is a Dirichlet boundary condition that imposes the velocity of the fluid on one side of the domain. The outflow boundary condition, not only imposes a zero normal derivative on the boundary but gives more degrees of freedom to the problem. There is therefore less constraint on the system of equations solved with an outflow boundary condition. A Dirichlet boundary condition imposing a velocity equal to zero instead of the new outflow would change the nature of the problem and make it more similar to the static boundary one (Dirichlet on the left, slip on top and bottom, outflow on the right).

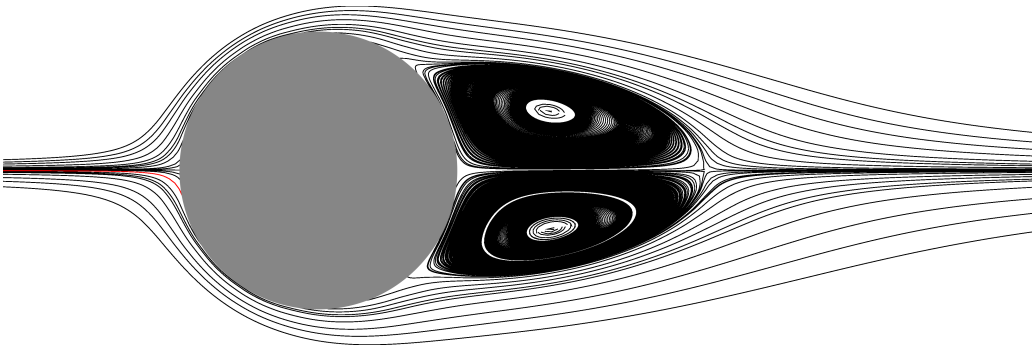

Figure 5.53. Streamlines for a moving cylinder translating in a fluid a rest at Re 20.

Table 5.5. Characteristics of the cylinder wake for Dirichlet and outflow boundary conditions at each end of the domain.

Re	l/d	a/d	b/d	Cd
10	0.276	0.106	0.280	3.71
15	0.591	0.239	0.364	2.98
20	0.908	0.345	0.427	2.59
25	1.222	0.440	0.485	2.34
30	1.534	0.524	0.522	2.16
35	1.842	0.591	0.559	2.03
40	2.153	0.689	0.589	1.92
45	2.457	0.779	0.611	1.84

The physical dimensions of the recirculation (Table 5.5) are in far better agreement with the static version of the code when a Dirichlet boundary condition is used. This also means that there is a very good match with the experimental results of Coutanceau and Bouard [Coutanceau and Bouard(1977)] (Figure 5.54) and good agreement with other published numerical results (Figure 5.55).

The excellent agreement with the static version of the code is the major point, as the differences between the static code and published experimental and numerical results have already been discussed.

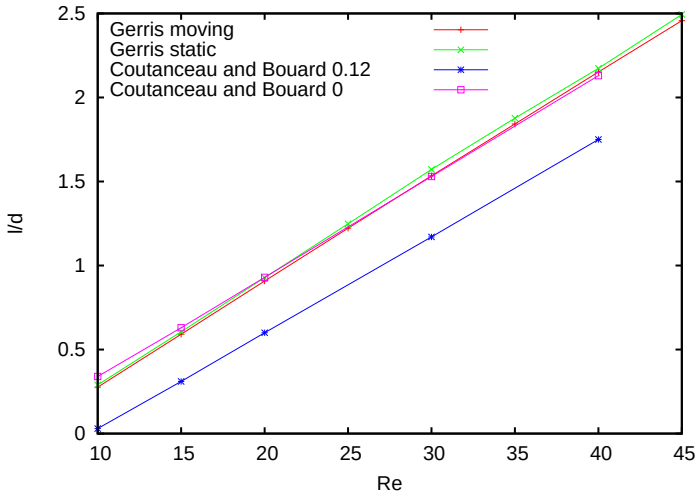

Figure 5.54. Length of the cylinder wake normalised by the cylinder diameter versus the Reynolds number for Dirichlet boundary condition at one end of the domain and outflow boundary condition at the other end. The results by Coutanceau and Bouard are for $\lambda = 0.12$ and 0. The Gerris simulation are for $\lambda = 0.125$.

There is also a very good agreement between the static and moving version of the code for the drag coefficient (Figure 5.55). Pressure forces have an important contribution to the total hydrodynamic forces experienced by the cylinder, proving that the pressure forces around the cylinder are computed accurately. This is of special importance as the implementation of the moving boundaries mainly lies in the computation of the solid fluxes near the boundary. Errors in the calculation of the solid flux are most likely to prejudice the non-divergence of the flow, which is corrected by the Poisson solver. Divergence correction and pressure update are closely linked, therefore obtaining a good pressure field demonstrates that the errors in computation of the solid fluxes remain reasonably small.

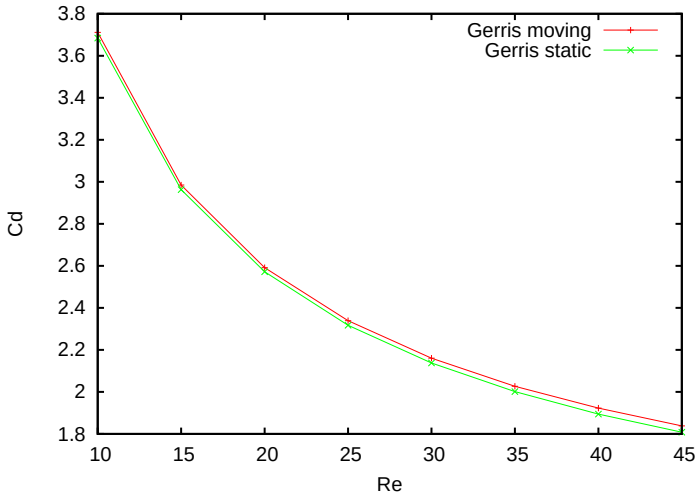

Figure 5.55. Comparison of the drag coefficients for the static and moving versions of the code.

Good performance of the two-dimensional moving adaptive version of the code has been demonstrated for the laminar regime.

It is clear that the use of Dirichlet boundary conditions instead of the inflow is necessary to have two problems that are equivalent from a mathematical point of view. Nevertheless, it is intuitively not obvious why the physical problem of a cylinder translating in a flow at rest should be described using Dirichlet boundary conditions rather than outflow ones.

Fluid entrainment

One possible explanation to the decreasing recirculation observed with the outflow boundary conditions at both ends of the domain is that the whole fluid domain is put into motion by the translating cylinder. With slip boundary conditions at the top and bottom ends of the domain and the two outflow ones, the is no resistance to streamwise motion of the fluid. Momentum is transmitted to the fluid by the cylinder in motion. Under that impulsion, the whole fluid starts progressively to get into motion. The relative speed of the cylinder therefore decreases with time, and the size of the recirculation decreases as well.

Boundary conditions and Poisson solver

Another interesting point is the sensitivity to boundary conditions that is related to the variation of shape of the cylinder due to the solid interface reconstruction. Despite the cylinder keeping a constant average shape, the "oscillations" it does around this average shape might be responsible for the extra sensitivity to the boundary conditions. These changes of shapes result in small variation of mass of the object. This means that at each time step there will be a small excess or shortage of mass in the vicinity of the object. To ensure mass-conservation, the Poisson solver will have to compensate for the missing or extra fluid. As the fluid is incompressible in the whole domain, this can only be done through the boundary conditions.

Another way of seeing this problem is to say that the compatibility conditions for the Poisson solver,

$$\int_{\partial\Omega(t)} \nabla \cdot \boldsymbol{u}\,\mathrm{ds} = \int_{\partial\Omega_d(t)} \nabla \cdot \boldsymbol{u}\,\mathrm{ds} + \int_{\partial\Omega_s(t)} \nabla \cdot \boldsymbol{u}\,\mathrm{ds} = 0,$$

has to been satisfied. $\partial\Omega(t)$ is the boundary of the problem, i.e. the boundary of the rectangular domain $\partial\Omega_d$(t) and the boundary of the solid object $\partial\Omega_s(t)$. A change of geometry of the solid object implies a change in the solid boundary term of the compatibility condition $\int_{\partial\Omega_s(t)} \nabla \cdot \boldsymbol{u}\mathrm{ds}$, which has to be counterbalanced in the domain boundary term. This way, solid object and domain boundary conditions are closely linked.

Dirichlet boundary conditions impose the velocity and therefore the flux of mass through the boundary, so, they strongly constraint the problem. Conversely, outflow boundary conditions only ensure a zero normal derivative on the boundary giving more degrees of freedom to the problem and allowing an adaptation of the mass flux through the boundary that the Poisson solver can use to satisfy the compatibility condition.

When two outflow boundary conditions are used at each end of the domain, there is interaction between the solid object and both outlets. It would be little surprising if the position and size of the domain influences the fact that the solid object is interacting more with one boundary condition than the other and therefore the problem is different and the solution is different. This way, the problem would continuously change and therefore the solution to the problem continuously would change as well, potentially influencing the fact that the size of the wake never stabilises.

When only one outflow is used, the problem is more constrained and the influence of boundary conditions does not changed with time. Therefore, the problem does not change and convergence should not get affected.

It has to be stated that the use of Dirichlet boundary conditions on the whole domain boundary is not permitted, otherwise the compatibility condition will never be fulfilled and then the Poisson solver will never be able to convergence. This remark is of special interest regarding the inclusion of solid propagules within the CFD model of the stirred box (see previous chapter). It is not possible to use a closed box in this case. Modelling the open top of the box by a lid is not an option anymore and more freedom should be given to the system at this place.

Vortex-shedding regime - Re 200-450

For the reasons explained above, the inflow boundary condition of the static problem is replaced by a Dirichlet boundary condition of velocity equal to zero (i.e. slip-wall) for all the following simulations. The refinement used near the interface is down to level 10. Simulations were run for the same range of Reynolds numbers as for the static code to compare both versions.

Quantitatively, as expected vortex-shedding takes places in all of our simulations (Figure 5.56). The vorticity and pressure fields, which are both independent from the static or moving nature of the problem, look very similar in both cases.

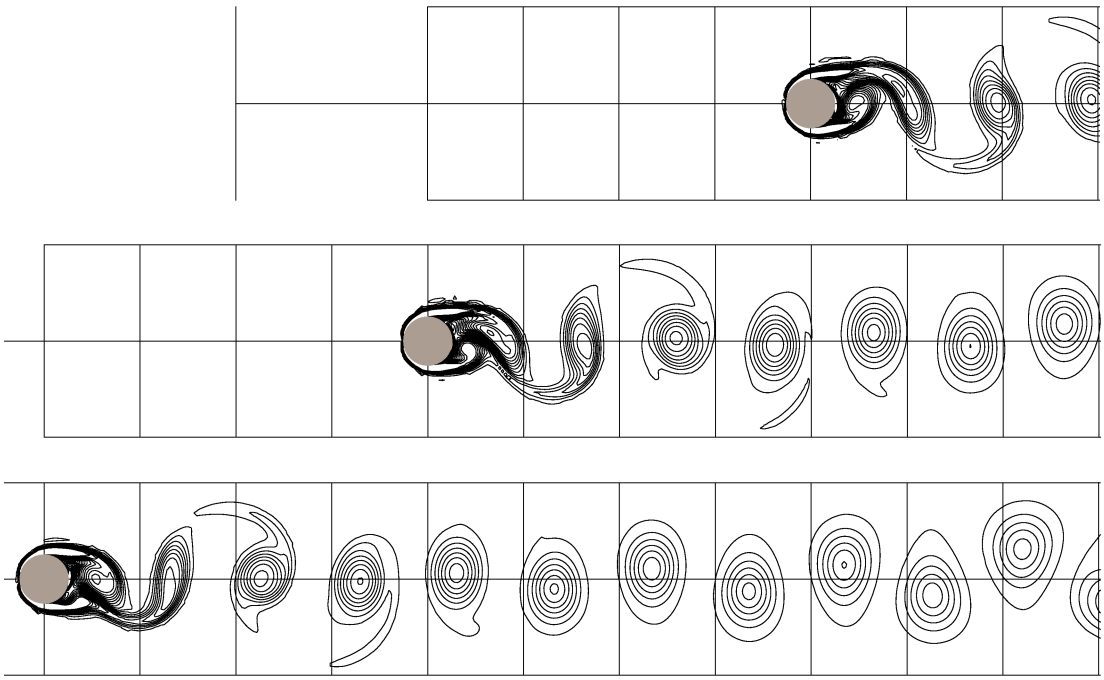

Figure 5.56. Isoline of vorticity for a cylinder translating in a fluid at rest at Re 450. Pictures from top to bottom correspond to time 5, 6 and 7.

Strouhal number

As in the static case, it is assumed that the static version of the code has been validated and can be used as a reference. Comparisons of the results are still based on the Strouhal number of the flows and their drag coefficients. Very good agreement is found between the static and the moving cylinder for the vortex shedding frequency or Strouhal number (Figure 5.57).

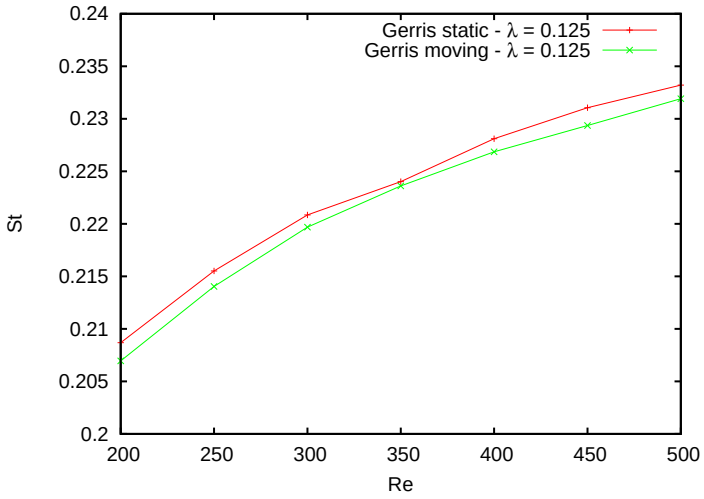

Figure 5.57. Strouhal number versus Reynolds number of the static and moving code.

Drag coefficients

Even though the drag coefficients are almost the same for the static and the moving cases (Figure 5.58), the results obtained for the translating cylinder are not as smooth as the ones obtained in the static case.

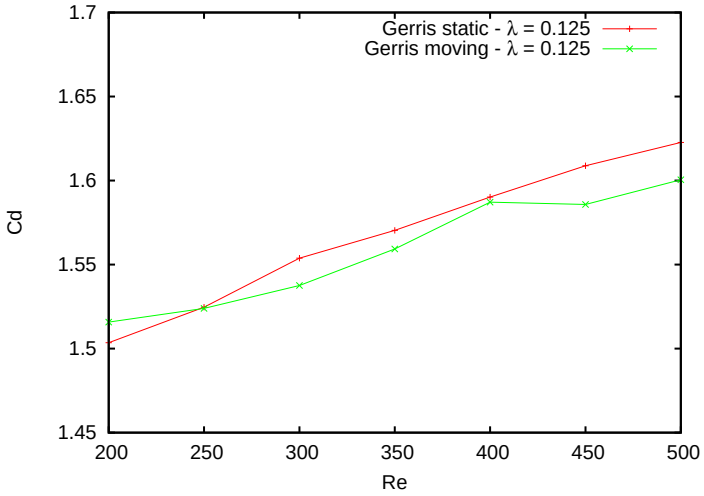

Figure 5.58. Drag coefficient versus Reynolds number of the static and moving code.

A closer look at the drag and lift coefficients for Reynolds numbers of 200 and 400 on Figure 5.59 suggests that the difference in drag coefficient must be related to the relatively high level of noise on these curves.

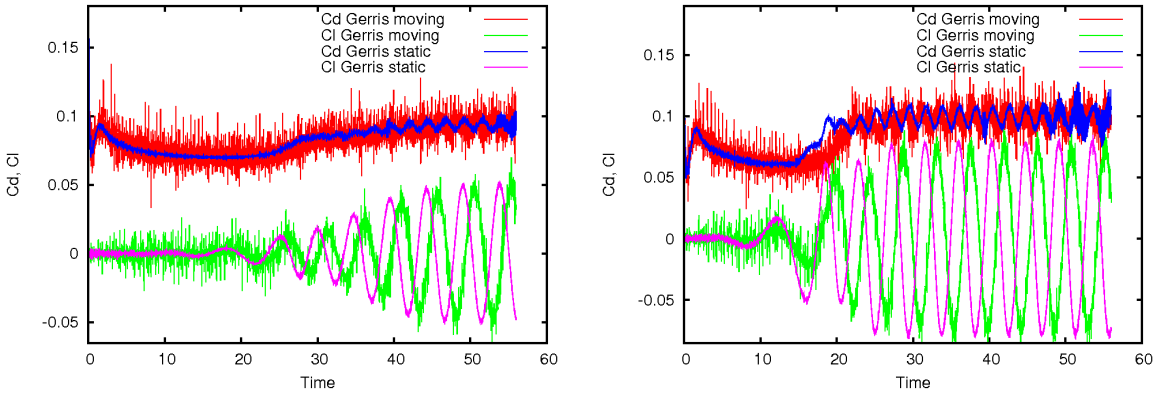

Figure 5.59. Evolution of the drag and lift coefficients with time for (a) Re 200 and (b) Re 400.

For both the moving and the static case, the drag coefficient curves look similar and have the same amplitude when in the oscillatory regime. There is more noise in the moving case which is not a surprise as all the reconstruction errors are located around the solid interface at the same place where the pressure and viscous forces on the solid are computed. The main difference between the drag coefficient evolution for static and moving cylinders is the clear difference in phase between both cases. The frequency is quasi-identical, as demonstrated by comparing the Strouhal numbers for both situations.

A priori one would expect to the drag coefficients for static and moving boundaries oscillate with the same phase or opposite phase. The oscillation of the drag coefficient is directly linked to the vortex shedding. Transition to turbulence happens when the viscosity of the fluid cannot damp the instabilities of the flow. As the starting configuration is symmetrical, there is no reason for the first shed vortex to be of positive or negative polarity. This depends on small perturbations that are not controlled. Therefore, there is equal chance of having the drag coefficients for static and moving boundaries oscillation with the same phase or with opposite phase.

On Figure 5.59, it is possible to see in the lift coefficient curves that the oscillations seem to be starting at the same time for both static and moving cylinders, but nevertheless the first oscillations for the translating cylinder seem to be more absorbed. As well, it takes more time for the oscillation to fully develop and reach their "steady state" frequency.

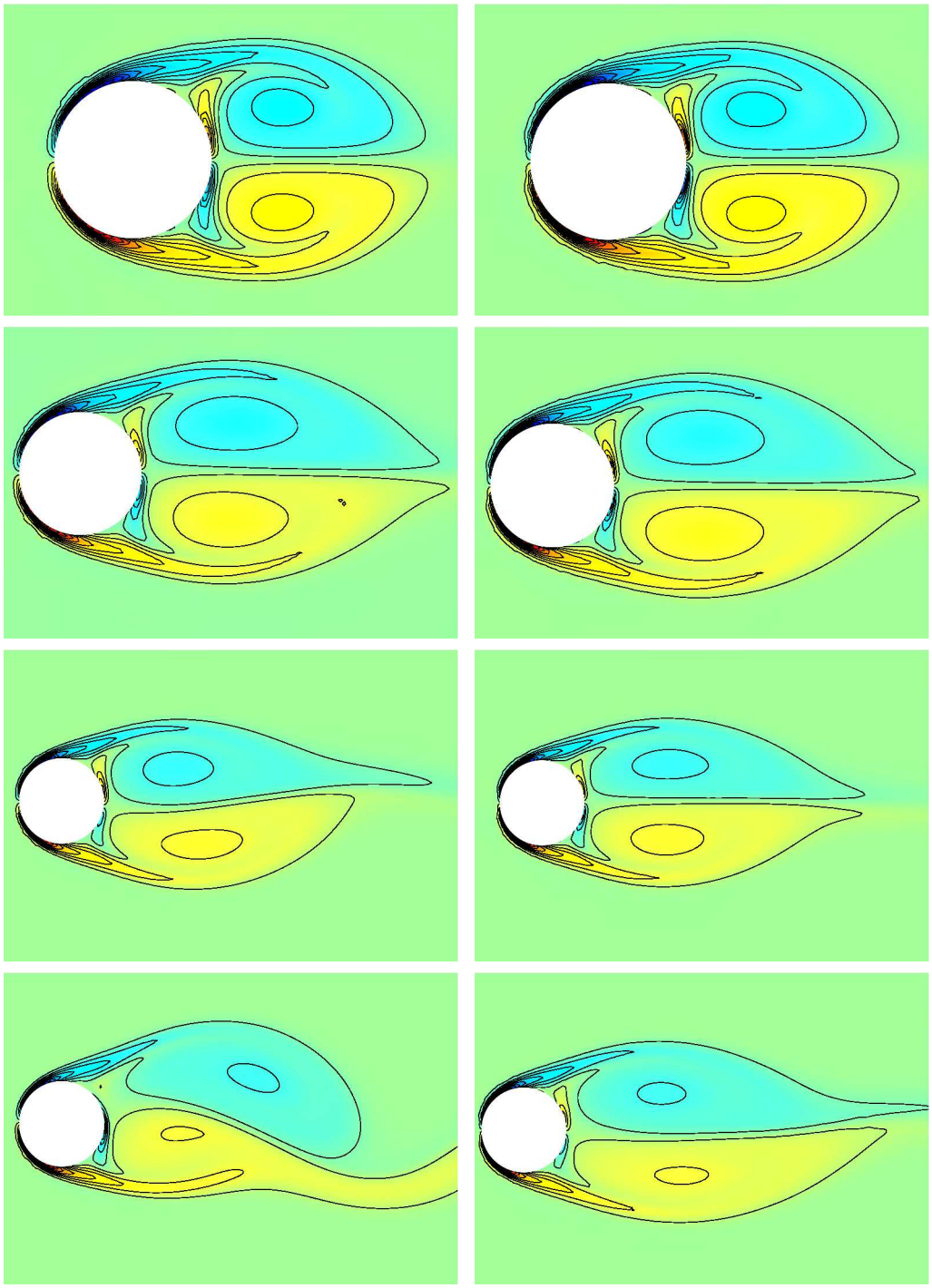

Figure 5.60. Vorticity field and isolines at time 0.5, 1., 1.5 and 2 for the static and translating cylinder at Re 400. The 30 vorticity isolines are evenly spread from -300 to 300.

Comparisons of the evolution of the vorticity field with time (Figure 5.60) confirm that the transition to turbulence and vortex shedding regime is different for both simulations. Both simulations remain quasi-identical while the flow is symmetrical with the wake growing the same way and the vorticity isolines looking similar.

5.8 Translating sphere

Whereas the second order method tested in the previous section requires additional programming to be extended to three-dimensional flow, the first order method is *a priori* directly generalisable to 3-D. The benchmark test of the flow past a sphere at a Reynolds number of 100 was chosen to address the behaviour of the method in 3-D. Numerous results can be found in the literature [Fadlun et al.(2000)] [Fornberg(1988)] [Zhang and Zheng(2007)] [Blanco and Magnaudet(1995)] [Masliyah and Epstein(1970)] [Taneda(1956)] [Batchelor(1967)] for that test case.

A computational domain of size $1.5 \times 1.5 \times 1.5$ was used for a sphere of radius 0.05 which should ensure a limited influence of the boundary conditions. A viscosity 5×10^{-4} and translating speed of magnitude 1 were used. The adaptive mesh was used to ensure a resolution down to level 9 (cells of size $0.00195 \times 0.00195 \times 0.00195$). A constant time step of 5×10^{-6} time units was used which is several times smaller than the time-step corresponding to a CFL of 0.5.

For a Reynolds number of 100, transition to periodical regime has not happened yet and a stable wake forms (Figure 5.61). Similarly to the 2-D case, the size of the wake increases and then stabilises (Figure 5.62). The length of this recirculation can be used for comparisons with other published results.

Only that resolution and lower resolution have been tested and no convergence study was made, this is therefore not an attempt to find the exact solution of the problem with this method but more on illustrating the behaviour of the first order method at moderate resolution.

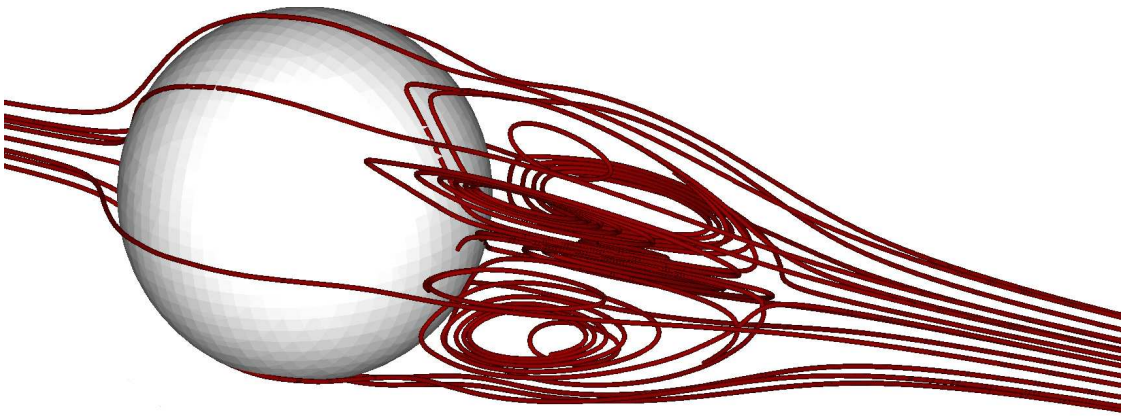

Figure 5.61. Streamlines for a sphere translating in a fluid initially a rest for a Reynolds number of 100.

Streamlines plots allows to visualise the structure of the wake behind the sphere (Figure 5.61 and Figure 5.63). Smooth streamlines form a symmetric wake. The 2-D streamlines for a cross-section corresponding to a plan of symmetry of the problem look fairly similar to the results obtained for the 2-D problem of the flow past a cylinder, with two detachment points and a stagnation point at the back of the sphere.

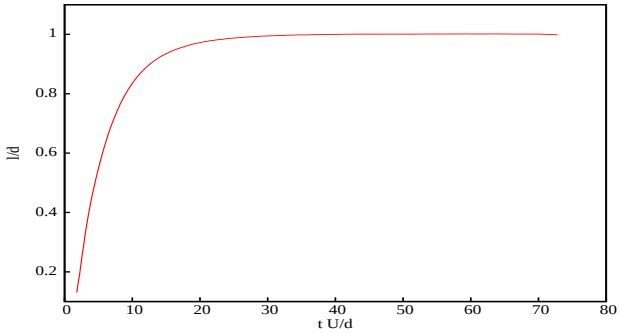

Figure 5.62. Evolution in time of the size of the recirculation behind a sphere translating in a fluid initially a rest for a Reynolds number of 100.

Qualitatively, the new moving boundary code predicts a fully developed wake of size similar to the sphere diameter for a Reynolds number of 100 (i.e. 1 length unit). This is slightly higher than what is reported in the literature or predicted in the case of a static sphere (Figure 5.64). The calculations were made using an arbitrary resolution, and therefore, the wake size does not correspond to the converged solution to the problem. In such case, a wake of smaller size would be expected because of the higher numerical viscosity due to low refinement or time-step.

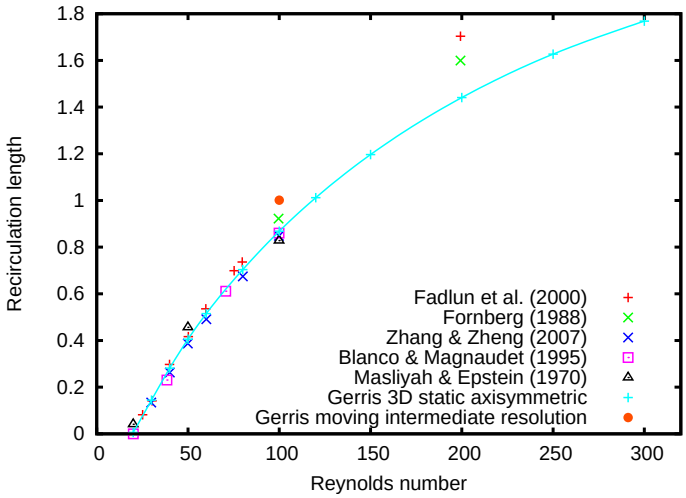

Figure 5.64. Wake length versus Reynolds number from several published studies and results for Gerris static and moving at intermediate resolution.

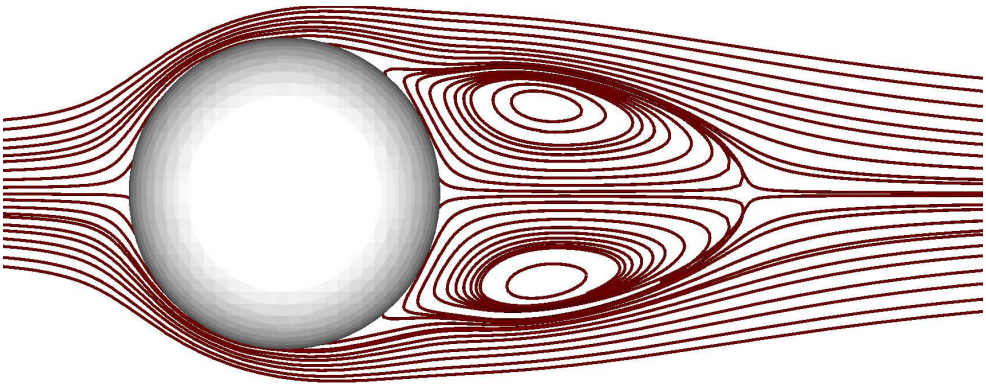

Figure 5.63. Streamlines for a sphere translating in a fluid initially a rest for a Reynolds number of 100 in the plane of symmetry of the simulation.

The longer recirculation observed here is likely to be associated with an extra production of vorticity near the solid interface. This is probably due to the deformation of the solid interface when the sphere moves. The evolution of the pressure field over 30 time-steps displayed on Figure 5.65 is an illustration of what must be similar to the peaks of error reported on the 2-D model. At time t, perturbations in the pressure field can be observed on the upstream boundary of the sphere. This is due to the corrections required from the Poisson solver in the case of error in the computation of the solid fluxes. Then, over 30 time-steps, no peak of error occurs and the pressure solution smooths out, ending eventually fairly close to the real solution (Figure 5.66). This happen regularly over the simulation and is likely to be responsible for the bias measured in the size of the recirculation.

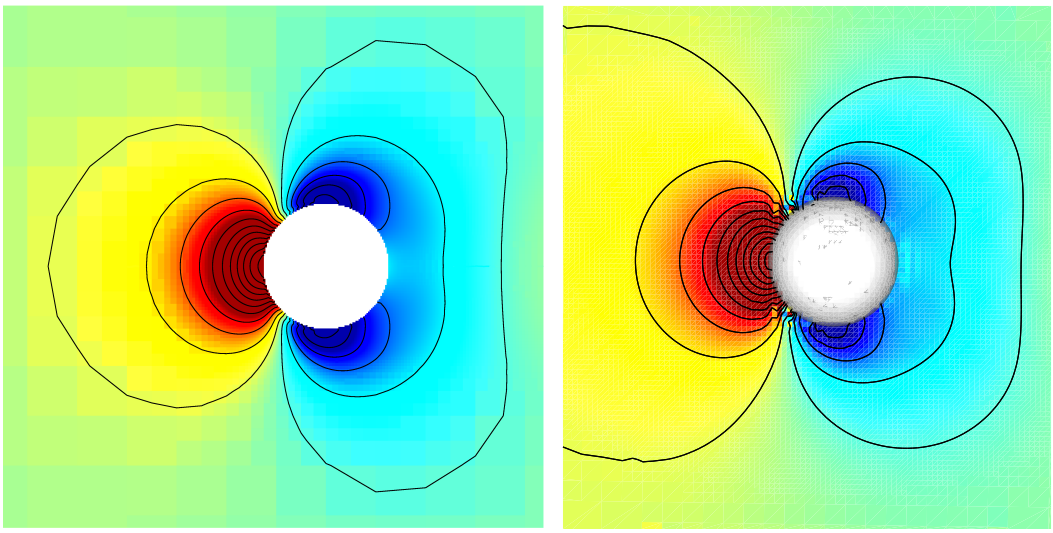

Gerris Static Axisymmetric Gerris Moving First-Order

Figure 5.66. Pressure field around the sphere at steady state for a Reynolds number of 100. 40 pressure isolines are evenly spread from P = -1 to 1.

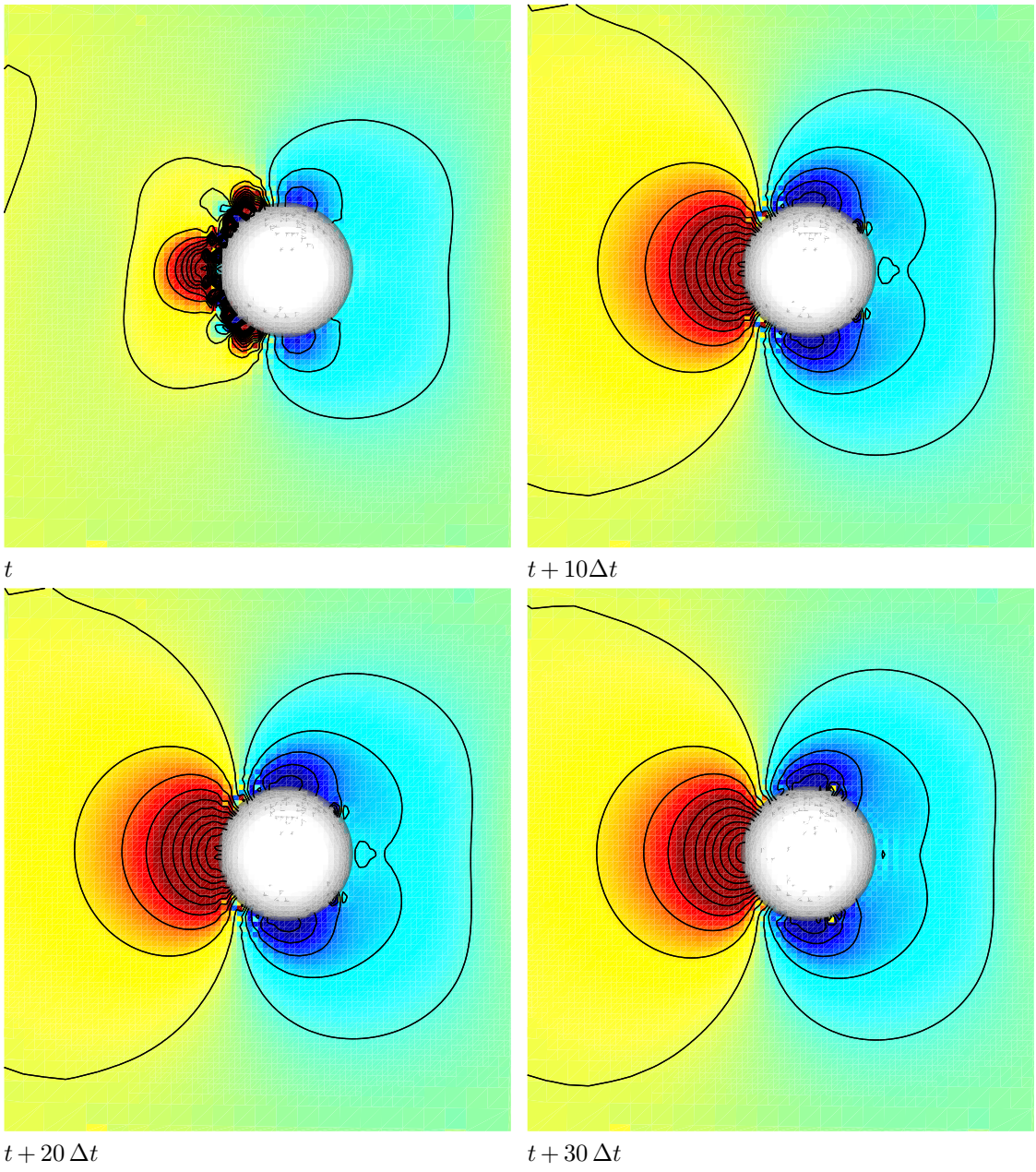

Figure 5.65. Evolution of the pressure field after a peak of error caused by change in geometry of the sphere. 40 pressure isolines are evenly spread from P = -1 to 1.

The velocity field obtained from the 3-D model, similarly to the pressure field, is close but not identical to the real solution (assuming the static solution is the truth). The isoline of the different components of the velocity (Figure 5.67) are quasi identical to the "truth" for the upstream part of the sphere, but noticeable differences can be seen in the wake.

A) Gerris moving 3D

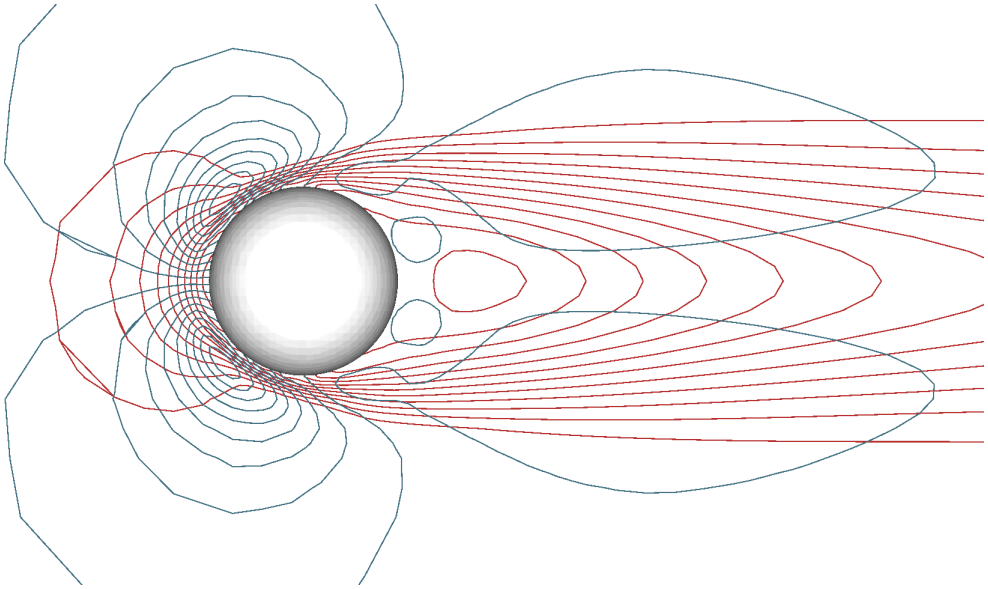

B) Gerris static axisymmetric

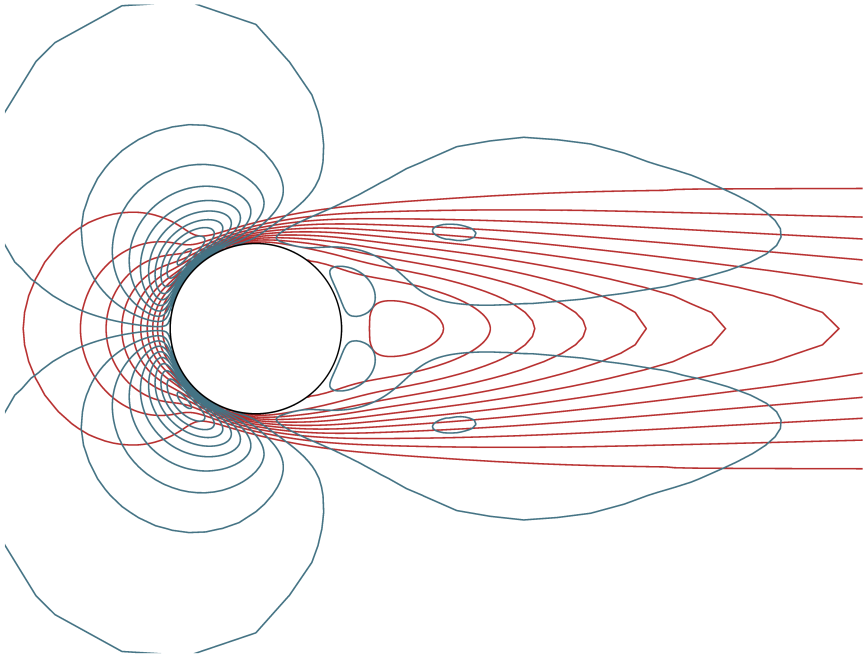

Figure 5.67. Isoline for the x (red) and y (blue) components of the velocity for a sphere translating in a fluid initially a rest for a Reynolds number of 100 in the plane of symmetry of the simulation. 21 isolines are evenly spread from -1 to 1 for U and 40 for V.

The 3-D version of the moving boundary code displays here an interesting but imperfect behaviour. Consistency is obtained with what was already found with the 2-D first-order code, with the change of geometry of the solid object creating non negligible perturbations that can influence the solution potentially over the whole domain. The results obtained here are certainly close to what is expected, but not exactly like the ones expected.

Despite the relatively good results obtained here, the change in shape of the solid objects remains the critical problem to the first as well as second-order methods. It deteriorates locally the quality of the pressure field around the interface and can create errors further away from the solid object. More importantly, the peaks of error observed here prevent the code to be really first or second-order in space as, past a certain resolution, an increase in resolution can result in getting a poorer estimation of the solution to the studied problem.

Additionally, the code can surely be improved by implementing a second-order type method similar to the one developed in 2-D. This has not been done yet as several additional cases to the 2-D algorithm must be implemented. The idea behind the 2-D method remain possible to extend to 3-D even though one must be cautious not to forget any case.

5.9 Summary

A new solid/fluid interaction model was implemented in the Gerris Flow Solver and tested on diverse cases. Mass-conservation is ensured by exact calculation of the solid-fluxes. The model is fully compatible with the adaptive refinement of the mesh.

Two different algorithms were implemented, a first and a second order one. Whereas the second order one is yet to be extended to 3D, the first-order scheme is working in both cases. In all cases, this method is the first adaptive tree-based conservative solid/fluid interaction model working in both 2D and 3D.

The ability of the model to handle a moving cylinder (or sphere) was assessed. Good results (comparable with the static case) were obtained for the flow around the cylinder as well as for the drag and lift force experienced by the cylinder in 2-D. Those are two key points for the use of the model in the context of fluid/particle interaction. The test of the 3-D flow past a sphere seems to show the limitations of the first-order algorithm, this is mainly due to the way moving solid object are discretised (and changing volume slightly when moving).

Several improvements can be implemented to strengthen this moving-boundary scheme. The extension of the second-order scheme to 3-D is possible and should be feasible fairly easily. More importantly, it is possible to change the way the solid fractions derived from the discretisation of solid object on the quadtree/octree mesh are calculated to ensure that solid objects do not change volume over time. This would allow to ensure that the compatibility condition for the Poisson solver is ensured at any time when moving boundaries are involved. Significant improvement in the quality of the solutions and particularly the pressure field around moving objects is expected from that modification. Practically, such discretisation of the solid triangulated surface included in simulations was used to be used by the static version of the Gerris Flow Solver but was replaced for performance reasons by the actual method. It is therefore possible to restore the old discretisation and adapt it to the current code.

Other topics of investigation from a numerical point of view are the way the divergence gets distributed within the groups of merged cells. The use of a finer redistribution algorithm could help improving the order of the solid/fluid interaction scheme. Also, the redistribution of the solid fluxes, notably when a cell disappears, which is done arbitrarily using the advection cell-merging algorithm, can be improved by the additional geometrical operations allowing better redistribution to all the neighbouring cells.

Propagules can now be modelled into the Gerris Flow Solver. The only requirement is to define a law of motion for the propagules which is possible to do from the parameter file.

Beside particle modelling, this model opens new perspectives to the Gerris Flow Solver as moving solid can be used in many applications. The code should be published soon as part of the stable version of the Gerris Flow Solver [Popinet(2001a)].

Chapter 6
General discussion

6.1 Summary

This thesis covers a wide range of topics, all motivated by the central problem of the attachment of seaweed zygotes on a rocky substrate in turbulent conditions. Ecological, physical and numerical problems have been addressed, most of them directly related to experimental settlement results obtained from a stirred tank.

Flow and friction close to the bed (where propagule attachment takes place), recreated in a benthic stirred chamber, were investigated here using several methods. Stirred tanks are very practical devices to generate complex turbulent flow within a small environment. They are cheap and easy to build, require a limited amount of space, are easily transportable and fairly easy to use. Nevertheless, these very appreciable practical operational properties come at the price of difficulties in fully characterising the flow, as well as being an imperfect field simulator.

Rather than giving firm and precise measurements or estimation of the bottom stresses, orders of magnitudes were obtained. Indeed, despite the number of studies focused on many aspects of turbulence, turbulence remains an open problem and few situations besides fully-isotropic turbulence and logarithmic layers can be considered as close to be understood. In the case of wall-bounded turbulence, the hypothesis of constant shear layer remains a keystone to more or less all methods of turbulence characterisation (based on mean flow, mean fluctuations or energy spectra).

Tank flows are strongly influenced by the presence of corners which, despite the apparent simplicity of the domain, complicate the turbulent structure of the flow, notably through the presence of large-scale instabilities. No theoretical velocity profile exactly stands in that case and methods based on the logarithmic turbulent boundary layer lead to results of limited accuracy. Flow properties were nevertheless found to be consistent with analytical approaches, particularly the proportionality found between propeller stirring rate and friction velocity.

Estimation of the friction velocity in the tank was used to investigate propagule settlement experiments in the tank. From these velocities, the magnitude of the hydrodynamical forces experienced by the settled propagules were evaluated. Whereas noticeable differences can be

observed in the magnitude of the detachment forces experienced by the propagules (or particle Reynolds number at detachment), the hydrodynamical stress withstood by the newly settled propagules is essentially size-independent. Therefore, the adhesiveness of the different propagules can be directly related to the friction velocity at the bottom of the tank at detachment. In that respect, the stickiness derived from the settlement curves matched with the geographical observations made in the field with higher stickiness found for the species exposed to the highest level of turbulent stress and vice versa.

For two of the New Zealand species studied, *Durvillaea antarctica* and *Cystophora torulosa*, bimodal results were found with two characteristic adhesiveness strengths, derived for the same species. This is probably related to the ability of propagules to clump together in groups up to of four which seems to enhance their ability to remain attached to their substrate.

Comparison between the characteristic detachment strength derived from the stirred tank and estimation of the bottom friction in the field derived from a friction drag model shown that no matter the species, attachment can only take place under calm sea-conditions (waves of less than 0.12 m) which is not contradictory with the key role played by the stickiness of propagule mucus in their settlement process.

The particularly regular shape of the propagule sinking curves was workworthy. Given the apparent proximity between the different sinking velocities and the Stokes velocity of the propagules, it was thought that the sinking curves would be relatively easy to explain and could eventually lead to a better understanding of the propagules.

The hypothesis of permanent homogeneous mixing in time was examined ("Perfect mixing" model). Fitting of the predicted sinking curves to the experimental results led to an asymptotic errors of around 15%. More importantly, this model showed that even in the case of perfect mixing within the tank, the propagule mean sinking speed is given by the settlement speed in the boundary layer used as boundary condition in the model. Settling curves are therefore independent of the core tank flow.

A Lagrangian approach was tested involving advection of propagules using their Stokes velocities and diffusion through the turbulent-diffusion of the flow. Mass turbulent-diffusion was derived from the estimation of the Péclet number in the tank. Turbulent-diffusion profiles of various shapes, some of them including a modified particle turbulent-diffusion in the boundary-layer, were used. Using an adjoint model that allows one to get the residence time of the propagules in the tank and solving numerically the advection-diffusion equation using the Gerris Flow Solver, it was showed that propagule sinking speed is essentially independent of the turbulent-diffusion profile and controlled only by the Péclet number. For all the Péclet numbers

investigated, sinking curves of the shape $(1 - \exp(-a\,x))$ were found which is the shape of the sinking curves predicted by the perfect mixing model. It was also shown that within the core of the tank, turbulent-diffusion fully dominates propagule transport. Nevertheless, when a boundary-layer model is included in the turbulent-diffusion profile, variations in the propagule sinking speed were observed, leading to results more in agreement with the experimental data.

There is no such process as "turbulent sinking" within the tank experiment. The stirring is important enough to ensure quasi-homogeneity of the propagule repartition at any time. Propagule settlement should therefore be mainly dependent on the propagule flux near the substrate and therefore on boundary layer mechanics. Propagule sinking through the turbulent boundary layer should therefore be addressed.

A more detailed investigation of the tank dynamics was undertaken by setting up computational fluid dynamic models of the stirred tank. A 2D model was first set up to investigate some aspects of the problem in a relatively fast way. Propellers were modelled as a constant source of velocity and calibration was realized through the kinetic energy measurements obtained from the PTV. Differences were found between mean circulation given by the model and the PTV measurements due to the 3D nature of the circulation within the tank. Consequently, poor estimations of the bottom friction are provided by the 2D model (about 3 times lower than expected).

It was shown how it is possible to compute the hydrodynamical forces experienced by a solid propagule in the tank by taking advantage of the adaptive mesh. The computed forces were found to be reasonably lower than the ones expected from a particle drag model, which is consistent with an underestimation of the bottom friction. It does however provide an interesting perspective on the frequency and the magnitude of the lift and drag forces experienced by the propagules attached on their substrate.

The approach to 3-D modelling started with the observation that 3-D direct numerical simulation of a 3-D model of the tank is not feasible due to computational limits and that therefore a turbulence closure scheme was needed. As no turbulence model was available in the Gerris Flow Solver, it was decided to test the use of a Large Eddy Simulation model. From a review of Large Eddy Simulation methods a fairly new LES approach involving the use of an eddy-viscosity term was identified to be potentially promising given its simplicity of implementation and the good behaviour it showed on other problems. Implementation of the turbulence model led to the question of the best averaging technique to use to get a good convergence of the model. An evaluation/validation framework was designed for the LES method in the context of a turbulent lid-driven cavity flow which has many similarities to the stirred tank problem.

Despite the use of a turbulence closure scheme, the cavity runs remain quite expensive in terms of computer time and the problem was parallelised and run on a computer cluster. The question of the performance of the Shear-Improved Smagorinsky on the lid-driven cavity problem in the case of time-averaging of the subgrid-stress tensor remains open.

3-D simulations of the stirred tank model were given using a standard Smagorinsky closure scheme. Whereas the mean circulation obtained from the simulations realized at low Reynolds number was very similar to the one observed with particle tracking velocimetry, this is not obvious on the first turbulent simulation.

The implementation of a Lagrangian/Eulerian fluid particle model in the Gerris Flow Solver was made in the more general framework of solid/fluid interaction methods. A new solid/fluid method was designed and implemented in the Gerris Flow Solver. This method is fully conservative, and works in 2D and 3D and is compatible with the use of an adaptive mesh which makes it unique of its kind. A first order (2D and 3D) and a second order (2D) methods were implemented.

The method has been validated against simple test cases and the complex test case of the translating cylinder in a flow at rest. In both laminar and periodic regimes very good agreement was found with the static case and published results. Concerns still remain about the interaction between the small variations of shape of the moving solid objects in the code due to their representation and the boundary conditions.

This new model allows simulation of particles (propagules) fully interacting with the fluid. In contrast with a standard Lagrangian approach where particles are carried by the background flows, in that case, particles can have their own law of motion involving their properties as mass and density. As well, feedback is exerted on the flow by the propagules. More than a new numerical method, this fluid/solid interaction model should be seen as a new tool at the cutting edge of small-scale biophysics and physical ecology.

6.2 Discussion

Before commenting further on the outcome of this work, it is worth coming back to the initial ideas of this thesis. The framework was a broad multidisciplinary project focusing on the settlement process (attachment/detachment) of seaweed zygotes on a rocky substrate in turbulent conditions. The main questions were to understand the physical processes and determine the physical properties of propagules. One of the key points was to tackle the problem from several angles by involving ecologists, physicists, chemists and numerical modellers. This means that specialists would be involved from each domain. As well, it means that each specialist should be

able to develop understanding of the other specialities involved in order to be able to communicate within the group. For that reason, this thesis covers at the same time of the ecology, physics and numerical modelling aspects of this problem whilst at the same time seeking to be at the leading edge of a particular discipline.

The Gerris Flow Solver, because of its multiscale orientation, was believed to be the ideal tool to realize a direct numerical study of propagules behaviour within the viscous boundary layer, given the development of a solid/fluid interaction model. Furthermore, its ability to deal with multi-phase flows offered the possibility of modelling propagule mucous as a very viscous fluid. The idea was quite simple but technically challenging as it involved complex coding before the use of the model. It was ambitious as direct numerical simulation is very demanding in terms of computer power and the question of turbulence modelling had to be tackled as well.

To synchronise this work with the rest of the project, it was decided at the same time to take advantage of the propagule data obtained by Dr. David Taylor. Indeed, this was a great opportunity to understand more about the properties of the propagules and especially their stickiness which was one of the key points of the model. Despite the very complex nature of the stirred tank flow which made it very frustrating at first, it led to the experimentation of many different methods of characterisation of turbulence, particle sinking or detachment.

Following the study of the experimental data from the stirred tank, there was a need to set up a CFD model of the tank in order to support the experimental measurements and refine our knowledge of the dynamics of the tank while developing in parallel a fluid/particle model. Whereas the guideline followed in this approach is certainly suited to get the best out of the tank experiments, the focus of the study was moved from boundary layer to a larger scale. Despite the conclusion of the models used to explain propagule settlement which shows that boundary-layer crossing is likely to control the sinking curves, the tank models remain of interest particularly because they deliver an estimation of the fluctuations of the drag and lift forces exerted on propagules attached to their substrate.

It is best to completely dissociate the range of applicability of the fluid/particle model and the simulation of the tank. The particle model can be applied to the investigation of propagule sinking within a boundary layer whereas the tank is likely to be more suited for removal and connection with real data. Ideally, a simple logarithmic layer should be used so as not to overload the simulation with additional parameters at first (like a whole tank). A 3D channel flow using periodic and symmetry boundary conditions should allow the set up of a 3D turbulent logarithmic layer within a channel flow. The sinking of a single propagule could be investigated using u_* as a single flow parameter and then given the choice of a proper law of motion for the

propagule, propagule parameter (diameter, density, initial velocity) can be varied. It can also be envisaged to include a layer of mucilage of variable density, modelled as a very viscous fluid around the propagules. This would still require a fair amount of work, and in a second time it could be imagined to increase the complexity of the boundary layer mechanics by modelling a wave-driven boundary-layer or work with various substrate shapes.

As indicated earlier, more information can still be taken out of the stirred tank model without using any moving propagule. Drag, lift and moment of surface stress can be computed and then recombined using propagule detachment criteria to point at the detachment events. Numerical models are totally deterministic and, therefore, it is possible to produce a detailed velocity field in space and time and detail the events responsible for propagule detachment.

Many other aspects of the problem can be examined especially as, propagule size and density are known and now we have an estimation of the propagules adhesiveness, the other characteristics of the propagules are still not known.

The thesis has developed some groundwork and a tool for exploration of solid-fluid interaction. The opportunities are substantial:

- boundary layer crossing.
- settlement in various topography.
- detachment in various topography.
- propagule fertilisation

Algae strategy

Even though the propagules investigated here originate from five different species, the relatively similar physical properties (density and diameter) of *Hormosira banksii* and *Fucus gardneri* and of *Cystophora torulosa* and *Pelvetiopsis limitata* allow only to consider three types of different propagules. Despite the fact that the real importance of the mucilage for the sinking process of the propagules remains to assess, there is no fundamental difference between the studied species when it comes to transport to the substrate. They all, by the mean of a larger size or a larger density, have comparable Stokes velocities. They are negatively buoyant, but sufficiently little to be considerate as relying mainly on turbulent transport.

Attachment probability was first considered from an asymptotic point of view and related to the adhesiveness of the propagules (Chapter 3). At equilibrium, mucous adhesiveness is by far the most important property and propagule density and size are expected to have a limited importance. That way, the species adapted to the most extreme environment are certainly producing more adhesive propagules.

Differences in deposition speed have been recorded between the propagules that could not be related in a simple way to propagule characteristics. This might come from an under-estimation of the attachment problem. Attachment requires propagules to enter the viscous sub-layer, to cross it and to perform attachment before eventually getting dislodged by an extreme event [Stevens et al.(2008)]. Why would *Durvillaea antarctica* have more chances to settle in a more extreme environment as observed on the field? Experiments show that *Durvillaea antarctica* is the quickest, or at least one of the most efficient, species at settling. It is clear that *Durvillaea antarctica* is the species that displays the strongest adhesiveness [Taylor and Schiel(2003)]. Nevertheless, this is *a priori* independent of the time needed for a propagule to manage initial attachment. *Durvillaea antarctica* is by far the propagule with the smallest Stokes velocity. This suggests, given the little importance of propagule inertia [Stevens et al.(2008)], that for a given viscous sub-layer size it should take more time than other species to cross the viscous sub-layer and therefore should have more chances to get re-entrainment by the compression of the viscous sub-layer associated with an extreme event. Once in contact with the substrate, the amplitude of the hydro-dynamical forces experienced by such small propagules is surely less for *Durvillaea antarctica* than for other species, but so is the surface of contact of with the substrate. The efficiency of its attachment mechanism could eventually exceed the one of the other species and compensate for its slower sinking speed. Or its smaller size could improve its propagule chances to find a place in an interstice. As well, at the first stage of attachment, the weight of the propagules is likely to be of importance as a first adhesion mechanism. A low weight could favour quick resuspension, which is going against the propagules interest except if it can afford to decide to get resuspended to explore another potentially suitable substrate.

Propagule deposition

Because of their physical properties (size and density), seaweed propagules properties fall in between the main categories usually distinguished in most particle/turbulence interaction studies. Their size makes their settlement process independent of Brownian diffusion [Stevens et al.(2008)], which controls boundary layer crossing in the case of aerosol particle (usually of size of the order of a micron). Their density, close to seawater density, makes the velocity scale associated with their sedimentation velocity too small compare to the scale of the flow velocity fluctuations which excludes them from the heavy particle category. It is nevertheless clear from the experimental results that seaweed propagule settlement is controlled in a large extent by their Stokes velocity.

The variation in average settling velocity measured between the different propagules should be possible to connect to a general boundary layer crossing model. Correlations were investigated using a parametrisation similar to the ones found in the particle turbulent sinking literature [Brucato et al.(1998)] (see Appendix E). This assumed that the interaction between turbulent fluctuations and propagules that take place within the turbulent boundary layer, where the scale of the velocity fluctuations becomes comparable to the ones of propagules sinking, can be described in a similar way as the in a fully turbulent flow far from boundaries..

Sediment deposition models (e.g. [Gross and Dade(1991)]) define sediment flux to the substrate as the combination of gravitational sinking and Brownian diffusion of the sediments available near the substrate. To that settlement flux, an erosion term is added to take into account an eventual re-entrainment of sediments. Other studies investigating particle behaviour in a turbulent boundary layer suggest that the effective settlement flux is the sum of gravitational or Brownian flux of propagule to the settlement substrate minus the re-entrainment of propagules due to the presence of turbulent bursts in the viscous sub-layer [Cleaver and Yates(1976)] [Vatistas(1992)]. The nature of the re-entrainment mechanism is in reality a bit more complex than simple periodic succession of high and low period of turbulent stress [Yung et al.(1989)] but does involves coherent funnel-shaped vortical structures responsible for spacial and temporal variations of the shear-stress on the settling wall and in the whole viscous sub-layer [Kaftori et al.(1995)].

Additional to this resuspension mechanism, the sedimentation velocity of the propagules is different from the Stokes velocity in the boundary layer due to the influence of shear stress [Rouhiainen and Stachiewiz(1970)]. A shear-induced lift force acts together with the Stokes drag and buoyancy forces propagules crossing the turbulent boundary layer.

These two processes combined together must explain the variations with size, density and friction velocity in propagule deposition flux observed experimentally.

Propagule deposition on the rocky-shores depends on boundary layer mechanics, but also on the availability of propagules in the vicinity of the settlement area. In their larval settlement numerical model, Gross et al. [Gross et al.(1992)] decomposed the larvae flux near the substrate as a function of the quantity of propagules available for settlement, their Stokes velocity and the probability a propagule has to be successful in settling when close enough to the substrate (which should include boundary layer mechanics). A bedload layer is defined whose concentration in larvae is used to calculate the settlement flux. From a parametric study of the model they show that larval availability is governed mainly by the Rouse number, $\frac{V_s}{\kappa\, u_*}$, representative

of the relative strength of downward flux due to fall velocity versus the upward turbulent suspension flux [Hendriks et al.(2006)]. The thickness of the viscous boundary layer, $\frac{5\,\nu}{u_*}$, is of little importance in the larval supply to the bedload layer.

Even though the processes that act on particle deposition are well identified, their relative importance and total influence is still non-trivial to determine. This especially as particle deposition is also strongly dependent on particle adhesion mechanism [Vatistas(1989)] and as most probably most turbulent boundary layer must have dynamics slightly more complex than the ideal channel flow.

Péclet number and turbulent sinking

Experimental measurements allowed to quantify the mixing within tank and low Péclet numbers were found to characterise the tank flow (Chapter 2). At any time, "perfect mixing" is ensured in the tank and a quasi-homogeneous distribution of the propagules (Chapter 3). Similar Péclet numbers are often representative of propagule vertical transport in the rocky-shores environment given the highly energetic wave climate prevailing there. This supports the thesis that vertical turbulent-diffusion can increase a lot the efficiency of the transport toward the substrate of a significant part of propagule population. In the same spirit, the mucous of the propagules of interest, which is positively buoyant, acts to compensate with the negative buoyancy of the propagules and makes the ensemble close to neutral buoyancy. This suggests that propagules do not rely heavily on their own sinking properties and have a strategy based on transport by turbulent eddies, at least outside the turbulent boundary-layer.

Especially for non-motile organisms, which only rely on their own weight and turbulence for settling, very energetic environments, such as the intertidal, still provide propagules with very high chances of meeting several times the substrate within short time-scales [Abelson and Denny(1997)]. That way propagules would still be able to choose their location of settlement in a selective manner.

On the other hand, the tank experiments reported here (Chapter 3) aim at determining the critical shear stress conditions under which settlement can occur and, at the same time, at estimating their adhesiveness. Results suggest a need for calm sea conditions for the propagules to settle. This is consistent with the numerical settlement model of Gross et al. [Gross et al.(1992)] predicting that, for tidal or wave oscillations, most settlement should occur at and near periods of slack water. This put together with the observations from the two previous paragraphs points out at two different aspects of the propagule settlement process for

which ideal flow conditions are apparently opposite. Turbulent sinking is more efficient for high levels of turbulence whereas attachment benefits the most from calm conditions.

Clearly, except if the survival of the seaweed species of interest is down to the chances propagules have to end in a pit or crevice (micro-cavity, e.g. [Abelson and Denny(1997)]), the shear stress near the substrate should the limiting factor to the attachment process. Two other points seem to discredit the possibility for propagules to settle in a rough wave climate. For the species of interest, eggs and sperm seem to be preferably released in relatively quiet conditions [Taylor et al.(2009)], which should be without doubt a good time for successful settlement. Also, propagules are exposed to horizontal turbulent diffusivity. Horizontal turbulent diffusivity, usually significantly higher than the vertical one [Denny and Shibata(1989)], has a positive impact on seaweed recruitment by allowing at some extent to increase the chance for gametes to meet (fertilisation process). Nevertheless, if the level of turbulence is too high, it lowers the chances of fertilising by diluting too efficiently the gametes [Denny and Shibata(1989)] and by carrying propagules out to the deep sea. This suggests that optimum and realistic conditions for settlement to succeed are intermediate turbulence levels which on a rocky-shore corresponds to relatively calm conditions.

Denny and Shibata derived a simple estimations of the ensemble-averaged time needed for a non-motile organism to be transported from a distance y from the substrate to the substrate in the surf-zone [Denny(1988)] [Denny and Shibata(1989)]. This estimation is based on transport of the propagules by eddy-viscosity with eddy-viscosity profiles based on the mixing-length model

$$D_z = \kappa\, u_* z.$$

A first estimation for the time, $T(y)$, to reach the substrate is given by

$$T(y) = (y - y\ln(y) + y\ln(h))/\kappa\, u_*,$$

where h is the height of the water-column.

With the time-scale associated with gravitational sinking of a propagule being of the order of y/V_s, the Péclet number associated with sinking through the water column can be estimated to

$$\mathrm{Pe} = \frac{T(h)}{h/V_s} = \frac{V_s}{\kappa\, u_*}.$$

It is equal to the Rouse number which is representative of the importance of gravitational sinking over turbulent mixing in the turbulent boundary layer [Deleersnijder et al.(2006)]. Assuming that turbulence has a significant impact on propagule sinking time for $\mathrm{Pe} < 0.5$, friction velocities of the order of $\frac{2\,V_s}{\kappa} \sim 5\ V_s$ are required for propagule transport to be turbulent. Using estimates of propagules settling speeds determined from a sinking column

[Taylor et al.(2009)], this leads to $u_* > 1.45$ mm.s^{-1} for the slowest sinking propagules (*Durvillaea antarctica*) and $u_* > 3.15$ mm.s^{-1} for the fastest sinking propagules (*Pelvetiopsis limitata*). Recalling that the maximum friction velocities under which settlement is possible are around 5.8 to 11.6 mm.s^{-1} depending on species, and their eventual ability to clump together, this effectively leaves a relatively narrow window when all conditions coincide for turbulent settlement to happen.

The narrowness of this of optimal window suggests several conclusions:

- the huge number of released propagules by adult algae gives an hint that the success rate in settlement of propagules must be reasonably low (already less than 1% for fertilisation [Denny and Shibata(1989)]). This seems to be the case as well for the attachment process given the calm conditions required.

- it is likely that estimates of the shear-stress at detachment for each species was underestimated or part of the attachment mechanism not taken into account. The use of a clean Hardi-flex plate as a settlement substrate in the experiment assumes relatively low characteristic length for the roughness elements, a flat substrate and also, the absence of other organisms on the substrate (like microbial film [Abelson and Denny(1997)]). These parameters have some influence on flow and Reynolds stress experienced by the attached propagules and in the strength of their attachment.

- turbulent transport might not dominate propagule sinking as much as previously thought. For a water column of 1 meter high, the time-scale associated with gravitational sinking is of the order of half an hour to a whole hour which is still low enough to be a realistic water-column crossing mechanism. This would also mean that chances for a non-motile propagule to get resuspended and to be selective in the choice of a substrate is quite low. This is *a priori* not in contradiction with the mixing requirements of the fertilisation process as low levels of turbulence are often more propitious to a higher rate of fertilisation [Denny and Shibata(1989)].

Variability

A major question that remains is the importance of variability at the different scales as it influences the probability of recruitment of propagules. Even though the friction velocity is a mean quantity representative to some degree of the velocity fluctuations acting on the propagules, u_*, it does not account for all the variability of the system. It was shown in the 2-D tank model (Chapter 4) that together with u_*, the maximum amplitude of propagule removal forces, their frequency and peak duration are as many factors that can affect settlement laws. Also, these variations originate from several processes as boundary layer instabilities

[Cantwell(1981)][Kaftori et al.(1995)] or at much larger scale, the water column/boundary layer forcing by breaking waves of various strength and wavelength.

[Crimaldi et al.(2002)] linked the probability of attachment of larvae to the variability of the Reynolds stress in the viscous sub-layer by assuming that larvae need a period of time (anchoring time) when the Reynolds stress is lower than a threshold value to manage successful settlement. Probability estimations can be made in that case from the well investigated structure of turbulence in the logarithmic boundary layer. On the field or in a stirred tank, flow conditions are not as ideal and large scale instabilities at the scale of the water-column or of the tank add themselves to the "bursts" of the viscous sub-layer. This implies much extreme variations of the boundary layer mechanism and notably periodic compressions of the viscous sub-layer possibly key to the sinking through the viscous sub-layer [Stevens et al.(2008)]. This is the kind of mechanisms that cannot be studied using the classical logarithmic turbulent boundary layer generated in a channel flow. In that respect, stirred tanks could provide a better understanding of the role of large-scale instabilities. Assuming the frequency of the large-scale instabilities can be controlled through the aspect ratio of the tank(s) and the average u_* kept constant, a set of experiments could be designed to investigate the influence of the large scale dynamics on propagule settlement.

Additional to the flow variability associated with wave climate and water-column structure, spatial variability is also of great importance at several levels. At the boundary layer scale, substrate roughness has a strong influence on the structure of boundary layer [Jimenez(2004)]. Nevertheless, turbulent "bursts" due to the presence of coherent structures are present regardless of substrate roughness [Grass(1971)]. At larger scale, substrate morphology or bathymetry is responsible for the presence of much more complex flows than considered here and can have a strong influence on the maximum forces affecting propagule settlement (e.g. limitation of wave exposure [Helmuth and Denny(2003)]). Also, at most place, boundary layer forcing is very different from wave forcing on a flat substrate. Finally, spatial variability can possibly affect directly the propagule anchoring process by providing more or less favourable area or settlement either though its micro-topological structure or through hosting other living organisms susceptible to interact with the propagules [Abelson and Denny(1997)].

Much progress has been made in the past 20/30 years on the understanding of the processes related to water-column crossing, boundary layer-crossing, attachment and re-entrainment of propagules, larvae or sediments in relatively simple or idealised environments. Despite, the knowledge accumulated on these fundamental processes, big steps remain to surmount to generalised existing models to the reality of rocky-shores. The challenges for the future are therefore

to extend the developed knowledge to more complex environments possibly representative of the different microsites that can be found in the intertidal.

Appendix A

Time and number of settled zygotes at threshold

In this appendix are reported the experimental time values and number of settled zygotes at threshold from the tank experiments used in Chapter 3.

RPM	Time at threshold s	Number of settled zygotes at threshold	Mean settling velocity mm.s^{-1}
0	540	26.8	0.26
250	587	19.8	0.24
400	730	16.8	0.19
500	360	2.4	0.39
750	900	2	0.16
1000	xxx	0	xxx

Table A.1. Time and number of settled zygotes at threshold, and settling rate for *Hormosira banksii*.

RPM	Time at threshold s	Number of settled zygotes at threshold	Mean settling velocity mm.s^{-1}
0	540	6.6	0.26
250	720	4.6	0.19
300	832	4.8	0.17
400	360	2.8	0.39
500	720	3	0.19
750	xxx	0	xxx
1000	xxx	0	xxx

Table A.2. Time and number of settled zygotes at threshold, and settling rate for *Cystophora torulosa*.

RPM	Time at threshold s	Number of settled zygotes at threshold	Mean settling velocity mm.s^{-1}
0	630	23.2	0.22
250	900	15.6	0.16
500	900	15.4	0.16
600	1070	8.6	0.13
750	1200	12.2	0.12
1000	1200	0.6	0.12

Table A.3. Time and number of settled zygotes at threshold, and settling rate for *Durvillaea antarctica*.

RPM	Time at threshold s	Number of settled zygotes at threshold	Mean settling velocity $\text{mm}.s^{-1}$
0	440	12.0	0.32
250	655	14.2	0.21
300	680	12.4	0.21
350	1200	9.8	0.12
400	855	7.4	0.16
500	540	6.0	0.26
600	1200	4.0	0.12
750	720	1.6	0.19
1000	1000	0.2	0.14

Table A.4. Time and number of settled zygotes at threshold, and settling rate for *Fucus gardneri*.

RPM	Time at threshold s	Number of settled zygotes at threshold	Mean settling velocity $\text{mm}.s^{-1}$
0	460	17.8	0.30
250	900	11.4	0.16
300	60	3.6	2.33
500	540	0.4	0.26
750	900	0.6	0.16
1000	xxx	0.0	xxx

Table A.5. Time and number of settled zygotes at threshold, and settling rate for *Pelvetiopsis limitata*.

Appendix B

Fitting of the sinking curves obtained from the perfect mixing model to the experimental results

In this appendix are the results of the fits on the experimental sinking data.

B.1 Two degrees of freedom

Curves of equation

$$f(t) = a\,(1 - \exp(-b\,t))$$

RPM	a	b	Asymptotic Standard Error on a (%)	Asymptotic Standard Error on b (%)
0	21.019	0.00046	3	12
250	20.532	0.00024	13	28
400	2.472	0.00120	6	29
500	5.364	0.00006	95	116
750	xxx	xxx	xxx	xxx
1000	xxx	xxx	xxx	xxx

Table B.1. Fits of $f(t) = a\,(1 - \exp(-b/0.14\,t))$ on experimental curves with a and b free parameters for *Hormosira banksii.*

RPM	a	b	Asymptotic Standard Error on a (%)	Asymptotic Standard Error on b (%)
0	24.142	0.00050	2	11
250	17.578	0.00026	7	16
500	16.987	0.00028	5	13
600	10.640	0.00020	10	19
750	17.816	0.00013	27	44
1000	0.0647	0.00045	12	43

Table B.2. Fits of $f(t) = a\,(1 - \exp(-b/0.14\,t))$ on experimental curves with a and b free parameters for *Durvillaea antarctica.*

B.2 One degree of freedom

Curves of equation

$$f(t) = (1 - \exp(-a/0.14\,t))$$

RPM	a	Asymptotic Standard Error on a (%)
0	0.000557	9
250	0.000324	11
500	0.000340	9
600	0.000252	8
750	0.000226	18
1000	xxx	xxx

Table B.3. Fits of $f(t) = (1 - \exp(-a/0.14\,t))$ on the normalised experimental curves with a free parameter for *Durvillaea antarctica*.

RPM	a	Asymptotic Standard Error on a (%)
0	0.000632	8
250	0.000558	10
400	0.000355	14
500	0.001262	26
750	0.000234	19
1000	xxx	xxx

Table B.4. Fits of $f(x) = (1 - \exp(-a/0.14\,x))$ on the normalised experimental curves with a free parameter for *Hormosira banksii*.

RPM	a	Asymptotic Standard Error on a (%)
0	0.000534	14
250	0.000360	16
300	0.000368	14
400	0.000647	33
500	0.000257	32
750	xxx	xxx
1000	xxx	xxx

Table B.5. Fits of $f(t) = (1 - \exp(-a/0.14\,t))$ on the normalised experimental curves with a free parameter for *Cystophora torulosa*.

RPM	a	Asymptotic Standard Error on a (%)
0	0.001091	11
250	0.000302	13
300	0.001449	245
500	xxx	xxx
750	xxx	xxx
1000	xxx	xxx

Table B.6. Fits of $f(t) = (1 - \exp(-a/0.14\,t))$ on the normalised experimental curves with a free parameter for *Pelvetiopsis limitata*.

RPM	a	Asymptotic Standard Error on a (%)
0	0.001082	14
250	0.000943	9
300	0.000441	12
350	0.000150	17
400	0.000364	8
500	0.000533	13
600	0.000280	19
750	0.000377	47
1000	xxx	xxx

Table B.7. Fits of $f(t) = (1 - \exp(-a/0.14\,t))$ on the normalised experimental curves with a free parameter for *Fucus gardneri*.

Appendix C

Implementation of the Smagorinsky and Shear Improved Smagorinsky models in Gerris

C.1 Smagorinsky model

The Smagorinsky approach consists of adding an extra eddy viscosity term to the Navier-Stokes equations with the eddy viscosity defined as

$$\nu_t = (C_s\,\bar{\Delta})^2 |\bar{S}\,|,$$

with C_S the Smagorinsky constant. For now, we can consider that C_S has the value determined by Lilly [Lilly(1966)] of 0.165.

The implementation of the Smagorinsky model in Gerris is straightforward as it is possible to define functions in Gerris parameter files. Therefore, instead of defining the viscosity as a constant, it can be defined as a function. Another very useful feature of the parameter files is that any function defined in it will be evaluated in each cell of the domain and can access any other variable defined in the cell. It is also possible to access and use any routine of the Gerris library within the new defined function.

One of the variables stored in each cell at each time is the magnitude of the resolved stress tensor $|\bar{S}\,|$. This variable is called D2 in Gerris. Actually, one has to be careful because in Gerris the norm of the resolved stress tensor is defined as $|\bar{S}\,| = \sqrt{\bar{S}_{\mathrm{ij}}\,\bar{S}_{\mathrm{ij}}}$ and not $|\bar{S}\,| = \sqrt{2\,\bar{S}_{\mathrm{ij}}\,\bar{S}_{\mathrm{ij}}}$. Therefore, one should use $|\bar{S}\,| = \sqrt{2}\,D2$.

The variable dL returns the size $\bar{\Delta}$ of the cell.

Given these two points, to implement the Smagorinsky model in a Gerris simulation, one simply defines the viscosity of the fluid as:

$$\mu_{\mathrm{total}} = \mu + \rho(0.165\ \mathrm{dL})^2\,\sqrt{2}\,D2$$

or in Gerris syntax

```
SourceViscosity {}  {return μ + ρ*pow((0.165*dL), 2.)*sqrt(2.)*D2;}
```

where μ has to be replaced by the non-dimensional dynamic viscosity of the fluid, ρ by the non-dimensional density of the fluid and 0.165 is Lilly's value of the Smagorinsky constant.

C.2 Shear-improved Smagorinsky model

In the case of the Shear-Improved Smagorinsky model, the formulation is quite similar except for the fact that the norm of the time-averaged rate of strain tensor has to be subtracted from the instantaneous rate of strain tensor.

$$\nu = \nu_{\text{fluid}} + \nu_t = \nu_{\text{fluid}} + (\bar{\Delta}\, C_S)^2\, (|\bar{S}\,| - |\langle \bar{S}\,\rangle|).$$

In the case of a temporally stationary flow, the average of $\bar{S}$ over a sufficiently long period of time should converge toward $|\langle \bar{S}\,\rangle|$. The average in this case should be defined as:

$$\langle \bar{S}\,\rangle^{n+1} = \frac{1}{t^{n+1}} \sum_{k=0}^{n+1} \Delta t^n\, \bar{S}^{\,n}.$$

It has to be stressed that $|\langle \bar{S}\,\rangle|$ is the norm of the average of $\bar{S}$ and not the average of the norm. Therefore, this time we cannot use the variable D2 and have to average the six terms of the rate of strain tensor (symmetric tensor).

This can be done using the keyword `EventSum` which stores the time integral of a given quantity.

For example the command line

◇`EventSum { start = 0. istep = 1 } dx("U") SSxx`

stores in the time integral of $\frac{\partial u}{\partial x}$ in the variable SSxx. The integral is stored from time 0. and the timestep used for the integration is the same as the global step used in the simulation. Therefore, at time t, we will have

$$\text{SSxx} = \int_0^t \frac{\partial u_x}{\partial x}\,\text{dt}.$$

The same command can be used to store the five other components (SSyy, SSzz, SSxy, SSxz and SSyz) of the rate of strain tensor.

Just as for the Smagorinsky model, the total viscosity can be defined as a function in the parameter file:

```
SourceViscosity {}  { return μ + ρ*pow((0.165*ftt_cell_size(cell)), 2.) *
                    sqrt(2.)*(D2 - sqrt((SSxx*SSxx + SSyy*SSyy + SSzz*SSzz
                    + 2*SSxy*SSxy + 2*SSxz*SSxz + 2*SSyz*SSyz)/(t*t)));}
```

with t the time. Indeed, the `SSij` have to be divided by t as they are the time integrals of the rate of strain tensor components and not their average.

Unfortunately, the two papers [Leveque et al.(2007)][Toschi et al.(2006)] published on the SISM provide no information on the way $|\langle \bar{S}\,\rangle|$ converges in time or the way the time averaging has been made for the channel and the backward-facing step.

Choice of the time-averaging window

Assuming that $|\langle \bar{S} \rangle|$ can be estimated from a time-averaging of the SGS tensor, the main question that needs to be answered is how to average it. Obviously, the proper mean-SGS tensor can only be obtained from a time-average on a time-scale relative to the problem of interest and, therefore, the model is always going to need to be adapted to the situation at hand.

From the formulation of the model, until $|\langle \bar{S} \rangle|$ has converged to its final value, it is going to be strongly coupled with the code. Each variation of $|\langle \bar{S} \rangle|$ is going to change the flow and each variation of the flow is going to change $|\langle \bar{S} \rangle|$. This means that the system could potentially become unstable very quickly. The period when the model is most at risk of growing unstable is the initial regime. Therefore, averaging was initiated several time units after the start of the simulation either using under-resolved DNS or standard Smagorinsky model. As the Smagorinsky model is known to be too dissipative [Zang et al.(1993)], it is worth just using the under-resolved DNS as there will be more chances to reach a fully turbulent state at the end of the transitory regime.

Once the flow is close to becoming well-established, the averaging of $\bar{S}$ starts. As the fluctuations of $\bar{S}$ are turbulent, use of the SISM at the same time is still dangerous for the stability of the system and therefore averaging of $\bar{S}$ is only started 100 timesteps later.

Several averaging techniques can be envisaged. The ideal would be to use an arithmetic mean of $\bar{S}$ over a moving averaging window of length T, where T is a time-scale statistically relevant to the flow. This is not an option, however as it requires the storage of the whole time series used to compute the average, which is much too expensive.

The averaging can be done on all the values of the SGS tensor from the beginning of the simulation. This is feasible, but would lead to very slow convergence in the model.

The arithmetic mean can be used on smaller time series but the moving window is not possible to implement. As an alternative it is possible to start several averaging at different times in the simulation and switch from one to the other during the simulation. Many attempts were conducted on very coarse meshes on a 3-D lid-driven cavity problem. At first this appeared quite effective with good convergence of the total mean of the SGS tensor, but the whole system would eventually become fully unstable at some random moment without any obvious reason.

A different averaging strategy that allows the use of an averaging window is to perform an averaging of the form

$$\langle \bar{S} \rangle^{n+1} = \frac{(t^n - a^{n+1}\,\Delta t)\langle \bar{S} \rangle^n + (1 + a^{n+1})\,\Delta t\,\bar{S}^{n+1}}{t^n + \Delta t},$$

where a^{n+1} can be a random coefficient or just a constant that dictates the length of the averaging window [Butterweck(2008)]. The main disadvantage of this method is that a different weighting is applied on the different points of the time-series with more importance being given to the most recent SGS tensors. Good convergence results of the SISM using this type of averaging, has per reported [Butterweck(2008)] therefore it was decided to adopt this approach.

Appendix D

Characteristics of the wake past a cylinder reported in the literature

This appendix consists of two table reporting characteristics of the wake past a cylinder found in the literature and useful to validate the 2-D model.

	Re	l	a	b	Cd	λ
Coutanceau and Bouard [Coutanceau and Bouard(1977)]	10	0.03	0.01	0.12	-	0.12
-	10	0.16	0.06	0.24	-	0.07
-	10	0.28	0.11	0.29	-	0.024
-	10	0.34	0.12	0.31	-	0
-	15	0.31	0.12	0.31	-	0.12
-	15	0.45	0.17	0.36	-	0.07
-	15	0.58	0.21	0.39	-	0.024
-	15	0.63	0.23	0.40	-	0
-	20	0.60	0.22	0.39	-	0.12
-	20	0.73	0.27	0.42	-	0.07
-	20	0.87	0.31	0.45	-	0.024
-	20	0.93	0.33	0.47	-	0
Ye et al. [Ye et al.(1999)]	20	0.92	-	-	2.03	0.033
Le et al. [Le et al.(2006)]	20	0.93	-	-	2.05	0
Calhoun [Calhoun(2002)]	20	0.92	-	-	2.19	0.0625
Taira et al. [Taira and Colonius(2007)]	20	0.94	0.37	0.43	2.06	0.0167
-	20	0.97	0.39	0.43	2.07	0.0167
Linnink et al. [Linnick and Fasel(2005)]	20	0.93	0.36	0.43	2.16	0.056
-	20	0.93	0.36	0.43	2.06	0.023
Saiki and Birringen [Saiki and Biringen(1996)]	25	1.41	0.53	0.5	1.54	0.2
Gresho et al. [Gresho et al.(2005)]	25	1.15	0.38	0.47	2.26	-
Coutanceau and Bouard [Coutanceau and Bouard(1977)]	30	1.17	0.42	0.47	-	0.12
-	30	1.31	0.48	0.50	-	0.07
-	30	1.46	0.52	0.53	-	0.024
-	30	1.53	0.55	0.54	-	0
Saiki and Birringen [Saiki and Biringen(1996)]	30	1.7	0.62	0.5625	1.38	0.2
Coutanceau and Bouard [Coutanceau and Bouard(1977)]	40	1.75	0.62	0.52	-	0.12
-	40	1.89	0.68	0.56	-	0.07
-	40	2.04	0.73	0.58	-	0.024
-	40	2.13	0.76	0.59	-	0
Marella et al. [Marella et al.(2005)]	40	2.30	-	-	1.52	0.033
Ye et al. [Ye et al.(1999)]	40	2.27	-	-	1.52	0.033
Le et al. [Le et al.(2006)] moving	40	2.15	-	-	1.67	0
- static	40	2.22	-	-	1.56	0
Calhoun [Calhoun(2002)]	40	2.18	-	-	1.62	0.0625
Taira et al. [Taira and Colonius(2007)]	40	2.33	0.75	0.60	1.55	0.0167
-	40	2.30	0.73	0.60	1.54	0.0167
Linnink et al. [Linnick and Fasel(2005)]	40	2.23	0.71	0.59	1.61	0.056
-	40	2.28	0.72	0.60	1.54	0.023

Table D.1. Published values of the physical characteristic of the cylinder's wake for laminar regime.

	Re	St	Cd	λ
Saiki and Birringen [Saiki and Biringen(1996)]	100	0.171	1.26	0.2
Gresho et al. [Gresho et al.(2005)]	100	0.18	1.76	-
Saiki and Birringen [Saiki and Biringen(1996)]	200	0.197	1.18	0.2
Gresho et al. [Gresho et al.(2005)]	200	0.21	1.76	-
Le et al. [Le et al.(2006)]	200	0.187	1.34	0
Taira et al. [Taira and Colonius(2007)]	200	0.196	1.35	0.0167
-	200	0.195	1.34	0.0167
-	200	0.197	1.36	0.0167
Linnink et al. [Linnick and Fasel(2005)]	200	0.199	1.37	0.056
Linnink et al. [Linnick and Fasel(2005)]	200	0.197	1.34	0.023
Marella et al. [Marella et al.(2005)]	300	0.22	1.28	0.033
Ye et al. [Ye et al.(1999)]	300	0.21	1.38	0.033
Le et al. [Le et al.(2006)]	300	0.2	1.34	0
Saiki and Birringen [Saiki and Biringen(1996)]	400	0.22	1.18	0.2
Gresho et al. [Gresho et al.(2005)]	400	0.22	1.78	-

Table D.2. Published values of the physical characteristic of the cylinder's wake for vortex shedding regime.

Appendix E
Turbulent drag model

In this appendix, an early investigation of the propagule mean sinking velocity is reported. An Eulerian description of the propagule dynamics was adopted and Newton's law of motion was applied to the propagules. In most cases, particle motion is described by a transient state followed by an equilibrium state where particles sink at their terminal velocity. The influence of external forces on the particle at steady state can usually be described by a drag coefficient [Michealides(1997)].

Considering the relatively constant slopes observed, it can be assumed that propagule sinking can be described by the constant terminal velocity of the propagules. Effective drag coefficient can be derived from the experimental measurements and it should then be possible to relate to the parameters of the problem (Re_p, R_ρ and R_V).

In the absence of turbulence (RPM = 0), as explained earlier, the Stokes sinking velocity formula, representative of the balance between the buoyancy forces, $\frac{4}{3}\pi\, r^3\, (\rho_P - \rho_f)\, g$, and the viscous drag, $-6\,\pi\, r\, \mu\, V_s$, can be used :

$$V_s = \frac{2}{9} r^2 \frac{(\rho_p - \rho_f)}{\mu} g.$$

For higher Reynolds numbers, the action of hydro-dynamical forces is often modelled using similar viscous drag forces with an additional empirical correction factor expressed as a function of the particle Reynolds number [Michealides(1997)]:

$$F_d = C_1\, (6\,\pi\, r\, \mu\, V_s),$$

where C_1 is the standard Schiller-Neumann drag law [Rowe(1961)]

$$1 + 0.15\, \mathrm{Re}_p^{0.667}.$$

This law stands in the context of particle sinking in a laminar flow but cannot be used in the case of a turbulent flow.

For turbulent flows, no universal law is known, but many studies have attempted to quantify the effect of turbulence on the drag coefficient of particles [Doroodchi et al.(2008)]

[Bagchi and Balachandar(2003)] [Clamen and Gauvin(1969)], some of them in the case of free-stream turbulence in a stirred vessel [Brucato et al.(1998)] [Uhlherr and Sinclair(1970)].

Uhlherr and Sinclair [Uhlherr and Sinclair(1970)] suggested that the drag coefficient is a function of the particle Reynolds number, Re_p, and of the ratio over root mean square value of turbulent fluctuations in the direction of the average particle motion and the average sinking velocity of the particles (which is similar to R_V when V_s is replaced by V_p). Assuming that the turbulent fluctuations are proportional to propeller speed [Brucato et al.(1998)], R_V can be redefined in the context of tank flow as

$$R_V = \frac{V_s}{Nh},$$

where N is the propeller speed and h a length-scale, which we take equal to the tank's height.

For each data point, the drag coefficient C_d can be estimated as

$$C_d = \frac{4\,g\,r\,(\rho_p - \rho_f)}{3\,\rho_f}\,\frac{1}{V_p^2},$$

where V_p is the measured terminal velocity of the propagules or their averaged sinking speed.

Uhlherr and Sinclair [Uhlherr and Sinclair(1970)] was tested without success (Figure E.1), which was hardly a surprise as it is valid only when turbulent fluctuations are smaller than the particle Stokes velocity. Drag coefficient increases as a function of $1/R_V$ (Figure E.2) do not allow identification of any clear trends. Nevertheless, it can be observed that globally the drag coefficient increases with the stirring which matches the decrease of 30 to 50% of particles sinking speed that was seen in the literature [Brucato et al.(1998)]. A drop in drag coefficient can be observed for most species except for *Durvillaea antarctica*. It is unclear what this drop could correspond to.

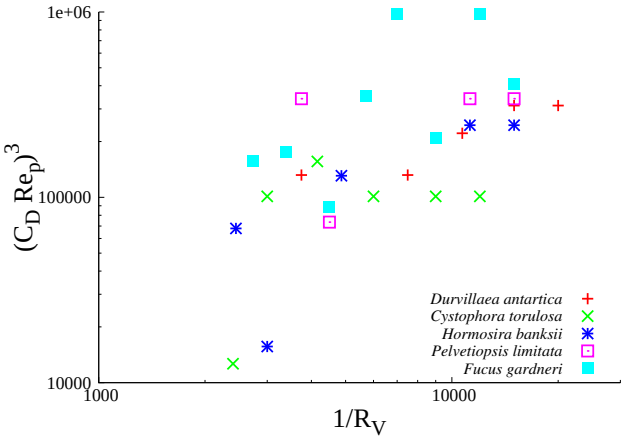

Figure E.1. Comparison of experimental results with Uhlherr and Sinclair[Uhlherr and Sinclair(1970)] correlation.

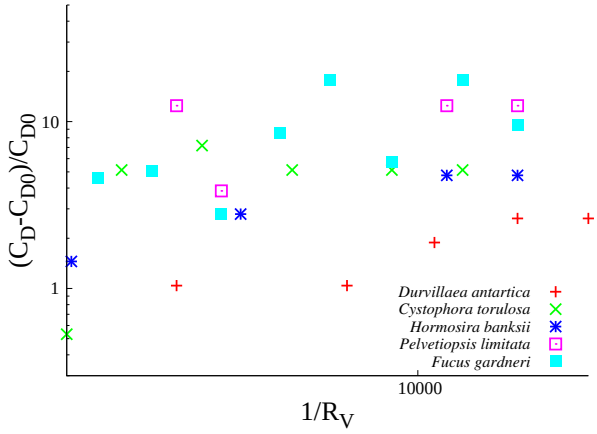

Figure E.2. Relative increase in drag coefficient as a function of $1/R_V$.

Despite the linear slopes observed on almost all the sinking curves, no good correlation was found between the observed results and the global parameters R_ρ, Re_p and R_V. No way was found to connect these data with other published results. Brucato et al. [Brucato et al.(1998)], in their study of the influence of turbulence on particle drag coefficient in a stirred vessel using solid particles did not find good correlation between Re_p, R_V and their experimental drag coefficients. Nevertheless, their results were in good agreement with the ones of Magelli et al. [Magelli et al.(1990)], suggesting the use of the ratio of the particle diameter to the Kolmogorov scale as the main parameter controlling the influence of turbulence on particle drag.

It is interesting to note that beyond the correlation between particle drag and Kolmogorov micro-scale, Brucato et al. [Brucato et al.(1998)] showed that, in their stirred vessel, large scale structures had little influence on particle sinking. Nevertheless, lower turbulence regimes where used for their study. Using simple scaling arguments, the Kolmogorov length-scale was estimated to scale with $(1/N)^{3/4}$ (See Chapter 5). From that estimation, our data were plotted against Brucato et al.'s correlation (Figure E.3). No good correlation is found.

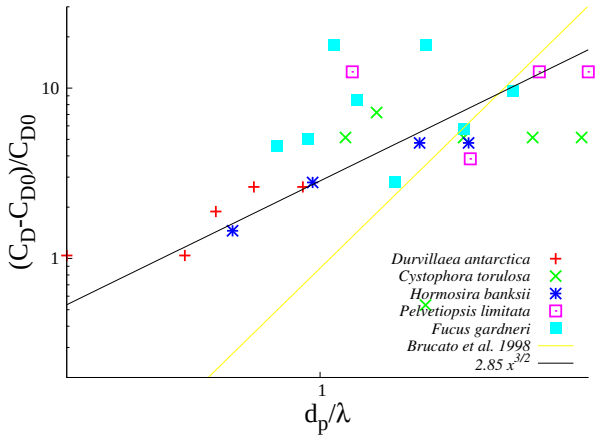

Figure E.3. Comparison of experimental results with Brucato et al.[Brucato et al.(1998)] correlation.

There could be several explanations to the absence of correlation. It could be that the estimation of the Kolmogorov micro-scale is too coarse, there is too much variability in the data, or too much heterogeneity in the system. A last reason could be that R_V as well as the propagule properties are beyond the bounds of this method and, for example, propagules are fully transported by the turbulent flow in the core of the tank. This last conclusion was proved to be right.

References

[Abbott and Hollenberg(1976)] Abbott, I. A., Hollenberg, G. J., 1976. Marine Algae of California. Stanford University Press.

[Abelson and Denny(1997)] Abelson, A., Denny, M., 1997. Settlement of marine organisms in flow. Annual Review of Ecological Systems 28, 317–339.

[Adams(1994)] Adams, N. M., 1994. Seaweed of New Zealand. Canterbury University Press.

[Aftosmis et al.(2000)] Aftosmis, M. J., Berger, M. J., Adomavicius, G., 2000. A parallel multilevel method for adaptively refined cartesian grids with embedded boundaries. AIAA 2000-0808.

[Aidun et al.(1991)] Aidun, C. K., Triantafillopoulos, N. G., Benson, J. D., 1991. Global stability of a lid-driven cavity with throughflow: Flow visualization studies. Physics of Fluids A. 3(9), 2081–2091.

[Airy(1841)] Airy, G. B., 1841. Tides and waves. Encyclopaedia Metropolitana 3, 1817–1845.

[Altunbas et al.(2002)] Altunbas, A., Kelbaliyev, G., Ceylan, K., 2002. Eddy diffusivity of particles in turbulent flow in rough channels. Aerosol Science 33, 1075–1086.

[Arfken(1985)] Arfken, G., 1985. Mathematical Methods for Physicists, 3rd ed. Orlando, FL: Academic Press.

[Auteri et al.(2002)] Auteri, F., Parolini, N., Quartapelle, L., 2002. Numerical investigation on the stability of singular driven cavity flow. Journal of Computational Physics 183, 1–25.

[Bagchi and Balachandar(2003)] Bagchi, P., Balachandar, S., 2003. Effect of turbulence on the drag and lift of a particle. Physics of Fluids 15(11), 3496–3513.

[Bakker et al.(1996)] Bakker, A., Myers, K. J., Ward, R. W., Lee, C. K., 1996. The laminar and turbulence flow pattern of a pitched blade turbine. Transactions of Institution of Chemical Engineers 74, 485–491.

[Bardina et al.(1983)] Bardina, J., Ferziger, J. H., Reynolds, W. C., 1983. Improved turbulence models based on large eddy simulation of homogeneous, incompressible, turbulent flows. Ph. D. dissertation, Department of Mechanical Engineering, Stanford University.

[Batchelor(1967)] Batchelor, G. K., 1967. An introduction to fluid dynamics. Cambridge.

[Benard(1908)] Benard, H. C. R., 1908. Formation de centres de giration a l arriere d un obstacle en mouvement. Comote Rendus de l' Academie des Sciences de Paris 147, 839.

[Blanco and Magnaudet(1995)] Blanco, A., Magnaudet, J., 1995. The structure of the axisymmetric high-reynolds number flow around an ellipsoidal bubble of fixed shape. Physics of Fluids 7, 1265–1274.

[Bloor(1964)] Bloor, M. S., 1964. The transition to turbulence in the wake of a circular cylinder. Journal of Fluid Mechanics 19, 290–304.

[Bouffanais et al.(2006)] Bouffanais, R., Deville, M. O., Fischer, P. F., Leriche, E., Weill, D., 2006. Large-eddy simulation of the lid-driven cubic cavity flow by the spectral element method. Journal of Scientific Computing 27, 151–162.

[Boussinesq(1877)] Boussinesq, J., 1877. Theorie de l ecoulement tourbillant. Memoire Presentes par Divers Savants a l Academie Royale des Sciences de l Institut de France 23, 46–50.

[Brown et al.(2001)] Brown, D. L., Cortez, R., Minion, M. L., 2001. Accurate projection methods for the incompressible navier-stokes equations. Journal of Computational Physics 168, 464–499.

[Brucato et al.(1998)] Brucato, A., Grisafi, F., Montante, G., 1998. Particle drag coefficients in turbulent fluids. Chemical Engineering Science 53(18), 3295–3314.

[Buchholtz-TenBrink et al.(1989)] Buchholtz-TenBrink, M. R., Gust, G., Chavis, D., 1989. Calibration and performance of a stirred benthic chamber. Deep-Sea Research 36(7), 1083–1101.

[Buckingham(1914)] Buckingham, E., 1914. On physically similar systems; illustrations of the use of dimensional equations. Physical Review 4, 345–376.

[Burdick et al.(2001)] Burdick, G. M., Berman, N. S., Beaudoin, S. P., 2001. Describing hydrodynamic particle removal from surfaces using the particle reynolds number. Journal of Nanoparticle Research 3, 455–467.

[Butman and Grassle(1992)] Butman, C. A., Grassle, J. P., 1992. Active habitat selection by capitella larvae: Two-choice experiments in still water and flume flows. Journal of Marines Research 50, 669–715.

[Butterweck(2008)] Butterweck, M., 2008. Personal correspondence.

[Calhoun(2002)] Calhoun, D., 2002. A cartesian grid method for solving the two-dimensional streamfunction-vorticity equations in irregular regions. Journal of Computational Physics 176, 231–275.

[Callow et al.(2000)] Callow, J. A., Crawford, S. A., Higgins, M. J., P. Mulvaney, R. W., 2000. The application of atomic force microscopy to topographical studies and force measurements on the secreted adhesive of the green alga enteromorpha. Planta 211, 641–647.

[Callow and Callow(2002)] Callow, M. E., Callow, J. A., 2002. Marine biofouling: a sticky problem. Biologist 49, 10–14.

[Caltagirone(2004)] Caltagirone, J. P., 2004. Physique des ecoulements continus. Cours de mecanique des fluides - 3eme annee- Ecole MATMECA.

[Cantwell(1981)] Cantwell, B. J., 1981. Organized motion in turbulent flow. Annual Review of Fluid Mechanics 13, 457–515.

[Canuto(2000)] Canuto, V. M., 2000. Turbulent convection: is 2d a good proxy of 3d? Astronomy and Astrophysics 357, 177–179.

[Champagne et al.(1977)] Champagne, F. H., Friehe, C. A., LaRue, J. C., 1977. Flux measurements, flux estimation techniques, and fine-scale turbulence measurements in the unstable surface layer over land. Journal Atmospheric Sciences 34, 515–530.

[Chang and Cowen(2002)] Chang, K.-A., Cowen, E. A., 2002. Turbulent prandtl number in neutrally buoyant turbulent round jet. Journal of Engineering Mechanics 128(10), 1082–1087.

[Chapman(1995)] Chapman, A. R. O., 1995. Functional ecology of fucoid algae: twenty-three years of progress. Phycologia 34(1), 1–32.

[Choi et al.(2007)] Choi, J., Oberoi, R. C., Edwards, J. R., Rosati, J. A., 2007. An immersed boundary method for complex incompressible flows. Journal of Computational Physics 224, 757–784.

[Chorin(1968)] Chorin, A. J., 1968. Numerical solution of the navier-stokes equations. Mathematics of Computation 22, 745–762.

[Clamen and Gauvin(1969)] Clamen, A., Gauvin, W. H., 1969. Effects of turbulence on the drag coefficients of spheres in a supercritical flow regime. American Institute of Chemical Engineering Journal 15, 184–189.

[Clayton(1992)] Clayton, M. N., 1992. Propagules of marine macroalgae: structure and development. British Phycology Journal 27, 219–232.

[Cleaver and Yate(1973)] Cleaver, J. W., Yate, B., 1973. Mechanism of detachment of colloidal particles from a flat substrate in a turbulent flow. Journal of Colloid and Interface Science 44, 464–474.

[Cleaver and Yates(1976)] Cleaver, J. W., Yates, B., 1976. The effect of re-entrainment on particle deposition. Chemical Engineering Science 31, 147–151.

[Cooper et al.(2001)] Cooper, K., Gupta, A., Beaudoin, S., 2001. Simulation of the adhesion of particles to surfaces. Journal of Colloid and Interface Sc. 234, 284–292.

[Coutanceau and Bouard(1977)] Coutanceau, M., Bouard, R., 1977. Experimental determination of the main features of the viscous flow in the wake of a circular cylinder in uniform translation. part 1. steady flow. Journal of Fluid Mechanics 79, 231–256.

[Crank(1957)] Crank, J., 1957. The mathematics of diffusion. Oxford, at the clarendon press.

[Crimaldi et al.(2006)] Crimaldi, J. P., Koseff, J. R., Monismith, S. G., 2006. A mixing-length formulation for the turbulent prandtl number in wall-bounded flows with bed roughness and elevated scalar sources. Physics of Fluids 18, 095102–095102–9.

[Crimaldi et al.(2002)] Crimaldi, J. P., Thompson, J. K., Rosman, J. H., Lowe, R. J., Koseff, J. R., 2002. Hydrodynamics of larval settlement: the influence of turbulent stress events at potential recruitment sites. Limnology Oceanography 47, 1137–1151.

[Davies(1945)] Davies, C. N., 1945. Definitive equations for the fluid resistance of spheres. Proceedings of the Physical Society 57(4), 259–270.

[Delanaye et al.(1999)] Delanaye, M., Aftosmis, M. J., Berger, M. J., Liu, Y., Pulliam, T. H., 1999. Automatic hybrid-cartesian grid generation for high-reynolds number flows around complex geometries. 37th AIAA Aeroscape Sciences Meeting and Exhibit 99-0777, 1–17.

[Deleersnijder et al.(2006)] Deleersnijder, E., Beckers, J.-M., Delhez, E. J. M., 2006. The residence time of settling particles in the surface mixed layer. Environmental Fluid Mechanics 6, 25–42.

[Delhez et al.(2004)] Delhez, E. J.-M., Heemink, A. W., Deleersnijder, E., 2004. Residence time in a semi-enclosed domain from the solution of an adjoint problem. Estuarine, Coastal and Shelf Science 61, 691–702.

[Denny(1988)] Denny, M. W., 1988. Biology and the mechanics of the wave-swept environment. Princeton University Press.

[Denny and Shibata(1989)] Denny, M. W., Shibata, M. F., 1989. Consequences of surf-zone turbulence for settlement and external fertilization. American Naturalist 134(6), 859–889.

[Derjaguin et al.(1997)] Derjaguin, B. V., Muller, V. M., Toporov, Y. P., 1997. Effect of contact deformations on the adhesion of particles. Journal of Colloid and Interface Science 190, 253–257.

[Deshpande and Milton(1998)] Deshpande, M. D., Milton, S. G., 1998. Kolmogorov scales in a driven cavity flow. Fluid Dynamics Research 22, 359–381.

[Deshpande and Shankar(1994)] Deshpande, M. D., Shankar, P. N., 1994. Transition and turbulent flow in a three-dimensional cavity. National Aerospace Laboratory Document PD CF 9411, Bangalore, India: National Aerospace Laboratory.

[Devlin(2002)] Devlin, K. J., 2002. The millennium problems: The seven greatest unsolved mathematical puzzles of our time. Basic Books.

[Dillon et al.(1995)] Dillon, R., Fauci, L. J., Graver, D., 1995. A microscale model of bacterial swimming, chemotaxis and substrate transport. Journal of Theoretical Biology 177, 325–340.

[Doroodchi et al.(2008)] Doroodchi, E., Evans, G. M., Schwarz, M. P., Lane, G. L., Shah, N., Nguyen, A., 2008. Influence of turbulence intensity on particle drag coefficients. Chemical Engineering Journal 135, 129–134.

[Ebert et al.(2001)] Ebert, U., Arrayas, M., Temme, N., Sommeijer, B., Huisman, J., 2001. Critical conditions for phytoplankton blooms. Bulletin of Mathematical Biology 63, 1095–1124.

[Eckman(1990)] Eckman, J. E., 1990. A model of passive settlement by planktonic larvae onto bottoms of differing roughness. Limnology and Oceanography 35(4), 887–901.

[Eggels(1996)] Eggels, J. M. G., 1996. Direct and large eddy simulation of turbulent fluid flow using the lattice boltzmann scheme. International Journal of Heat and Fluid Flow 17, 307–323.

[El-Hady et al.(1993)] El-Hady, N. M., Zang, T. A., Piomelli, U., 1993. Dynamic subgrid-scale modelling for high-speed transitional boundary layers. ASME FED 162, 103.

[Erturk(2005)] Erturk, E., 2005. Numerical solutions of 2-d steady incompressible driven cavity flow at high reynolds numbers. International Journal of Numerical Methods in Fluids 48(7), 747–774.

[Fadlun et al.(2000)] Fadlun, E. A., Verzicco, R., Orlandi, P., Mohd-Yusof, J., 2000. Combined immersed-boundary finite-difference methods for three-dimensional complex flow simulations. Journal of Computational Physics 161, 35–60.

[Ferziger(1998)] Ferziger, J. H., 1998. Direct and large eddy simulation of turbulence - Numerical Methods in Fluid Mechanics. Vol. 16. Ed. Alain Vincent - American Mathematical Society.

[Finlay et al.(2002)] Finlay, J. A., Callow, M. E., Schultz, M. P., Swain, G. W., Callow, J. A., 2002. Adhesion strength of settled spores of the green alga. Biofouling 18(4), 251–256.

[Fleagle and Businger(1980)] Fleagle, R. G., Businger, J. A., 1980. An Introduction to Atmospheric Physics, 2d ed. Academic Press.

[Fletcher and Callow(1992)] Fletcher, R. L., Callow, M. E., 1992. The settlement, attachment and establishment of marine algal spores. British Phycology Journal 14, 69–81.

[Fogelson(1992)] Fogelson, A. L., 1992. Continuum models of platelet aggregation: Formulation and mechanical properties. SIAM Journal of Applied Mathematics 52, 1089–1110.

[Fornberg(1988)] Fornberg, B., 1988. Steady viscous flow past a sphere at high reynolds numbers. Journal of Fluid Mechanics 190, 471–489.

[Friedlander and Johnstone(1957)] Friedlander, S. K., Johnstone, H. F., 1957. Deposition of suspended particles from turbulent gas stream. Ind. Eng. Chemical 49, 1151–1156.

[Galassi et al.(1983)] Galassi, M., Davies, J., Theiler, J., Gough, B., Jungman, G., Booth, M., Rossi, F., 1983. Gnu scientific library (gsl) - reference manual. http://www.gnu.org/software/gsl/.

[Galvin(1972)] Galvin, C. J., 1972. Wave breaking in shallow water. In R. E. Meyer ed., Waves on beaches and the resulting sediment transport.

[Garcia et al.(2005)] Garcia, C. M., Cantero, M. I., Nino, Y., Garcia, M. H., 2005. Turbulence measurements with acoustic doppler velocimeters. Journal of Hydraulic Engineering 124(6), 1062–1073.

[Gargett(1984)] Gargett, A. E., 1984. Vertical eddy diffusivity in the ocean interior. Journal of Marine Research 42(2), 359–393.

[Garraffo et al.(2001)] Garraffo, Z. D., Mariano, A. J., Griffa, A., Veneziani, C., Chassignet, E. P., 2001. Lagrangian data in a high-resolution numerical simulation of the north atlantic. i. comparison with in situ drifter data. Journal of Marine Systems 29, 157–176.

[Geankoplis(2003)] Geankoplis, C. J., 2003. Transport processes and separation process principles. 4th Edition.

[Germano et al.(1991)] Germano, M., Piomelli, U., Moin, P., Cabot, W. H., 1991. A dynamic subgrid-scale eddy viscosity model. Physics Fluids A 3(7), 1760–1765.

[Ghia et al.(1982)] Ghia, U., Ghia, K. N., Sin, C. T., 1982. High-re solutions for incompressible flow using the navier-stokes equations and multigrid method. Journal of Computational Physics 48, 387–411.

[Gidhagen et al.(1989)] Gidhagen, L., Rahm, L., Nyberg, L., 1989. Lagrangian modelling of dispersion, sedimentation and resuspension process in marine environment. Ocean Dynamics 42(3-6), 249–270.

[Giri et al.(2004)] Giri, S., Shimizu, Y., Surajate, B., 2004. Laboratory measurements and numerical simulation of flow and turbulence in a meandering-like flume with spurs. Flow Measurements and Instrumentation 15, 301–309.

[Goldstein et al.(1993)] Goldstein, D., Handler, R., Sirovich, L., 1993. Modeling a no slip flow boundary with an external force field. Journal of Computational Physics 105, 354–366.

[Goodrich et al.(1990)] Goodrich, J. W., Gustafson, K., Halasi, K., 1990. Hopf bifurcation in the driven cavity. Journal of Computational Physics 90, 219–261.

[Goring and Nikora(2002)] Goring, D. G., Nikora, V. I., 2002. Despiking acoustic doppler velocimeter data. Journal of Hydraulic Engineering 124(6), 117–126.

[Gotwols et al.(1990)] Gotwols, B. L., Sterner, R. E., McGregor, J. A., 1990. Johns Hopkins University/Applied Physics Laboratory IDL Information Page. http://fermi.jhuapl.edu/s1r/idl/idl.html.

[Grass(1971)] Grass, A. J., 1971. Structural features of turbulent flow over smooth and rough boundaries. Journal of Fluid Mechanics 50, 223–256.

[Green(1992)] Green, M. O., 1992. Spectral estimates of bed shear stress at subcritical reynolds numbers in a tidal boundary layer. Journal Physical Oceanography 22, 903–917.

[Gregoire et al.(1996)] Gregoire, Y., Bourget, E., Verrette, J. L., 1996. Deposition of mimics of planktonic invertebrate larvae on simple and complex substrata in flumes flows. Marine Ecology Progress Series 135, 89–100.

[Grenville et al.(1995)] Grenville, R. K., Ruszkowski, S., Garred, E., 1995. Blending of miscible liquids in the turbulent and transitional regimes. Paper 1.5, 15th NAMF Mixing Conference, Banff, Canada.

[Gresho et al.(2005)] Gresho, P. M., Chan, R., Upson, C., Lee, R., 2005. A modified finite element method for solving the time-dependent, incompressible navier-stokes equations: Part 2: applications. International Journal of Numerical Methods in Fluids 4, 619.

[Gross and Dade(1991)] Gross, T. F., Dade, W. B., 1991. Suspended sediment storm modeling. Marine Geology 99, 343–360.

[Gross et al.(1992)] Gross, T. F., Werner, F. R., Eckman, J. E., 1992. Numerical modeling of larval settlement in turbulent bottom boundary layer. Journal of Marine Research 50, 611–642.

[Habisreutinger et al.(2007)] Habisreutinger, M. A., Bouffanais, R., Leriche, E., Deville, M. O., 2007. A coupled approximate deconvolution and dynamic mixed scale model for large-eddy simulation. Journal of Computational Physics 224, 241–266.

[Hadfield(1986)] Hadfield, M. G., 1986. Settlement and recruitment of marine invertebrates: a perspective and some proposals. Bulletin of Marine Science 39, 155–167.

[Hay(1994)] Hay, C. H., 1994. *Durvillaea*(bory). In: Akatsuka, I. (Ed.), Biology of Economic Algae. SPB Academic Publisher, The Hague, The Neherlands, 353–384.

[Helmuth and Denny(2003)] Helmuth, B., Denny, M. W., 2003. Predicting wave exposure in the rocky intertidal zone: Do bigger waves always lead to larger forces? Limnology and Oceanography 48(3), 1338–1345.

[Hendriks et al.(2006)] Hendriks, I. E., van Duren, L. A., Herman, P. M. J., 2006. Turbulence levels in a flume compared to the field: implications for larval settlement studies. Journal of Sea Research 55, 15–29.

[Huisman(2000)] Huisman, J. M., 2000. Marine plants of Australia. University of western Australia press. ISBN 1-876-26833-6.

[Huntley(1988)] Huntley, D. A., 1988. A modified inertial dissipation method for estimating seabed stresses at low reynolds numbers, with application to wave/current boundary layer measurements. Journal of Physical Oceanography 18, 339–346.

[Hurd(2000)] Hurd, C. L., 2000. Water motion, marine macroalgal physiology, and production. Journal of Phycology 36(3), 453–472.

[Ivey et al.(2008)] Ivey, G. N., Winters, K. B., Koseff, J. R., 2008. Density stratification, turbulence, but how much mixing? Annual Review Fluid Mechanics 40, 169–184.

[Jaworski et al.(1996)] Jaworski, Z., Nienow, A. W., Dyster, K. N., 1996. An lda study of the turbulent flow field in a baffled vessel agitated by an axial, down pumping hydrofoil impeller. Canadian Journal of Chemical Engineering 74, 3–15.

[Jeanmart and Winckelmans(2002)] Jeanmart, H., Winckelmans, G. S., 2002. Comparison of recent dynamic subgrid-scale models in turbulent channel flow. Center for Turbulence Research, Proceedings of the Summer Program 2002, 105–116.

[Jimenez et al.(2008)] Jimenez, A., Crespo, A., Migoya, E., Garcia, J., 2008. Larde-eddy simulation of spectral coherence in a wind turbine wake. Environmental Research Letter 3, 1–9.

[Jimenez(2004)] Jimenez, J., 2004. Turbulent flows over rough walls. Annual Review of Fluid Mechanics 36, 173–196.

[Johnson et al.(1971)] Johnson, K. L., Kendall, K., Roberts, A. D., 1971. Surface energy and the contact of elastic solids. Proceedings of the Royal Society of London. Series A 324, 301–313.

[Jordan and Ragab(1994)] Jordan, S. A., Ragab, S. A., 1994. On the unsteady and turbulent characteristics of three-dimensional cavity flow. Journal of Fluids Engineering 116, 439–449.

[Kaftori et al.(1995)] Kaftori, D., Hetsroni, G., Banerjee, S., 1995. Particle behavior in the turbulent boundary layer. i. motion, deposition, and entrainment. Physics of Fluids 7(5), 1095–1106.

[Karmann(1912)] Karmann, T. V., 1912. Gottingen Nachr. Math. Phys. Kl. 12, 209.

[Karniadakis et al.(1988)] Karniadakis, G. E., Mikic, B. B., Patera, A. T., 1988. Minimum-dissipation transport destabilization: Reynolds analogy revisited. Journal of Fluid Mechanics 192, 365–391.

[Kays(1994)] Kays, W. M., 1994. Turbulent prandtl number - where are we? Transactions of ASME Journal of Heat Transfer 116, 284–295.

[Khokhlov(1998)] Khokhlov, A. M., 1998. Fully threaded tree algorithms for adaptive refinement fluid dynamics simulations. Journal of Computational Physics 143(2), 519–543.

[Kim et al.(2001)] Kim, J., Kim, D., Choi, H., 2001. An immersed boundary finite-volume method for simulations of flow in complex geometries. Journal of Computational Physics 171, 132–150.

[Kim et al.(2000)] Kim, S.-C., Firedrichs, C. T., Maa, J. P.-Y., Wright, L. D., 2000. Estimating bottom stress in tidal boundary layer from acoustic doppler velocimeter data. Journal Hydraulic Engineering 126(6), 399–406.

[Koehl and Wainwright(1977)] Koehl, M. A. R., Wainwright, S. A., 1977. Mechanical adaptations of a giant kelp. Limnology and Oceanography 22, 1067–1071.

[Kolmogorov(1941)] Kolmogorov, A. N., 1941. The local structure of turbulence in an incompressible fluid with very large reynolds number. Compte Rendu de l'Academie des Sciences 30, 301.

[Kresta and Wood(1993)] Kresta, S. M., Wood, P. E., 1993. The flow field produced by a pitched blade turbine: Characterization of the turbulence and estimation of the dissipation rate. Chemical Engineering Science 48, 1761–1773.

[Lai and Peskin(2000)] Lai, M., Peskin, C. S., 2000. An immersed boundary method with formal second-order accuracy and reduced numerical viscosity. Journal of Computational Physics 160, 705–719.

[Lamb(1994)] Lamb, H., 1994. Hydrodynamics, 6th edition. Cambridge University Press.

[Landau and Lifchitz(1976)] Landau, L., Lifchitz, E., 1976. Fluid Mechanics. Mir, Moscow.

[Lane(2003)] Lane, A., 2003. Development of a lagrangian sediment model to reproduce the bathymetric evolution of the mersey estuary. Ocean Dynamics 55, 541–548.

[Lanzani and Tamponi(1995)] Lanzani, G., Tamponi, M., 1995. A microscale lagrangian particle model for the dispersion of primary pollutant in a street canyon. sensitivity analysis and first validation trials. Atmospheric Environment 29(23), 3465–3475.

[Launder and Rodi(1983)] Launder, B. E., Rodi, W., 1983. The turbulent wall jet - measuring and modelling. Annual Review of Fluid Mechanics 15, 429–459.

[Le et al.(2006)] Le, D. V., Khoo, B. C., Peraire, J., 2006. An immersed interface method for viscous incompressible flows involving rigid and flexible boundaries. Journal of Computational Physics 220, 109–138.

[Lee(2003)] Lee, L., 2003. An immersed interface method for the incompressible navier-stokes equations. SIAM Journal of Scientific Computing 171, 822–842.

[Leonard and Luther(1995)] Leonard, L., Luther, M., 1995. Flow hydrodynamics in tidal marsh canopies. Limnology and Oceanography 40, 1474–1484.

[Lesieur and Metais(1996)] Lesieur, M., Metais, O., 1996. New trends in large-eddy simulation of turbulence. Annual Review of Fluid Mechanics 28, 45–82.

[Lesoinne and Farhat(1996)] Lesoinne, M., Farhat, C., 1996. Geometric conservation laws for flow problems with moving boundaries meshes, and their impact on aeroelastic computations. Computational Methods for Applied Mechanical Engineering 134, 71–90.

[Leveque et al.(2007)] Leveque, E., Toschi, F., Shao, L., Bertoglio, J.-P., 2007. Shear-improved smagorinsky model for large-eddy simulation of wall-bounded turbulent flows. Journal of Fluid Mechanics 570, 491–502.

[Leveque and Li(1994)] Leveque, R. J., Li, Z., 1994. The immersed interface method for elliptic equations with discontinuous coefficients and singular sources. SIAM Journal on Numerical Analysis 31, 1001–25.

[Leveque and Li(1997)] Leveque, R. J., Li, Z., 1997. Immersed interface method for stokes flow with elastic boundaries or surface tension. SIAM Journal of Scientific Computing 18(3), 709–735.

[Lewis(1964)] Lewis, J. R., 1964. The Ecology of Rocky Shores. English Universities Press, London.

[Li and Lai(2001)] Li, Z., Lai, M. C., 2001. The immersed interface method for the navier-stokes equation with singular forces. Journal of Computational Physics 171, 822–842.

[Li and Wang(2003)] Li, Z., Wang, C., 2003. A fast finite difference method for solving the navier-stokes equations on irregular domains. Communications in Mathematical Sciences 1(1), 180–196.

[Lilly(1966)] Lilly, D. K., 1966. On the application if the eddy viscosity concept in the inertial sub-range of turbulence. NCAR Manuscript No. 123, National Center for Atmospheric Research, Boulder, CO.

[Lilly(1992)] Lilly, D. K., 1992. A proposed modification of the germano subgrid-scale closure method. Physics Fluids A 4(3), 633–635.

[LimaESilva et al.(2003)] LimaESilva, A. L. F., Silveira-Neto, A., Damasceno, J. J. R., 2003. Numerical simulation of two-dimensional flows over a circular cylinder using the immersed boundary method. Journal of Computational Physics 189, 351–370.

[Linnick and Fasel(2005)] Linnick, M. N., Fasel, H. F., 2005. A higher order immersed interface method for simulating unsteady incompressible flows on irregular domains. Journal of Computational Physics 204, 157–192.

[Liu and Agarwal(1974)] Liu, B. Y. H., Agarwal, J. K., 1974. Experimental observation of aerosol deposition of turbulent flow. Aerosol Science 5(2), 145–155.

[Lopez and Garcia(1998)] Lopez, F., Garcia, M., 1998. Open-channel flow through simulated vegetation: suspended sediment transport modeling. Water Resources Research 34(9), 2341–2352.

[Lu et al.(2002)] Lu, Z., Liao, Y., Qian, D., McLaughlin, J. B., Derksen, J. J., Kontomaris, K., 2002. Large eddy simulations of a stirred tank using the lattice-boltzmann method on a nonuniform grid. Journal of Computational Physics 181, 675–704.

[Magelli et al.(1990)] Magelli, F., Fajner, D., Nocentini, M., Pasquali, G., 1990. Solids distribution in vessels stirred with multiple impellers. Chemical Engineering Science 45, 615–625.

[Marella et al.(2005)] Marella, S., Krishnan, S., H. Liu, H. S. U., 2005. Sharp interface cartesian grid method i: An easily implemented technique for 3d moving boundary computations. Journal of Computational Physics 210, 1–31.

[Masliyah and Epstein(1970)] Masliyah, J., Epstein, N., 1970. Numerical study of steady flow past spheroids. Journal of Fluid Mechanics 44(3), 493–512.

[Massel(1996)] Massel, S. R., 1996. Ocean surface waves: their physics and prediction. Vol. Advanced Series on Ocean Engineering - Volume 11. World Scientific.

[Mednikov(1981)] Mednikov, E. P., 1981. Turbulent transfer and sedimentation of aerosols. Moscow: Nauka.

[Micale et al.(2000)] Micale, G., Montante, G., Grisafi, F., Brucato, A., Godfrey, J., 2000. Cfd simulation of particle distribution in stirred vessels. Journal of Chemical Engineering 78(A), 435–444.

[Michealides(1997)] Michealides, E. E., 1997. Review - the transient equation of motion for particles, bubbles, and droplets. Journal of Fluids Engineering 119, 233–247.

[Minion(1996)] Minion, M. L., 1996. A projection method for locally refined grids. Journal of Computational Physics 127, 158–177.

[Mitrovic and Pavassiliou(2003)] Mitrovic, B. M., Pavassiliou, D. V., 2003. Transport properties for turbulent dispersion from wall sources. AIChE Journal 49(5), 1095–1108.

[Mittal and Iaccarino(2005)] Mittal, R., Iaccarino, G., 2005. Immersed boundary methods. Annual Review of Fluid Mechanics 37, 239–261.

[Mohd-Yusof(1996)] Mohd-Yusof, J., 1996. Interaction of massive particle with turbulence. Ph.D. Dissertation, Dept of Mechanical and Aerospace Engineering, Cornell Univ.

[Moin and Kim(1982)] Moin, P., Kim, J., 1982. Numerical investigation of turbulent channel flow. Journal Fluid Mechanics 118, 341–377.

[Moin et al.(1991)] Moin, P., Squires, K., Cabot, W., , Lee, S., 1991. A dynamic subgrid-scale model for compressible turbulence and scalar transport. Physics Fluids A 3, 2746–2757.

[Msadek(2005)] Msadek, R., 2005. Hydrodynamic tidal model of cook strait. Technical Report, National Institute of Water and Atmospheric research.

[Murman et al.(2003)] Murman, S. M., Aftosmis, M. J., Berger, M. J., 2003. Implicit approaches for moving boundaries in a 3d cartesian method. AIAA J. 1119.

[Muschenheim et al.(1986)] Muschenheim, D. K., Grant, J., Mills, E. L., 1986. Flumes for benthic ecologists: theory, construction and practice. Marine Ecology Progress Series 28, 185–196.

[Newtown(1687)] Newtown, I., 1687. Principia - axioms, or laws of motion.

[Nienow(1990)] Nienow, A. W., 1990. Agitators for mycelial fermentation. Trends in biotechnology 8, 224–233.

[Nienow(1997)] Nienow, A. W., 1997. On impeller circulation and mixing effectiveness in the turbulent flow regime. Chemical Engineering Science 52(15), 2557–2565.

[Nikora and Goring(1998)] Nikora, V. I., Goring, D. G., 1998. Adv measurements of turbulence: can we improve their interpretation? Journal of Hydraulic Engineering 124(6), 679–690.

[Nokes(2005)] Nokes, R. I., 2005. Fluidstream v6.01: User's guide. Software manual. University of Canterbury Christchurch, New Zealand.

[Norton(1992)] Norton, T. A., 1992. Dispersal by macroalgae. British Phycological Journal 27, 779–789.

[Nowell and Jumars(1987)] Nowell, A. R. M., Jumars, P. A., 1987. Flumes: Theoretical and experimental consideration for simulation of benthic environments. Ocean Marine Biology Annual Review 25, 91–112.

[O'Brien et al.(2003)] O'Brien, K. R., Ivey, G. N., Hamilton, D. P., Waite, A., Visser, P., 2003. Simple mixing criteria for the growth of negatively buoyant phytoplankton. Limnology Oceanography 48(3), 1326–1337.

[Ohmi and Li(2000)] Ohmi, K., Li, H.-Y., 2000. Particle-tracking velocimetry with new algorithms. Measurement Science and Technology 11, 603–616.

[Oldham et al.(2004)] Oldham, C. E., Ivey, G. N., Pullin, C., 2004. Estimation of a characteristic friction velocity in stirred benthic chambers. Marine Ecology Progress Series 279, 291–295.

[ONeill(1968)] ONeill, M. E., 1968. A sphere in contact with a plane wall in a slow linear shear flow. Chemical Engineering Science 23, 1293–1298.

[Otnes and Enochson(1978)] Otnes, R. K., Enochson, L., 1978. Applied time series analysis. Wiley, New York Vol. 1.

[Palmer et al.(2004)] Palmer, M., Neft, H., Petterson, T., Ackerman, J., 2004. Observations of particle capture on a cylindrical collector: implications for particle accumulation and removal in aquatic systems. Limnology and Oceanography 49, 76–85.

[Peng et al.(2003)] Peng, Y., Shiau, Y.-H., Hwang, R. R., 2003. Transition in a 2-d lid-driven cavity flow. Computers and Fluids 32, 337–352.

[Peskin(1972)] Peskin, C. S., 1972. Flow patterns around heart valves: a numerical method. Journal of Computational Physics 10, 220–252.

[Peskin(1977)] Peskin, C. S., 1977. Numerical analysis of blood flow in the heart. Journal of Computational Physics 25, 220–252.

[Peskin(2002)] Peskin, C. S., 2002. The immersed boundary method. Acta Numer 1.

[Peyret and Taylor(1983)] Peyret, R., Taylor, T. D., 1983. Computational Methods for Fluid Flow. Springer Verlag, New York/Berlin.

[Philip(1994)] Philip, J. R., 1994. Some exact solutions of convection-diffusion and diffusion equations. Water Resources Research 30(12), 3545–3551.

[Piomelli(1993)] Piomelli, U., 1993. High reynolds number calculations using the dynamic subgrid-scale stress model. Physics Fluids A 5(6), 1484–1490.

[Piomelli and Balaras(2002)] Piomelli, U., Balaras, E., 2002. Wall-layer models for large-eddy simulations. Annual Review of Fluid Mechanics 34, 349–374.

[Popinet(1999)] Popinet, S., 1999. GNU Triangulated Surface Library. http://gts.sourceforge.net.

[Popinet(2001a)] Popinet, S., 2001a. The Gerris Flow Solver website. http://gfs.sourceforge.net.

[Popinet(2001b)] Popinet, S., 2001b. Gerris test suite. http://gfs.sourceforge.net/tests/tests/index.html.

[Popinet(2003)] Popinet, S., 2003. Gerris: a tree-based adaptive solver for the incompressible euler equations in complex geometries. Journal of Computational Physics 190, 572–600.

[Popinet and Rickard(2007)] Popinet, S., Rickard, G., 2007. A tree-based solver for adaptive ocean modelling. Ocean Modelling 16, 224–249.

[Popiolek et al.(2006)] Popiolek, T. L., Awruch, A. M., Teixeira, P. R. F., 2006. Finite element analysis of laminar and turbulent flows using les and subgrid-scale models. Applied Math. Modelling 30, 177–199.

[Povitsky(2001)] Povitsky, A., 2001. Three-dimensional flow in cavity at yaw. NASA/CR-2001-211232. ICASE Report No. 2001-31., 1–18.

[Prandtl(1904)] Prandtl, L., 1904. Uber flussigkeitsbewegung bei sehr kleiner reibung. Proceedings of the 3rd International Mathematics Congress, Heidelberg, 484-491, Teuber, Leipzig, 484–491.

[Prasad and Koseff(1998)] Prasad, A. K., Koseff, J. R., 1998. Reynolds number and end-wall effects on a lid-driven cavity flow. Physics of Fluids A 1(2), 208–218.

[Quirk(1994)] Quirk, J. J., 1994. An alternative to unstructured grid for computing gas dynamic flows around arbitrarily complex two-dimensional bodies. Computer and Fluids 23, 125–142.

[Reidenbach et al.(2006)] Reidenbach, M. A., Monismith, S. G., Koseff, J. R., Yahel, G., Genin, A., 2006. Boundary layer turbulence and flow structure over a coral reef. Limnology and Oceanography 51(5), 1956–1968.

[Reynolds(1975)] Reynolds, A. J., 1975. Prediction of turbulent prandtl and schmidt numbers. International Journal of Heat Transfer 18, 1055–1069.

[Roberts and Webster(2001)] Roberts, P. J. W., Webster, D. R., 2001. Turbulent diffusion. In Environmental Fluid Mechanics - Theories and Applications, ASCE.

[Roshko(1953)] Roshko, A., 1953. On the development of turbulent wakes from vortex street. NACA Report 1191, 1–82.

[Rouhiainen and Stachiewiz(1970)] Rouhiainen, P. O., Stachiewiz, J. W., 1970. On the deposition of small particles from turbulent streams. Journal of Heat Transfer 92, 169–177.

[Rowe(1961)] Rowe, P. N., 1961. The drag coefficient of a sphere. Transaction of Institute of Chemical Engineering 39, 175–181.

[Ruiz(1996)] Ruiz, J., 1996. The role of turbulence in the sedimentation loss of pelagic aggregates from the mixed layer. Journal of Marine Research 54, 385–406.

[Ruszkowski(1994)] Ruszkowski, S., 1994. A rational method for measuring blending performance and comparison of different performance and comparison of different impeller types. Proceedings of the 8th European Mixing Conference, 283–291.

[Saiki and Biringen(1996)] Saiki, E. M., Biringen, S., 1996. Numerical simulation of a cylinder in uniform flow: application of virtual boundary method. Journal of Computational Physics 1233, 450–465.

[Schiel(1990)] Schiel, D. R., 1990. Macroalgal assemblages in new zealand: structure, interactions and demography. Hybiologia 192, 59–76.

[Schiel(2004)] Schiel, D. R., 2004. The structure and replenishment of rocky shore intertidal communities and biographic comparisons. Journal of Experimental Marine Biology and Ecology 300, 309–342.

[Schiel and Foster(2006)] Schiel, D. R., Foster, M. S., 2006. The population biology of large brown seaweeds: consequences of multi-phase life histories in dynamic coastal environments. Annual Review of Ecology and Systematics 37, 343–372.

[Schlichting and Gersten(2004)] Schlichting, H., Gersten, K., 2004. Boundary layer theory, 8th ed.. Springer-Verlag.

[Schwartzberg and Treybal(1968)] Schwartzberg, H. G., Treybal, R. E., 1968. Fluid and particle motion in turbulent stirred tanks. Industrial and Engineering Chemistry Fundamentals 7(1), 1–12.

[Shankar and Deshpande(2000)] Shankar, P. N., Deshpande, M. D., 2000. Fluid mechanics in the driven cavity. Annual Review of Fluid Mechanics 32, 93–136.

[Shen(1990)] Shen, J., 1990. Hopf bifurcation of the unsteady regularized driven cavity flow. Journal of Computational Physics 95, 228–245.

[Sheng et al.(1998)] Sheng, J., Meng, H., Fox, R. O., 1998. Validation of cfd simulations of a stirred tank using particle image velocimetry data. The Canadian Journal of Engineering 76, 611–625.

[Singha and Shy(2007)] Singha, R., Shy, W., 2007. Three-dimensional adaptive cartesian grid method with conservative interface restructuring and reconstruction. Journal of Computational Physics 224(1), 150–167.

[Smagorinsky(1963)] Smagorinsky, J. S., 1963. General circulation experiments with the primitive equations. i. the basic experiment. Monthly Weather Review 91, 99–164.

[Soltani and Ahmadi(2001)] Soltani, M., Ahmadi, G., 2001. On particle adhesion and removal mechanisms in turbulent flow. Journal of Nanoparticle Research 3, 455–467.

[Soo and Ihrig(1960)] Soo, S. L., Ihrig, H. K., 1960. Experimental determination of statistical properties of two-phase turbulent motion. Transactions ASME D 82(3), 609–621.

[Soulsby and Dyer(1981)] Soulsby, R. L., Dyer, K. R., 1981. The form of the near-bed velocity profile in a tidally accelerating flow. Journal of Geophysical Research 86-C9, 8067–8074.

[Speziale(1991)] Speziale, C. G., 1991. Analytical methods for the development of reynolds-stress closures in turbulence. Annual Review of Fluid Mechanics 23, 107–157.

[Stapleton and Huntley(1995)] Stapleton, K. R., Huntley, D. A., 1995. Seabed stress determinations using the inertial dissipation method and the turbulent kinetic energy method. Earth surface process. and landforms 20, 807–815.

[Stephenson and Stephenson(1949)] Stephenson, T. A., Stephenson, A., 1949. The universal feature of zonation between the tide-marks on rocky coasts. Journal of Ecology 36, 289–305.

[Stevens and Imberger(1996)] Stevens, C., Imberger, J., 1996. The initial response of a stratified lake to a surface shear stress. Journal of Fluid Mechanics 312, 39–66.

[Stevens et al.(2003)] Stevens, C. L., Hurd, C. L., Isachsen, P. E., 2003. Modelling of diffusion boundary-layers in subtidal macroalgal canopies: The response to waves and currents. Aquatic Sciences 65, 81–91.

[Stevens et al.(2002)] Stevens, C. L., Hurd, C. L., Smith, M. J., 2002. Field measurement of the dynamics of the bull kelp durvillaea antarctica (chamisso) heriot. Journal of Experimental Marine Biology and Ecology 269, 147–171.

[Stevens and Taylor(2005)] Stevens, C. L., Taylor, D. I., 2005. Personnal communication.

[Stevens et al.(2008)] Stevens, C. L., Taylor, D. I., Delaux, S., Smith, M. J., Schiel, D. R., 2008. Characterization of wave-influenced macroalgal propagule settlement. Journal of Marine Systems 74(1-2), 96–107.

[Stohl et al.(1998)] Stohl, A., Hittenberger, H., Wotawa, G., 1998. Validation of the lagrangian particle dispersion model flexpart against large-scale tracer experiment data. Atmospheric Environment 32(24), 4245–4264.

[Sutton(1932)] Sutton, O. G., 1932. A theory of eddy diffusion in the atmosphere. Proceedings of the Royal Society of London. Series A. 135(826), 143–165.

[Taira and Colonius(2007)] Taira, K., Colonius, T., 2007. The immersed boundary method: A projection approach. Journal of Computational Physics 225(2), 2118–2137.

[Tan(2007)] Tan, Z., 2007. Adaptive moving mesh methods for two-dimensional resistive magneto-hydrodynamic pde model. Computers and Fluids 36, 758–771.

[Taneda(1956)] Taneda, S., 1956. Experimental investigation of the wake past a sphere at low reynolds numbers. Journal of the Physical Society of Japan 11(3), 1104–1108.

[Taylor et al.(2009)] Taylor, D. I., Delaux, S. D., Stevens, C. L., Nokes, R., Schiel, D. R., 2009. Settlement rates of macroalgal zygotes: Cross-species comparisons of settlement in a turbulent environment. Manuscript.

[Taylor and Schiel(2003)] Taylor, D. I., Schiel, D. R., 2003. Wave-related mortality in zygotes of habitat-forming algae from different exposures in southern new zealand: the importance of 'stickability'. Journal of Experimental Marine Biology and Ecology 290, 229–245.

[Taylor(1915)] Taylor, G. I., 1915. Eddy motion in the atmosphere. Philosophical Transaction of the Royal Society of London 215, 1–16.

[Taylor(1921)] Taylor, G. I., 1921. Diffusion by continuous movements. Proceedings of the London Mathematical Society 20, 196–211.

[Tennekes and Lumley(1972)] Tennekes, H., Lumley, J. L., 1972. A first course in turbulence. The MIT Press.

[Thornton and Guza(1983)] Thornton, E. B., Guza, R. T., 1983. Transformation of wave height distributions. Journal of Geophysical Research 88(C10), 5925–5938.

[Toschi et al.(2006)] Toschi, F., Kobayashi, H., Piomelli, U., Iaccarino, G., 2006. Backward-facing step calculations using the shear improved smagorinsky model. Center for Turbulence Research, Proceedings of the Summer Program, 87–97.

[Toschi et al.(2000)] Toschi, F., Leveque, E., Ruiz-Chavarria, G., 2000. Shear effects in non homogeneous turbulence. Physical Review Letters 85, 1436–1439.

[Tritton(1988)] Tritton, D. J., 1988. Physical Fluid Dynamics. 2nd Ed. Oxford Univ. Press, Oxford.

[Tsai et al.(1991)] Tsai, C. J., Pui, D. Y. H., Liu, B. Y. H., 1991. Elastic flattening and particle adhesion. Journal Aerosol Science and Technology 22, 737–764.

[Udaykumar et al.(2001)] Udaykumar, H. S., Mittal, R., Rampunggoon, P., Khanna, A., 2001. A sharp interface cartesian grid method for simulating flows with complex moving boundaries. Journal of Computational Physics 174, 345–380.

[Udaykumar et al.(1996)] Udaykumar, H. S., Shyy, W., Rao, M. M., 1996. Elafint: A mixed eulerian-lagrangian method for fluids flows with complex and moving boundaries. International Journal of Numerical Methods in Fluids 22, 691–705.

[Uhlherr and Sinclair(1970)] Uhlherr, P. H. T., Sinclair, C. G., 1970. The effect of free-stream turbulence on the drag coefficient of spheres. Proceedings Chemeca '70 1, 1–13.

[USACE(1977)] USACE, 1977. Shore Protection Manual, Third Edition. U.S.Army Coastal Engineering Research Center.

[Vadas et al.(1992)] Vadas, S. R. L., Johnson, S., Norton, T. A., 1992. Recruitment and mortality of early post-settlement stages of benthic algae. British Phycological Journal 27, 331–351.

[van der Meer et al.(1992)] van der Meer, J. J., Fryer, P. J., Rielly, C. D., 1992. A model for fluid flow and mixing in a cavity transfer mixer. Food and Bioproduct Processing 70c, 183–192.

[vanDriest(1956)] vanDriest, E. R., 1956. On turbulent flow near a wall. Journal of Aeronautical Sciences 23, 1007.

[Variano and Cowen(2008)] Variano, E. A., Cowen, E. A., 2008. A random-jet-stirred turbulence tank. Journal of Fluid Mechanics 604, 1–32.

[Vaschy(1892)] Vaschy, A., 1892. Annual Tel. 12, 25.

[Vatistas(1989)] Vatistas, N., 1989. The effect of adhesion time on particle deposition. Chemical Engineering Science 44(8), 1603–1608.

[Vatistas(1992)] Vatistas, N. T., 1992. Effect of adhesion time on particle deposition: Reentrainement and rolling. Industrial Engineering Chemical Research 31, 1549–1554.

[Vermeer et al.(2003)] Vermeer, L. J., Sorensen, J. N., Crespo, A., 2003. Wind turbine wake aerodynamics. Progress in Aerospace Science 39, 467–510.

[Voulgaris and Trowbridge(1998)] Voulgaris, G., Trowbridge, J. H., 1998. Evaluation of the acoustic doppler velocimeter (adv) for turbulence measurements. Journal of Atmospheric and Oceanic Technology 15, 272–289.

[Vreman et al.(1994)] Vreman, B., Geurts, B., Kuerten, H., 1994. On the formulation of the dynamic mixed subgrid-scale model. Physics Fluids A 6(12), 4057–4059.

[Walters et al.(1999)] Walters, L. J., Miron, G., Bourget, E., 1999. Adhesion in barnacles. in: Southward a j (ed). Barnacle biology. Balkema, Rotterdam, 389–403.

[Wang and Fogelson(1999)] Wang, N. T., Fogelson, A. L., 1999. Computational methods for continuum models of platelet aggregation. Journal of Computational Physics 151, 649–675.

[Wang and Bayyuk(1998)] Wang, Z. J., Bayyuk, S. A., 1998. An automated, adaptive, unstructured, cartesian prism-based technique for moving-boundary simulations. Numerical grid generation in computational field simulations.

[Wilcox(2006)] Wilcox, D. C., 2006. Turbulence modeling for CFD, 3rd Edition. DCW Industries.

[Williams and Kelley(1998)] Williams, T., Kelley, C., 1998. Gnuplot: An interactive plotting program. version 4.0. http://www.gnuplot.info/docs$_4$.0/gnuplot.html.

[Wu and Wang(2007)] Wu, C. J., Wang, L., 2007. Direct numerical simulation of self-propelled swimming of 3d bionic fish school. Computational Mechanics, Proceedings of ISCM.

[Yadav et al.(2003)] Yadav, A. K., Raman, S., Niyogi, D. D. S., 2003. A note on the estimation of eddy diffusivity and dissipation length in low winds over a tropical urban terrain. Pure and Applied Geophysics 160, 395–404.

[Yakhot et al.(1989)] Yakhot, A., Orszag, S. A., Yakhot, V., Israeli, M., 1989. Renormalization group formulation of large eddy simulation. Journal of Scientific Computing 4, 139–158.

[Ye et al.(1999)] Ye, T., Mittal, R., Udaykumar, H. S., Shyy, W., 1999. An accurate cartesian grid method for viscous incompressible flows with complex immersed boundaries. Journal of Computational Physics 156, 209–240.

[Yoon et al.(2003)] Yoon, H. S., Balachandar, S., Ha, M. Y., Kar, K., 2003. Large eddy simulation of flow in a stirred tank. Transaction of the ASME 125, 486–499.

[Yoon et al.(2001)] Yoon, H. S., Sharp, K. V., Hill, D. F., Adrian, R. J., Balachandar, S., Ha, M. Y., Kar, K., 2001. Integrated experimental and computational approach to simulation of flow in a stirred tank. Chemical Engineering Science 125, 486–499.

[Young(1999)] Young, I. R., 1999. Wind generated ocean waves. Vol. Volume 2. Elsevier.

[Young(2000)] Young, W. R., 2000. Lectures on stirring and mixing: Eddy diffusion.

[Yung et al.(1989)] Yung, B. P. K., Merry, H., Bott, T. R., 1989. The role of turbulent bursts in particle re-entrainment in aqueous systems. Chemical Engineering Science 44(4), 873–882.

[Zang et al.(1993)] Zang, Y., Street, R. L., Koseff, J. R., 1993. A dynamic mixed subgrid-scale model and its application to turbulent recirculating flows. Physics Fluids A 5(12), 3196–3186.

[Zhang and Zheng(2007)] Zhang, N., Zheng, Z., 2007. An improved direct-forcing immersed-boundary method for finite difference applications. Journal of Computational Physics 221, 250–268.

[Zoppou and Knight(1997)] Zoppou, C., Knight, J. H., 1997. Analytical solutions for advection and advection-diffusion equations with spatially variable coefficients. Journal of Hydraulic Engineering 123(2), 144–147.